A hybrid approach for inclusion of acoustic wave effects in incompressible LES of reacting flows

Gemma Febrer Alles

Ph.D Thesis
November 2012

Department of Aeronautical and
Automotive Engineering
Loughborough University

Acknowledgements

I would like to thank my supervisors, Prof. Jim McGuirk and Dr Zhiyin Yang for their valuable and crucial guidance and support. It has been a privilege and honour to work with them. I wish to express my special gratitude to Prof. McGuirk for giving me the opportunity to become part of the UTC, where I have greatly developed my academic knowledge and technical skills. His commitment and academic rigour, as well as his personal approach have been undoubtly inspirational and decisive for the completion of this PhD.

I would like to acknowledge Cambridge University for permission to use the LOTAN software within the current investigation along with the support of Rolls-Royce plc. The funding from Loughborough University to support the PhD is also gratefully acknowledged.

I would like to thank Simon Stow, whose support and help have been essential. I profoundly appreciate the time and dedication he has offered. He has also contributed to make this thesis possible.

A special thanks to the staff of the UTC and of the Department of Aeronautical and Automotive Engineering, who always provided their kind and useful assistance.

I also would like to thank the exceptional support and friendship of my colleagues in the Department: Jinghua, Zakia, Barani, Mehriar, Victor, Feng, thank you.

To Jinghua, who has been my best and unconditional friend during this PhD. We have shared many personal and academic experiences, inside and outside the department, that have certainly contributed to make this PhD an enjoyable experience.

Als meus pares i germana, perquè sens dubte part d'aquesta tesi també és seva. Sempre he rebut el seu suport incondicional, d'un valor incalculable, en totes les decisions que he pres. Moltes gràcies, de tot cor.

A n'en Cristian, perquè la seva inestimable, incondicional i imprescindible ajuda ha estat més que decisiva a l'hora de fer aquesta tesi. Sense aquest suport, tant moral com acadèmic, aquesta tesi no hauria estat mai possible.

A n'en Genís, ell més que ningú m'ha donat força per acabar aquesta tesi.

Abstract

Lean premixed combustion systems, attractive for low NOx performance, are inherently susceptible to thermo-acoustic instabilities - the interaction between unsteady heat release and excited acoustic wave effects. In the present work, a hybrid, coupled Large Eddy Simulation (LES) CFD approach is described, combining the computational efficiency of incompressible reacting LES with acoustic wave effects captured via an acoustic network model. A flamelet approach with an algebraic Flame Surface Density (FSD) combustion model was used. The ORACLES experiments - a perfectly premixed flame stabilised in a 3D sudden expansion - are used for validation. Simulations of the inert flow agree very well with experimental data, reproducing the measured amplitude and distribution of turbulent fluctuations as well as capturing the asymmetric mean flow. With reaction the measured data exhibit a plane wave acoustic mode at 50Hz. The influence of this plane wave must be incorporated into the LES calculation. Thus, a new approach to sensitise the incompressible LES CFD to acoustic waves is adopted. First an acoustic network model of the experimental geometry is analysed to predict the amplitude of the 50Hz mode just before the flame zone. This is then used to introduce a coherent plane wave at the LES inlet plane at the appropriate amplitude, unlike previous LES studies, which have adopted a "guess and adjust" approach. Incompressible LES predictions of this forced flow then show good agreement with measurements of mean and turbulent velocity, as well as for flame shape, with a considerable improvement relative to unforced simulations. To capitalise on the unsteady flame dynamics provided by LES, simulations with varying forcing amplitude were conducted and analysed. Amplitude dependent Flame Transfer Functions (FTFs) were extracted and fed into an acoustic network model. This allowed prediction of the stable/unstable nature of the flame at each forcing amplitude. An amplitude at which the flame changed from unstable to stable would be an indication that this coupled approach was capable of predicting a limit cycle behaviour. With the current simple FSD combustion model almost all cases studied showed a stable flame. Predictions showed considerable sensitivity to the value chosen for the combustion model parameter but specially to the acoustic geometric configuration and boundary conditions assumed showing evidence of limit cycle behaviour for some combinations. Nevertheless, further work is required to improve both combustion model and the accuracy of acoustic configuration and boundary condition specification.

Contents

Chapter 1

Introduction

1.1 Combustion in modern society : environmental effects

In modern society, around 86% of worldwide energy consumption relies on combustion technologies which use fossil fuels as the primary source of energy, a fact not expected to change substantially in the foreseeable future. Thus, with an ever increasing need for energy for domestic use, power generation, transportation, etc., and an annual growth rate of 2% since the 1980's, a thorough understanding of combustion, leading to enhanced ability to control combustion devices, is of essential scientific and technological interest. Improving the design of combustion equipment will, inevitably, contribute to increased fuel efficiency as well as reduced pollutant emissions.

The well-known disadvantage of non-renewable energy based on fossil fuel combustion is the resulting harmful environmental effects. The greenhouse gases produced by combustion processes, the most important being NO_x, CO_2, CO and to a lesser extent unburnt hydrocarbons (UHC) and soot, all contribute to environmental pollution and global climate change. Burning fossil fuels produces around 21.3 billion tonnes of CO_2 each year and it is estimated that only approximately half of this amount can be absorbed by natural processes [1].

The legislative pressure to reduce these adverse impacts of fossil fuel combustion has consequently been steadily increasing. Civil aviation, for instance, is estimated to be responsible for 2-3 % of CO_2 emissions, increasing to around 4% in 2050. The EU is using a target-driven approach (ACARE [2]) to reduce (by 2020 relative to 2000 levels) fuel consumption (hence CO_2) by 50% per passenger kilometre, NO_x by 80% (in the landing and take-off cycle) and perceived aircraft noise by 50%. Meeting these goals represents significant engineering challenges (and hence inevitably compromises). Figure 1.1 shows an illustrative example of the progress made towards meeting these objectives in the aviation industry. These efforts indicate that the aviation industry has recognised that growth will only be acceptable if both environmental sustainability

and operating efficiency targets are met.

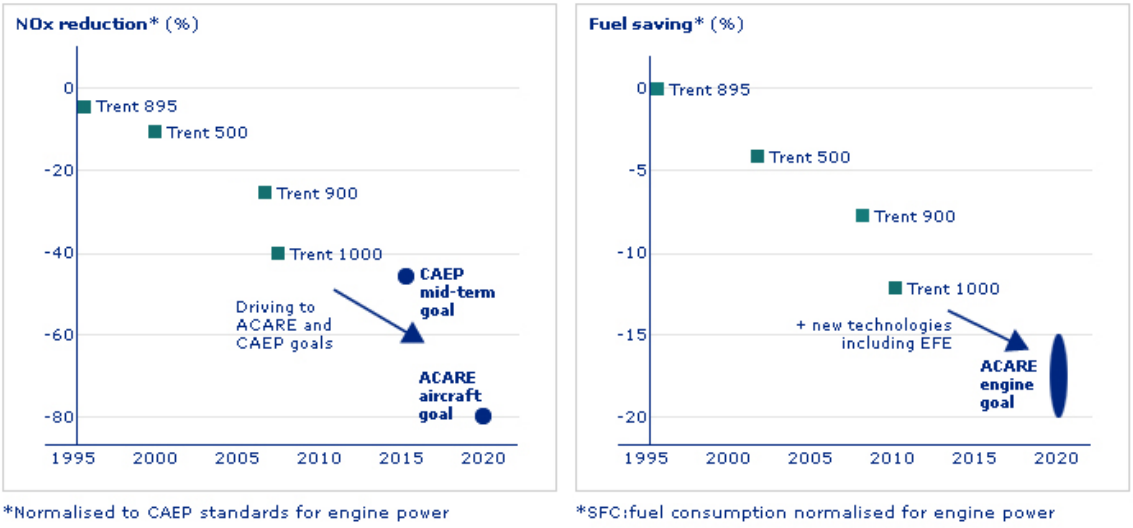

Figure 1.1: Progress towards achieving ACARE goals (NO_x and CO_2 reduction) by 2020, for the Rolls-Royce Trent family engines [3]

High levels of CO and UHC are the consequence of incomplete combustion. If the flame temperature is high enough and sufficient time is available, these products can to a great extent be further oxidised to CO_2 and water. However, even if this is achieved, a major pollutant of concern is NO_x. Most NO_x is generated by fixation of atmospheric nitrogen in the flame, called thermal NO_x. Thermal NO_x production rates drop sharply as flame temperature decreases (see Figure 1.2). However, decreasing temperature also affects CO and smoke emissions. Thus, a compromise must be made on the firing temperature to control both CO and NO_x emissions. For these reasons, the last decade has seen an upsurge of interest in lean-burn, and also possibly premixed, technology to achieve an appropriate $CO - NO_x$ trade-off, increase efficiency and reduce NO_x emissions. This technology represents the most promising forward-looking alternative to traditional rich-burn, non-premixed combustion. In particular, in lean premixed (LPM) combustion systems, fuel and oxidiser are mixed before entering the combustor at a deliberately lean equivalence ratio. The fuel-air ratio is approximately half of the stoichiometric level, meaning that twice as much air as is actually needed to burn the fuel is supplied to the combustion chamber. It is this excess of air that plays a key role to limit NO_x formation, which takes place only in a high temperature environment (see Figure 1.2). Such high temperatures will not be reached in very lean conditions, thus preventing NO_x production. In addition, premixing prevents the occurrence of local *hot spots* within the combustor volume, that

can also lead to significant NO_x formation. In general, LPM systems are designed to operate near the lean flammability limit, and are characterised by the above mentioned trade-off of CO/NO_x. At the combustor design point, both CO and NO_x are below targeted values although deviations from the design point flame temperature will cause emissions to increase.

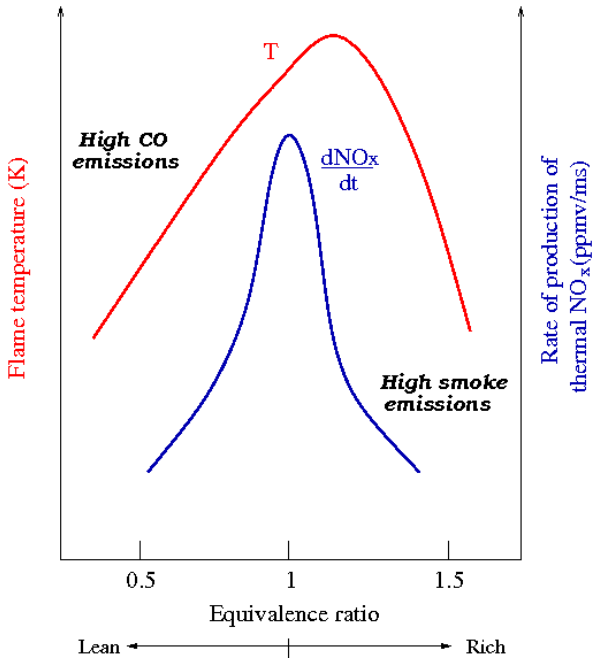

Figure 1.2: NO_x production rates [4]

It must be mentioned, however, that the main drawback of lean combustion systems is their vulnerability to thermo-acoustic instabilities. These are combustion-induced periodic oscillations in pressure sustained via a feedback mechanism between the combustion heat release and the acoustic waves propagating from the flame zone to the combustion system boundaries. Such combustion-sustained pressure oscillations can grow to reach levels which can be damaging to the combustion hardware. It is clear therefore that lean burn technology can only succeed if the problem of thermo-acoustic oscillations is given special attention to be either avoided or controlled; the subject of the impact of thermo-acoustic instabilities has been reviewed thoroughly in [5, 6].

The pollution reduction and specific fuel consumption improvements shown in Figure 1.1 for aeroengines have been achieved using rich-burn technology. This involves the liquid fuel being injected, evaporated and burnt in a rich (equivalence ratio $\phi \approx 1.5$) primary zone and under diffusion flame, swirl-stabilised conditions. Thus, the fuel and

air ($\approx 30\%$ of the compressor efflux) are introduced via the injector separately into the head of the combustor. The rest of the air flows around the combustor head, entering via cooling and dilution holes, which serve the purpose of keeping the combustor liner cool and adjusting the hot gas temperature to a profile that is acceptable by the turbine at combustor exit.

The improved design of fuel injectors and air admission schemes is what has lead rich-burn technology to progress in the manner indicated in Figure 1.1. There is, however, no doubt that continued development of the rich-burn paradigm is becoming ever harder, particularly for NO_x and, as indicated in Figure 1.1, new technologies will have to be introduced. For NO_x, lean-burn and possibly premixed combustion, which has already shown enormous benefits for low NO_x emissions in stationary, land-based gas turbines for power generation, is the technology of greatest industrial interest. To introduce lean, premixed, prevaporised (LPP) combustion must be the long term target for aeroengines, but this is extremely challenging. At the present time lean-burn systems are just beginning to be introduced [7] but even this step requires large changes to the fuel injector (e.g. increasing the airflow to 70%) and will take some time to realise.

Nevertheless, lean premixed turbulent (because of the high Reynolds numbers of practical devices) combustion must be studied vigorously if understanding is to be improved to the level where it can aid design. This is thus the technical driver of the research described in the present thesis. In particular, since Computational Fluid Dynamics (CFD) has made a significant contribution to both non-reacting and combusting turbulent flows [8–10], it is the type of CFD model most appropriate for premixed turbulent combustion that is the main focus of the project described here. As this brief introduction has indicated, the presence of thermo-acoustic instabilities cannot be ignored. The high-level objective of the present research was therefore to identify an optimum CFD approach to prediction of (i) premixed turbulent combustion, in association with (ii) thermo-acoustic oscillations; these two topics are therefore reviewed in the next two sections.

1.2 Turbulent premixed combustion - CFD prediction tools

Turbulent premixed combustion is a complex phenomenon that involves a wide range of disciplines, thermodynamics, chemical kinetics, molecular transport phenomena, heat and mass transfer in single and multiphase systems, radiation, turbulent fluid mechanics, acoustics, etc. An understanding of all these disciplines and their interaction, is

required to describe such complex processes fully. Combustion itself, even in the absence of turbulence, is an inherently complicated process involving a large range of chemical time scales for different reactions, as well as multicomponent fluid mechanics and mixing. Chemical mechanisms describing in detail and at a fundamental level even simple laminar flames may require hundreds of species and thousands of reactions [10–12]. Likewise, turbulence is probably the most complex aspect to deal with in any computational approach even in non-reacting fluid mechanics. Some aspects of the structure and full description of turbulence still remain open questions although an enormous amount of literature on this topic is available [13–15]. Thus, turbulent premixed combustion, a result of the two-way interaction of chemistry and turbulence, constitutes an even more complicated phenomenon, and its description and prediction represents an extremely challenging task.

Clearly, a relevant ingredient for design and optimisation of combustion equipment is a validated numerical prediction procedure that accurately captures the essential physical and chemical characteristics of turbulent premixed reacting flows. Hence, rigorous mathematical formulation of the equations governing turbulent combustion phenomena has been an important focus of study for at least 50 years [10–12, 15] . Turbulent combusting fluid dynamics is mathematically described via partial differential equations: the Navier-Stokes (NS) equations (formulated more than a century ago), the energy and species transport equations, and the equation of state. The ever-increasing development of both high performance computers and numerical and modelling analysis applied to fluid dynamics in the last 5 or 6 decades has established the basis for Computational Fluid Dynamics (CFD) [9, 16, 17] . CFD is a powerful tool for prediction of time-dependent flows, by numerical solution of the discretised modelled governing equations. CFD approaches differ depending on the level of description of turbulence, see Figure 1.3 - this displays an illustration of a high Reynolds number energy spectral density - the variation with the spatial wavenumber or the temporal frequency of the kinetic energy content of the wide range of fluctuating turbulent eddies which characterise turbulence. Direct Numerical Simulation, DNS, involves solution of the governing equations without any modelling assumptions but is computationally too expensive and limited to low Reynolds numbers and reduced chemical kinetics (recently DNS of laboratory jet flame experiments have been reported with realistic chemical kinetics [18, 19]). Thus, it is not able to meet the urgent need for industrially relevant predictive methods, although it is an extremely valuable research tool. RANS/U-RANS(Unsteady Reynolds Averaged Navier-Stokes) resolves unsteady mean flow structures but details of the turbulence spectrum as shown in Figure 1.3 are not taken into account. This has been found inadequate for flows which are strongly 3D or which contain separated regions, which are often involved in combustion processes. Despite this, it is still the tool most used in industry because of its robustness and affordable computational cost. LES (Large Eddy Simulation), where the larger (more

energetic) turbulent motions are explicitly resolved in the computational mesh and the effect of the smaller unresolved scales is modelled (via a so-called Sub-Grid-Scale (SGS) model), can be presented as a compromise and a tool potentially capable of more accurate representation of turbulence effects in the complex flows of practical industrial interest. Recent critical reviews of LES can be found in [14, 15, 20–25] . Although LES for reacting flows is still under development, with some issues still in need of clarification [15, 20, 22–25], the technique has been successfully applied to non-reacting flows [22, 26–29], and its level of maturity makes its demonstrated advantages (in particular an improvement over RANS of turbulent mixing processes) particularly useful for reacting flow simulations.

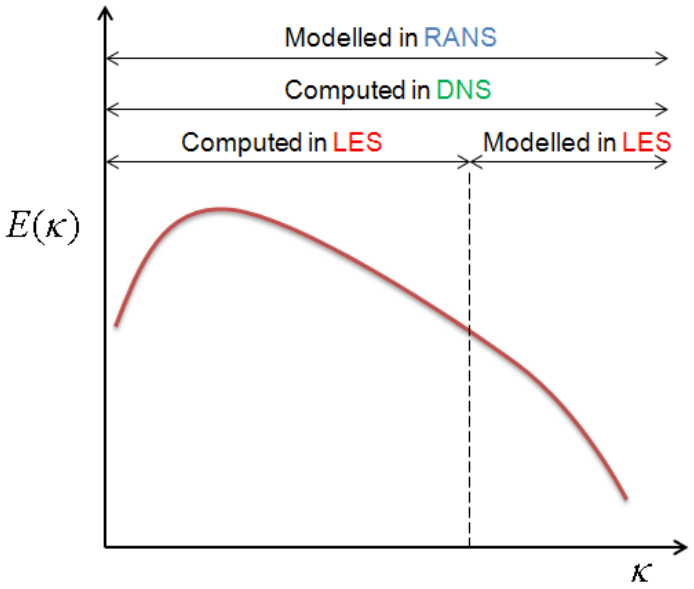

Figure 1.3: Computed and modelled scales in the turbulence energy spectrum for RANS, LES and DNS approaches. κ indicates spatial wavenumber or temporal frequency

In the present thesis LES is therefore the preferred CFD approach, since it is a very promising tool for combustion studies, as evidenced in [30, 31] . The main LES features endorsing this choice are: (i) the large scales, containing most of the turbulent kinetic energy and controlling the dynamics of the turbulence, are generally flow case dependent (geometry configuration, boundary conditions, etc) and these are explicitly resolved, whereas (particularly at high Re) smaller eddies have more universal features and are more suitable for modelling [32]; (ii) the mixing of fresh and burnt gas zones, having different mean flow and turbulence characteristics, are readily identified at the resolved grid level and a better description of turbulence-chemistry interaction can

thus be expected [24] ; (iii) although LES accuracy (adequate resolution of a sufficient range of energy containing turbulence structures) represents a difficult challenge near walls [14, 20–22, 33, 34] , important aspects of combustion (e.g. heat release reactions, pollution formation, etc.) frequently take place far away from walls; (iv) reacting flows exhibit large coherent structures, such as the ones observed when thermo-acoustic instabilities are present and LES offers prospects for capturing these [35] . Therefore, the use of LES, provided adequate SGS modelling and grid resolution are chosen, offers the ideal framework to solve accurately for the mixing and combusting processes of the detached flows commonly found in combustion systems. Details of the LES tools used in the present research are provided in later chapters.

Development of LES for turbulent combusting flows (CLES) has emerged as a field of wide interest in the 1990's. Reviews on progress and also difficulties and existing limitations on CLES, can be found in [24, 36–40]. CLES has already been applied to practically relevant combustion problems such as gas turbine combustion [41–43], pollutant prediction [44], reciprocating engine combustion [45], combustion, flashback and blow-off in premixed stationary power-generation gas turbine combustors [46–48], and combustion instabilities [49–51]. Since the governing equations (continuity, momentum, species mass fractions and enthalpy or equivalent) are spatially filtered in the LES approach (for details on filtering procedures see [20, 22, 23]), unknown terms known as unresolved residual or sub-grid-scale (SGS) terms appear that require closure modelling, e.g. SGS-stress tensor, SGS-species transport, also a filtered chemical reaction source term must be modelled. The SGS term represents the scalar mixing processes due to the unresolved fluctuations; these can be modelled adequately, at least for isothermal flows, in a manner analogous to the modelling of the SGS term for the unresolved stresses in the momentum equations, see for example Cheng et al. [52], where, for a non-reacting flow from a high swirl fuel injector, the scalar mixing is predicted very well using the standard Smagorinsky SGS model [53]. This thesis will use the same CFD code (referred to below as "LULES") as employed in the non-reacting study of [52] but extend this to allow premixed combustion.

Specifically, in LPM combustion systems, turbulent mixing stirs the unburnt mixture with hot combustion products. However, only mixing at the molecular level promotes chemical reaction. From a numerical point of view, the problem encountered in LES is that molecular mixing of scalar quantities and chemical reaction occur essentially at the smallest turbulence scales, hence at a scale much smaller than a typical LES grid size is able to resolve. The flame front cannot be resolved in the computation, and the filtered chemical source term, describing a combustion process occurring at a subgrid scale level, has to be entirely modelled, and the modelling of this term in the filtered LES equations represents the highest challenge in combusting LES.

The development of premixed combustion models in the RANS context started approximately 40 years ago, for example with the pioneering work of Spalding [54] followed some years later by a proposal for an Eddy Break Up model [55]. The fundamental concepts and basic ideas used in RANS models, which are still in use today, can also be applied to LES. Nonetheless, it is worth stressing that LES also offers new modelling opportunities to be explored (e.g. similarity models or dynamic formalisms where model parameters are automatically adjusted during the simulation). In what follows a brief overview of chemical source term models proposed for LES of turbulent premixed flows is given.

SGS premixed combustion models can be divided into two categories: flamelet and non-flamelet models [56]. In the former group are flame surface density/flame wrinkling models [57–59], G-equation models [60], turbulent flame speed models [61] and linear eddy models [62] . Non-flamelet models include thickened flame models [63] and an LES version of the Eddy-Break-Up model [64] . The three approaches most extensively used in the LES combustion community to date are briefly outlined here:

- **Artificially thickened flames:** This solution, first proposed by Butler and O'Rourke [65], to resolve and enable correct propagation of a premixed flame on a coarse grid, essentially thickens the flame front by modifying the species diffusion parameter so that it can be resolved on the LES computational mesh. Following simple theories of premixed flames ([11, 12]), the diffusivity is increased by a factor F and the pre-exponential constant in the chemical reaction source term is decreased by the same factor, producing a thickened premixed flame which is resolved spatially but which still maintains the correct flame speed (see Figure 1.4(a)). The factor F can also vary in the computational domain and be dynamically calculated, as proposed in [66]. However, when the flame thickness is modified, the interaction between turbulence and chemistry is also modified, since the flame sensitivity to turbulent motions is altered. This has been investigated using DNS in [63, 67]. To account for this effect, an efficiency function E, corresponding to an SGS wrinkling factor, is derived and incorporated in the formulation [63] . In general, the main advantage of this approach is that it has proved successful in capturing transient combustion phenomena such as ignition, extinction and flame-wall interaction, since the Arrhenius law and complex chemistry can be employed. Nonetheless, when complex chemistry is incorporated, as all chemical species have to be resolved on the numerical grid, some radicals or intermediate species may induce prohibitive thickening factors or may require larger numerical grids.

- **G-equation or flame tracking technique:** First proposed by Williams [11], the flame thickness is assumed to be zero and the flame front is considered to be a propagating surface tracked using a level-set function $\tilde{G}$. Likewise, in LES the

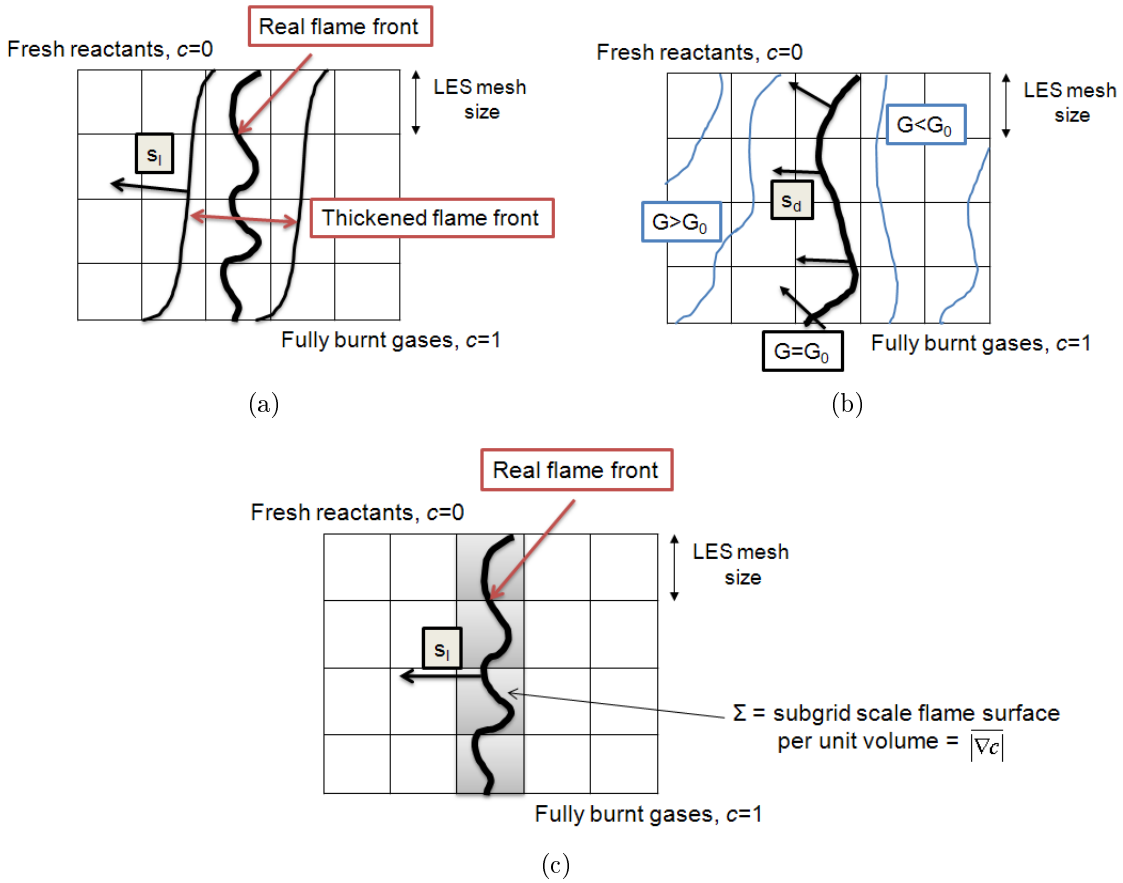

Figure 1.4: Schematic of (a) Thickened flame, (b) G-equation and (c) Flame Surface Density approaches for modelling of chemical source term

flame brush is associated with an instantaneous isocontour of $\tilde{G}$, say G_0. The value of $\tilde{G}$ away from the flame front is arbitrary within some limits but it is common to identify the flame front with the value $\tilde{G} = 0$; $\tilde{G} > 0$ is the unburnt mixture and $\tilde{G} < 0$ is the burnt gases (see Figure 1.4(b)). The G-equation is not strictly a flame model, but rather a numerical technique to overcome the flame resolution problem. Several LES formulations of the G-equation method have been proposed in the literature [56, 60, 68]. In addition, a formulation based on new filtering techniques consistent with the so-called generalised scaling symmetry [69] has been proposed by Pitsch [70]. The G-equation technique has become popular for LES of turbulent premixed combustion, since there is no need to follow progress variable gradients (see below) but instead the flame surface is captured via the level set, and only a model for the "turbulent" flame speed is needed. Nevertheless some well-known drawbacks are flame cusps that

are created, which require added artificial diffusion in order that these may be avoided [71].

- **Flame surface density/wrinkled flame formulations:** The premixed turbulent flame is here viewed as an ensemble of small laminar flame elements, or flamelets, with structure assumed to be close to a laminar (perhaps strained) flame. A spatially filtered reaction progress variable (c) balance equation is derived (see [57], details to be provided below), where the molecular diffusion term and the chemical reaction term are identified as a "flame front displacement term" (volumetric consumption rate of unburnt gases) and characterised by a local displacement speed of the flame isosurface c. The flame front displacement term is then modelled as the product of a laminar burning rate ($\rho_u s_l$, ρ_u = unburnt mixture density, s_l = unstrained laminar flame speed) times an overall flame surface area ($\Sigma = \Xi\,|\nabla \bar{c}|$, where $\bar{c}$ is the spatially filtered reaction progress variable (see Figure 1.4(c))). Σ is known as the SGS flame surface density (FSD), or flame surface area per unit volume at the subgrid scale level, whereas Ξ is the SGS flame wrinkling factor, or ratio between the SGS flame surface and its projection in the propagation direction. Models for Σ and Ξ are thus required. The FSD based reaction rate closure is well established in a RANS context, and these models have recently been extended to LES. Thus, algebraic expressions [57, 72, 73] , similarity models [74, 75] or balance equations [57–59] have been proposed (in [58] the model included the resolved contributions associated with effects of propagation, curvature and strain, typically neglected in RANS, although not much more accurate results were obtained after including these). In [76] extensive experimental data on flame surface density measurements in turbulent premixed combustion are available. For an exhaustive review on algebraic flame surface density models in the LES context see [73]. The main advantage of the FSD approach is that c and related quantities are physically defined and can be extracted from DNS or experimental measurements, and also fairly simple models have been found to provide reasonably accurate results.

In the present thesis, the algebraic FSD model of Boger et al. [57] in a progress variable framework has been selected for use. This model represents one of the simplest approaches to model the chemical source term, with a single model constant to be tuned. This approach has been extensively and successfully used in flows involving separation, which is an important element of most practical combustion devices. The simulation of a V-shaped premixed propane/air flame stabilised behind a triangular flame holder [72] showed good performance. It was demonstrated that the counter-gradient phenomenon, very difficult to predict using RANS models, could be observed with CLES using this algebraic model. Similarly, a turbulent premixed flame propagating through a chamber containing a square obstruction was simulated in [77, 78], obtaining very good predictions for flame speed, flame structure, overpressure and its rate of increase.

In [79], lean premixed methane/air combustion in turbulent opposed jets at moderate Reynolds numbers was simulated, with very good predictions for both velocity and progress variable fields. Finally, in [80], simulation of a premixed propane/air flame stabilised on a symmetric sudden expansion at moderate Reynolds number was performed. Good agreement with experimental data was achieved for first and second order statistics of the velocity field.

Based on these observations, and considering that the primary focus of the present thesis is the consideration of both turbulent premixed combustion and acoustic effects (rather than the development of an improved FSD model), this algebraic FSD model has been selected for the present work. The progress variable approach was already incorporated into the LES code mentioned above (LULES) and had been used for non-reacting scalar mixing for a high swirl fuel injector [52] , and for a premixed flame case without considering acoustics and with no detailed validation in [80]. Thus, for the present work, it is important to select a premixed flame experiment as a test case to ensure that the combustion model has been properly implemented into the LULES code to be used here. An ideal data set for such validation is the ORACLES (One Rig for Accurate Comparison with Large-Eddy Simulations) test case [81, 82] , which, as its name implies, was specially designed to validate LES premixed turbulent combustion phenomena and includes extensive data to validate large-scale flow unsteadiness and measurements of turbulence properties controlling turbulent transport and combustion features. It considers a turbulent flow stabilised behind a double symmetric, plane sudden expansion fed by two fully developed turbulent channel flows of perfectly (or partially) premixed air and propane. A schematic of the ORACLES geometry is shown in Figure 1.5. Flame visualisations for different reacting flow experiments are displayed in Figure 1.6, which illustrate the way in which large scale unsteadiness in separated flows causes thickening of the time-averaged flame "brush". Further, the ORACLES flame was observed to display self-sustained thermo-acoustic instabilities (see [82] for details), therefore seems particularly suitable in the context of this project. The ORACLES experiment will be described further below.

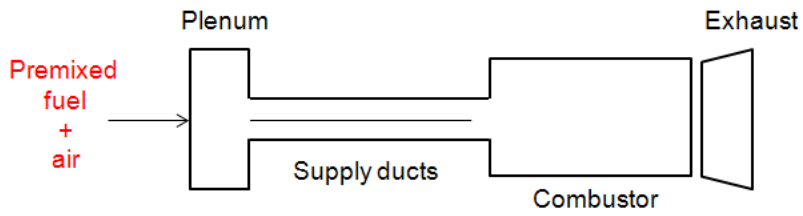

Figure 1.5: Schematic of the ORACLES [81, 82] test rig

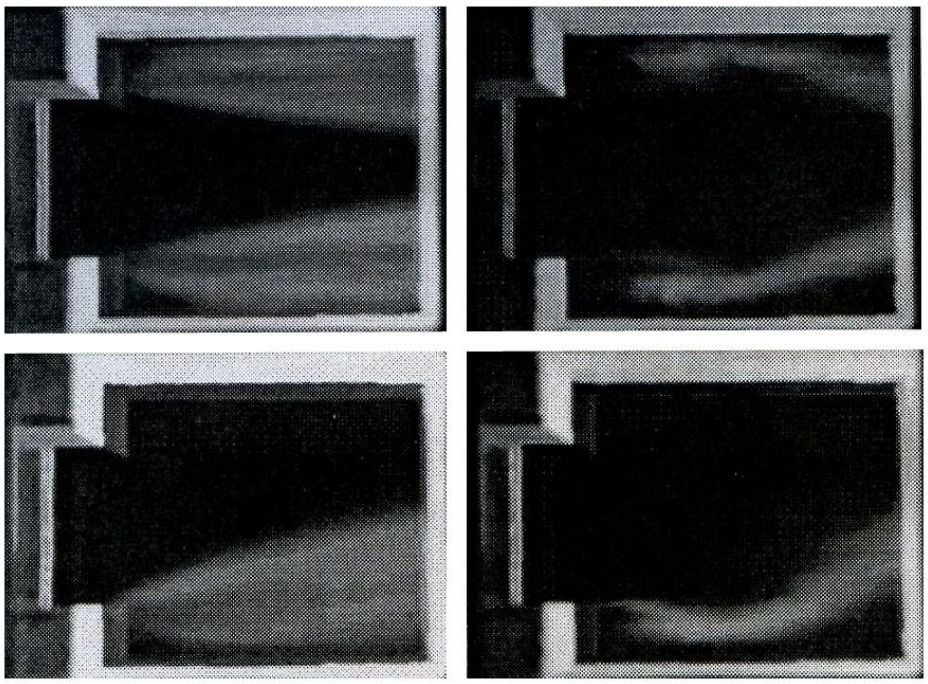

Figure 1.6: Self-luminescence visualisation of combustion zone of ORACLES test rig [81, 82] for cases named c_1 (top) and c_2 (bottom): mean (left column) and instantaneous (right column) flame brushes

1.3 Turbulent premixed combustion - thermo-acoustic instabilities - experiments and prediction

As pointed out earlier, the susceptibility of lean-premixed combustion systems to thermo-acoustic instabilities represents a major limitation and a challenging task for safe operation, demanding avoidance or control strategies. Acoustic waves produced by fluctuations in heat release can in turn generate more unsteady heat release leading to possible amplification and self-sustained feedback [83] . A thorough understanding of these instabilities, and the conditions under which they initiate and develop, is of crucial importance to be identified at the design stage, in order to create passive and active damping technologies.

The range of phenomena leading to instability are still a matter of discussion. At least two mechanisms have been identified: flame-vortex interaction [84, 85] and feed system coupling [86–90]. It is of course possible for both mechanisms to play a combined role. The former refers to interaction between the flame front and vortices that are periodically shed at the entrance of the combustor. The flame is stretched by the

vortex prompting either an increase in flame area (hence increase in heat release) or local extinction due to high strain rates (hence decrease in heat release). The second mechanism refers to fuel/air ratio modulation in the flow supplying reactants to the flame caused by changes in either fuel or (much more likely if the fuel is introduced in liquid form) air mass flow rates as a result of acoustic pressure fluctuations propagating from the flame to the supply system. This can alter the subsequent fuel/air mixing processes and, when convected to the flame front, result in amplification or damping of the heat release rate depending on the relative phase between pressure and heat release fluctuations. Specifically, in premixed combustors, this second mechanism has been identified as a key process controlling combustor stability [5, 88].

Thus, an essential element in the analysis of lean premixed systems and associated thermo-acoustic instabilities is a thorough understanding of the flame response to acoustically induced velocity perturbations. These inlet perturbations modulate the flame dynamics inducing periodic events (change in flame location, size and shape) that drive heat release oscillations. Likewise, the flame response will be considerably modified under varying conditions of perturbation frequency, amplitude, equivalence ratio, swirl number, etc. This relationship between flow conditions and heat release rate perturbations is quantitatively described by means of a Flame Transfer Function (FTF). This has been a continuous subject of analytical [91–95], numerical [94, 96–101] but most extensively experimental [96, 97, 102–112] studies.

In industry, experimental work still represents undoubtedly the major contribution to assessment of thermo-acoustic instabilities in combustion systems. However, much effort is also being invested into the development of CFD tools for this problem. In particular, LES-based CFD is believed to be especially suitable for the numerical study of combustion dynamics and acoustics [49–51, 94, 113], due to its inherent unsteady framework, and because the unsteady turbulent-energy containing motions (controlling mixing and large scale flame wrinkling) are explicitly calculated. Nonetheless, to date rather little numerical work on the study of thermo-acoustic instabilities and extraction of FTFs from CFD has been published, it is thus still at an early stage and further progress is required. One crucial aspect to consider is that for the numerical study of combustion thermo-acoustics, since acoustic processes have to be considered, some treatment of compressibility effects and the related finite speed of sound are essential. Right away this raises a challenge to identify the optimum CFD approach, since the majority of reacting flow predictions for complex geometry combustors, particularly in the LES domain, have adopted an incompressible formulation [114, 115], justified by the low Mach number (typically less than 0.3) of most gas turbine combustors, although some compressible CFD strategies have been adopted to include acoustics [94, 101]. Nevertheless, a fully compressible formulation could automatically capture the acoustics. Thus, based on reported studies and ongoing research work, three different

routes can be followed in order to obtain FTFs of a premixed combustion system:

- FTFs can be extracted experimentally. A loudspeaker is used to artificially excite a flame in a combustion test rig for a range of frequencies and amplitudes (acoustically sensitising the experiment); the resulting FTF extracted from the measurements is then used in an acoustic network model to examine the growth rate of the disturbance (stable or unstable) (Discussion on acoustic network models is provided in chapter 3 below). Figures 1.7 [103] and 1.8 [111] show experimental flame visualisations of flame response (at different phases of the forcing period) to loudspeaker-driven acoustic perturbations at 100 Hz (Figure 1.7) and 75Hz (Figure 1.8) in two different combustor configurations, and at different equivalence ratios, with extracted FTFs, expressed in terms of gain and phase characteristics of the flame response. In [103] fluid dynamics conditions of ring-vortex formation and stretching in a swirl burner due to the unsteady inlet flow caused by acoustic effects were observed for both isothermal and combusting flow, and FTFs of a lean-premixed flame were presented for a range of forcing frequencies, indicating a clearly differentiated frequency dependent dynamic behaviour of the flame for different swirl numbers. In [111] flame visualisations and FTFs were presented for a premixed backstep stabilised flame under varying conditions of excitation frequency and inlet velocity fluctuation amplitude achieved using a variable-speed siren. Nonlinear flame response was identified and characterised for a range of frequencies and inlet velocity fluctuation amplitudes.

- LES CFD calculations based on a fully compressible formulation can be applied as a tool to generate FTFs numerically. In this approach the mixing and combustion processes which effectively define the FTF are predicted, as well as the acoustics, which are automatically captured using a compressible approach. However, this then has the unfortunate consequence that a very small time step is required, due to the speed of sound entering the CFL number that limits the time step (for numerical reasons with explicit numerical methods, but on accuracy grounds even if implicit methods are used). For low-Mach number flames, this implies a large increase in computational cost in comparison to the equivalent incompressible LES calculation, since the maximum time step reduces by at least one order of magnitude (scales with the speed of sound in compressible LES but the flow speed in incompressible LES), but the computational/sampling time for the LES to achieve a statistically stationary state is long (a function of residence time, which scales with the low speed convective velocity). This approach has been recently applied to different flame configurations of industrial interest. For example in [101] flow topology and flame dynamics under acoustically forced conditions were identified and described for a swirled partially-premixed combustor, and predicted FTFs presented. Figure 1.9 displays a temperature isosurface (1000K) coloured by axial velocity at different phases of a pulsation cycle

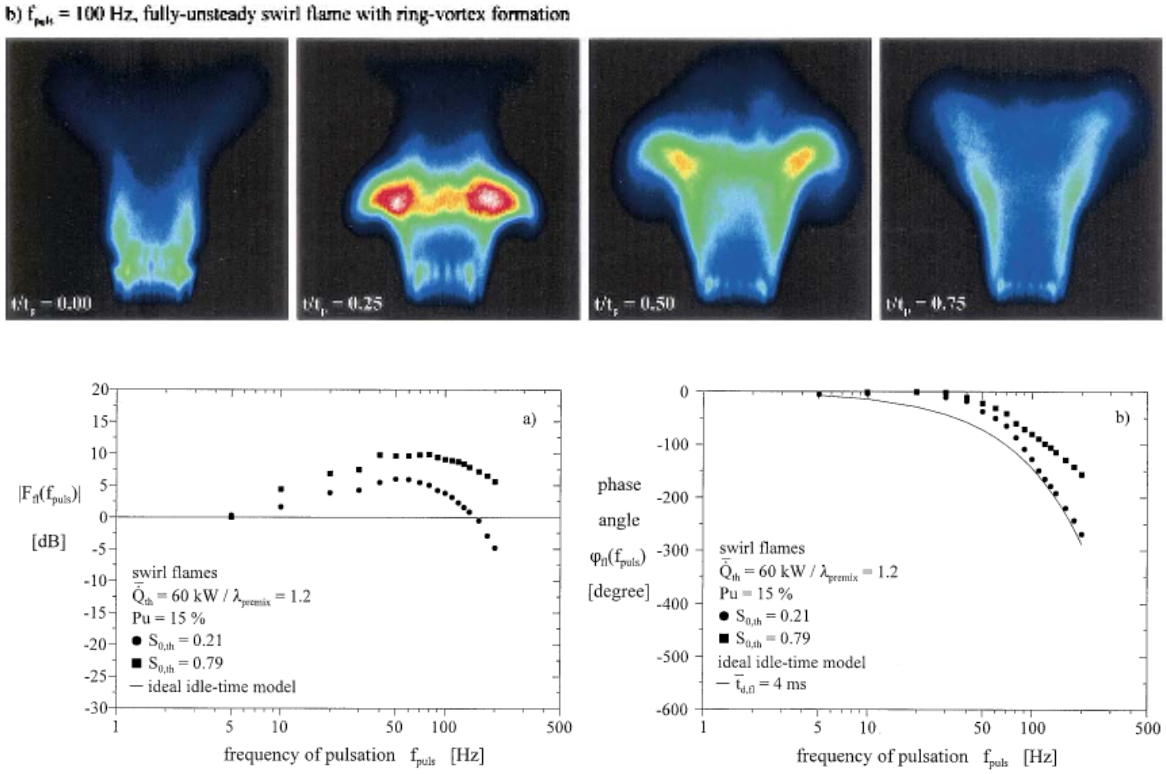

Figure 1.7: [103]: Phase-correlated image-recording of ring-vortex formation during one period of oscillation, $f = 100$Hz, $\phi = 0.83$,A=15% (top) and FTF at same inlet conditions and different swirl numbers versus frequency (bottom)

for a forced calculation at a frequency of 120Hz, showing the mushroom-shaped response of the forced flame and its associated strong variation in shape and size.

- An alternative coupled hybrid LES approach to FTF evaluation could be followed, which is similar to the experimental approach. This would couple: (i) an incompressible LES code used to solve for mixing and combustion, with (ii) an acoustic code provided by an acoustic network model. This approach has the attractive advantage of a large reduction in (LES) computational time compared to the use of compressible LES, probably around two orders of magnitude. A further benefit of this approach is that optimum numerical methods can be selected for turbulent mixing and reaction and for acoustic motions separately. Of course how the two codes should be coupled is by no means straightforward. In essence, information on the unsteady heat release has to be extracted from the LES and transferred to the acoustic code in the form of an FTF as in the experimental approach. Similarly, information on the acoustic waves excited by the unsteady

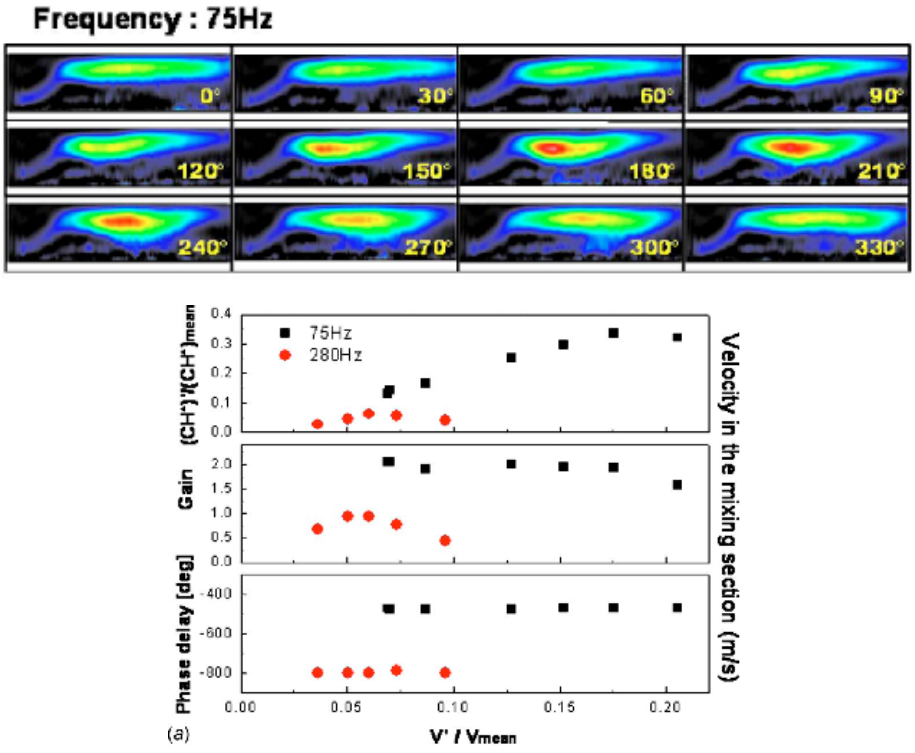

Figure 1.8: [111] : Flame structure for one period of oscillation, $f = 75\text{Hz}, V_{inlet} = 30m/s, \phi = 0.65$, A=7% (top) and FTF and nondimensional chemiluminiscence fluctuation at same inlet conditions and several frequencies versus forcing amplitude (bottom)

heat release has to be extracted from the acoustic code and transferred to the LES by means of altering the inlet flow boundary conditions for which the LES code is run, thereby acoustically "sensitising" the incompressible LES prediction in a similar manner to the loudspeaker or siren in the experimental approach. This third approach does not seem to have been explored to date computationally and thus investigation in this area is the main focus of the present thesis. The ORACLES experimental study [81, 82] previously introduced has been selected for CLES validation purposes. A self-excited self-sustained thermo-acoustic instability was found in the reacting flow measurements, which makes the experiment very suitable also for testing the hybrid LES/acoustic code coupling.

Previous CFD studies of the ORACLES test case using incompressible CLES have been reported [116–118]. The presence of acoustic wave effects was included by adding a plane wave perturbation to the inlet velocity at the frequency observed in the experiments. However, the amplitude of this forcing was not related at all to any acoustic

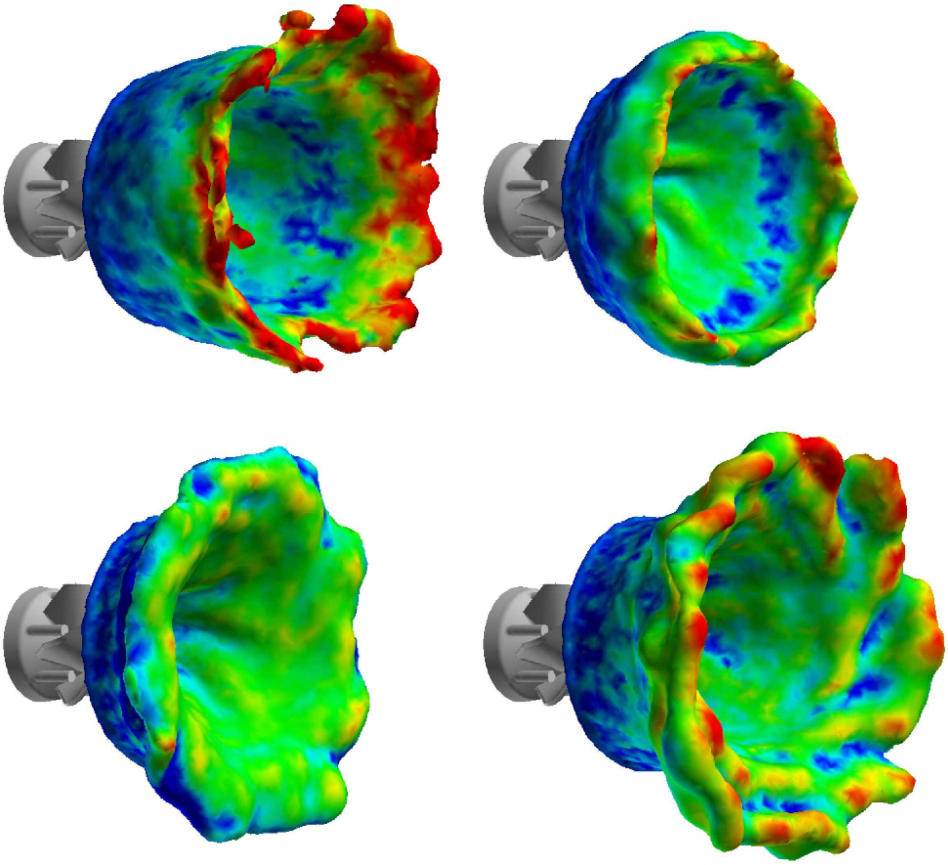

Figure 1.9: Temperature isocontours (1000K) coloured by axial velocity at four different phases of a periodic cycle, $f = 120Hz$ (taken from [101])

analysis of the system but chosen simply from trial and error. Thus, Duwig and Fureby [117] merely varied the forcing amplitude until saturation was observed. In the present thesis, the inlet velocity amplitude is obtained from an acoustic network model, calibrated using experimental data. This methodology is aimed at providing a rational framework for identifying the dimensional forcing amplitude, which avoids running a sequence of LES calculations merely as part of the trial an error approach. Analysis of the flame dynamics for a range of amplitudes of inlet velocity fluctuations is still required if FTFs which are amplitude dependent are to be identified to examine both linear and non-linear response. Indeed, it is notworthy that most of the experimental, analytical and numerical FTF studies have been devoted to characterise only the onset of instability by determining a linear transfer function of the system. Relatively few studies focus on mechanisms leading to saturation (limit cycles) or on effects of growing amplitude of forcing. Some experimental work has revealed nonlinear behaviour

of swirled flames subject to high-amplitude forcing [119], and analytical studies [120] have described the reduction in growth rate which leads to limit cycle behaviour due to saturation processes in response to increasing perturbation amplitude. In the present thesis, it is therefore a sub-objective of the work, having established a hybrid incompressible LES/acoustic network coupling methodology, to explore the possibility that the hybrid approach might be able to capture saturation/limit cycle behaviour.

1.4 Objectives of the current study

Based on the descriptions provided in the previous sections, where a background context to lean premixed combustion influenced by thermo-acoustics was presented, followed by a perspective on various approaches to numerical modelling by using LES of turbulent premixed reacting flow, the main objectives of the current study may be summarised as:

- Extend and validate an existing in-house LES code (LULES) to allow analysis of premixed reacting turbulent flows:
  - the extension will involve implemention of a methodology to generate appropriate (experimentally matched) 3D unsteady LES inlet boundary conditions,
  - validation of the code will be carried out by performing both inert and reacting flow simulations of the ORACLES test case [81, 82] for different operating conditions and detailed comparison with experimental data.
- Extend and validate the LES code to include acoustic wave effects into the simulations by means of acoustically sensitised inlet boundary conditions using an acoustic network code:
  - the acoustic network code will be used to determine the dimensional forcing amplitude of the acoustic mode found in the ORACLES experiments.
  - incorporate acoustic wave effects in the simulation by including a periodic coherent fluctuation at a specified frequency and previously determined forcing amplitude onto the incoming streamwise velocity field.
  - validate CLES predictions for velocity and progress variable fields against experimental data when acoustic effects are included in the simulation
- Establish coupling between the incompressible CLES code and the acoustic network code via analysis of the flame dynamic response under forcing at increasing amplitude, i.e. calculate amplitude dependent Flame Transfer Functions (FTFs):

- perform reacting flow simulations with acoustically sensitised inlet boundary conditions over a range of forcing amplitudes
- generate local FTFs for different regions of the flame, covering the whole heat release region. Examine these for evidence of linear and nonlinear regimes
- search for possible saturation effects in the nonlinear flame response
- incorporate the LES-deduced FTFs into a thermo-acoustic network code to explore the possibility of existence of a limit cycle behaviour

1.5 Outline of the thesis

In the remainder of the thesis six more chapters are presented. In chapter 2, the mathematical formulation for a multi-species, low-Mach number premixed turbulent reactive flow is developed. Chapter 3 then summarises the numerical methodology embodied in the in-house Loughborough University code LULES used to solve this system of equations. Chapter 4 presents a similar mathematical and numerical exposition of the acoustic network model used in the present work. The mathematical and numerical methods explained in previous chapters are then applied to the ORACLES test case and results discussed first in chapter 5 without consideration of acoustic wave effects. In chapter 6, acoustic effects are included in the simulations and results for velocity field, flame dynamics and flame response to acoustically induced velocity perturbations are analysed. The response is quantified in the form of an amplitude dependent Flame Transfer Function (FTF); linear and nonlinear regimes in the flame response are identified and saturation mechanisms leading to nonlinear flame response are discussed; also, sensitivity of the stability of the predicted modes (hence of the predicted limit cycle behaviour) to flame model and acoustic parameters is investigated. Finally, conclusions extracted from the present work and suggestions for future work are summarised in chapter 7.

Chapter 2

Premixed turbulent combustion - LES CFD tools and the flamelet modelling approach

This chapter presents the equations that are considered in this thesis to govern turbulent premixed combusting flows and whose numerical solution is sought. In the first section, the fundamental equations describing a multicomponent reactive flow following a continuum assumption as well as a few commonly made other simplifications are presented. Second, in the context of turbulent flow, modelling of the equations in an LES framework is considered. Third, the flamelet modelling approach used to describe the thermochemical state of the system is outlined. Finally, the complete set of modelled governing equations that are solved numerically in this project are summarised.

2.1 Governing equations for multicomponent reactive flows

The governing equations which express the laws of mass, momentum, energy conservation and species and mass transport for a multi-species, low-Mach number reactive gas flow, with no radiation and negligible body forces are the continuity, mass species transport, momentum, energy and state equations. These can be found in many textbooks on combustion [11, 121]. In the present thesis, the simplifications and assumptions as commonly made for such flows (see [10] for details) are as follows

- zero gravitational effects,
- all gaseous species and the mixture obey an ideal gas equation of state,
- zero radiative heat flux,
- zero Soret (species diffusion driven by temperature gradients) and Duffour (heat diffusion driven by species gradients) terms,

- species specific heat capacities ($C_{p,k}$) equal (but still temperature dependent),
- low Mach number approximation:
  - static pressure in the mixture equation of state is specified as thermodynamically constant
  - acoustic and viscous dissipation terms negligible in the energy equation

The final set of equations resulting from these approximations are written as:

$$\frac{\partial \rho}{\partial t} + \frac{\partial (\rho u_i)}{\partial x_i} = 0 \tag{2.1a}$$

$$\frac{\partial (\rho u_i)}{\partial t} + \frac{\partial (\rho u_i u_j)}{\partial x_j} = -\frac{\partial p}{\partial x_i} + \frac{\partial \tau_{ij}}{\partial x_j} \tag{2.1b}$$

$$\frac{\partial (\rho Y_k)}{\partial t} + \frac{\partial (\rho u_i Y_k)}{\partial x_i} = -\frac{\partial j_{k,i}}{\partial x_i} + \dot{\omega}_k \quad k = 1, ..., N \tag{2.1c}$$

$$\frac{\partial (\rho C_p T)}{\partial t} + \frac{\partial (\rho C_p u_i T)}{\partial x_i} = -\frac{\partial q_i}{\partial x_i} - \sum_{k=1}^{N} \dot{\omega}_k \Delta h^0_{f,k} \tag{2.1d}$$

$$\frac{P_0}{\rho} = \frac{R_u T}{M_{mix}} \tag{2.1e}$$

$$M^{-1}_{mix} = \sum_{k=1}^{N} M^{-1}_k Y_k \tag{2.1f}$$

$$C_p = \sum_{k=1}^{N} C_{p,k} Y_k \tag{2.1g}$$

N is the total number of species present in the mixture, ρ is the mixture density and u_i the i^{th} component of mixture velocity, Y_k is the mass fraction of species k, with $\dot{\omega}_k$ its net rate of mass production, p is the deviation in static pressure around P_0, the thermodynamically constant pressure, τ_{ij} is the viscous stress tensor, and similarly $j_{k,i}$ and q_i are the diffusive flux vectors of species k and heat due to molecular interactions, T is the mixture static temperature, C_p is the specific heat capacity of the mixture at constant pressure and M_k, M_{mix} are the individual species and mixture molar masses. Finally, $\Delta h^0_{f,k}$ is the standard heat of formation of species k at a reference temperature T_0 and R_u is the universal gas constant.

This system corresponds to a closed formulation of (8+N) equations for (8+N) primary variables or unknowns (ρ, u_i, p, Y_k, C_p, T, M_{mix}), assuming that (i) the fluid properties

$C_{p,k}$, $\Delta h^0_{f,k}$, M_k, P_0 and R_u are specified and known, and (ii) the molecular transport terms (τ_{ij}, $j_{k,i}$ and q_i) and the species k reaction rate ($\dot{\omega}_k$) can be related to the primary variables. The next sub-section §2.1.1 deals with the second of these; the consequences of turbulence on the above equations and the approach adopted to model combustion and the reaction rate term $\dot{\omega}_k$ are then outlined.

2.1.1 Modelling of molecular transport terms

2.1.1.1 Momentum transport

Assuming a Newtonian fluid, with zero bulk viscosity, the viscous stress tensor τ_{ij} can be formulated as being proportional to the strain rate:

$$\tau_{ij} = \mu \left(\frac{\partial u_i}{\partial x_j} + \frac{\partial u_j}{\partial x_i} \right) - \frac{2}{3} \mu \frac{\partial u_k}{\partial x_k} \delta_{ij} \tag{2.2}$$

where μ is the dynamic viscosity. The property μ is also assumed known.

2.1.1.2 Mass transport and Fick's Law for mass diffusion

Poinsot and Veynante [10] have described in detail how the molecular transport of species in a multicomponent mixture fundamentally requires consideration of diffusion velocities, leading to multi-species diffusion coefficients describing the diffusion of any species k into any other species p ($\mathcal{D}_{kp}$). The models for $\mathcal{D}_{kp}$ (e.g. Hirschfelder and Curtiss [122]) are complex and, given that in the high Re, highly turbulent flows are to be considered, the molecular transport terms will be assumed negligible compared to the SGS terms (see below), then the usual approach has been adopted to assume the simplest diffusion law for species molecular transport (Fick's law). If the assumption that all individual species coefficients are equal ($\mathcal{D}$) is made, this can be written:

$$j_{k,i} = -\rho \mathcal{D} \frac{\partial Y_k}{\partial x_i} \quad k = 1, ..., N \tag{2.3}$$

2.1.1.3 Heat transport

The molecular transport of heat, q_i (after ignoring Soret and Dufour effects) is associated only with a flux due to temperature gradients. Thus, the molecular transport of heat term in the energy equation is written as:

$$q_i = -\lambda \frac{\partial T}{\partial x_i} \tag{2.4}$$

where λ is the fluid heat conductivity (assumed known).

2.1.1.4 Unity Lewis number approximation

The above descriptions imply that to close the system of equations, values for the molecular transport properties μ, λ and $\mathcal{D}$ must be specified. Note that the heat and species transport properties may be related to each other via the Lewis number:

$$Le = \frac{\lambda/(\rho C_p)}{\mathcal{D}} \tag{2.5}$$

It is also normal in addition to assume a Lewis number of unity, which makes the molecular transport terms identical in the species and energy equations.

2.2 Turbulent flow

2.2.1 Nature of turbulent flows

Turbulent flow is a fluid regime always characterised by chaotic, stochastic, anisotropic, seemingly random, rotational, three-dimensional and time-dependent behaviour. This induces high momentum, heat and mass transfer rates (via turbulent fluctuations), high dissipation (by molecular processes) and rapid variations in space and in time of all fluid properties.

Turbulence causes the formation of eddies of many different length scales. The largest scales, L, are comparable in size to the local flow domain size and are flow and geometry dependent; the integral (energy-containing) scales, l_t, are smaller than L, but not much, and are also flow/geometry dependent and hence usually anisotropic; finally the smallest scales which possess fluctuating energy, η, (also called the Kolmogorov scales) are (at high Re) several orders of magnitude smaller than either L or l_t and, since these are the scales where viscous dissipation takes place, are usually assumed to be isotropic. More details on scales of turbulent motion can be found in textbooks on turbulence [13, 14].

Reynolds number Re is a dimensionless number describing the ratio of inertial to viscous forces in a fluid. It can be formed for any eddy size r. For the integral length scale l_t, the integral turbulent Reynolds number is obtained:

$$Re_t = \frac{u' l_t}{\nu} \tag{2.6}$$

where u' is the characteristic velocity of fluctuating motions of size l_t (approximately the average rms of the turbulence fluctuations) and ν is the fluid kinematic viscosity. Re_t is high in turbulent flows, and thus, the integral scales are controlled by inertial forces and are not affected directly by viscous dissipation. At the small scale level, a

Reynolds number can be formed using length and velocity scales of the Kolmogorov motions which, since viscous effects dominate at this scale, can be written $Re_\eta \approx 1$; the kinetic energy contained in eddies of size η is converted effectively immediately and irreversibly into internal energy (dissipated). This limiting length scale is thus, in dimensional terms, determined by the fluid viscosity ν and the dissipation rate ε.

Within a turbulent flow, an energy-transfer process between eddies, called the *energy cascade*, occurs. Thus, the fluctuating energy of the large scales is passed onto smaller scales due to eddy induced vortex stretching. Following a high Re equilibrium cascade argument, the rate at which this energy is transferred is constant for any eddy size and equals the dissipation rate ε of the turbulent kinetic energy k, and may be estimated as the ratio of the kinetic energy at any scale, $u'^2(r)$, to the turbulent time scale of eddy size r, $r/u'(r)$.

Based on definitions for ε and η the ratio of integral length to Kolmogorov scale can then be obtained [14]:

$$\frac{l_t}{\eta} = (Re_t)^{3/4} \tag{2.7}$$

which shows the Reynolds number dependence of the range of spatial scales that are present (and hence to be numerically resolved) in turbulent flow.

2.2.2 Turbulence modelling

Turbulence remains one of the last unresolved problems in classical mechanics. There is no universal model that adequately predicts the behaviour of all turbulent flows. Hence, turbulence motions have been the object of study for many centuries, since the first observations of Leonardo da Vinci in 1510, and huge efforts have been underway theoretically, experimentally, and numerically.

Numerical models of turbulence and numerical prediction schemes valid for practical flows emerged in the 1960s-70s, and have grown by leaps and bounds since, mainly due to the significant increase in computational capabilities. Extensive information on turbulence modelling can be found in [14, 17, 22] . Three different approaches to solve numerically the modelled governing equations are nowadays used in the Computational Fluid Dynamics (CFD) community. They differ on the level of description of the turbulence and are known as DNS, RANS and LES:

- **DNS** (Direct Numerical Simulation): The full instantaneous Navier-Stokes equations are solved without any model, thus no empirical information is introduced and all turbulence scales are explicitly determined (see Figure 1.3). Developed

rapidly in the last few decades thanks to the availability of high performance computers. It is usually limited to geometrically simplified cases and low Re (because of equation (2.7)), hence it is not a useful tool at an industrial level, but it is indoubtly a valuable research tool.

From the DNS limitation arises the need for alternative techniques to model turbulent flows. An ideal model should introduce the minimum amount of complexity while capturing the essence of the relevant physics. The main criteria to assess different modelling approaches are: i) level of description; ii) completeness; iii) cost and ease of use; iv) range of applicability; and v) accuracy [14]. Two different techniques in wide use are: RANS and LES.

- **RANS** (Reynolds Averaged Navier Stokes): This solves for statistical mean (or time-averaged) properties, thus the modelled equations are obtained by time-averaging the instantaneous equations. Some closure will be required, i.e. a turbulence model for the turbulent transport processes. During the last decades, this technique has been the most extensively used both in academia and industry because of its low computational cost. However, because of its empirical-based closures, this technique is penalised with low generality and precision.

- **LES** (Large Eddy Simulation): The large turbulent energy-containing scales are explicitly calculated whereas the effects of the smaller ones (which have a more universal behaviour because of their isotropy) are modelled using a subgrid scale closure model (SGS model) (see Figure 1.3). A spatial-averaging of the instantaneous equations is performed to filter out the modelled (residual) scales and numerically solve for the resolved scales. Subgrid scale models are required to take into account the effects that the smaller scales and the chemical reaction (occurring at the smallest scales) have on the dynamic behaviour of the large-scale flow. With a high computational cost compared to the RANS approach, but still suitable to deal with problems of engineering and industrial interest, LES is becoming a popular and promising tool with the increase of computational capacity.

2.2.3 LES turbulence modelling

In the present thesis, LES turbulence modelling has been selected for use. LES of realistic flows of engineering interest remains still a big challenge, because most of those flows involve complex geometries and high Reynolds numbers. A comprehensive description of LES turbulence modelling for inert and reacting flows is found in [10, 15, 22] .

2.2.3.1 Scale separation in Large Eddy Simulation

As stated previously, eddies covering a wide range of length and time scales are found in turbulent flows. The scale selection that LES is based on requires separation between large and small scales. A reference or cutoff length in physical space has to be determined, namely Δ, which is also called the filter width. Scales greater than the cutoff length are large or resolved scales, and those smaller are called small or subgrid scales (see Figure 2.1(a)). The effects of the latter on the evolution of the former are included in the equations by way of an SGS model (see also Figure 1.3).

The separation of large and small eddies occurs at high Reynolds numbers, when the turbulent kinetic energy (TKE) spectrum contains an inertial subrange in which there is essentially no net turbulence production or viscous dissipation (region B in Figure 2.1(b)). Since the filter width (Δ) is supposed to mark the boundary between resolved and residual eddies, the ideal is to choose the filter width such that the corresponding wavenumber (π/Δ) lies in the inertial subrange.

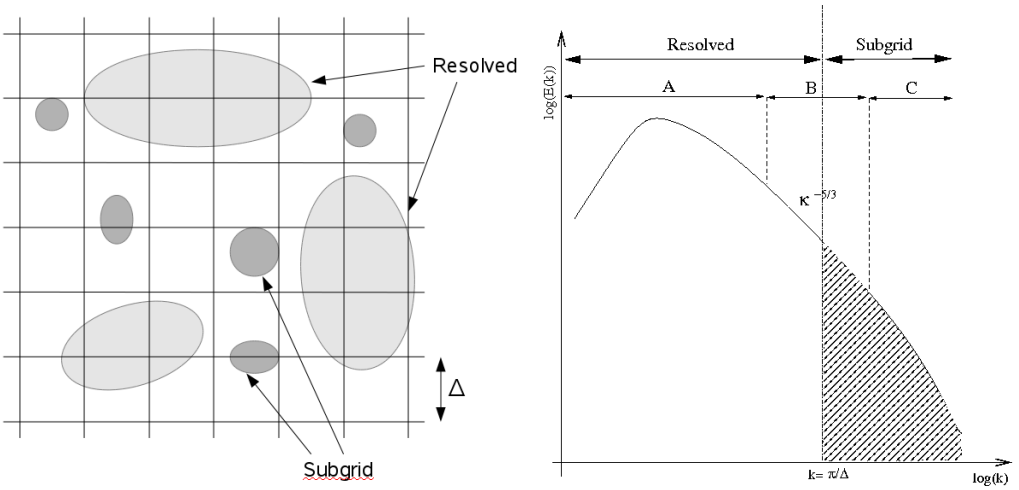

(a) (b)

Figure 2.1: Resolved and subgrid scales in high Reynolds number flow in (a) physical space and (b) Fourier space. In (b) schematic of TKE spectrum where A is region of energy-production, B is inertial subrange and C is dissipation range. κ is wavenumber [22]

2.2.3.2 Mathematical scale separation

Mathematically, the theoretical scale separation outlined above is formalised in the form of a frequency low-pass filter (or scale high-pass filter), which are represented in

physical space as a convolution product. Thus, the resolved part $\bar{\phi}(x_i, t)$ of an instantaneous variable $\phi(x_i, t)$ is defined by:

$$\bar{\phi}(x_i, t) = \int_{-\infty}^{+\infty} \phi(\xi_i, t) G(x_i - \xi_i) d\xi_i \tag{2.8}$$

in which the convolution kernel G is characteristic of the filter used, and is hence sometimes associated with the cutoff scale, Δ. In LES the emphasis is put on spatial filtering, but spatial filtering automatically implies implicit time filtering (equivalent to frequency filtering in Fourier space), since the coupled dynamics of the Navier-Stokes equations makes it impossible to isolate completely space and time variations. Thus, LES will capture only the lower frequency range variations.

The three classical filters used in LES are the box or top-hat filter, the gaussian filter and the spectral or sharp cutoff filter [22]. In particular, the top-hat filter in physical space performs (for the three-dimensional case) a volume average of ϕ over a volume of edge Δ, and in the mono-dimensional case is defined as:

$$G(x - \xi) = \begin{cases} \frac{1}{\Delta} & \text{if } |x - \xi| \leq \frac{\Delta}{2}, \\ 0 & \text{otherwise} \end{cases}$$

Although it is rarely mentioned, all conventional LES codes based on finite volume methods apply top-hat filtering, where the cutoff length scale Δ is linked to the local grid size. It is argued that the finite support of the computational mesh, together with the low-pass characteristics of the discrete differencing operators effectively act as a filter. Hence, this procedure is referred to as implicit filtering, since an explicit filter shape never appears in the solution procedure.

Although implicit filtering has been used extensively, it has some drawbacks. The low-pass filtering is associated with the discrete derivative operator and may differ for each direction. The implicit filtering approach is also influenced by numerical aliasing errors. Finally, when a nonuniform mesh is used, the cutoff length scale is different throughout the computational domain and the filtering operation and differentiation are strictly not commutative.

An explicit filtering approach where the filtering shape is chosen independently of the mesh, allows for the filter width to be maintained constant when refining the mesh. Although explicit filtering offers more independent control of filtering and other discretisation operators, there seems little evidence that this advantage makes any real difference and explicit filtering has not increased in popularity at all for complex

geometry LES. There is also growing opinion that the errors in implicit filtering are, for 2nd order discretisation methods, no larger than the truncation error that has to be reduced to an acceptable level by mesh refinement in any case. Thus, the present method adopts implicit filtering.

2.2.4 Mass-weighted filtering

In order to deal with variable density reacting flows, a mass-weighted (or density-weighted or Favre-averaged) version of filtering ($\tilde{}$) of the instantaneous Navier-Stokes equations is normally used:

$$\tilde{\phi} = \frac{\overline{\rho\phi}}{\bar{\rho}} \tag{2.9}$$

where $\tilde{\phi}$ represents a mass-weighted variable and ($\bar{}$) stands for the spatial averaging.

Thus, the decomposition of an instantaneous variable ϕ is performed as follows:

$$\phi = \tilde{\phi} + \phi'' \tag{2.10}$$

where ϕ'' represents the residual part of the instantaneous value of ϕ.

2.2.5 LES formulation and SGS model - flow field

The fluid dynamics is described primarily by the continuity and momentum equations. In an LES context, the instantaneous flow field equations as defined in §2.1 above are spatially filtered by means of the mass-weighted filtering operation defined by equations (2.9) and (2.10), leading to:

$$\frac{\partial\bar{\rho}}{\partial t} + \frac{\partial(\bar{\rho}\tilde{u}_i)}{\partial x_i} = 0 \tag{2.11a}$$

$$\frac{\partial(\bar{\rho}\tilde{u}_i)}{\partial t} + \frac{\partial(\bar{\rho}\tilde{u}_i\tilde{u}_j)}{\partial x_j} = -\frac{\partial\bar{p}}{\partial x_i} + \frac{\partial\bar{\tau}_{ij}}{\partial x_j} - \frac{\partial\psi_{ij}}{\partial x_j} \tag{2.11b}$$

where $\bar{\tau}_{ij}$ is the spatially-averaged resolved molecular stress tensor and ψ_{ij} is the residual or SGS momentum flux:

$$\psi_{ij} = \bar{\rho}(\widetilde{u_i u_j} - \tilde{u}_i\tilde{u}_j) \tag{2.12}$$

The molecular viscosity in $\bar{\tau}_{ij}$ is considered constant and following the assumption made in equation (2.2) $\bar{\tau}_{ij}$ becomes:

$$\bar{\tau}_{ij} = 2\mu\tilde{S}_{ij} \quad , \quad \tilde{S}_{ij} = \frac{1}{2}\left(\frac{\partial\tilde{u}_i}{\partial x_j} + \frac{\partial\tilde{u}_j}{\partial x_i}\right) - \frac{1}{3}\delta_{ij}\frac{\partial\tilde{u}_k}{\partial x_k} \tag{2.13}$$

where $\tilde{S}_{ij}$ is the Favre-average strain rate tensor.

An eddy viscosity SGS model based on the simple Smagorinsky formulation [53] is used to model the unclosed term ψ_{ij}. ψ_{ij} is formulated by analogy with the viscous stresses, $\bar{\tau}_{ij}$, and the SGS stresses may be written:

$$\psi_{ij} = -2\mu_t \tilde{S}_{ij} \tag{2.14}$$

where μ_t is a subgrid scale viscosity.

The local equilibrium *"production equals dissipation"* approximation is assumed in the Smagorinsky SGS model [53]. This leads to a formulation for the eddy viscosity μ_t as being proportional to a turbulent length scale l_{SGS} ($l_{SGS} = C_s\Delta$, where Δ is the filter width), and to a turbulent velocity scale u_{SGS} (approximated using dimensional analysis similar to that used in Prandtl's (RANS) mixing length model via $u_{SGS} = l_{SGS}|\tilde{S}|$). This implies:

$$\mu_t = \bar{\rho}\left(C_s\Delta\right)^2 |\tilde{S}| \tag{2.15}$$

where C_s is a model constant called the Smagorinsky coefficient, and $|\tilde{S}| = \sqrt{2\tilde{S}_{ij}\tilde{S}_{ij}}$ corresponds to the magnitude of $\tilde{S}_{ij}$.

For an anisotropic filter (e.g. implicit filtering on a nonuniform mesh), the filter width used in equation (2.15) is defined as:

$$\Delta = \left(\Delta x\, \Delta y\, \Delta z\right)^{1/3} \tag{2.16}$$

where Δx, Δy and Δz are the local grid size in directions x, y and z, respectively.

Whilst the above model performs adequately in free shear layers far removed from solid surfaces, for wall boundary layers additional modelling is required to make the SGS viscosity reduce more rapidly as the wall is approached than implied by the standard model. In these cases, it has been found that C_s must be decreased as the wall is approached (again similar to Prandtl's RANS mixing length experience). This is accomplished by using a damping function d, which modifies the length scale and becomes zero when approaching a wall. Then, the turbulent viscosity reads:

$$\mu_t = \bar{\rho}\left(C_s\Delta d\right)^2 \left|\tilde{S}\right| \tag{2.17}$$

where d is the Van Driest damping function [123], defined as

$$d = 1 - \exp(-\frac{y^+}{A^+}) \tag{2.18}$$

$A^+ = 25$ is a model constant and y^+ is distance normal to a wall in wall units defined as

$$y^+ = \frac{yu_\tau}{\nu} \tag{2.19}$$

This is a very simple SGS model and alternative and more complex models have been suggested [22]. However, as already noted in Chapter 1, the Smagorinsky model has performed well for both momentum and scalar property mixing in LES calculations of non-reacting flows relevant to combustion scenarios (fuel injectors) and hence this model has been retained for the present work.

Thus, the filtered momentum equation (2.11b) can be rewritten as:

$$\frac{\partial(\bar{\rho}\tilde{u}_i)}{\partial t} + \frac{\partial(\bar{\rho}\tilde{u}_i\tilde{u}_j)}{\partial x_j} = -\frac{\partial \bar{p}^*}{\partial x_i} + \frac{\partial}{\partial x_j}\left((\mu + \mu_t)\left(\frac{\partial \tilde{u}_i}{\partial x_j} + \frac{\partial \tilde{u}_j}{\partial x_i}\right)\right) \tag{2.20}$$

where the isotropic parts of the viscous and SGS stresses have been added to the resolved pressure leading to:

$$\bar{p}^* = \bar{p} + \frac{2}{3}\mu\frac{\partial u_k}{\partial x_k} + \frac{1}{3}\psi_{kk} \tag{2.21}$$

The model described in this section allows for simulations of the fluid dynamics as long as the filtered density ($\overline{\rho}$) can be determined. However, density is calculated effectively from the filtered equation of state which requires information on temperature and mixture molar mass. Thus, attention should now be given to the LES filtered version of the species and energy equation and this requires us to consider an approach to solution of turbulent premixed combustion, which is addressed next.

2.3 Premixed combustion

A one-dimensional laminar flame propagating steadily into a perfectly premixed gas constitutes a basic problem in combustion. From a theoretical point of view it can be seen as a simple flame configuration that allows even for analytical study of its structure. From a numerical point of view, it is a configuration where detailed comparison between theory, computations and experiments can be carried out to validate chemical models, and it can be regarded as an elementary building block for more complex configurations such as turbulent flames. Turbulent combustion describes the two-way interaction between turbulence and chemistry: on the one hand, a turbulent flow is modified by strong acceleration through the flame front caused by the heat release and because of the strong change in the kinematic viscosity caused by temperature changes ("flame-generated turbulence"). On the other hand, combustion is modified

by turbulence, either by enhancing chemical reaction (increase of mass consumption rate and overall flame thickness) or, in extreme cases, inhibiting it (leading to flame quenching). Many concepts and numerical techniques developed for laminar premixed combustion have direct use in numerical models for turbulent combustion, and thus a few important concepts are described in the following sections.

2.3.1 Laminar premixed flame speed

In perfectly premixed combustion, the reactants (fuel and oxidiser) are completely and uniformly mixed before entering the combustion zone, and once the mixture is ignited, the flame is described as a propagating wave travelling towards the fresh mixture through diffusion and reaction mechanisms. This flame front, separating fresh cold reactants from hot burnt products, travels at flame speed s_l (laminar flame speed). Some simplified expressions for s_l and the flame structure have been derived, e.g. the fully analytical solution using a simplified reaction rate expression developed by Poinsot and Veynante [10] .

However, in the present context explicit, analytical expressions for s_l are not needed, since computational codes based on user-selected chemical kinetics mechanisms are available for predicting details of 1D laminar premixed flames. In the present thesis, the open source code CANTERA [124] was employed to derive s_l and other flame parameters, such as the adiabatic temperature, which are needed (see below) to describe the combustion process occurring at the subgrid scale level.

2.3.2 Premixed turbulent combustion regimes

An essential ingredient for constructing turbulent combustion models is a framework to describe the flame dynamics and interactions with turbulent structures in order to identify different combustion regimes. A continuous sheet-like flame mildly perturbed by turbulent velocity fluctuations cannot be modeled in the same way as a flame front fragmented into different pockets of reacting gas by high intensity and large length scale turbulence. Physical analysis and intuitive arguments comparing the velocity time and length scales of both turbulence and flames have been used to construct *turbulent combustion diagrams*. Various diagrams based on length and velocity scale ratios characterising different modes of combustion have been proposed in the literature [125–131]. Note these diagrams are mainly for guidance, since they are based on dimensional analysis, intuitive arguments and necessary simplification; for example turbulence is usually characterised by single rms velocity (u') and length l_t scales (usually integral energy-containing scales are used) and is also considered unaffected by heat release.

Turbulent premixed combustion may be described as the interaction between a flame front (thickness δ_l^0 and velocity s_l) and an ensemble of eddies, ranging from the Kolmogorov scales (size η and velocity u'_k) to the integral length scales (size l_t and velocity u'). If focus is placed on the integral scales, the energy/equilibrium cascade assumption implies:

$$\frac{u'^3}{l_t} = \varepsilon \tag{2.22}$$

where ε is the local dissipation rate of turbulent kinetic energy. A turbulence time scale for the integral length scale can be defined as:

$$\tau_t(l_t) = \frac{l_t}{u'} = \frac{l_t^{2/3}}{\varepsilon^{1/3}} \tag{2.23}$$

A characteristic combustion or chemical time scale can be specified as:

$$\tau_c = \frac{\delta_l^0}{s_l} \tag{2.24}$$

From these relations, the following non-dimensional parameters may be formed:

- A **turbulent Reynolds number**

$$Re_t = \frac{u' l_t}{\nu} \tag{2.25}$$

- A **Damköhler number** Da defined as the ratio of turbulent and chemical time scales:

$$Da = \frac{\tau_t(l_t)}{\tau_c} = \frac{l_t/u'}{\delta_l^0/s_l} \tag{2.26}$$

- A **Karlovitz number** Ka, which is the ratio of the chemical time scale to the Kolmogorov time scale:

$$Ka = \frac{\tau_c}{\tau_k} = \frac{\delta_l^0/s_l}{u'_k/\eta} \tag{2.27}$$

  It can also be shown that

$$Ka = \left(\frac{\delta_l^0}{\eta}\right)^2 \tag{2.28}$$

Finally, using expressions from Pope [14] for Kolmogorov length and velocity scales, it can further be shown that the above parameters are related by:

$$Re_t = Da^2 Ka^2 \tag{2.29}$$

Using the non-dimensional numbers defined above, a turbulent premixed combustion diagram can be constructed, as shown in Figure 2.2, and different combustion regimes determined:

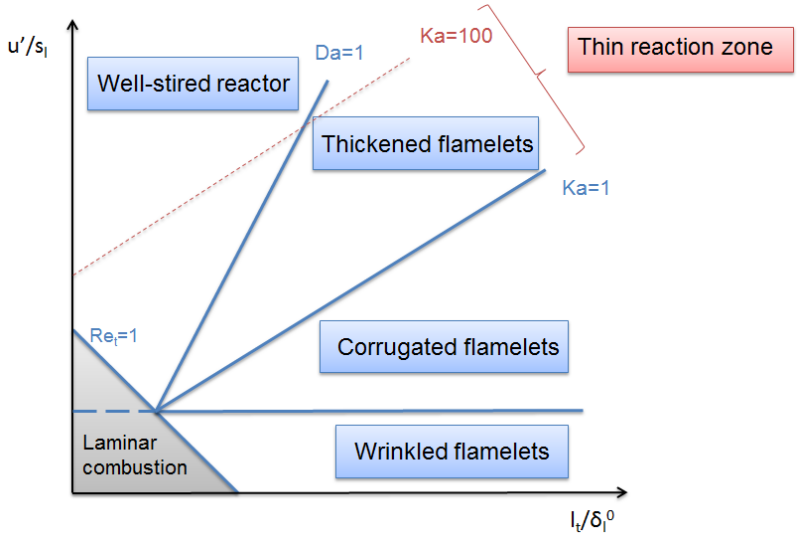

Figure 2.2: Classical turbulent combustion diagram: combustion regimes in terms of velocity (u'/s_l) and length (l_t/δ_l^0) scales ratios in a log-log scale [128]

- If $Da << 1$ the chemical time is much larger than the turbulent time. Thus, mixing of reactants and products is fast and the overall reaction rate is therefore limited by chemistry. This regime is known as the ***well-stirred reactor*** limit.
- If $Da >> 1$ the chemical time becomes much smaller than the turbulent integral time.
  - If in addition $Ka << 1$ the chemical time is smaller than all turbulent time scales, even than the smallest (Kolmogorov) scale, and it follows that all turbulent length scales, even the smallest Kolmogorov scale, are larger than the flame thickness. The flame has an inner structure which remains close to a laminar flame (since the turbulent scales cannot penetrate the inner flame structure) and the flame front is wrinkled by turbulent motions. Hence, the mean burning rate can be estimated from the laminar burning rate multiplied by the overall flame surface. This regime is called the ***thin flame*** regime or ***flamelet*** regime. The paradigm of laminar flamelets has been described fully by Peters [15], assuming infinitely fast chemical reactions and a reaction zone formed by flamelets which have the same structure as a laminar flame - thus locally 1D and experiencing the same strain rate as created locally by the turbulence. Depending on the velocity ratio u'/s_l, this regime can be divided into two different subregimes:
    - if $u'/s_l < 1$ the turbulent motions are too weak to affect the flame front

significantly and only wrinkling is caused. This regime is thus called the ***wrinkled flamelet*** regime.

* if $u'/s_l > 1$ the turbulent motions are more energetic than the flame speed and able to distort the flame front much more. This may lead to the formation of pockets of fresh and burnt gases. Nontheless, the Kolmogorov scales are still larger than the flame thickness, so cannot penetrate the laminar flame structure. Hence, the flame-turbulence interaction is weak (mainly kinematic) and the chemical and transport processes within the flame remain as in a laminar flamelet. This regime is called the ***corrugated flamelet (CF)*** regime.

– If $Ka >> 1$ the chemical time scale is greater than the Kolmogorov scale. The Kolmogorov length scale is smaller than the flame thickness so that the inner flame structure is distorted by turbulence, which modifies chemical and transport processes. Thus, quenching of the flame can occur: the stretch induced by the Kolmogorov scales could exceed the critical "flame stretch" s_l/δ_l^0. This regime is called the ***thickened flamelet*** regime or ***distributed reaction zone***.

The line separating corrugated flamelets and thickened flames, that is the condition $Ka = 1$, is known as the Klimov-Williams criterion.

Note that the most recent version of this combustion regime diagram for premixed turbulent combustion [131] extends the traditional flamelet regime, i.e. wrinkled and corrugated flame regions further up to $Ka = 100$ (from the previous upper limit $Ka = 1$). This region between $Ka = 1$ and $Ka = 100$ is called the *thin reaction zone*, and flamelet assumptions are claimed to be still valid [131] .

Reacting flow in the ORACLES test rig, used for validation purposes in this thesis, can be assumed to be close to the "frontier" between the thickened flame regime and the corrugated flamelet regime [82] (see Table 5.1 below for estimation of Da and Ka using measured flow parameters), thus the flamelet assumption would seem to be appropriate, and this has guided the combustion model selection below.

2.3.3 Stoichiometry in premixed flames

In any combustion regime, multiple species and radicals are involved, and multiple reactions take place. Certain species and reactions will inevitably dominate over others and will determine the effective chemical scheme describing the reaction. The ratio of fuel and oxidiser mass fractions is often used to characterise the flame. Assuming

a simplified one-step irreversible chemical scheme with only 2 reactants (fuel and oxidiser), under stoichiometric conditions, when all fuel and oxidiser are combined during the combustion process, the **mass stoichiometric ratio** s is defined as:

$$s = \upsilon'_O M_O / \upsilon'_F M_F \tag{2.30}$$

where υ'_F and υ'_O are the fuel and oxidiser stoichiometric coefficients respectively in the chemical reaction equation.

Thus, fuel and oxidiser mass fractions Y_F and Y_O will correspond to stoichiometric conditions when:

$$\left(\frac{Y_O}{Y_F}\right)_{st} = s$$

The **equivalence ratio** ϕ of a given mixture is then defined as:

$$\phi = s\frac{Y_F}{Y_O} = \left(\frac{Y_F}{Y_O}\right) \Big/ \left(\frac{Y_F}{Y_O}\right)_{st} \quad \text{or also} \quad \phi = s\frac{\dot{m}_F}{\dot{m}_O} \tag{2.31}$$

where $\dot{m}_F$ and $\dot{m}_O$ are fuel and oxidiser mass flow rates, respectively.

ϕ is a crucial parameter in premixed combustion; this indicates a rich combustion regime (excess of fuel) when $\phi > 1$, and lean combustion regime (oxidiser in excess) when $\phi < 1$.

2.3.4 Relationship between temperature and fuel mass fraction

Poinsot and Veynante [10] have presented a simplified analysis of a laminar steady one-dimensional premixed flame, which indicates under certain conditions (similar to those made above in §2.1) that relations may be derived between unburnt and fully burnt gas conditions:

$$C_p(T_2 - T_1) = Q_{hr} Y_F^1 \quad \Longrightarrow \quad T_2 = T_1 + \frac{Q_{hr} Y_F^1}{C_p} \tag{2.32}$$

where T_2 and T_1 represent temperatures for fully burnt (adiabatic flame temperature) and in the unburnt mixture respectively, Y_F^1 is the fresh fuel mass fraction and Q_{hr} is the fuel heat of reaction.

The heat released due to combustion, $\dot{\omega}_T$ (see equations (2.1d)), can be defined as:

$$\dot{\omega}_T = -\sum_{k=1}^{N} \Delta h^0_{f,k} \dot{\omega}_k \tag{2.33}$$

where $\Delta h^0_{f,k}$ is the standard heat of formation of species k (in kJ/kg). In the case that only one species is considered to contribute to combustion heat release (fuel), equation (2.33) simplifies to

$$\dot{\omega}_T = -\Delta h^0_{f,F} \dot{\omega}_F \tag{2.34}$$

where $\Delta h^0_{f,F} = Q_{hr}$ is the heat released by the combustion of 1 kg of fuel.

The fuel mass fraction and energy (temperature) equations may be non-dimensionalised by introducing the following reduced variables:

$$Y = Y_F / Y_F^1 \quad \text{and} \quad \Theta = \frac{C_p(T - T_1)}{Q_{hr} Y_F^1} = \frac{T - T_1}{T_2 - T_1} \tag{2.35}$$

The species and energy (temperature) conservation equations may then be manipulated to derive an equation for the variable $(Y + \Theta)$, which (if unity Lewis number is assumed) turns out to be an equation for a passive scalar, i.e. to have no source terms, just convection/diffusion terms. Since $Y + \Theta$ equals 1 in both fresh and burnt gases, it may be concluded that the solution throughout the premixed flame is:

$$Y + \Theta = 1 \tag{2.36}$$

Thus, the energy (temperature) and fuel mass fraction equations are not independent. Therefore, from a numerical point of view, this implies that only one variable (Y or Θ) needs to be solved for, and it is usual to choose the fuel mass fraction equation (in fact a related variable, the reaction progress variable c ($=1-Y$ or $=\Theta$) is solved, see below).

2.3.5 LES formulation and SGS model - combustion- reaction progress variable approach

Although the arguments were provided in the previous section for a laminar flame, the relation between reduced temperature and reduced fuel mass fraction can also be used for a turbulent premixed flame. The transport equation for the reaction progress variable c is derived from the transport equation for the reduced fuel mass fraction $Y = Y_F/Y_F^1$; the relation $c = 1 - Y$ is used so that, as noted above, $c = 0$ in the unburnt gas and $c = 1$ in the fully burnt gases. Then, once the equation for c is solved, since all species mass fractions and temperature equations may be shown to be linearly related, then all thermodynamic and combustion processes can be described via this single scalar c. Hence, the thermochemistry can be expressed as a simple function of the progress variable c (these relations may be recovered from a chemical kinetics calculation using CANTERA, see below):

$$T = T(c) \qquad \rho = \rho(c) \qquad Y_k = Y_k(c) \tag{2.37}$$

The next step is therefore to formulate a transport equation for the reaction progress variable, mass-weighted filter this and numerically solve this once closure models for the SGS flux term and the reaction rate term are provided; this is done in the following sections. Then, the values of all resolved thermochemical properties can be determined from equations (2.37). The final aspect which is needed is to consider turbulence-chemistry interaction. Equations (2.37) are applicable to instantaneous variables, and some account has to be taken of the fluctuating nature of the flow. This is carried out in the present work using the Bray-Moss-Libby approach and this is described in §2.3.5.4.

2.3.5.1 Filtered reaction progress variable transport equation

The progress variable c essentially represents the extent of conversion from reactants to products within the flame. The balance equation for the reaction progress variable c may be simply derived from equation (2.1c) with $Y_k = Y_F$, dividing by Y_F^1, the value in the unburnt gases, and setting $c = 1 - Y$:

$$\frac{\partial \rho c}{\partial t} + \frac{\partial \rho u_i c}{\partial x_i} = \frac{\partial}{\partial x_i}\left(\rho D \frac{\partial c}{\partial x_i}\right) + \dot{\omega}_c \tag{2.38}$$

where ρ is the density, u_i is the velocity vector, $\mathcal{D}$ is the molecular diffusivity, $\dot{\omega}_c = \dot{\omega}_F / Y_F^1$ is the source term for c, where $\dot{\omega}_F$ is the fuel reaction rate and Y_F^1 is the fuel mass fraction in the fresh mixture.

A low-pass filter is again applied to equation (2.38):

$$\frac{\partial \bar{\rho}\tilde{c}}{\partial t} + \frac{\partial}{\partial x_i}\left(\bar{\rho}\tilde{u}_i\tilde{c}\right) + \frac{\partial}{\partial x_i}\left(\bar{\rho}\left(\widetilde{u_i c} - \tilde{u}_i\tilde{c}\right)\right) = \overline{\frac{\partial}{\partial x_i}\left(\rho D \frac{\partial c}{\partial x_i}\right)} + \overline{\dot{\omega}_c} \tag{2.39}$$

The three LHS terms in equation (2.39) correspond to unsteady effects, resolved convective fluxes and unresolved SGS transport, respectively. On the RHS, the two terms denote filtered molecular diffusion and filtered source term, respectively. Although the flame front is much thinner than the LES filter (mesh spacing), the flame position and displacement can be obtained via the filtered progress variable field. This approach has been previously used in numerical simulations of turbulent reactive flows, as it simplifies the thermodynamic and combustion processes to a single equation [10],[57]-[118].

The unresolved SGS transport and flame front displacement terms (RHS) require closure. The closure models applied in the present work are presented in the next sections.

2.3.5.2 Unresolved transport model: gradient assumption

An SGS model for the unresolved turbulent transport is required. A gradient assumption is used in the present work:

$$\bar{\rho}\left(\widetilde{u_i c} - \tilde{u}_i \tilde{c}\right) = -\frac{\mu_t}{Sc_t}\frac{\partial \tilde{c}}{\partial x_i} \tag{2.40}$$

where μ_t is the SGS viscosity used in the momentum equations, and Sc_t is the SGS Schmidt number (Sc_t has been given the value 0.7 in all calculations presented in this thesis).

Counter-gradient turbulent transport has been observed in experimental studies [138, 139] and DNS simulations [140], a phenomenon which is controlled by flame parameters such as the level of heat release or mean pressure gradient across the flame front. However, it has been shown [57] that the unresolved transport term is much smaller than the resolved transport term in an LES context, and SGS model uncertainties should therefore be less dramatic on final results than in, for example, a RANS context. Therefore the simple gradient assumption is adopted here. In an LES context in any case the counter-gradient transport will be partly captured at the resolved large-scale level (which does not happen in a RANS context).

2.3.5.3 Filtered flame front displacement: Algebraic Flame Surface Density (FSD) approach

The flamelet closure used in the present work to model the filtered flame front displacement corresponds to a geometrical approach based on the Flame Surface Density (FSD) concept.

In equation (2.39) two terms remain to be modelled, the filtered molecular diffusion and the filtered reaction rate. These filtered terms can be represented by a single term [57], the flame front displacement, which is defined as:

$$\overline{\rho s_d |\nabla c|} = \overline{\frac{\partial}{\partial x_i}\left(\rho D \frac{\partial c}{\partial x_i}\right)} + \overline{\dot{\omega}_c} \tag{2.41}$$

where s_d is the displacement speed. This is the speed of propagation of a considered c-isosurface level, relative to the flow. Piana et al. [141] have proposed the following argument for modelling the flame front displacement:

$$\overline{\rho s_d |\nabla c|} = \int_{-\infty}^{+\infty} \rho s_d |\nabla c| G(x - x') dx' \tag{2.42}$$

$$= \int_{-\infty}^{+\infty} \int_0^1 \rho s_d |\nabla c| \delta(c - c^*) G(x - x') dc^* dx' \tag{2.43}$$

$$= \int_0^1 \langle \rho s_d \rangle_s^* \Sigma^* dc^* = \langle \rho s_d \rangle_s \Sigma \tag{2.44}$$

where G is a convolution kernel (characteristic of the filter used), δ is the Dirac delta function, Σ^* is the subgrid flame surface density (i.e., the flame surface area per unit volume) of the surface defined by $c = c^*$ and $\langle . \rangle_s^*$ denotes a conditional averaging along the surface $c = c^*$.

Quantities Σ and $\langle \psi \rangle_s$ can be regarded as generalised (e.g. for all c-isosurface levels) subgrid flame surface density and surface average, respectively, and according to equation (2.44) may be defined as

$$\Sigma = \int_0^1 \Sigma^* dc^* = \overline{|\nabla c|} \quad \text{and} \tag{2.45}$$

$$\langle \psi \rangle_s = \frac{1}{\Sigma} \int_0^1 \langle \psi \rangle_s^* dc^* = \frac{\overline{\psi |\nabla c|}}{\Sigma} \tag{2.46}$$

If a thin flame front is assumed, the surface density Σ^* does not depend on the chosen c^*-isosurface and the generalised flame surface area corresponds approximately to the subgrid flame surface area (i.e., $\Sigma \approx \Sigma^*$).

Focusing on equation (2.44) to model the filtered flame front displacement, a first step consists of assuming that the inner structure of the reaction zone is not affected by turbulence and as a consequence $\langle \rho s_d \rangle_s = \rho_u s_l$ can be estimated, where ρ_u is the density of the fresh mixture and s_l is the unstretched laminar flame speed. In this case the inner flame structure remains close to a laminar flame and the mean burning rate (or filtered flame front displacement) can be estimated from the laminar burning rate ($\rho_u s_l$) multiplied by the overall flame surface (Σ) (i.e. the total reaction rate and total flame surface density are linearly related by a constant $\rho_u s_l$ that corresponds to the local reaction rate). The above argument has been verified using DNS results by Colin et al. [63] .

This model has been applied in the present work. Validation test cases lie within the flamelet regime (see section §2.3.2), thus a thin flame front (and hence a unique c-isosurface) can be assumed. In addition, the flamelet chemistry (to model $\langle \rho s_d \rangle_s$ term)

can be based on an unstretched flamelet, as this is a reasonable assumption if the flame is in the thin reaction zone [142] .

In addition, an algebraic expression for the flame surface density Σ is used in the present thesis [57]:

$$\Sigma = 4\beta \frac{\bar{c}(1-\bar{c})}{\Delta} \tag{2.47}$$

where Δ is the LES filter size (grid spacing) and β is a model constant. The expression above is similar to a Bray-Moss-Libby (BML) expression for flame surface density as used in a RANS context [141] and the length $\Delta/(4\beta)$ can be viewed as a wrinkling length scale of the subgrid flame surface. Although more refined algebraic models, with for instance dynamic expressions for β, can be applied, it is argued in [57] that this parameter depends only slightly on the turbulence level and the filter size Δ, thus it may be assumed constant. Nonetheless, this value should be calibrated such that, for a specific mesh size Δ, the subgrid flame front wrinkling, a consequence of the SGS turbulent motions, is adequately represented.

Validation of equation (2.47) was performed using DNS by Boger et al. [57] . DNS simulations of a premixed flame interacting with a time-evolving 3D homogeneous isotropic turbulence, under different conditions of turbulence intensities and heat release factors were carried out. Then, the term corresponding to the filtered molecular diffusion plus the filtered reaction rate in the c balance equation (see equation (2.39)) was computed from the DNS results and compared against equation (2.47), and found to be very close at least for the simple flame studied. The slight difference found was attributed to the finite value of the flame thickness, which is expected to decrease when the filter width of the filtering operation becomes large compared to the flame thickness.

Boger et al. [57] used various values of β for the laminar premixed flame interacting with a homogeneous and isotropic turbulent field (for different velocity ratios and heat release factors) ranging from 0.25 to 1.6, with larger values for increasing reduced filter size ratio Δ/Δ_m, where Δ_m is the DNS grid size and Δ the filter width. Other authors using the same combustion model proposed in [57] used different values. Kirkpatrick et al. [77] assumed a value of β such that the ratio Δ/β was of the order of unity (with filter width $\Delta = 2(\Delta_x\Delta_y\Delta_z)^{1/3}$) for a premixed flame moving through a chamber containing an obstruction. Masri et al. [78] used a value of $\beta = 1.2$, and also the same filter width definition, for a premixed flame in a squared cavity containing an square obstacle. Finally, in the LES simulation carried out by Stein et al. [79] of premixed combustion in a turbulent opposed jets configuration the filter size was taken to be $\Delta = \Delta_x$, where Δ_x was the grid size in the axial direction, and β was adjusted such that profiles of mean reaction progress variable matched the experimentally measured profile. Given the low turbulence level of the flow they studied and the reasonably fine

filter width adopted, $\beta = 0.225$ was chosen, similar to the value used in the other calculations described earlier. Chakraborty and Klein [73] compared their power-law based algebraic FSD model with 13 other algebraic FSD models for two DNS calculations of freely propagating statistically planar turbulent premixed flames. One model was that from Boger et al. [57], where they used a value $\beta = 0.25$. They pointed out that this value gave reasonable predictions for small filter size, although a larger value was recommended for increased filter widths. Thus they corroborated the grid dependence of the β parameter.

In the present thesis, $\beta = 0.2$ has been used initially. Based on previous works pointed out above, and the fine grid size used in the simulations this value of β seemed appropriate, in order to obtain an adequate ratio of Δ/β representing the subgrid wrinkling factor. Nevertheless, sensitivity of LES solutions to the value of β should be examined, and this will be discussed further in chapter 6.

It is worthwhile mentioning an important drawback of flamelet closure models, which is the assumption made on the thickness of the flame front, considered to be infinitely thin compared to the filter size. Recently, Duwig and Fuchs [136] have suggested a new formulation accounting for finite flame thickness. They performed LES calculations of turbulent flames using this flamelet formulation based on the filtered c equation [136, 137]. In addition, Fureby [143] compared this model to other techniques and highlighted the potential of the approach, showing very encouraging results although some theoretical aspects remained to be tested and discussed. Nevertheless, although the thin thickness assumption limits considerably the applicability of a model, it is often found to be a reasonable assumption for simulation of industrial devices, such as gas turbine combustors, see for example [135].

2.3.5.4 Turbulence-chemistry interaction: Bray-Moss-Libby analysis

In order to provide full closure to the set of equations in §2.1, a model for the turbulence-chemistry interaction is necessary. As previously pointed out in §2.3.5, all thermodynamic variables (temperature, density and species mass fractions) can be described by a single scalar, the progress variable, in the present formulation. Equations (2.37) relating T, ρ, Y_k to c are of course valid for instantaneous quantities. In LES calculations, only unsteady filtered (resolved) values (rather than instantaneous values) of the primitive variables are available. Equations (2.37) have therefore to be converted into relations including filtered progress variable; and this is the nature of turbulence-chemistry interaction in LES.

In 1977, Bray, Moss and Libby [144] proposed the BML model. It essentially combines a statistical approach, using probability density functions, and a physical analysis. The model has produced evidence of some special features present in turbulent premixed combustion such as counter-gradient turbulent transport and flame turbulence generation.

The BML analysis has been applied in [10] to a progress variable c formulation, with assumptions of a one-step irreversible chemical reaction between fresh gases and combustion products, perfect gases, incompressible flow, equal heat capacities and unity Lewis numbers. These are the assumptions which lead directly to the c equation. Next, a shape for the probability density function of the progress variable is assumed. When an infinitely thin flame front limit is assumed (high Reynolds and Damköhler numbers) the progress variable c can only have two values: $c = 0$ in fresh gases and $c = 1$ in fully burnt ones. Therefore, the presumed PDF shape for c is assumed to be a two-delta function located at values $c = 0$ and $c = 1$:

$$p(c) = \alpha\delta(c) + \gamma\delta(1 - c) \tag{2.48}$$

It follows also that $\alpha + \gamma = 1$.

On the other hand, the mean value $\bar{f}$ of any quantity f is then defined by:

$$\bar{f} = \int_0^1 f(c)p(c)dc = \alpha\bar{f}^u + \gamma\bar{f}^b \tag{2.49}$$

where $\bar{f}^u$ and $\bar{f}^b$ are respectively the conditional averages of f in fresh and burnt gases. Then, applying equation (2.49) to c:

$$\bar{c} = \int_0^1 c\, p(c)dc = \alpha(c = 0) + \gamma(c = 1) = \gamma \tag{2.50}$$

showing that the unweighted averaged progress variable $\bar{c}$ is the probability to be in burnt gases.

Furthermore, the Favre-averaged progress variable $\tilde{c}$ is related to the unweighted average value by:

$$\tilde{c} = \frac{\overline{\rho c}}{\bar{\rho}} = \frac{\rho_b\gamma}{\bar{\rho}} = \frac{\rho_b\bar{c}}{\bar{\rho}} \tag{2.51}$$

where ρ_b is the density of the burnt gases. From equation (2.49), the mean density is given by:

$$\bar{\rho} = \alpha\rho_u + \gamma\rho_b = (1 - \gamma)\rho_u + \gamma\rho_b \tag{2.52}$$

where ρ_u is the density of the fresh gases. Equation (2.52) may be recast as:

$$\bar{\rho}\,(1 + \tau\tilde{c}) = \rho_u = \rho_b\,(1 + \tau) \tag{2.53}$$

τ is the heat release factor, defined as:

$$\tau = \frac{\rho_u}{\rho_b} - 1 = \frac{T_b}{T_u} - 1 \tag{2.54}$$

and T_u and T_b are fresh and burnt gases temperatures, respectively. Combining expressions (2.51) and (2.52) leads to expressions for α and γ:

$$\alpha = \frac{1 - \tilde{c}}{1 + \tau\tilde{c}} \quad \text{and} \quad \gamma = \frac{(1+\tau)\,\tilde{c}}{1 + \tau\tilde{c}} \tag{2.55}$$

Then, using equation (2.55), an expression relating Favre and unweighted averages of any quantity f may be obtained:

$$\tilde{f} = \frac{\overline{\rho f}}{\bar{\rho}} = \frac{1}{\bar{\rho}}\left(\alpha\rho_u\bar{f}^u + \gamma\rho_b\bar{f}^b\right) = (1-\tilde{c})\bar{f}^u + \tilde{c}\bar{f}^b \tag{2.56}$$

i.e. the Favre-averaged value of the quantity f is a weighted average of Reynolds-averaged values in fresh and burnt gases, with weighting coefficients based upon the Favre-averaged progress variable $\tilde{c}$. Likewise, equations (2.50), (2.54) and (2.55) are used to relate $\tilde{c}$ and $\bar{c}$:

$$\bar{c} = \frac{(1+\tau)\,\tilde{c}}{1+\tau\tilde{c}} = \frac{\tilde{c}\rho_u}{\tilde{c}\rho_u + (1-\tilde{c})\rho_b} \quad \text{or} \quad \tilde{c} = \frac{\bar{c}}{(1+\tau) - \tau\bar{c}} = \frac{\bar{c}\rho_b}{\bar{c}\rho_b + (1-\bar{c})\,\rho_u} \tag{2.57}$$

Finally, considering equations (2.49) and (2.56) the thermochemical variable relations can be derived:

$$\bar{Y}_k = \bar{c}Y_{k,b} + (1-\bar{c})Y_{k,u} \quad \text{and} \quad \tilde{Y}_k = \tilde{c}Y_{k,b} + (1-\tilde{c})Y_{k,u} \tag{2.58}$$

$$\bar{T} = \bar{c}T_b + (1-\bar{c})T_u \quad \text{and} \quad \tilde{T} = \tilde{c}T_b + (1-\tilde{c})T_u \tag{2.59}$$

$$\bar{\rho} = \bar{c}\rho_b + (1-\bar{c})\rho_u \quad \text{and} \quad \tilde{\rho} = \tilde{c}\rho_b + (1-\tilde{c})\rho_u \tag{2.60}$$

where $Y_{k,b}$, T_b and ρ_b have been obtained by solving a one-dimensional steady premixed flame with detailed chemistry. In the present work the CANTERA software [124] has been used.

CANTERA [124] is a collection of object-oriented software tools for problems involving chemical kinetics, thermodynamics, and transport processes. Among other things, it can be used to conduct kinetic simulations with large reaction mechanisms, to compute chemical equilibrium, to evaluate thermodynamic and transport properties of mixtures and to evaluate species chemical production rates. For the present application it was applied to the combustion of a propane/air premixed mixture.

A freely-propagating premixed flame calculation was performed, using the San Diego mechanism [145] at inlet conditions corresponding to two of the ORACLES reacting test cases. Resulting predictions for temperature, local reaction rates and main species mass fractions against axial distance are plotted in Figure 2.3. Points represent discrete nodes used in the calculation, with a higher concentration of these in the zones where steep gradients of the variables were found (note not all nodes are shown for the sake of clarity). The equivalence ratios selected from the ORACLES study for simulation here have been chosen (for reasons given in next chapters). Both are perfectly premixed experiments at equivalence ratios ϕ=0.65 and 0.75, with slightly different initial temperatures. The lower equivalence ratio leads to a lower reaction rate (by $\approx$ a factor of 0.5) and a lower final burnt (adiabatic) flame temperature. As seen in Figure 2.3 the species mass fraction changes follow expected trends with ϕ, with no CO in the final burnt mixture, although this is created in the flame zone itself.

2.4 Mass-weighted filtered set of modelled governing equations

The final set of mass-weighted filtered equations, describing the evolution of a turbulent low-speed premixed combusting flow, that may be solved numerically are presented below. These are modelled mass transport, momentum and reaction progress variable transport equations, and equations relating the mass-weighted progress variable and thermodynamic properties. They correspond to the set of equations presented in section 2.1 after filtering, modelling closures and thermochemistry assumptions have been applied.

$$\frac{\partial \bar{\rho}}{\partial t} + \frac{\partial (\bar{\rho}\tilde{u}_i)}{\partial x_i} = 0 \tag{2.61a}$$

$$\frac{\partial (\bar{\rho}\tilde{u}_i)}{\partial t} + \frac{\partial (\bar{\rho}\tilde{u}_i\tilde{u}_j)}{\partial x_j} = -\frac{\partial \bar{p}^*}{\partial x_i} + \frac{\partial}{\partial x_j}\left(\mu_t\left(\frac{\partial \tilde{u}_i}{\partial x_j} + \frac{\partial \tilde{u}_j}{\partial x_i}\right)\right) \tag{2.61b}$$

$$\frac{\partial \bar{\rho}\tilde{c}}{\partial t} + \frac{\partial}{\partial x_i}\left(\bar{\rho}\tilde{u}_i\tilde{c}\right) = -\frac{\partial}{\partial x_i}\left(\frac{\mu_t}{Sc_t}\frac{\partial \tilde{c}}{\partial x_i}\right) + \rho_u s_l \Sigma \tag{2.61c}$$

$$\mu_t = \bar{\rho}\left(C_s\Delta\right)^2|\tilde{S}| \tag{2.61d}$$

$$\Sigma = 4\beta\frac{\bar{c}(1-\bar{c})}{\Delta} \tag{2.61e}$$

$$\bar{Y}_k = \bar{c}Y_{k,b} + (1-\bar{c})Y_{k,u} \tag{2.61f}$$

$$\bar{T} = \bar{c}T_b + (1-\bar{c})T_u \tag{2.61g}$$
$$\bar{\rho} = \bar{c}\rho_b + (1-\bar{c})\rho_u \tag{2.61h}$$

This set of governing equations must now be discretised, incorporated into an LES solver and used to solve for turbulent premixed combusting problems.

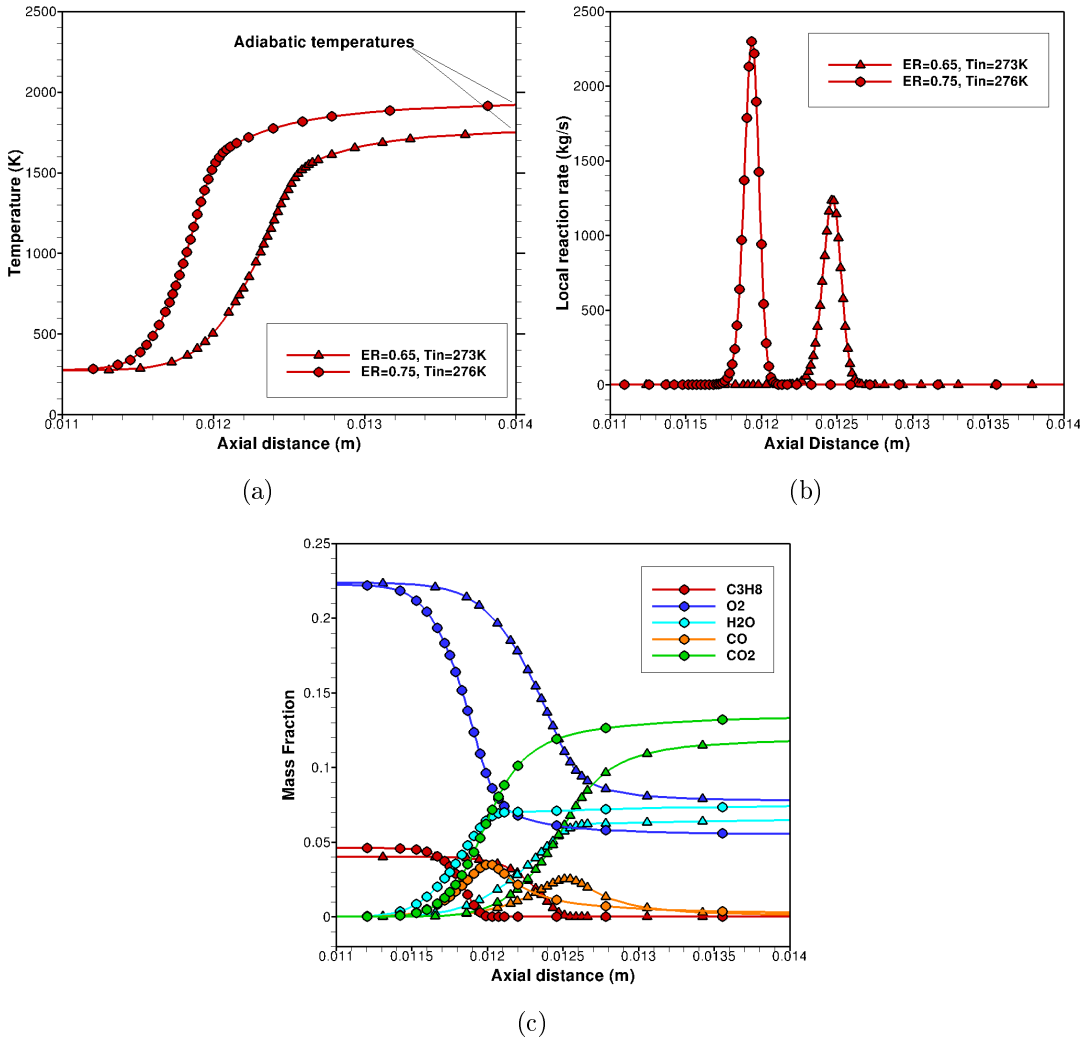

Figure 2.3: (a) Temperature, (b) local reaction rate and (c) main species mass fraction plotted against axial distance for a freely-propagating premixed flat flame. Results extracted from CANTERA. Circle and delta symbols correspond to inlet conditions of $T = 276K$ and $\phi = 0.75$, and $T = 273K$ and $\phi = 0.65$, respectively

Chapter 3

Large Eddy Simulation - numerical methodology and code details

3.1 Numerical methodology

CFD predictive capabilities rely on two fundamental building blocks. On the one hand, adequate physical modelling which ensures that the set of PDEs and mathematical relations formulated replicate accurately real physical phenomena. On the other hand, numerical methods - efficient, robust and reliable algorithms to solve the PDEs - must be devised to provide accurate solutions of these equations. The numerical methods selected for use in the present work and some information on their stability, accuracy and calculation efficiency are described in this chapter.

It is widely acknowledged that accurate LES predictions rely even more than RANS CFD on aspects such as mesh density, grid quality and boundary conditions, as commented upon many times in published work since the LES technique first appeared in the 1970-80's. Although for optimum geometric flexibility unstructured CFD codes are preferred, the fundamentally higher quality of a structured mesh code (particularly with an orthogonal mesh) has been preferred for the present project, since the ORACLES geometry is fairly simple (see Figure 1.5) and a multi-block structured mesh option offers sufficient geometrical capability. The LULES code to be used here [146] allows for curvilinear orthogonal meshes, but only Cartesian meshes are required for the current work. The form of the equations to be discretised has thus been given in Cartesian tensor form at the end of the last chapter and this simple co-ordinate frame is all that was required for the simulations presented later.

Another relevant aspect is the arrangement of the variables on the grid. The storage arrangement can be staggered or non-staggered [9, 16]. Non-staggered arrangements provoke the well-known checkerboard problem, requiring smoothing to remove spatial oscillations. The staggered arrangement solves this problem by avoiding the need to interpolate pressure in the momentum equations and velocities in the continuity equation. In addition, a staggered arrangement, used together with second-order central

difference schemes and good quality meshes (low expansion ratios), provides full conservation (mass, momentum and kinetic energy are conserved simultaneously) [147], which is clearly beneficial in an LES context. Therefore, the staggered arrangement is used in the present thesis.

Regarding optimum numerical discretisation schemes, in an LES context any numerical and artificial dissipation is to be avoided, since this contaminates the solution and can even overcome the modelled subgrid stresses [148]. The use of second-order differencing schemes on as close to uniform Cartesian grid as possible minimises numerical diffusion and offers global kinetic energy conservation, which is a desirable property to ensure numerical stability. The numerical methods in this chapter have been introduced into a CFD code, LULES, developed at Loughborough University [146]. It is a robust and reliable code able to carry out LES predictions for flows in reasonably complex geometries. Extensive validation for different flow configurations has been conducted, including fully developed turbulent channel flow, flow in a 180^o bend in a square duct and in a dump diffuser[146], impinging jet in crossflow [149], non-swirling isothermal flow in combustor geometries [150], isothermal scalar mixing in co-axial jet flows [151] and in high swirl fuel injectors [52] and finally reacting flow in a dump combustor [80]. The objective of using this code in the present thesis was to implement the flow and combustion model described in chapter 2, validate via application to the ORACLES turbulent premixed flow and then to extract amplitude dependent Flame Transfer Functions from the combusting LES predictions to feed into an acoustics code (to be described in chapter 4) for hybrid/coupled thermoacoustics analysis.

3.1.1 Finite volume method and spatial discretisation

Equations (2.61a-c) are the set of mass, momentum and scalar transport partial differential equations which must be discretised. Discretisation of the solution domain is carried out by dividing this into cells or control volumes (CVs), by means of a mesh with discrete grid points (nodes) located at the geometrical centre of the CVs. Figure 3.1 displays a typical CV, with central node P and neighbour nodes E (east), W (west), N (north), S (south), T (top) and B (bottom). Nodes E, N and T are located at positive x, y and z directions, whereas W, S and B correspond to negative displacements from P. Also, lower case letters e, w, n, s, t and b refer to cell faces in the corresponding directions.

Figure 3.2 shows a uniform Cartesian mesh in the xy plane. Scalars and pressure are evaluated at nodes. Since a staggered grid is used for velocity components, velocity nodes for u, v and w are located at cell faces in x, y and z directions, respectively. Accordingly, CVs for velocity components will be displaced with respect to scalars and

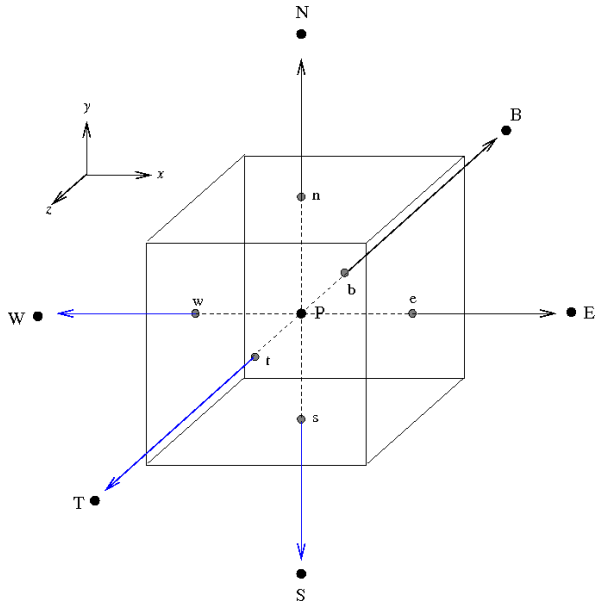

Figure 3.1: Control volume in a cartesian mesh, with cell-centrered node P and labelled neighbour nodes and cell faces

pressure CVs. Nodes are numbered from 1 to nip1 (resp. njp1 and nkp1) in the x (resp. y and z) direction. Likewise, a node located at position (i, j, k) will be identified by a single index ijk, defined as

$$ijk = i + (j-1)\, nip1 + (k-1)\, nip1\, njp1 \tag{3.1}$$

Note that the CVs in dashed lines in Figure 3.2 correspond to virtual or "ghost" cells, outside the physical domain; these are used for implementation of boundary conditions and information transfer between adjacent blocks.

The discretisation process is performed using a finite volume method to obtain a set of algebraic discretised linear equations. A volume integration of equations (the governing equations) is performed over each CV. Equation (3.2) shows a typical (1D for the sake of simplicity and easily generalised to 3D) generic equation for an arbitrary variable ϕ

$$\underbrace{\frac{\partial(\rho\phi)}{\partial t}}_{\text{transient term}} + \underbrace{\frac{\partial(\rho u\phi)}{\partial x}}_{\text{convection term}} = \underbrace{\frac{\partial}{\partial x}\left(\Gamma_\phi \frac{\partial\phi}{\partial x}\right)}_{\text{diffusion term}} + \underbrace{S_\phi}_{\text{source term}} \tag{3.2}$$

where Γ_ϕ is a diffusion coefficient and ϕ is any transported variable.

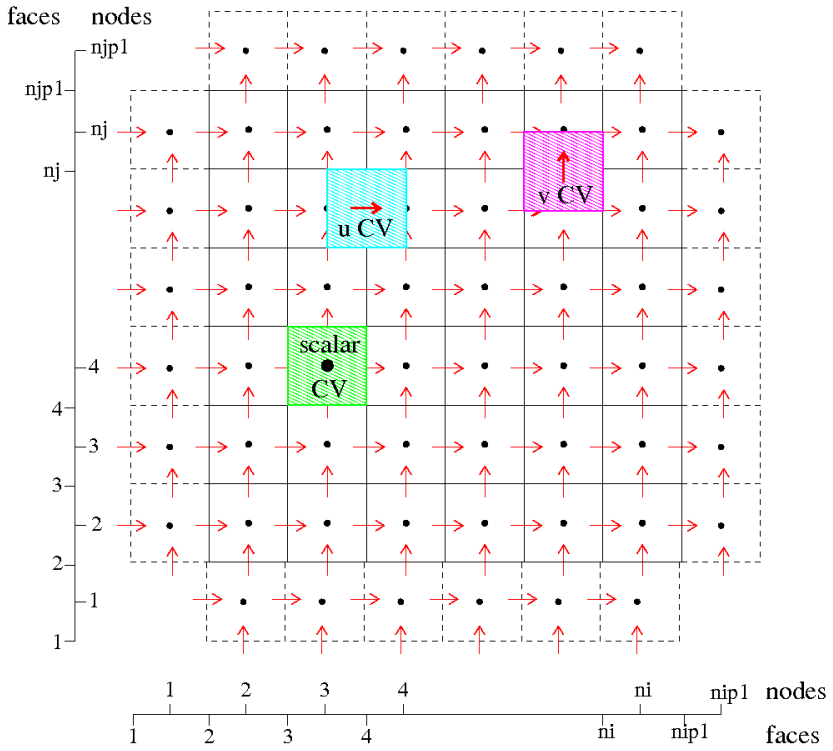

Figure 3.2: 2D Cartesian mesh, with numbered nodes and faces. CVs for scalar and velocities are indicated

Volume integration gives:

$$\frac{\partial}{\partial t}\int_V \rho\phi \, dV + \int_S \rho u\phi \, dS = \int_S \Gamma_\phi \frac{\partial \phi}{\partial x} \, dS + \int_V S_\phi \, dV \tag{3.3}$$

where V represents the volume over which the integration is performed (a CV), S is the surface bounding the volume V and dS is the magnitude of a discrete area of the surface. Integrals are approximated via quadrature formulae, to obtain an algebraic equation for each CV where neighbour nodal values will appear. The different approximations for volume and surface integrals used in the LULES code are presented next.

3.1.1.1 Volume integrals

Transient and source terms require volume integration over a CV. The transient term will be discussed in §3.1.2. A 2nd order accurate approximation for the source term is:

$$Q = \int_{V_{CV}} q \, dV = \bar{q} \, V_{CV} \approx q_P \, V_{CV} \tag{3.4}$$

where $\overline{q}$ is the mean value of the integrand and q_P stands for the value at node P.

3.1.1.2 Surface integral of diffusive flux

The surface integrals of diffusive fluxes correspond to integrals over the faces of CVs. These integrals are approximated by means of the midpoint rule [9], i.e, as the product of the face area times the averaged value of the integrand evaluated at the face centre. As an example, the discretised 1D integral over face e of the diffusive flux of a variable ϕ, $f_e^\phi = \Gamma_\phi \left(\frac{\partial \phi}{\partial x}\right)$, reads:

$$\int_e f_e^\phi \, dS = S_e \bar{f}_e^\phi \approx S_e f_e^\phi \tag{3.5}$$

$$= S_e (\Gamma_\phi)_e \left(\frac{\partial \phi}{\partial x}\right)_e \tag{3.6}$$

where S_e is the east face area. It is straightforward to obtain analogous expressions for all other faces by making appropriate index substitution. To preserve second-order accuracy, the value of the integrand at the CV face centre has to be computed with at least second-order accuracy. A central differencing scheme (CDS) is employed:

$$\varphi_e = \lambda_e \varphi_E + (1 - \lambda_e)\varphi_P \tag{3.7}$$

where φ represents any variable and the weighting factor λ_e depends on geometric quantities:

$$\lambda_e = \frac{x_e - x_P}{x_E - x_P} \tag{3.8}$$

where x_e, x_P and x_E indicate locations in the x direction of face e and nodes p and E, respectively.

CDS for the diffusion coefficient $(\Gamma_\phi)_e$ and a linear profile assumption for variable ϕ between nodes P and E produces the diffusive flux integration as:

$$\int_e f_e^\phi \, d\vec{S} = S_e (\Gamma_\phi)_e \frac{\phi_E - \phi_P}{\delta x_e} \tag{3.9}$$

For the 3D case, the net flux through the 6 faces bounding a CV will be the summation of surface integrals over each face:

$$\int_S f \, d\vec{S} = \int_{S_e} f_e^\phi \, d\vec{S} + \int_{S_w} f_w^\phi \, d\vec{S} + \int_{S_n} f_n^\phi \, d\vec{S} + \int_{S_s} f_s^\phi \, d\vec{S} + \int_{S_u} f_u^\phi \, d\vec{S} + \int_{S_b} f_b^\phi \, d\vec{S} \tag{3.10}$$

Equations (3.9) and (3.10) have been applied to surface integrals of diffusive fluxes in the scalar transport and momentum equations.

3.1.1.3 Surface integral of convective flux

The midpoint rule approximation expressed in equation (3.5) is also employed to approximate the convective fluxes in the momentum equations, e.g. $f_e^{\phi} = (\rho u \phi)_e$. In addition, linear interpolation is utilised to approximate the velocity component values at the CV face centre, u_e; the values of the density at the face centres, ρ_e, in the u velocity mesh are also evaluated using linear interpolation. This approach has been used to obtain surface integrals of convective fluxes in the mass conservation and momentum equations, but not the scalar equation, as explained next.

3.1.1.4 TVD scheme for surface integral of convective flux

CDS can display spatial oscillations or "wiggles" due to dispersion errors. Thus, CDS is avoided for the convective fluxes of scalar properties, such as the reaction progress variable c, whose value is bounded by physically imposed limits. Instead, a second-order Total Variation Diminishing (TVD) scheme [152] is employed to approximate the convective fluxes to avoid spurious oscillations caused by dispersion errors and ensure the value of c to be bounded between 0 and 1. The TVD scheme applied in the present work is a second-order, oscillation free, explicit scalar difference scheme which consists of a first-order formulation to which a limited anti-diffusive flux is added (the difference between the flux of a high order scheme and that of a low order scheme, which has been "limited" in such a way as to ensure the resulting scheme is TVD).

Dianat et al. [151] considered several such schemes and, on the basis of an optimum reduction of numerical diffusion judged against a range of scalar transport test problems, selected the Branley and Jones [153] scheme, which has been implemented in LULES for the reaction progress variable equation. Details of this scheme are given in full in [151] and [153].

3.1.2 Time-marching scheme and Poisson equation for pressure

The Adams-Bashforth time-marching scheme is used to approximate the solution of a variable ϕ at instant $n+1$ based on values of the variable and its derivatives at previous instants of time. First a Taylor series for variable ϕ at instant $t + \Delta t$ is considered:

$$\phi^{n+1} = \phi^n + \Delta t \left(\frac{\partial \phi}{\partial t}\right)^n + \frac{(\Delta t)^2}{2}\left(\frac{\partial^2 \phi}{\partial t^2}\right)^n + \text{Higher Order Terms} \tag{3.11}$$

$$\approx \phi^n + \Delta t \left(\frac{\partial \phi}{\partial t}\right)^n + \frac{(\Delta t)^2}{2}\frac{\left(\frac{\partial \phi}{\partial t}\right)^n - \left(\frac{\partial \phi}{\partial t}\right)^{n-1}}{\Delta t} \tag{3.12}$$

$$\approx \phi^n + \frac{3}{2}\Delta t \left(\frac{\partial \phi}{\partial t}\right)^n - \frac{1}{2}\Delta t \left(\frac{\partial \phi}{\partial t}\right)^{n-1} \tag{3.13}$$

where superscripts $n-1$, n and $n+1$ indicate that the variable is evaluated at instants $t - \Delta t$, t and $t + \Delta t$, respectively. This time-marching scheme was applied to the momentum and reaction progress variable transport equations. The progress variable c is computed first and density at the new time level is then obtained as a function of c^{n+1}. Velocities are then computed (density at the new time step is needed) from momentum equation solution. Finally the pressure is calculated by imposing a continuity constraint, which leads to the need to solve an inhomogeneous Poisson equation.

The continuity equation at instant $n+1$ can be written as:

$$\left(\frac{\partial \bar{\rho}}{\partial t}\right)^{n+1} + \frac{\partial(\bar{\rho}^{n+1}\tilde{u}_i^{n+1})}{\partial x_i} = 0 \tag{3.14}$$

In addition, the i-momentum equation reads as

$$\frac{\partial(\bar{\rho}\tilde{u}_i)}{\partial t} = \bar{C}_i - \frac{\partial \bar{p}}{\partial x_i} \tag{3.15}$$

where $\bar{C}_i$ includes both convective and diffusive terms. Applying equation (3.13) to $\phi = \bar{\rho}\tilde{u}_i$ in equation (3.15), the following is obtained:

$$\bar{\rho}^{n+1}\tilde{u}_i^{n+1} = \bar{\rho}^n\tilde{u}_i^n + \frac{3}{2}\Delta t\left(\bar{C}_i^n - \frac{\partial \bar{p}^n}{\partial x_i}\right) - \frac{1}{2}\Delta t\left(\bar{C}_i^{n-1} - \frac{\partial \bar{p}^{n-1}}{\partial x_i}\right) \tag{3.16}$$

Equation (3.16) is applied in two steps. Firstly, an intermediate velocity is calculated by omitting the first pressure term; the pressure term is included in a second correction step:

$$1) \qquad \bar{\rho}^{n+1}\tilde{u}_i^* = \bar{\rho}^n\tilde{u}_i^n + \frac{3}{2}\Delta t\bar{C}_i^n - \frac{1}{2}\Delta t\left(\bar{C}_i^{n-1} - \frac{\partial \bar{p}^{n-1}}{\partial x_i}\right) \tag{3.17}$$

$$2) \qquad \bar{\rho}^{n+1}\tilde{u}_i^{n+1} = \bar{\rho}^{n+1}\tilde{u}_i^* - \frac{3}{2}\Delta t\frac{\partial \bar{p}^n}{\partial x_i} \tag{3.18}$$

Applying a divergence operator $\partial/\partial x_i$ to equation (3.18) gives:

$$\frac{\partial(\bar{\rho}^{n+1}\tilde{u}_i^{n+1})}{\partial x_i} = \frac{\partial(\bar{\rho}^{n+1}\tilde{u}_i^*)}{\partial x_i} - \frac{3}{2}\Delta t\frac{\partial^2 \bar{p}^n}{\partial x_i^2} \tag{3.19}$$

and equation (3.14) is substituted into the LHS of equation (3.19)

$$-\left(\frac{\partial\bar{\rho}}{\partial t}\right)^{n+1} = \frac{\partial(\bar{\rho}^{n+1}\tilde{u}_i^*)}{\partial x_i} - \frac{3}{2}\Delta t\frac{\partial^2\bar{p}^n}{\partial x_i^2} \tag{3.20}$$

Rearranging, a Poisson equation for pressure is obtained:

$$\frac{\partial^2\bar{p}^n}{\partial x_i^2} = \frac{2}{3\Delta t}\left(\left(\frac{\partial\bar{\rho}}{\partial t}\right)^{n+1} + \frac{\partial(\bar{\rho}^{n+1}\tilde{u}_i^*)}{\partial x_i}\right) \tag{3.21}$$

The time-derivative of density is calculated by a first order method:

$$\frac{\partial\bar{\rho}^{n+1}}{\partial t} = \frac{\bar{\rho}^{n+1} - \bar{\rho}^n}{\Delta t} \tag{3.22}$$

Solution of equation (3.21) provides the $\bar{p}^n$ field needed in equation (3.18) to update the intermediate velocity field $\tilde{u}_i^*$. (Note that following the nomenclature of the Adams-Bashforth method the velocity/pressure field at the new time level are written as $\tilde{u}_i^{n+1}$ and $\bar{p}^n$).

3.1.3 Boundary conditions

In this section, boundary conditions implemented in the code LULES are described. For the present flow problem these boundary conditions are inflow, outflow and rigid wall conditions.

3.1.3.1 Inflow conditions

The flow conditions at an inflow plane require velocity and scalar values to be prescribed. However, in LES a 3 component unsteady velocity map over the 2D inlet plane is required, which matches local experimental conditions and represents physically realistic turbulent flow conditions (note since the mixture is perfectly premixed a spatially uniform condition $c = 0$ is the imposed inlet condition for the scalar, which cannot then fluctuate in time whereas, due to high velocity gradients, the velocity clearly does). A two-step methodology has been used to generate LES velocity inlet conditions for the ORACLES test case. First, a feedback method has been employed in a separate precursor calculation to reproduce the experimentally observed fully developed turbulent flow velocity profiles in the rectangular approach ducts. Secondly, velocity profiles from a specific axial plane in this precursor calculation were stored for a long enough period to ensure no time correlation between first and last time instants. These stored data were then imposed at the inlet plane of the main combusting simulation computational domain (see §5.3 for details).

3.1.3.2 Outflow conditions

The flow conditions prescribed at the outflow plane are also dependent on the variable under consideration. For the scalar a simple zero-gradient condition is imposed. For the velocity field a convective outflow condition was imposed. This assumes the flow near the outflow plane to be approximately represented by:

$$\frac{\partial(\rho u)}{\partial t} + \bar{U}\frac{\partial \rho u}{\partial x} = 0 \tag{3.23}$$

where $\bar{U}$ is the bulk velocity at the outflow plane and u is the axial velocity component.

In order to be consistent with the time-marching scheme used previously, velocity at the outflow plane was determined by:

$$\rho^{n+1}u^{n+1} = \rho^n u^n - \frac{3}{2}\Delta t\bar{U}\frac{\partial \rho^n u^n}{\partial x} + \frac{1}{2}\Delta t\bar{U}\frac{\partial \rho^{n-1}u^{n-1}}{\partial x} \tag{3.24}$$

In addition, a scaling procedure was also applied in order to satisfy global continuity. The continuity conservation condition in a continuous form reads:

$$\frac{\partial \bar{\rho}}{\partial t} + \frac{\partial(\bar{\rho}\tilde{u})}{\partial x} = 0 \tag{3.25}$$

When this is integrated over the whole computational domain the following is obtained

$$\int_V \frac{\partial \bar{\rho}}{\partial t} dV = -\int_S \bar{\rho}\tilde{u}_n \, d\vec{S} \tag{3.26}$$

where $\tilde{u}_n$ represents the velocity normal to the domain bonding surface S. The integrand under the surface integral will be non-zero only at inflow and outflow planes and zero for all solid walls. For the ORACLES geometry, the only planes where flow crosses the boundaries are normal to the x direction so $\tilde{u}_n = \tilde{u}$. Equation (3.26) can be recast as:

$$\dot{m}_{change} = \int_V \frac{\partial \bar{\rho}}{\partial t} dV = -\left(\int_{S_{in}} \bar{\rho}\tilde{u} \, d\vec{S}_{in} - \int_{S_{out}} \bar{\rho}\tilde{u} \, d\vec{S}_{out}\right) = -\dot{m}_{in} + \dot{m}_{out} \tag{3.27}$$

A scaling factor is defined as:

$$SF = \frac{\dot{m}_{change} + \dot{m}_{in}}{\dot{m}_{out}^{n+1}} \tag{3.28}$$

where

$$\dot{m}_{out}^{n+1} = \int_{S_{out}} \bar{\rho}\tilde{u}^{n+1} \, d\vec{S}_{out} \tag{3.29}$$

before scaling. Applying this scaling factor to $\tilde{u}^{n+1}$ ensures that the resulting outflow mass rate $\dot{m}_{out}$ fulfils equation (3.27), hence mass conservation is globally satisfied.

3.1.3.3 Rigid wall condition

Boundaries representing rigid solid walls are treated with a zero-gradient condition (zero flux) for the scalar; a wall function approach was adopted for velocities.

For the sake of simplicity, only a 2D illustration is provided here, where the y-direction is normal to the wall, as displayed in Figure 3.3. Initially, the y^+ of the first node located next to the wall is calculated:

$$y_P^+ = \frac{u_\tau y_P \rho}{\mu} \tag{3.30}$$

y_P corresponds to wall normal distance to the first grid point P, $u_\tau = \sqrt{\tau_w/\rho}$ stands for the friction velocity, τ_w is the wall shear stress and μ and ρ are viscosity and density, respectively. Note τ_w is based on an instantaneous estimate of the wall shear using the current time-step resolved velocity. This is used to determine whether wall nodes are located either in the log-law region or in the laminar sub-layer. Different u velocity profiles are assumed depending on the y_P^+ value:

- Within the laminar sub-layer ($y_P^+ < 11.3$) a linear profile is assumed, leading to:

$$\tau_w = \mu \frac{\tilde{u}(x,y,t)}{y_P} \tag{3.31}$$

- For $y_P^+ > 11.3$ a log-law profile is assumed leading to:

$$\tau_w = \tilde{u}(x,y,t) \frac{\langle \tau_w \rangle}{\langle \tilde{u}(x,y,t) \rangle} \tag{3.32}$$

  where $\langle . \rangle$ indicates a time-averaged quantity, and $\langle \tau_w \rangle$ is obtained assuming $\langle \tilde{u} \rangle$ and y_P are used in a log-law relation to find the time-averaged wall shear stresses.

Furthermore, the impermeability condition is applied, hence:

$$v|_{y=0} = w|_{y=0} = 0 \tag{3.33}$$

3.1.4 Relaxation method for density

In flows where combustion is present, steep gradients in space and time of the density are commonly found. Due to the non-diffusive spatial and temporal schemes used in LES, these gradients (particularly if underesolved by the mesh) can introduce high frequency noise in the solution that can destabilise the numerical simulation (since in a

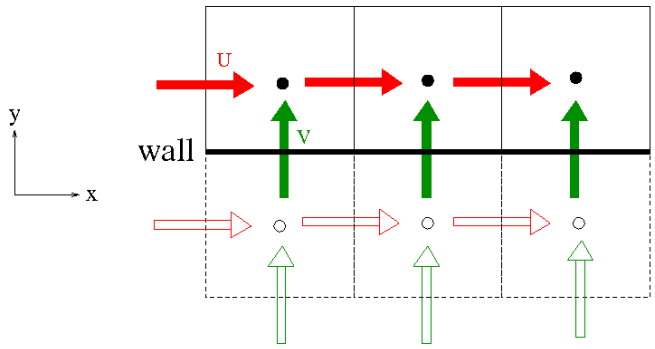

Figure 3.3: Velocity arrangements for wall boundary condition implementation

pressure-based low-Mach number formulation a temporal density derivative is present in the pressure equation source term). Thus, for density ratios of approximately three or greater occurring in short distances, instabilities, which pollute the numerical solution, are observed [154]. An effective method, proposed by Forkel and Janicka [155] that consists of damping out high frequencies from the density solution by using a relaxation method, has been adopted in the present work. Other solutions to deal with steep/rapid density variations in LES solutions have been proposed in the literature [63, 65, 154, 156–161] but the method of density relaxation is attractive on the grounds of both effectiveness and simplicity of implementation. Thus, the temporal density term, which enters the Poisson equation in the form of a source term, is smoothed out, hence preventing the destabilisation of the solution.

A relaxation in time applied to the density implies:

$$\overline{\rho}^{n+1} = (1-\alpha)\overline{\rho}^{n+1}_{est} + \alpha\overline{\rho}^{n} \tag{3.34}$$

where $\overline{\rho}^{n+1}_{est}$ is an estimated density obtained initially using the progress variable at the new time level $n+1$, and α is a relaxation factor defined as

$$\alpha = e^{-\Delta t/T_{relax}} \tag{3.35}$$

where $\Delta t = t^{n+1} - t^{n}$ is the LES time step and T_{relax} is a chosen relaxation time.

This relaxation procedure may be viewed as a filtering in the time domain [80]. Thus the $\overline{\rho}^{n+1}$ value can be written as a convolution integral of the $\overline{\rho}^{n+1}_{est}$ value:

$$\overline{\rho}^{n+1} = \int_{0}^{+\infty} \overline{\rho}^{n+1}_{est}(t^{n+1} - t')\, G(t')\, dt' \tag{3.36}$$

where $G(t')$ is the convolution kernel and $t' = t^{n+1} - t$. The convolution kernel $G(t')$ may be interpreted as the impulse response of the filter in the time domain, and written

as:

$$G(t') = \frac{e^{-t'/T_{relax}}}{T_{relax}} H(t') \quad \text{and} \tag{3.37}$$

where $H(t')$ is the Heaviside function (=1 if $t' \geq 0$, =0 if $t' < 0$).

The Laplace transform of the filtered $\bar{\rho}^{n+1}$ variable can provide insight into the effects that this filtering procedure creates in the frequency domain. A useful property of Laplace transforms is that the Laplace transform of a convolution of two signals in the time domain equals the convolution of the two Laplace transforms in the frequency domain:

$$\mathcal{L}((f * g)(t)) = \mathcal{L}(f(t)) \cdot \mathcal{L}(g(t)) \tag{3.38}$$

Thus,

$$\mathcal{L}(\bar{\rho}^{n+1}) = \mathcal{L}(\bar{\rho}_{est}^{n+1}(t^{n+1} - t')) \cdot \mathcal{L}(G(t')) \tag{3.39}$$

The Laplace transform of the convolution kernel is:

$$F(s) = \mathcal{L}(G(t')) = A \exp^{i\phi} \tag{3.40}$$

where $s = i\omega$ is a complex variable, ω is a frequency, and A is the gain of the Laplace transform defined as [162]

$$A = \frac{1}{\sqrt{1 + (\omega T_{relax})^2}} \tag{3.41}$$

and ϕ is the phase angle written as:

$$\phi = \arctan(-\omega T_{relax}) \tag{3.42}$$

The Power Spectral Density of $F(s)$ for various values of T_{relax} may be computed and is plotted in Figure 3.4. It can be seen that T_{relax} controls the shape of the Laplace transform convolution kernel in such a way that the larger T_{relax} the wider the range of frequencies that are damped.

In order to establish a value to ensure stability, but also to identify the acceptable effect of the relaxation method on numerical accuracy of the current LES predictions, various simulations, using different T_{relax} were performed. The values of T_{relax} tested were $2 \cdot 10^{-5}$, $5 \cdot 10^{-5}$, $1 \cdot 10^{-4}$, $2.5 \cdot 10^{-4}$ and $5 \cdot 10^{-4} s$.

First, spectra of the fluctuating streamwise velocity, at a point located in the flame front region, for the different simulations performed are shown in Figure 3.5(a). The effect of the relaxation method on the stability is clearly observed in these spectra. For values of $T_{relax} \leq 5 \cdot 10^{-5} s$ two distinctive peaks at frequencies around 1840Hz and 3300Hz are observed, exhibiting the unstable nature of the numerical solution. For these two cases,

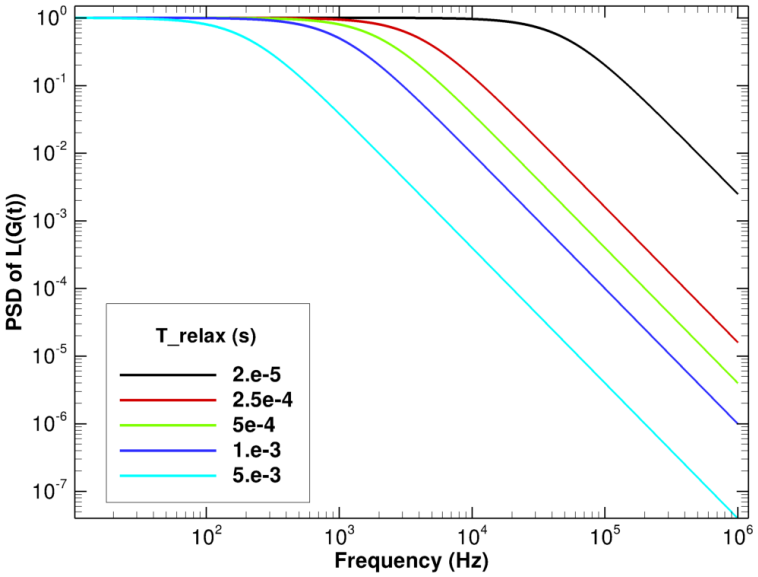

Figure 3.4: Power Spectral Density of the Laplace transform of the low-pass filter kernel

LES time steps of $\approx 2.5 \cdot 10^{-6}s$ and $5 \cdot 10^{-6}s$ are dynamically calculated. When T_{relax} is reduced to $1 \cdot 10^{-4}s$, the peak at frequency 1840Hz is completely removed and the peak at 3300Hz, although still present, has been significantly reduced in intensity by ≈ 4 orders of magnitude. For values of $T_{relax} \geq 2.5 \cdot 10^{-4}s$ the spikes in the spectra are completely removed, reflecting the numerical stability achieved. For $T_{relax} \geq 1 \cdot 10^{-4}s$, LES time steps of $\approx 1.2 \cdot 10^{-5}$ are used. Thus, the value of $T_{relax} = 2.5 \cdot 10^{-4}s$ has been employed in all the LES simulations presented below.

Note that the spectra of fluctuating streamwise velocity plotted at other locations in the reaction zone showed the same trend (amplitude and location of the peaks). This is in all probability linked to the strongly elliptic effect of pressure in incompressible flows, since the velocity field over the whole domain is instantaneously coupled to the pressure field and thus, any instability affecting the pressure at any point propagates and can influence the velocity throughout the flow domain. The spectra plotted for other velocity components and variables (progress variable and density), exhibited a similar tendency, although peak amplitudes were lower than for the axial velocity.

Despite the fact that the noise peaks were successfully removed when increasing T_{relax}, there are some drawbacks. The $-5/3$ region in the inertial subrange is attenuated, giving a slightly flatter profile. Forkel and Janicka [155] have also mentioned that excessive damping of the density can cause poor simulation accuracy.

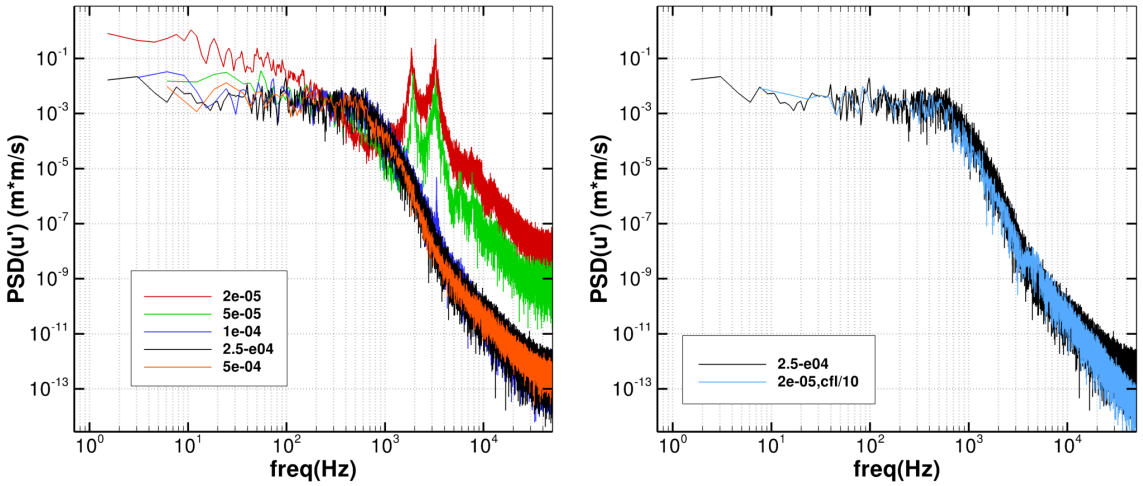

(a) (b)

Figure 3.5: Spectra of fluctuating streamwise velocity for simulations using (a) relaxation factor values of $T_{relax} = 2 \cdot 10^{-5}$, $5 \cdot 10^{-5}$, $1 \cdot 10^{-4}$, $2.5 \cdot 10^{-4}$ and $5 \cdot 10^{-4} s$ and (b) relaxation factor $T_{relax} = 2.5 \cdot 10^{-4} s$ and $T_{relax} = 2 \cdot 10^{-5} s$ with reduced CFL number

To bring to light the effect stronger temporal filtering has on the results, a further test was carried out. As has already been pointed out, high frequency density oscillations may not be supported by the time-step/temporal discretisation scheme, necessitating the relaxation to prevent numerical noise from growing and causing unstable solutions. Thus, a finer temporal mesh should reduce the instability problem, with less need for relaxation. This implies a decreased CFL number. The reduction explored (a factor of 10) was considerable, in order to obtain a significant increase in temporal resolution. This implies a dynamically calculated LES time step of the order of $1 \cdot 10^{-7} s$. Thus, this option, in general, is not desirable as a way to avoid/eliminate instabilities. However, it was explored to test the effects of the temporal filtering.

The value of $T_{relax} = 2 \cdot 10^{-5} s$, which initially gave an unstable numerical solution, was recalculated with a reduction of the CFL number by a factor of 10. This successfully removed the instabilities, as indicated in the spectra free of peaks, as seen in Figure 3.5(b). This stable solution can now be compared with the simulation using $T_{relax} = 2.5 \cdot 10^{-4} s$ (a stable numerical solution but with a much larger CFL), in order to assess the numerical accuracy of the results obtained with $T_{relax} = 2.5 \cdot 10^{-4} s$. Both spectra for fluctuating streamwise velocity, at the same point located in the flame front, are compared in Figure 3.5(b). The differences are very small and the curves collapse in almost the whole frequency range. For this reason, the relaxation method with $T_{relax} = 2.5 \cdot 10^{-4} s$ was selected for all results presented in this thesis.

3.1.5 Multigrid solver

Multigrid (MG) solvers, introduced in the 60s by Russian scientists are one of the most efficient approaches to solve PDEs. In the present work, an MG solver is employed to solve the pressure Poisson equation (see §3.1.2). This is a high CPU consuming task, which accounts for approximately 80% of the global CPU time needed per time step. Consequently, an efficient solver is required in order to obtain reduced overall computational time.

In LULES, the MG solver developed by Zeng and Manners [163] is implemented. A brief description of this method is provided here. Consider a general discretised PDE equation:

$$Lx = S \tag{3.43}$$

where L is a differential operator, x is the vector of unknowns and S is a known function, all defined over a domain Ω^1. Specifically, for the case concerning this work, L is the 3D Laplacian operator, x represents the pressure and S is the source term which comprises a temporal term and a convective term (see equation (3.21)). The goal is to find x. An iterative process is constructed, and each global iteration is split into three different steps:

1. **Pre-smoothing:**
   An initial guess for x is considered (x^1) and an iterative algorithm (e.g. Gauss-Seidel), is used to solve equation (3.43). This algorithm is not used to obtain an accurate solution for this equation but instead is used as a *smoother* that will reduce the high-frequency components of the initial guess. If $\tilde{x}^1$ is the approximation of x after ν_1^1 iterations, then the error y^1 is:

   $$y^1 = x - \tilde{x}^1 \tag{3.44}$$

   which is referred to as the error of the algebraic approximation, or the convergence error. If the operator L is applied to equation (3.44) the following is obtained

   $$Ly^1 = r^1 \tag{3.45}$$

   where r^1, the residual of $\tilde{x}^1$, is defined as:

   $$r^1 = S - L\tilde{x}^1 \tag{3.46}$$

2. **Correction:**
   We now want to solve equation (3.45), to calculate y^1 and therefore correct $\tilde{x}^1$ to obtain x^1. However, this would be a numerical task as difficult as direct solution of equation (3.43). Thus, instead, several procedures are carried out:

(a) *Restriction:* Let I_1^2 be a restriction operator such that:

$$I_1^2 : \Omega^1 \longrightarrow \Omega^2$$

where Ω^2 represents a grid coarser than Ω^1, with typically half of the nodes. Then, the fine-to-course transfer operator I_1^2 can be applied to equation (3.45) to give

$$L^2 y^2 = r^2 \tag{3.47}$$

where $L^2 = I_1^2 L$, $y^2 = I_1^2 y^1$ and $r^2 = I_1^2 r^1$

(b) *Solving:* Suppose that, by any means, equation (3.47) is solved exactly, to obtain $y^2 = (L^2)^{-1} r^2$

(c) *Prolongation:* Let be I_2^1 an operator (prolongation) such that

$$I_2^1 : \Omega^2 \longrightarrow \Omega^1$$

By applying this coarse-to-fine transfer operator to y^2, the solution of equation (3.47), a value for x^1 can be obtained

$$\hat{x}^1 = \tilde{x}^1 + I_2^1 y^2$$

3. **Post-smoothing:**
Although equation (3.47) can be solved exactly, $\hat{x}^1$ is not the exact solution for x^1 in equation (3.43), since $I_2^1 y^2$ is still an approximation of y^1. Therefore, ν_2^1 iterations of an iterative algorithm (the same used in the pre-smoothing process) are performed, using $\hat{x}^1$ as initial guess

In general, iterative solvers are efficient at reducing high frequency components of error; after several sweeps, the lower frequency components remain and the solver becomes inefficient. The correction process, based on an extrapolation of y^2, decreases the low frequency components of y^1, although it increases the high frequency components, since the information that it contains has been obtained from a lower resolution discretisation. The increase in the high frequency component error generated on the lower resolution grid is solved by applying, after the correction, a post-smoother to reduce them.

Figure 3.6 shows a representative illustration of the evolution of the norm of the residual r^1 with and without coarse-grid correction, which clearly manifests the benefit of applying a correction.

Including more levels

In the previous description of the multigrid solver, it has been assumed that equation (3.47) can be solved exactly. However, depending upon the dimensions of Ω^2, this

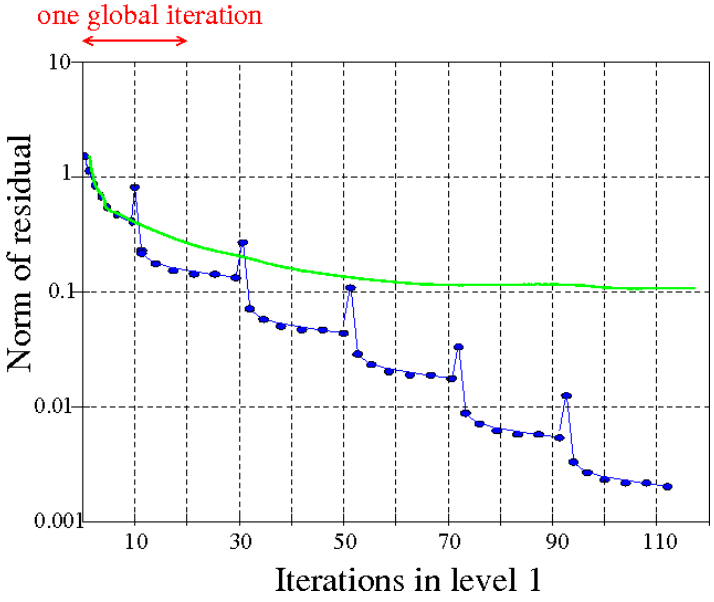

Figure 3.6: Residual evolution with (blue) and without (green) coarse grid correction

equation might still be too expensive to solve. Therefore, when in level 2, the same methodology used in level 1 can be invoked again. Thus, after ν_1^2 sweeps of the pre-smoother algorithm, $L^3 y^3 = I_2^3 r^2$ is derived, and this can be repeated until a level N, in which the equation

$$L^N y^N = r^N \tag{3.48}$$

can be solved, either directly or iteratively. It is worth mentioning that the number of sweeps in each level can be different.

In the case that more levels are included in the resolution procedure, the way in which those levels are visited needs to be selected. These are referred to as multigrid cycles or the multigrid schedule. The commonly used options are V-cycle, F-cycle and W-cycle. Figure 3.7 depicts the V and W cycle multigrid schedules, where the red circle represents the pre-smoothing process, the green square is the correction and the blue triangle represents the post-smoothing.

In LULES, one multigrid level has been solved, the number of global iterations (pre-smoothing+correction+post-smoothing) has been set to 7, the number of iterations for the correction is 10, whereas for pre and post-smoothing is 1. The tolerances for the three solvers are 10^{-9}, as well as the tolerance for the global iterations.

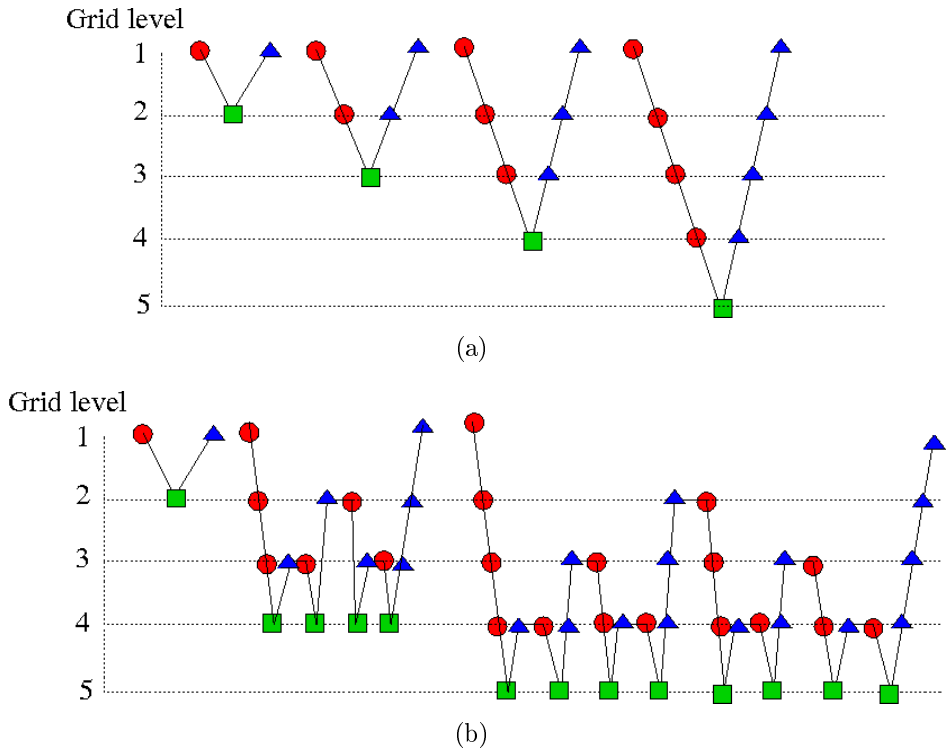

Figure 3.7: (a) V-cycle and (b) W-cycle multigrid schedules

3.1.6 Solution stability control

When explicit schemes are used as in LULES, the time step must be appropriately selected as small enough to avoid unstable numerical solutions. Thus, the time step must be limited, based on numerical considerations. Two nondimensional parameters are used in LULES to control the time step. For a 3D case these correspond to:

- **Courant-Friederich-Lewy (CFL) number**:

$$CFL = \Delta t \; Max \left(\frac{|u|}{\Delta x} + \frac{|v|}{\Delta y} + \frac{|w|}{\Delta z} \right) \tag{3.49}$$

- **Diffusion (DFS) number**:

$$DFS = \Delta t \left(\frac{\mu + \mu_{SGS}}{\rho} \right) \; Max \left(\frac{1}{(\Delta x)^2} + \frac{1}{(\Delta y)^2} + \frac{1}{(\Delta z)^2} \right) \tag{3.50}$$

To ensure numerical stability, both CFL and DFS numbers must be kept below critical values, $CFL < \alpha_{CFL}$ and $DFS < \alpha_{DFS}$ (α_{CFL},α_{DFS} are always < 1). This will

ensure that the time step Δt is less than the time needed for convective and diffusive waves to travel from one grid node to the next. The Δt is then computed by imposing both conditions and taking the minimum Δt obtained. In high Re flows the convective effects are more important than diffusive effects, therefore the CFL condition becomes the most restrictive and it is usually unnecessary to impose a DFS condition. Note that the DFS condition might become important when singularities on the mesh are present (e.g. at a centreline with a polar mesh), in which case the diffusivity (the DFS number) in that region becomes very large. In the present project, based on flow and mesh characteristics, only the CFL condition is imposed and a value $\alpha_{CFL} = 0.35$ used.

3.1.7 Solution procedure

As mentioned earlier, the Adams-Bashforth time marching scheme has been used in the algorithm to solve for the set of unsteady governing equations. As a final outline of the numerical methodology applied in the present work, this section describes the detailed steps of the algorithm implemented in the LULES code and also the procedure followed in each temporal iteration to advance the solution variables in time:

1. The SGS eddy viscosity is computed using the standard Smagorinsky model, including a Van Driest damping function in the vicinity of the walls (see §2.2.5):

$$\mu_t = \bar{\rho} \left(C_s \Delta d\right)^2 \left|\tilde{S}_{ij}\right| \tag{3.51}$$

2. The Adams-Bashforth scheme is applied to obtain the density weighted progress variable $\bar{\rho}\tilde{c}$ at time step $n+1$, using variables at previous time steps $n-1$ and n, which are already known:

$$\begin{aligned}(\bar{\rho}\tilde{c})^{n+1} = {} & (\bar{\rho}\tilde{c})^{n} \\ & + \Delta t \frac{3}{2}\left(-\nabla\cdot(\bar{\rho}^{n}\tilde{u}^{n}\tilde{c}^{n}) + \nabla\cdot\left(\frac{\mu^{n}_{SGS}}{Sc_t}\right)\nabla\tilde{c}^{n} + \rho_u s_l \Sigma^{n}\right) \\ & - \Delta t \frac{1}{2}\left(-\nabla\cdot(\bar{\rho}^{n-1}\tilde{u}^{n-1}\tilde{c}^{n-1}) + \nabla\cdot\left(\frac{\mu^{n-1}_{SGS}}{Sc_t}\right)\nabla\tilde{c}^{n-1} + \rho_u s_l \Sigma^{n-1}\right)\end{aligned} \tag{3.52}$$

3. An intermediate value of the progress variable, c^*, is calculated:

$$c^* = \frac{(\bar{\rho}\tilde{c})^{n+1}}{\bar{\rho}^{n}} \tag{3.53}$$

4. This intermediate value is used to obtain an estimated value of the density at time step $n+1$, from the thermochemical relations:

$$\bar{\rho}_{est}^{n+1} = \rho_u(1-c^*) + \rho_b c^* \tag{3.54}$$

5. The relaxation method (§3.1.4) is then applied to the density in order to ensure numerical stability; a value for the density at time step $n+1$ is obtained:

$$\bar{\rho}^{n+1} = (1-\alpha)\bar{\rho}_{est}^{n+1} + \alpha\bar{\rho}^n \tag{3.55}$$

and accordingly, the progress variable at time step $n+1$ is modified to preserve consistency with the updated density

$$\tilde{c}^{n+1} = \frac{(\bar{\rho}\tilde{c})^{n+1}}{\bar{\rho}^{n+1}} \tag{3.56}$$

6. Once the progress variable at time step $n+1$, $\tilde{c}^{n+1}$, is known, other thermodynamic variables may be calculated if needed:

$$\begin{aligned} \tilde{Y}_k^{n+1} &= \tilde{c}^{n+1}Y_{k,b} + (1-\tilde{c}^{n+1})Y_{k,u} \\ \tilde{T}^{n+1} &= \tilde{c}^{n+1}T_b + (1-\tilde{c}^{n+1})T_u \end{aligned} \tag{3.57}$$

7. Using the Adams-Bashforth time scheme, the momentum equations are solved to calculate the intermediate velocities $\tilde{u}_i^*$, obtained by including only the pressure term at time step $n-1$:

$$\begin{aligned} \bar{\rho}^{n+1}\tilde{u}_i^* = \bar{\rho}^n\tilde{u}_i^* &\\ + \Delta t\frac{3}{2}\left(ConvTerm + DiffTerm\right)^n &\\ - \Delta t\frac{1}{2}\left(ConvTerm + DiffTerm\right)^{n-1} + \frac{1}{2}\frac{\partial\bar{p}^{n-1}}{\partial x_i} & \end{aligned} \tag{3.58}$$

The convective outflow boundary condition (§3.1.3.2) is then applied to the intermediate velocities u_i^* to ensure mass is conserved.

8. A multigrid solver (§3.1.5) is used to solve the pressure Poisson equation (§3.1.2) to obtain the pressure at time step n:

$$\frac{\partial^2\bar{p}^n}{\partial x_i^2} = \frac{2}{3\Delta t}\left(\left(\frac{\partial\bar{\rho}}{\partial t}\right)^n + \frac{\partial(\bar{\rho}^{n+1}\tilde{u}_i^*)}{\partial x_i}\right) \tag{3.59}$$

9. Finally, the intermediate velocity field u_i^* is updated by adding the pressure term at time step n, obtained from the solution of the Poisson equation. Thus, the velocities at time step $n+1$ are:

$$\begin{aligned} \tilde{u}^{n+1} &= \frac{1}{\bar{\rho}^{n+1}} \left[\bar{\rho}^{n+1} u_i^* - \frac{3\Delta t}{2} \frac{\partial \bar{p}^n}{\partial x_i} \right] \\ &= u_i^* - \frac{3\Delta t}{2\bar{\rho}^{n+1}} \frac{\partial \bar{p}^n}{\partial x_i} \end{aligned} \tag{3.60}$$

Again, the convective outflow boundary condition is applied to the updated velocity field, to ensure mass conservation.

Chapter 4

Thermo-acoustic phenomena - 1D network modelling approach

The computational methodology described in the previous chapter is restricted to an incompressible formulation. Hence, if any acoustic effects are to be introduced (e.g. via periodic forcing at the inlet boundary as has been used by Duwig [118] and Duwig and Fureby [117]), the details of the forcing should ideally come from an acoustic analysis that has to be conducted in a separate acoustic code. Equally, if this acoustics code is to receive and use the Flame Transfer Function (FTF) information extracted from combusting LES calculations, this requires a transfer route into the acoustics code from the LES predictions (a heat release description). The acoustics code used in the present work to achieve this two-way transfer of information is described in the present chapter.

Acoustics codes normally deal only with linear acoustics, requiring linearisation of the compressible form of the governing equations about some presumed mean flow field. Solution methods in linear acoustics codes are of two types - frequency domain methods (e.g. [164, 165]) and time domain methods [166]. Whilst the latter are more naturally extended to non-linear problems, the former are much more popular and it is this type which has been used in the present work. Both frequency and time domain methods have been developed for 1D and 3D applications, but for the present problem a 1D linear acoustic method model is sufficient.

In the present thesis, the thermo-acoustic network model LOTAN (Low-Order Thermo-Acoustic Network) has been used. The LOTAN code has been developed at Cambridge University in collaboration with Rolls-Royce plc for the simulation of both axial and circumferential acoustic waves in both axial and annular combustion systems. The fundamental basis, development and application of LOTAN has been described in several papers ([6, 167]). The code uses linear acoustics theory and provides predictions of the frequencies of resonant modes, and their stabilities (positive or negative growth rates) and mode shapes. In the next sections, the acoustic modelling employed and the simplifications and assumptions made in LOTAN are briefly described. The approach to using LOTAN in the two modes described above are also outlined namely: (i) providing quantitative information on the details of acoustic forcing to an incompressible

LES calculation that can best mimic the presence of acoustic modes, and (ii) inputting an FTF description of fluctuating heat release into the acoustic network model. The latter requires selection of the modelling approach used in the flame-acoustics module in the LOTAN code, the *time-delay* model [168, 169] .

4.1 Fundamentals of acoustic modelling

The mathematical framework for the acoustic theory applied in LOTAN is 1D linear acoustics. Thus, all flow and thermodynamic variables are considered to be decomposed into a mean (time-average) value and an acoustic perturbation, which is assumed small compared to the corresponding mean, i.e.,

$$\phi = \overline{\phi} + \phi' \qquad \text{where} \qquad \phi' << \overline{\phi} \tag{4.1}$$

The mean values are assumed to be prescribed, e.g. from RANS or LES solutions. In addition, a harmonic wave description is assumed for all perturbation quantities, in which spatial and temporal variations may be decoupled by writing:

$$\phi' = \Re(\phi_\omega(x) e^{-i\omega t + in\theta}) \tag{4.2}$$

where ϕ_ω is a complex variable, $\Re()$ represents the real part, ω is a complex frequency and n is the circumferential wave number (both axial and circumferential waves are included in the LOTAN software, but only plane axial waves are considered in the calculations presented below).

The equations of motion for a compressible fluid, ignoring viscosity and heat conduction effects may be written (see [6]):

$$\frac{\partial \rho}{\partial t} + \frac{\partial(\rho u_i)}{\partial x_i} = 0 \tag{4.3a}$$

$$\frac{\partial(\rho u_i)}{\partial t} + \frac{\partial(\rho u_i u_j)}{\partial x_j} = -\frac{\partial p}{\partial x_i} \tag{4.3b}$$

$$\frac{\partial(\rho E)}{\partial t} + \frac{\partial(\rho u_i E)}{\partial x_i} = -\frac{\partial(p u_i)}{\partial x_i} + q \tag{4.3c}$$

where E is the total internal energy ($E = e + 1/2(\rho u_i u_j)$) and q is the rate of heat release.

If it is assumed that the fluid is an ideal gas (C_p and C_v constant), manipulation of these equations and conversion of the energy equation into one for entropy, followed by

linearisation about the prescribed steady mean flow leads to the following equations [6]:

$$\frac{\partial \rho'}{\partial t} + \overline{u}_i \frac{\partial \rho'}{\partial x_i} + \overline{\rho} \frac{\partial u_i'}{\partial x_i} = 0 \tag{4.4a}$$

$$\frac{\partial u_i'}{\partial t} + \overline{u}_i \frac{\partial u_i'}{\partial x_i} + \frac{1}{\overline{\rho}} \frac{\partial p'}{\partial x_i} = 0 \tag{4.4b}$$

$$\overline{\rho}\overline{T} \left(\frac{\partial s'}{\partial t} + \overline{u}_i \frac{\partial s'}{\partial x_i} \right) = q' \tag{4.4c}$$

$$\frac{\partial \xi_i'}{\partial t} + \overline{u}_i \frac{\partial \xi_i'}{\partial x_i} = 0 \tag{4.4d}$$

where equations (4.4c) and (4.4d) represent linearised equations for entropy and vorticity perturbations (the former obtained by manipulating the energy equation and the latter by manipulating the momentum equations). This leads to the classical description which shows that any perturbation may be decomposed into three modes [170], each of one is a familiar type of disturbance. The modes are: (i) sound mode (isentropic and irrotational), subject of conventional acoustics, (ii) entropy mode (incompressible and irrotational), which is familiar as temperature fluctuations in low sped turbulent heat transfer problems and (iii) vorticity mode (incompressible and isentropic), which occurs in incompressible turbulent flows. These are independent of each other, so for the acoustic disturbance governed by equations (4.4a) and (4.4b) (since $s' = 0$ and $\xi_i' = 0$) the first two equations may be manipulated to give the convective wave equation:

$$\frac{1}{\overline{c}^2} \frac{\overline{D}^2 p'}{Dt^2} - \nabla^2 p' = \frac{\gamma - 1}{\overline{c}^2} \frac{\overline{D} q'}{Dt} \tag{4.5}$$

where $\frac{\overline{D}}{Dt} = \partial/\partial t + \overline{u} \cdot \nabla$ and $\overline{c}$ is the steady speed of sound.

To illustrate further, if the mean flow is assumed to be zero with no heat release and only plane 1D longitudinal acoustic waves in long ducts are considered, the above equation reduces to the traditional 1D wave equation:

$$\frac{1}{\overline{c}^2} \frac{\partial^2 p'}{\partial t^2} - \frac{\partial^2 p'}{\partial x^2} = 0 \tag{4.6}$$

The solution of this is a superposition of left and right travelling waves:

$$p'(x,t) = A^+ e^{i(\kappa x - \omega t)} + A^- e^{i(-\kappa x - \omega t)} \tag{4.7}$$

where κ is the wavenumber, and the acoustic velocity is defined as:

$$u'(x,t) = \frac{1}{\overline{\rho}\,\overline{c}} \left(A^+ e^{i(\kappa x - \omega t)} - A^- e^{i(-\kappa x - \omega t)} \right) \tag{4.8}$$

The constants A^+ (right travelling wave amplitude) and A^- (left travelling) and whether a given frequency ω corresponds to a possible mode shape which fits a duct of a given length are determined by the boundary conditions at the ends of the duct. Thus, to match the exact conditions corresponding to a duct of length L with an acoustically closed end at $x = 0$ and an open end at $x = L$ (for explanation of these boundary conditions see §4.3), LOTAN would consider each frequency ω and identify that only for certain frequencies (corresponding in this case to the 1/4 wave, 3/4 wave, etc of the duct) would a harmonic perturbation at these given frequencies and with the input amplitude given at $x = 0$ provide a solution which gives the correct amplitude at $x = L$. This is an example of how an acoustic "module" (in this case a duct of length L) can be constructed with a known solution that satisfies the governing linear equations, whose unknown parameters and range of valid frequencies can be identified by demanding compatibility with given acoustic boundary conditions.

This approach can be applied not just to a simple module of a plane duct of length L; other module descriptions can be constructed for components such as a plenum, a duct area change (increase or decrease), and devices which drive acoustic energy such as a loudspeaker or even a flame zone (with both a mean heat release ($\overline{q}$) and a fluctuating heat release (q')). Geometries of interest can then be modelled by connecting together appropriate acoustic modules into a network (for further details the user manual of the LOTAN code may be consulted [171]). Acoustic analysis (see [6, 167]) then leads to identification of transfer matrices connecting the acoustic perturbations at inlet and outlet of the modules. A network of such modules may be built up for any given geometry. Hence, provided the geometry is detailed, acoustic boundary conditions are specified, a model for q is chosen and a mean flow solution specified, equation (4.5) can effectively be solved numerically, where p' and u' are of the form indicated in equation (4.1). Thus, solutions for the complex valued ω are obtained; the frequency of a possible resonant mode is $\Re(\omega)/2\pi$ and its growth rate is defined as $-\Im(\omega)$. If the growth rate is negative the mode is linearly stable and the magnitude of the perturbation will decay with time; a positive growth rate indicates a linearly unstable mode and perturbations will grow until nonlinear effects become important.

4.2 Geometry

As noted above, the actual geometry of the combustion system is converted into a network of *modules*, linked consecutively, that conveniently describes its relevant acoustic features. Thus, the dimensions (cross-sectional areas and lengths) of modules must be provided as well as the transfer matrices corresponding to the acoustic characteristics of each particular module. Whilst complicated multiply-connected flow paths can be

handled by LOTAN [171] only a simple once-through left to right network of modules is required here. Some of the types of modules that can be specified and have been used in the results presented later are:

- **Straight duct**: A uniform axial duct of given length and cross-section.
- **Area increase (or decrease)**: Treated as an abrupt change in area as long as the distance over which the geometry changes is small in comparison to the acoustic wavelength being considered. This is usually true in the present context where, for frequencies of order 100Hz and typical combustion gas temperatures, the acoustic wavelengths are equivalent to many metres. Note that if the flow becomes supersonic in an area decrease the LOTAN calculation will fail.
- **Combustion zone**: This indicates a region where heat release takes place. Mean and perturbation combustion models need to be provided (see below).
- **Loudspeaker**: This indicates that a loudspeaker is attached to the duct. The acoustic input of the loudspeaker corresponds to an added unsteady mass flow rate at a specified frequency at the duct location where the loudspeaker module is placed, with an associated energy change, but no change in momentum.

An illustrative example of a geometry set-up with LOTAN to model the ORACLES experimental configuration is shown in Figure 4.1. This consists of a longitudinal combustion system starting with an inlet boundary condition to a plenum (an acoustically closed inlet - see below), followed by a supply duct, a combustion chamber containing a flame module (assumed of zero length) and finally an outlet boundary condition.

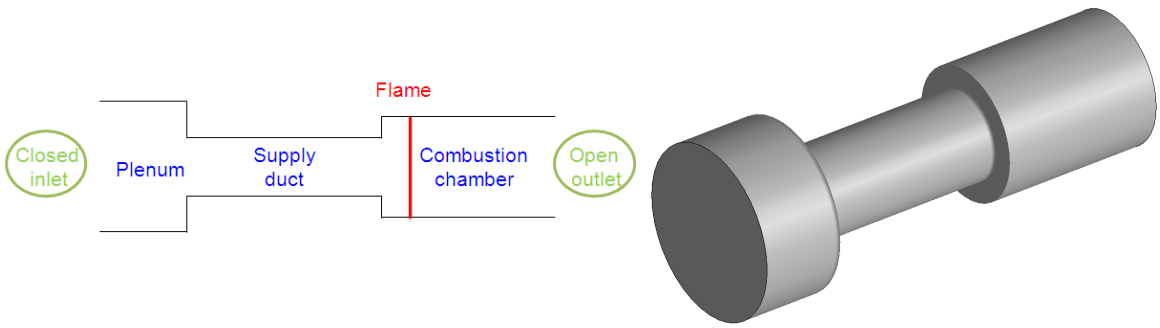

Figure 4.1: Schematic diagram of a geometry set-up of the ORACLES experimental configuration in LOTAN, with 2D (left) and 3D (right) representations

4.3 Boundary conditions

At inlet and outlet of the combustion system, boundary conditions to be satisfied by the acoustic waves must be imposed. In LOTAN, different options are available, to describe a range of physical situations, which model acoustic characteristics of inlets and outlets found in gas turbine combustor systems. Some of these are:

- **Open**: An acoustically open end, $p' = 0$. Approximates the presence of a large plenum chamber attached to this end or a large area increase into atmosphere.
- **Closed**: An acoustically closed end, $u' = 0$. Approximates a large area decrease at this end of the system.
- **Choked**: Boundary conditions to apply to flow perturbations are derived from asymptotic analysis [172]. For a choked inlet, a wave travelling upstream is reflected and a shock wave is assumed to be present at inlet. When the shock wave's position and flow perturbations interact acoustic, entropy and vorticity waves will be produced. For a choked outlet, either an acoustic, vorticity or entropy wave is assumed to travel downstream. The asymptotic analysis finds the reflected wave that is created.
- **Nonreflective boundary**: This states that no disturbances arrive from outside and enter the combustion system. Thus, there are only left (or right depending on the location of the boundary at the start or end of the network) travelling waves and the amplitude of right (or left) travelling waves is zero. That is, the reflection coefficient R is 0 (or ∞), where R is defined as:

$$R = \frac{A^+(t - x_0/\overline{c})}{A^-(t + x_0/\overline{c})} = \frac{Z+1}{Z-1} \tag{4.9}$$

  where x_0 is a given axial position and Z is impedance, defined as:

$$Z = \frac{1}{\overline{\rho}\,\overline{c}} \frac{p'}{u'} \tag{4.10}$$

  This condition approximates a very long duct outside the boundary location.
- **Specified reflection coefficient/impedance**: A reflection coefficient or the equivalent impedance (real and imaginary parts) can be specified. Thus, fully or partial transmission of left/right travelling waves across the boundaries can be imposed (i.e, specify the amount that crosses the boundaries and the amount that is reflected). At outlet, e.g., R=1 indicates a fully reflective boundary conditions whereas $R = \infty$ indicates no waves are reflected.

Further details of the whole range of module types and boundary conditions available in LOTAN are given in the user manual [171].

4.4 Actions

In LOTAN, different "actions" can be performed. These predict and describe resonant modes of the system when different acoustic features are included and varied. Some of the actions used in the present thesis are:

1. **STEADY**: Calculation of the resonant modes of a system where combustion is present (changing the temperature in various zones and hence the speed of sound) but no unsteady flame-acoustics coupling is allowed. Effectively, the fluctuating heat release is set to 0. The output is the modeshape of possible resonant modes, although the stability of these modes (growth rate) is not predicted.

2. **FORCED**: Calculation of the resonant modes of a system when a specific module (flame/loudspeaker) is set as a source of a forcing. Hence acoustic waves are generated at a specific location in the system, which interact with the boundaries. The frequency of the forcing is specified and its amplitude is iterated to satisfy the main-end boundary conditions.

4.5 Acoustic analysis to inform incompressible LES forcing

From the ORACLES experimental data [81, 82] it is known that a self-sustained acoustic mode at 50Hz is present under some reacting conditions. To investigate this, LOTAN allows for the option of carrying out a forced calculation (FORCED action), by placing a loudspeaker somewhere in the prescribed geometry (the obvious place to locate this is at the inlet region of the combustion chamber, where the flame intensity must be greatest, see Figure 4.1), with forcing at the specified frequency of 50Hz. This calculation then allows determination of the modeshape and therefore predicts the axial variation of acoustic pressure and velocity (subject to the pre-specified inlet and outlet boundary conditions). Note, it is important to remember that, since the acoustic analysis is linear LOTAN carries out calculations for an inlet reference amplitude. Thus, the modeshape is effectively in non-dimensional form and some reference value taken from experiments is required to convert this into a dimensional quantity. This allows the acoustic velocity amplitude to be predicted at any convenient position in the ORACLES geometry so that the incompressible LES inlet conditions can then be "acoustically sensitised". See section §6.2 for details.

4.6 Method for transferring FTFs extracted from LES into the LOTAN acoustics code

A flame module in LOTAN is specified such that information on both mean and fluctuating heat release ($\overline{\dot{Q}}$ and $\dot{Q}'$) are required. This information is included in LOTAN by means of an FTF, which effectively describes how the flame responds to approach flow perturbations. Thus, a series of LES calculations including acoustic forcing (to be described below) are performed and time-varying heat release rates are predicted throughout the reacting flow. These data are postprocessed to obtain values for mean heat release ($\overline{\dot{Q}}$) and fluctuating heat release ($\dot{Q}'$) as described in chapter 6. The flame module in LOTAN contains a heat release model following a *time-delay* formulation [168, 169]:

$$\dot{Q}' = |\dot{Q}'|e^{-i\omega\tau} \tag{4.11}$$

where τ is the time-delay. The FTF relationship from the LES may be written:

$$\frac{\dot{Q}'}{\overline{\dot{Q}}} = K\frac{u'}{\overline{u}} \tag{4.12}$$

where K is the gain and u' and $\overline{u}$ are the fluctuating velocity (caused by the acoustics) and the mean velocity at the inlet to the combustion region. The overall fluctuating heat release input into LOTAN is thus specified as

$$\dot{Q}' = K\overline{\dot{Q}}\frac{u'}{\overline{u}}e^{-i\omega\tau} \tag{4.13}$$

The extraction of the FTF parameters K and τ from a forced LES is described in detail in chapter 6.

Chapter 5

Incompressible LES of a turbulent premixed flame - ORACLES test case

5.1 Introduction

The numerical and modelling framework of the LULES code for LES premixed combustion, described in previous chapters, has been validated against selected experimental data and these results are presented in this chapter. The main objective is to assess LES predictive capabilities for turbulence and to validate the implemented combustion model in a relevant turbulent premixed flame problem. The ORACLES test case [81, 82] has been chosen for validation purposes and details of this experimental study are presented first. The numerical strategy to generate instantaneous LES inlet conditions which match the experimental set-up is then described, followed by results for both inert and reacting flows compared against available experimental data.

5.2 The ORACLES test case

The ORACLES (One Rig for Accurate Comparison with Large-Eddy Simulations) test case [81, 82] comprises a turbulent flame stabilised behind a double symmetric, plane sudden expansion fed by two fully developed turbulent channel flows of premixed air and propane; the equivalence ratio in each channel can be varied, but for the present project only the perfectly premixed case of equal mixture strength was considered. The measurements have previously been used as a test case for RANS modelling [173]. Laser Doppler Anemometry (LDA) measurements were performed within the European project MOLECULES [174]. Measurements were conducted in the approach ducts as well as in the combustor, for both non-reacting and reacting cases. Thus, this test case can be thought of as a relevant benchmark for testing turbulence and/or combustion modelling approaches for lean premixed prevaporised (LPP) combustors [81, 82].

It is important to note that the ORACLES experiments revealed (under certain equivalence ratio conditions) the presence of strong self-excited and self-sustained acoustic waves. In the present work the hybrid coupled incompressible LES plus acoustic network methodology has been adopted. To set a benchmark for testing the effectiveness of the coupled approach the results presented in this chapter do not include any acoustic effects. The description of the acoustic coupling methodology and its application to improve results are presented in chapters 4 and 6.

Other authors have previously performed LES simulations of the ORACLES test case. Some authors, e.g. [175, 176] have considered partially premixed cases, which are not of immediate relevance to the present work. Domingo et al. [116] proposed and validated their FSD-PDF model, coupled with a fully compressible LES code, for a case with equivalence ratio 0.75 in both streams. It is interesting that, although their compressible formulation could in principle capture acoustic modes directly, they avoided simulating the full experimental system geometry (which it would have been necessary to include all upstream and downstream acoustic impedances that can influence the resonant acoustic modes) and instead they performed simulations which merely perturbed the flow in the approach ducts by adding sinusoidal forcing at the specific frequency and amplitude observed in the experiments to mimic the acoustic mode observed in the measurements. It is odd that this approach, which is more relevant to an incompressible calculation should be used in conjunction with a compressible LES code, with the associated computational time-step penalty. Fureby [134] has used a progress variable approach with a fractal flame-wrinkling closure model for the chemical reaction term and tested this model for the case of equivalence ratio 0.65 in both incoming ducts. No acoustic mode as found in the experiments was included. Duwig and Fureby [117] used a mixture fraction/progress variable approach and a low-Mach number formulation for a uniform equivalence ratio of 0.75, with sinusoidal forcing at inlet to mimic acoustic waves at the experimentally observed frequency. An arbitrary (trial and error) series of forcing amplitudes (A) were considered until the response of the system was observed to saturate and an amplitude of 27% of the bulk-average inlet velocity was finally chosen, although with no attempt made to justify this based on any acoustic analysis. Finally, Wang [80] used a progress variable approach and an algebraic FSD combustion model for the test case with equivalence ratio 0.65 in both streams, with no allowance made for acoustic waves. In all the above studies, only limited information on the inert flow simulations has been reported and little information on the LES inlet condition generation details. In the results from the present work provided below, comparison will also be made with previous predictions.

5.2.1 The ORACLES test rig

A 2D sketch of the ORACLES test rig, located at the Ecole Supérieure de Mécanique et D'Áeronautique in Poitiers (France), is depicted in Figure 5.1. This $10m$-long rig consists of 4 main sections: 1) two mixing chambers feeding into separate plenum/settling chambers; 2) a $3.27m$ long straight section of two constant rectangular cross-section ($0.0304m$ high x $0.150m$ wide) ducts, required to obtain fully developed turbulent channel flow upstream of the sudden expansion (to facilitate LES inlet condition setting), and the two approach ducts were separated by a splitter plate, which is recessed with respect to the sudden expansion to avoid possible anchoring of the flame at the tip of the plate; 3) a $2m$ long combustion chamber thermally insulated (to allow for the use of adiabatic combustion models); 4) an exhaust section (whose dimensions were not specified) that follows the combustion chamber, equipped with water-pressurised injectors and a fan extractor. It is also unclear from the data and description provided whether the exhaust section is attached to the combustion chamber or a gap is left in between the two. The fuel and air are supplied to the two inlet channels from high-pressure storage reservoirs and are premixed and homogenised in two separate mixing chambers that are acoustically isolated from the rest of the rig by $4mm$ thick circular porous plugs (size of porosity less than 8 μm) at the junction between mixing and settling chambers. This aims to minimise any effects that acoustic waves travelling upstream might cause on the mass flow rates of the premixed air/fuel streams.

5.2.2 Simulation test cases

In the present thesis, two inert (denoted nc_1 and nc_2) and two reacting (denoted c_1 and c_2) cases have been investigated. The main flow parameters of the different cases are summarised in Table 5.1.

Case	Stream	$\dot{m}$(g/s)	Re_{ch}	$U_{bulk}(m/s)$	ϕ	Da	Ka	Exp. data
nc_1	Upper	52.8	24556	8.8	NA	-	-	[81]
	Lower	52.8	24966	8.8	NA	-	-	[81]
c_1	Upper	52.8	24566	8.8	0.65	8.44	9.31	[81]
	Lower	52.8	25784	8.8	0.65	8.44	9.31	[81]
nc_2	Upper	65	25000	11.0	NA	-	-	[82]
	Lower	65	25000	11.0	NA	-	-	[82]
c_2	Upper	65	25000	11.0	0.75	21.41	3.70	[82]
	Lower	65	25000	11.0	0.75	21.41	3.70	[82]

Table 5.1: Main flow parameters of the simulated cases

The test rig described above operates at atmospheric pressure and the mass flow rate and equivalence ratio in each stream can be varied between 0.05-0.2 kg/s and 0.6-1.0 respectively. For cases nc_1 and c_1 [81], the temperature of the incoming streams was

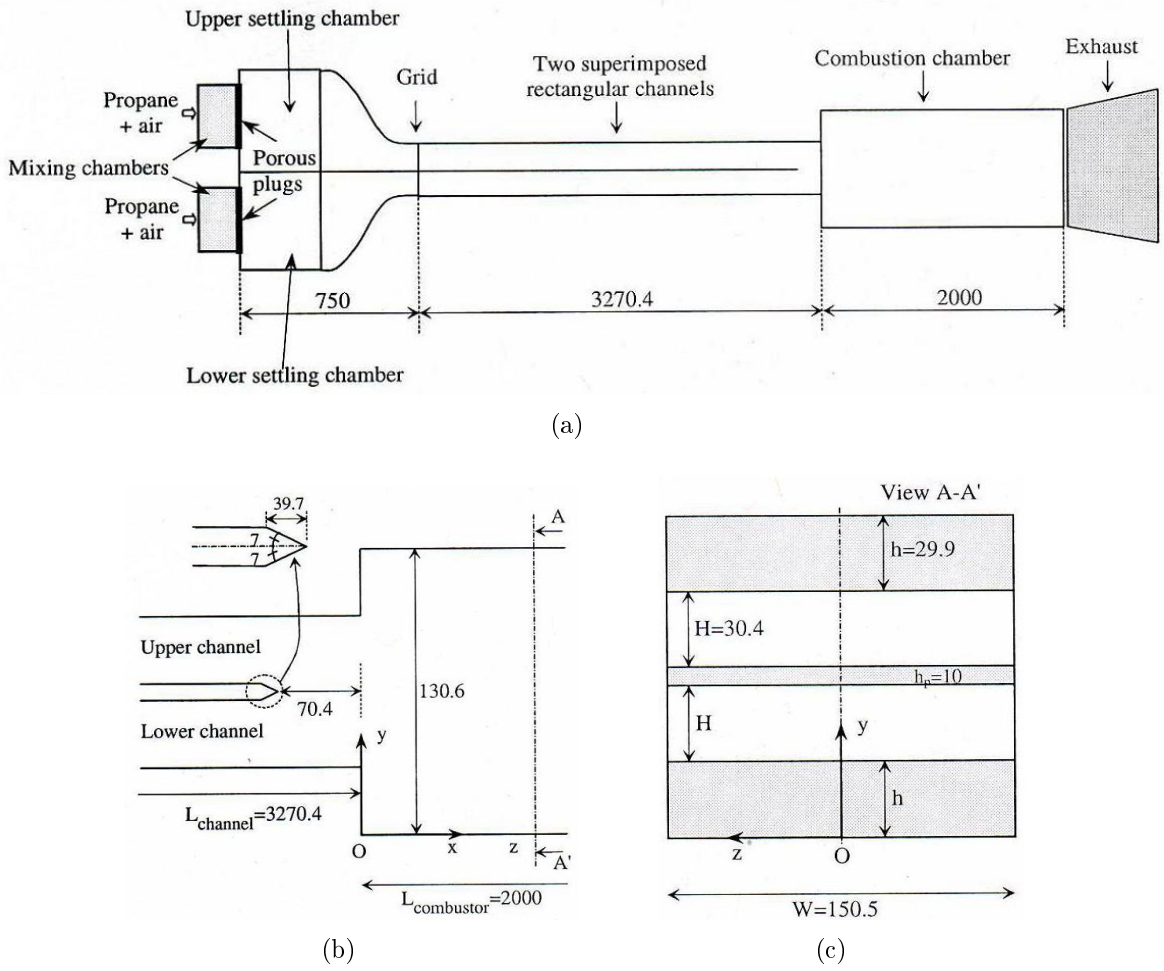

Figure 5.1: 2D sketch of (a) ORACLES test rig, and detailed geometry (b) of the splitter plate, and (c) at the dump plane. (Dimmensions in mm) [82]

$273 \pm 10K$, whereas for cases nc_2 and c_2 [82] the temperature was $276 \pm 11K$.

The mixture supply Reynolds number, Re_{ch} (≈25000), is evaluated based on the channel height $H_{ch} = 30.4mm$, the kinematic viscosity of the fresh mixture at the reference temperature and the channel centreline velocity U_c in Besson et al. [81] but with the bulk velocity U_{bulk} in Nguyen et al. [82]. Also, to obtain estimated values of the Da and Ka numbers (see definitions in §2.3.2) at inlet conditions several parameter values have been assumed, following Nguyen et al. [82]. Thus, the turbulence macroscale L was set equal to $10mm$ (one third of the height of the incoming channel), and the root-mean-square velocity fluctuation u' was chosen to be 0.6 m/s, which is the channel centreline typical value. A Kolmogorov scale η of $0.105mm$ and a Taylor microscale λ

of $1.51mm$ may be deduced from these conditions. The laminar flame thickness was calculated using the ratio between the estimated scalar diffusivity $\mathcal{D}$ and the laminar flame speed s_l. Following Kurenov et al. [173], the diffusivity at an intermediate temperature of $1178K$ was estimated as $\mathcal{D} \approx 5.210^{-5} m^2/s$, and s_l was taken as $0.18m/s$ and $0.25m/s$ for equivalence ratios of 0.65 and 0.75, respectively.

5.3 Generation of velocity inlet boundary conditions

As is well known, LES CFD is potentially highly sensitive to the unsteady inflow conditions that have to be prescribed. High quality specification of the incoming flow (matching experiments as far as possible) is essential, as it may have a decisive influence on the prediction of the downstream field.

Different approaches can be adopted in order to generate LES inflow conditions. The simplest consists of superimposing white (or random) noise on an assumed mean velocity profile. However, the energy spectrum of the inflow signal thereby obtained implies an energy content equally distributed over all frequencies. This uncorrelated nature of the fluctuations means that they decay very quickly. After perhaps just a few cells downstream the inflow data no longer possess realistic turbulent characteristics. More refined methods have been proposed in the past, e.g. the digital-filter method [177, 178], which uses experimental data to generate an unsteady velocity field by matching statistical quantities (first and second order one-point statistics) using input assumptions on a specified autocorrelation function. The major drawback of this method is the necessity for guesses of integral time and length scales that are not commonly measured. The prescription of turbulent velocity fluctuations at an inlet plane could be based on the method proposed in [179], who suggested to reproduce a turbulent signal by solving a stochastic differential equation based on a Langevin equation modified to ensure a -5/3 power decay of the spectrum of the generated signal. However, this technique can also be applied only when rms-velocity fluctuation and integral time scales are available. Alternatively, turbulent inflow data with realistic turbulence characteristics can be generated by an auxiliary (precursor) simulation, which, for example, generates fully developed flow by extracting the velocity field from a downstream location and continuously recycling this instantaneous velocity field as new inlet conditions (similar to imposing periodic boundary conditions in a homogeneous direction). This procedure can be run in an independent simulation to generate and save inflow data, to be read in later into the main simulation.

The precursor method is clearly the most appropriate to the ORACLES conditions and has been adopted here. A separate two-block domain was generated corresponding to

a chosen length L of the double rectangular channels which supply the premixed gas to the combustion chamber (see Figure 5.1). The cross-sectional mesh in the two channels was identical to that in the short section of the inlet channels which was included in the main simulation domain (see later). The inlet plane of this short section coincided with an axial location where LDA measurements were available ($\approx 0.1m$ upstream of the dump plane). The length L of the precursor simulation domain was chosen so that it would be long enough not to constrain the axial size of the largest energy containing turbulent eddies generated by the LES (checked later), but not so long to allow fully developed flow conditions to have been established at $x = L$ from uniform inlet profiles (hence requiring the recycling technique described above). The boundary condition used at the precursor domain outlet was a convective outlet condition.

In this precursor simulation the velocity field was extracted from an axial plane located at x_{ds} (just upstream of the precursor simulation domain outlet) and was fed back to the domain inlet. At the same time, scaling was applied to ensure the targeted (experimental) mass rate, $\dot{m}_{in}$, was maintained. Since the main flow was in the x direction the following scaling procedure was applied to the recycled inlet velocity field:

$$u_{in}(j,k) = \frac{\dot{m}_{in}}{\dot{m}_{ds}} u_{ds}(j,k) \tag{5.1}$$

$$v_{in}(j,k) = v_{ds}(j,k) \tag{5.2}$$

$$w_{in}(j,k) = w_{ds}(j,k) \tag{5.3}$$

where subscripts in and ds indicate inlet plane and downstream plane respectively and $\dot{m}_{ds}$ is the mass flow rate at the recycling plane. The recycling plane was located a small distance upstream of the precursor domain exit plane to prevent the convective outflow condition exerting a strong effect. The distance between the recycling and inlet planes must be larger than the axial length of the largest turbulence structures. DNS results of turbulent flow in a square duct ([180]) showed that the axial two-point correlation coefficient was close to zero within a distance of 3.2H and thus the domain should be at least twice this length. For simulations of rectangular duct flows ([181]) a domain length of $8H_{ch}$ was used (H_{ch} being channel height), while in [182] domain lengths of both $10H_{ch}$ and $20H_{ch}$ were employed. In the present simulation, the distance from the inlet plane to the recycling plane was set to $10H_{ch}$. Based on these data an axial length of $15H_{ch}$ was chosen for the precursor simulation. Once fully developed velocity profiles had been attained in the approach ducts (after $\approx$ 96000 time steps), profiles at the recycling plane were saved to disc at every LES time step for a time period which ensured no temporal correlation between first and last data sets. The length of the data saving period was estimated from autocorrelation information of the saved velocity time-series. Figure 5.2 shows the autocorrelation function of the streamwise

velocity at two different points located in the approach ducts. One point in the centre of the lower duct (Figure 5.2)(a)) and one point located in the boundary layer of the upper duct (Figure 5.2)(b)). At the first point the first zero-crossing is reached after $\approx$ 2000 time steps, although it peaks 3 more times until it reaches an average value of 0 after $\approx$ 10000 time steps. At the second point smaller turbulent scales are observed and the first zero-crossing is observed after just 1000 time steps and reaches an average zero value after 8000 time steps. Autocorrelation functions at other points were similar. Thus, the "sampling time" for data storage was set at 14000 time steps. The data saved (a set of 2D instantaneous u, v and w values over 14000 time steps) were then read in as inlet condition data in the main flow simulation described below. If these simulations ran for longer times, the data were merely looped through as many times as needed.

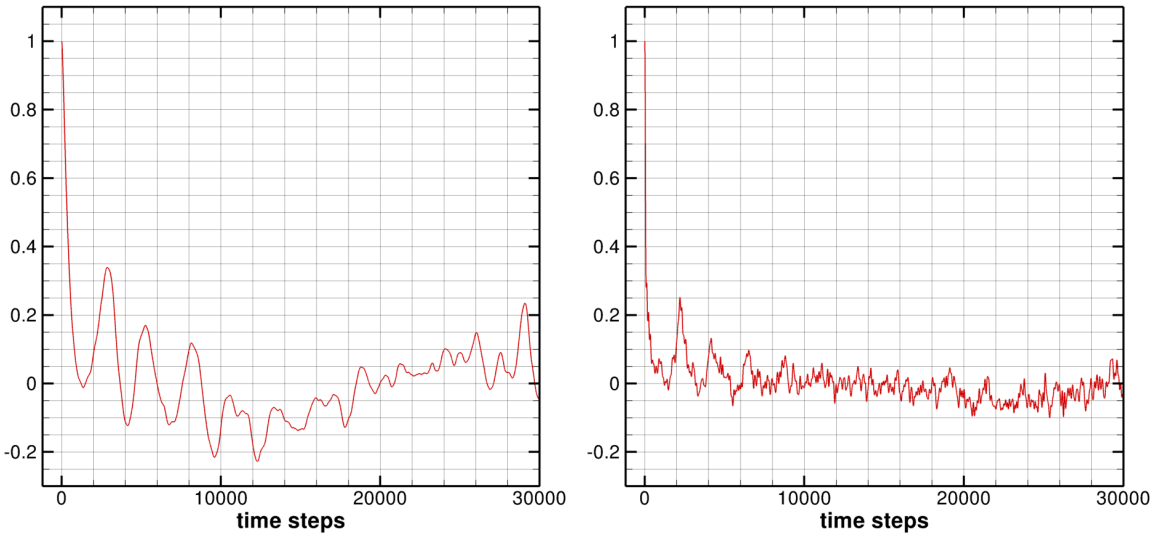

Figure 5.2: Autocorrelation functions of streamwise velocity in points located in (a) the centreline and (b) the boundary layer of the approaching ducts

5.4 Results

In this section, LES simulations of the ORACLES test case are presented. The computational domain and mesh configuration used are described and validation for the inlet boundary conditions imposed carried out. Numerical results for both inert and reacting cases as indicated in Table 5.1 are presented, compared against experimental

data, and discussed. To ensure convergence of the mean values presented in the next sections, all simulations have been run to a minimum of 15 flow through times.

5.4.1 Domain size and grid resolution

Figure 5.3 illustrates the computational domain used in all simulations reported in this chapter. In the streamwise direction the domain extended from $0.21m$ (or $7H_{ch}$) upstream to $0.45m$ (or $14.6H_{ch}$) downstream of the dump expansion plane. The domain covered the whole wall-to-wall geometry of the test rig in the transverse ($0.1306m$) and spanwise ($0.1505m$) directions. Figure 5.3 also shows the 3D multiblock mesh utilised in the present work.

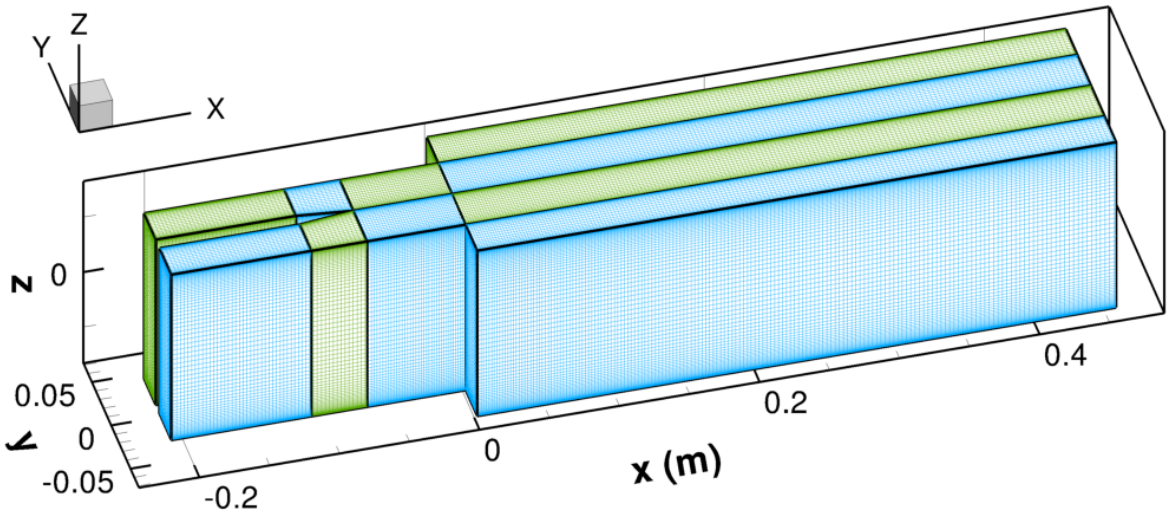

Figure 5.3: 3D multi-block geometry and mesh used in LES simulations

The computational mesh is an important element of any CFD calculation but is crucial in LES. Specific regions in the domain (near-wall regions, shear layers, wakes, etc.) need careful attention when the mesh is designed. Previous work has shown that a *wall-resolving* LES (resolving the scales of motion which control the near-wall dynamics) requires very fine mesh spacing, particularly at high Re. As noted above, since wall functions were being used, it was not intended for the near wall mesh to resolve the small integral scales, but the mesh was examined in this context.

Orthogonal meshes of 96x32x82 grid points in the streamwise, transverse and spanwise directions for the region upstream of the dump plane and 172x116x82 downstream of the dump plane have been used. This leads to a total number of 1.88 million grid cells.

The mesh is non-uniform and stretched in the near-wall regions (in the wall-normal (y or z) directions), in the region axially close to the dump plane (in the x direction) and in the shear layer region, near the step corners (in the y direction). In the inlet ducts, for example, near-wall mesh spacings of $\Delta x^+ = 68$, $\Delta y^+ = 8$ and $\Delta z^+ = 10$ measured in wall units were estimated; similar meshes occurred in the combustion region downstream of the dump plane. These are, in terms of wall normal distance, not quite at the level recommended by Piomelli and Balaras [183] for a wall-resolving LES mesh ($\Delta x^+ \approx 100$, $\Delta y^+ \approx 2$ and $\Delta z^+ \approx 10$), and this is the reason the wall-function boundary condition described above was implemented. It was believed, however, that the most important regions for resolution of turbulence were the shear layers issuing from the dump plane corners rather than the near-wall regions. Stretched meshes were generated by means of the one-parameter hyperbolic tangent function (specified for one direction):

$$x(j) = x_{ini} + L\left(1 + \frac{\tanh(\gamma\frac{j-1}{N-1})}{\tanh(\gamma)}\right) \tag{5.4}$$

where L is the length of the interval where nodes are distributed, x_{ini} is the initial co-ordinate of the interval, γ is the concentration factor and N is the total number of nodes in the interval.

A cross-section of the geometry in the xy symmetry plane and in the yz plane downstream of the dump plane are shown in Figure 5.4. $x = 0$ is located at the dump plane, $y = 0$ is fixed at the centreline of the combustor and $z = 0$ is located at the centre of the wall-to-wall distance in the z direction.

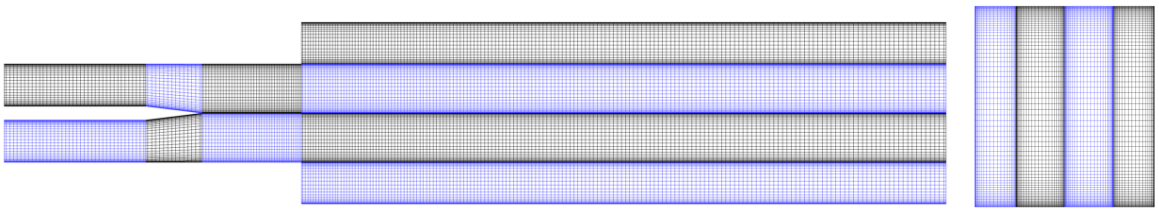

(a) (b)

Figure 5.4: (a) xy and (b) yz cross-sections of multi-block computational grid ((a) splitter plate region and (b) combustor zone)

For the time step, in the present work, a variable Δt was used, determined by a maximum CFL condition, which ensures that Δt is smaller than the time needed for a convective wave to travel from one cell node to the next one. The CFL_{max} number used

was ≈ 0.35; Other authors simulating the same test case used similar CFL numbers, viz: ≈ 0.2 [118], < 0.5 [134] and ≈ 0.2 [117].

5.4.2 Validating inlet flow conditions

In order to assess the validity of the procedure adopted for specifying LES inlet conditions, velocity profiles in the approach ducts were compared against experimental data. Note that it was observed in the experiments that mean flow profiles in the approach ducts were very similar (for the same mass flow) for both inert and reacting cases. This is due to the fact that the combustion process taking place does not affect the flow field upstream of the dump plane.

The predicted flow structure in a yz cross-section in the approach ducts, a distance $0.17m$ upstream of the dump plane, for case c_1 is displayed in Figure 5.5. Figure 5.5(a) shows predicted mean streamwise velocity contours, which exhibit a clear symmetry with respect to both y and z axes. The contours can be seen to bend towards the corners, a secondary flow effect found in non-axisymmetric cross-sections and driven by flow travelling towards corners along the corner bisectors. This is known to be caused by the anisotropy of the normal Reynolds stresses in the duct cross-sectional plane and requires a Reynolds stress transport model to predict this with a RANS closure, but is clearly picked up readily by LES. This effect is confirmed by the plots of the mean cross flow velocity magnitude in Figure 5.5(b), where regions of high magnitude coincide with the corner bisectors. The predicted peak magnitude of the mean cross flow ($0.241m/s$) is 2.7% of the bulk velocity ($8.8m/s$), which agrees well with the value of 2.6% obtained by Ham et al. [184] in their LES of turbulent flow in a square duct.

Predictions of streamwise velocity profiles, on $z = 0$ and at distance $0.17m$ upstream of the dump plane, are shown in Figure 5.6, compared with experimental data [81, 82]. Figures 5.6 (a) and (b) correspond to case nc_1 and (c) and (d) to case nc_2 simulations. In general, the agreement of numerical results and experimental data is very good in both cases. The profiles of $\overline{u}/U_{bulk}$ are typical of fully developed turbulent channel flow with a maximum non-dimensional velocity of 1.3-1.4. The value achieved in the current predictions (1.36 for c_1 and 1.34 for c_2), differs slightly from values reported in the literature. Dean's correlation $U_c/U_{bulk} = 1.28 \cdot Re_b^{-0.0116}$ [185] (Re_b is Reynolds number based on bulk velocity), would give a value of 1.14 for both cases nc_1 and nc_2. Of course, the present experiment is a rectangular duct of aspect ratio 4.5 rather than a 2D channel, so some difference may be expected. Regarding the fluctuating streamwise velocity profiles the largest discrepancy is in the near-wall region where the wall-function-based simulations underpredict the close to wall values as expected for a non-wall-resolved LES; nevertheless the profile shape is reasonable.

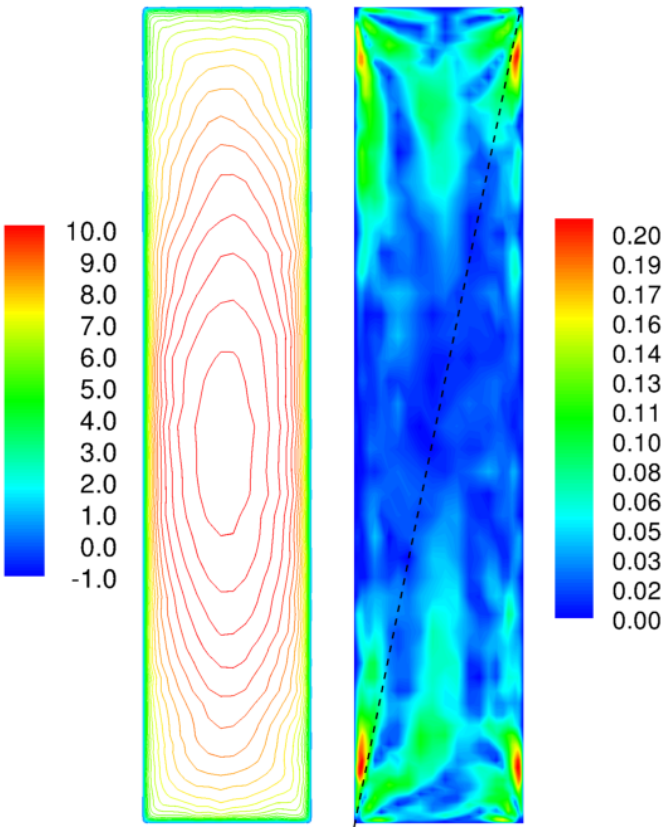

Figure 5.5: (a) Mean streamwise velocity contours and (b) mean cross flow magnitude in a yz cross-section in the inlet ducts, $0.17m$ upstream of the dump plane

For further validation of the inflow data provided by the precursor simulation, probability density functions (PDFs) of the streamwise velocity at the centreline of the upper duct $0.17m$ upstream of the dump plane are shown and compared with measurements in Figure 5.7. The PDF shapes are presented as well as values of skewness (S) and flatness (F) factors, defined by

$$S = \overline{u'^3} / \left(\overline{u'^2}\right)^{3/2} \qquad \text{and} \qquad F = \overline{u'^4} / \left(\overline{u'^2}\right)^{2} \tag{5.5}$$

On the top row of Figure 5.7, numerical and experimental PDFs corresponding to case nc_1 are displayed whereas the bottom row refers to case nc_2. In both cases the overall agreement between numerical results and experimental data is very good, exhibiting very similar morphologies, i.e. a close to Gaussian distribution. Also, in both cases, the left-hand tail is predicted to be longer than the right-hand one described by the negative skewness factor. The flatness factor, describing the spread of the PDFs, is reasonably

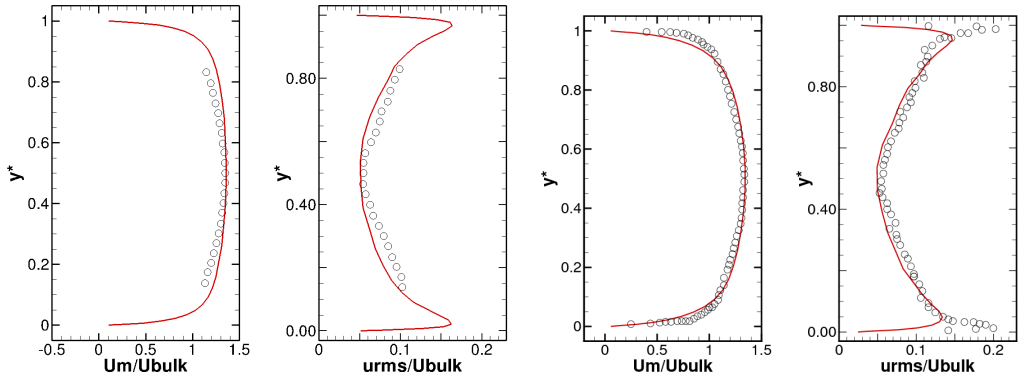

Figure 5.6: Transverse profiles of (a),(c) mean and (b),(d) fluctuating streamwise velocity at plane $z = 0$ and $x = -0.17m$. (a) and (b) from case nc_1, (c) and (d) from case nc_2 and $U_{bulk} = 11m/s$

well predicted by the numerical results, specially for case nc_2; a small overprediction of the skewness factor is observed, and the mean value is slightly shifted to lower values.

5.4.3 Cold flow

The inert flow cases nc_1 and nc_2 were first simulated in order to estimate and assess the prediction capabilities of the LES tool to solve for turbulence and mixing.

5.4.3.1 Contour plots

The most noticeable feature of the non-reacting flow is its asymmetry, with an upper recirculation zone much shorter than the lower. This can be observed in Figure 5.8 where instantaneous and mean streamwise velocity contours on plane $z = 0$ for case nc_1 are depicted (the same aerodynamic features characterise both inert cases (same Re), therefore corresponding figures for case nc_2 are not shown for brevity). This asymmetry is in accordance with experimental investigations of non-reacting flows behind double backward facing steps [186], which show that if the expansion ratio $A_r = (H + 2h)/H$ (where H (=0.0708m) is the channel height at the expansion plane and h is the step height) is greater than ≈ 1.50, then the mean flow will be asymmetric. In the OR-ACLES geometry, the expansion ratio is 1.84. A reason for this asymmetry is the Coanda effect [187] , i.e., the tendency of a jet to attach itself to a solid body due to a pressure variation perpendicular to curved streamlines. The predicted lower and

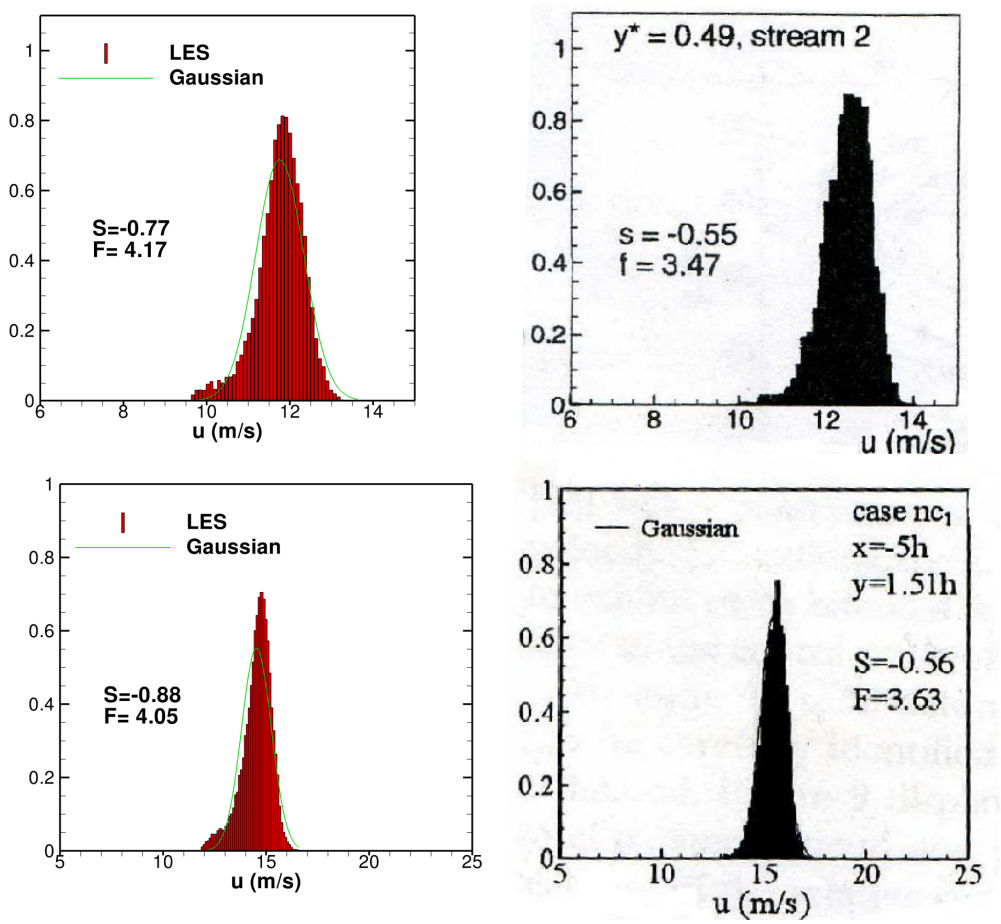

Figure 5.7: Probability density functions (PDFs) of streamwise velocity at centreline of upper duct and $0.17m$ upstream the dump plane for case nc_1 (top) and case nc_2 (bottom). Left column are LES results and right column are experimental data [81, 82]

upper reattachment locations are $10h$ and $5.12h$. The experimental values reported in [82] for case nc_2 are $8.0h$ and $5.5h$. It is important here to understand the importance of high quality turbulent inflow data prescribed at the computational domain inlet in order to obtain an accurate prediction of the jet deflection as noted by Duwig et al. [118, 188]. They performed a sensitivity analysis on the velocity fluctuations imposed onto the incoming flow, showing a significant effect on the extent of asymmetry, even recovering symmetry in some cases tested. They also found that a low grid resolution added additional numerical diffusion acting on the jet to smear it out and thus caused an underestimation of symmetry breaking. A third aspect which was observed to influence the prediction of jet deflection was the total spanwise (z) domain length. Duwig et al. overpredicted the jet deflection when only half of the geometric width was

considered, since this constrained the predicted eddy size in that direction, emphasising the importance of including the whole wall-to-wall distance in the computational domain.

It can also be seen in Figure 5.8 how the two incoming channel streams merge after the splitter plate creating a mixing layer at the centreline, which continues to develop as it approaches the combustion chamber. Likewise, the two jets generate shear layers at the two step corners as they enter the combustion chamber due to the sudden expansion. The growth of large scale eddies in these demonstrates the shear layer development. Furthermore, the intensity of the wake mixing layer formed at the tip of the splitter plate is lower compared to the intensity of the two shear layers created at the step corners. Therefore the presence of the central zone of turbulence downstream of the dump plane does not significantly modify the overall structure of the mean flow when compared with a one-stream expansion (note this would be different if the two streams had different mass flow rates).

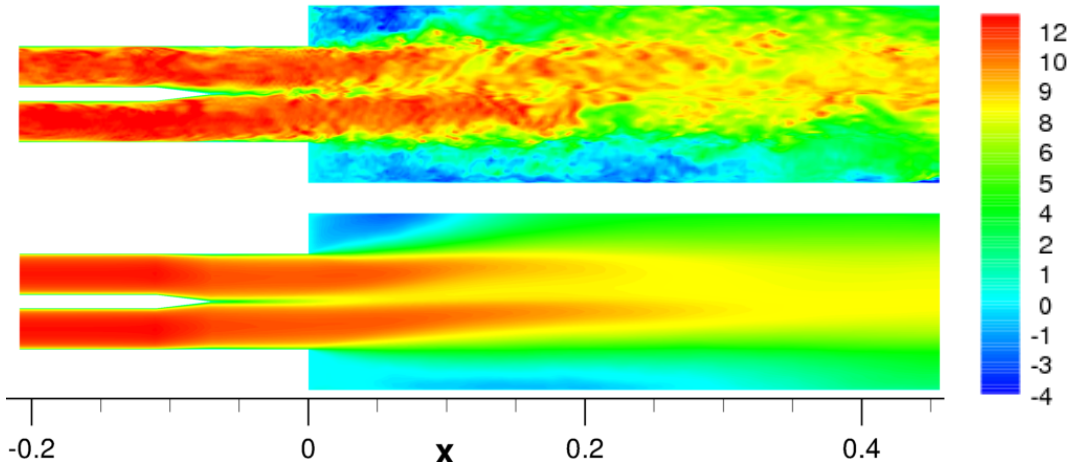

Figure 5.8: Instantaneous (top) and mean (bottom) streamwise velocity contours in plane $z = 0$

The 3D nature of the flow is well captured in the LES calculations, as can be seen in the contours of mean streamwise velocity shown in Figure 5.9. Contours in yz planes at different axial positions ($x = h$, $7h$ and $12h$) and in an xy plane ($z = -1.4h$) are plotted, evidencing again the asymmetry in the y direction. This is especially clear at the plane $x = 7h$. This observation is in accordance with the experimental findings of Pitz and Daily [189] and Escudier et al. [190] who noted the strong 3D nature of their backward facing step data, with aspect ratios of 6.9 and 5.33, respectively (present case is 5). Two central elliptically shaped zones of high velocity are observed in yz planes, which are a consequence of the two incoming channel flow streams entering the

combustion chamber, and progressively merging in the downstream direction.

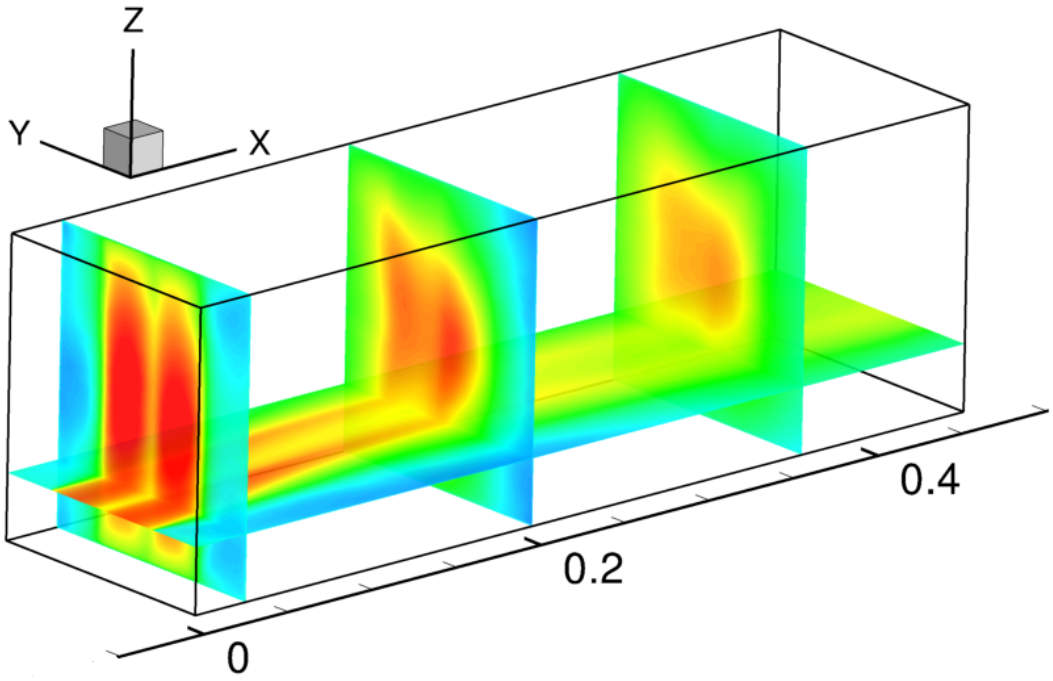

Figure 5.9: Mean streamwise velocity contours at an xy-plane, and yz-planes at different axial locations

5.4.3.2 Transverse profiles

Transverse profiles of mean and fluctuating streamwise and transverse velocities are plotted at different axial positions (see Figure 5.10) downstream of the dump plane, for both cases $nc1$ and $nc2$ in Figures 5.11-5.14. Overall the agreement of LDA measurements and LES results is very good, in both shape as well as in magnitude.

Figure 5.11 shows transverse profiles of mean streamwise velocity. The agreement is excellent, and the asymmetry mentioned earlier can again be observed at position $x/h = 6.35$, and is captured precisely by the LES results. Marginally overpredicted profiles are observed in the lower stream at axial positions $x/h \geq 3.68$ as well as a slight overprediction of the jet deflection for the maximum axial position $x/h = 8.36$.

Figure 5.12 displays mean transverse velocity profiles. The LES results again reproduce accurately the magnitude and shape of the velocity profiles. The largest discrepancy

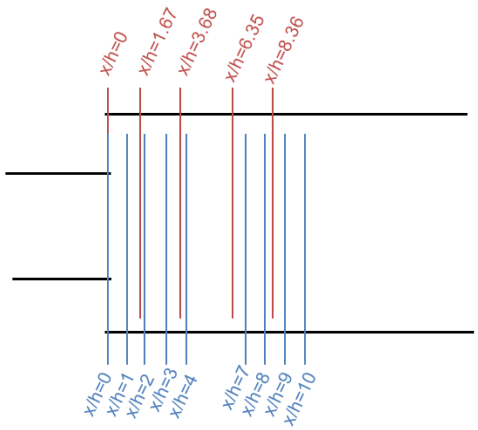

Figure 5.10: Axial positions where transverse profiles are extracted, for cases nc_1 (red, top) and nc_2 (blue,bottom)

is observed at axial position x/h =1.67, where there is an underprediction in the upper stream and an overprediction in the lower stream. The shape is well captured, specifically the peak seen at a location around $y = 0.12m$, which indicates the transverse velocity contributing to the bending effect. Note that the magnitude of the mean transverse velocity is much lower than the mean streamwise velocity.

Figures 5.13 and 5.14 correspond to fluctuating streamwise and transverse velocities respectively. They both share some noticeable common features. For positions downstream of the dump plane, the profiles present two marked peaks at transverse positions $y \approx 0.03$ and $y \approx 0.10$. These maxima correspond to the centre of the shear layers originating at the step corners and situated between the jet potential cores and the low-velocity recirculation zones. The peaks are shifted towards the upper stream, following the jet deflection mentioned earlier, especially at positions $x/h = 1.67$ and $x/h = 3.68$. This two-peak feature is particularly well captured in the LES, in both magnitude and location for both fluctuating velocities. For the fluctuating streamwise velocity, a slight underprediction is observed at positions $x/h = 3.68$ and $x/h = 6.35$ in the lower stream, and at positions $x/h \geq 6.35$ in the upper stream. Furthermore, for the fluctuating transverse velocity an underprediction is observed at axial positions $x/h \geq 3.68$ for both peaks. Another double-peak but of lower intensity is observed on the combustor centreline for position $x/h \leq 3.68$, for both fluctuating velocities. This local maximum evidences the interaction of the two incoming streams and the wake originating from the tip of the splitter plate, which weakens further downstream until it is no longer observed. The central double-peak is accurately reproduced by the LES results for positions $x/h = 1.67$ and $x/h = 3.68$, for both fluctuating velocities,

although is considerably overpredicted at the dump plane, as previously reported by Duchamp de Lageneste and Pitsch[175] and Duwig [118].

5.4.3.3 3D contour plots

Figure 5.15 displays $\overline{u}$-isosurfaces, for $\overline{u} = 7.7m/s$ and $\overline{u} = -0.1m/s$, in the combustion chamber. These allow the asymmetry in the transverse direction to be highlighted, with the recirculation zone, indicated by the negative velocity isosurface, being much longer on the lower wall. Also, the 2 conical isosurfaces, which merge further downstream, show the origin of the asymmetry, indicating the strong bending of the incoming jet to the lower wall.

5.4.3.4 Conclusions

The ability of an LES formulation to capture the main features of the flow has been demonstrated in this section for an inert flow case. The quantitative agreement of measurements and LES results is excellent. The second order statistics are also accurately predicted. Finally, the validation of the approach adopted for specification of the inflow data has been verified and adequacy of the mesh resolution confirmed.

5.4.4 Reacting flow

The reacting flow cases c_1 and c_2, whose main parameters have been specified in Table 5.1, were simulated next. The reacting cases represent a more challenging task, with added features that need to be modelled and evaluated. In particular, the validation of the combustion model is a prime example. The combustion model employed describes the flame front displacement by means of an algebraic FSD approach [57] (see §2.3.5.3) and the model constant β was chosen to be 0.2 in the results presented here (the next chapter will address the sensitivity of predicted results to the value of this model constant). Values of the β parameter used by other authors have been provided in §2.3.5.3. Unfortunately no temperature measurements were available from the ORACLES experiments, thus, only velocity and in particular the turbulence measurements can therefore be used to judge the quality of the combustion model performance by means of the induced axial acceleration. Note that the mixture equivalence ratio in the approach ducts is different for the two reacting cases (0.65 for c_1 and 0.75 for c_2). This implies that different Da and Ka numbers characterise the flames, the difference is not great, but the increase in heat release as ϕ increases makes the risk of thermoacoustic behaviour more likely, and, as will be pointed out below, this is indeed the case.

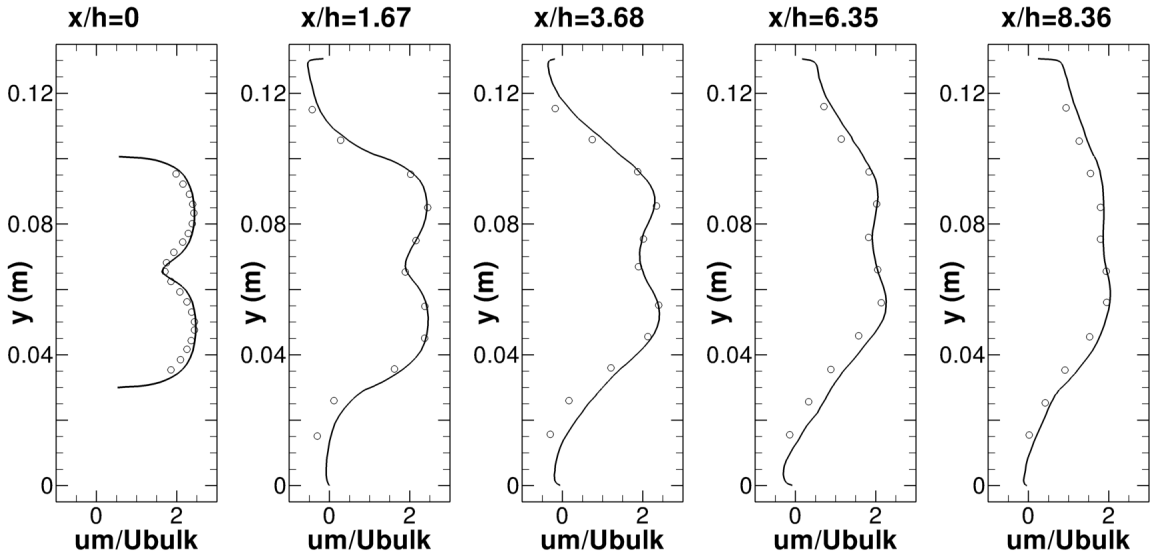

Figure 5.11: Normalised mean streamwise velocity for case nc_1 at different axial positions. U_{bulk} = $4.4m/s$. Experimental data (o) from Besson et al. [81]

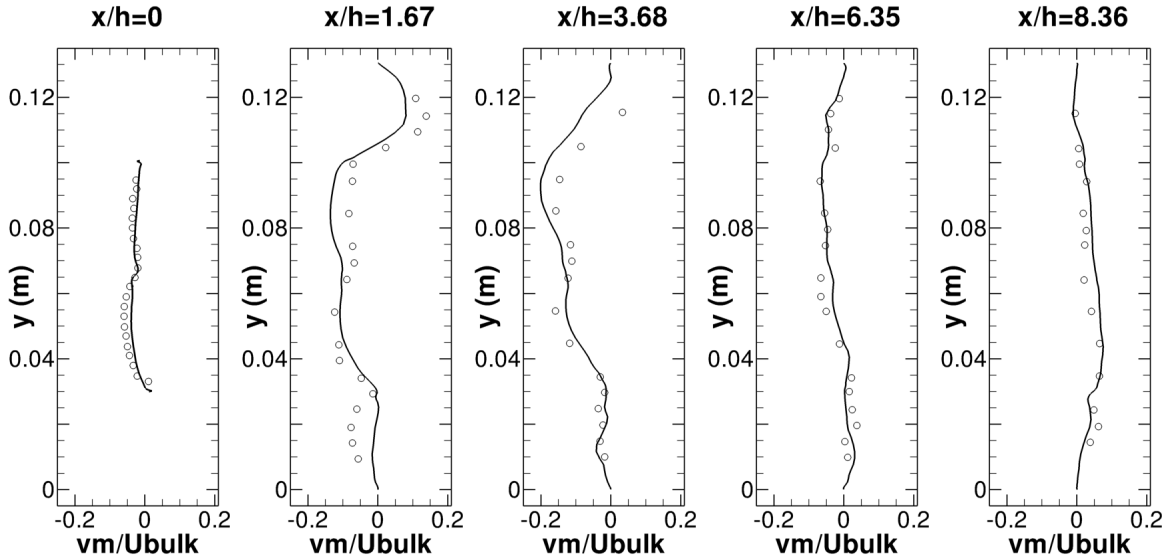

Figure 5.12: Normalised mean transverse velocity for case nc_1 at different axial positions. U_{bulk} = $4.4m/s$. Experimental data (o) from Besson et al. [81]

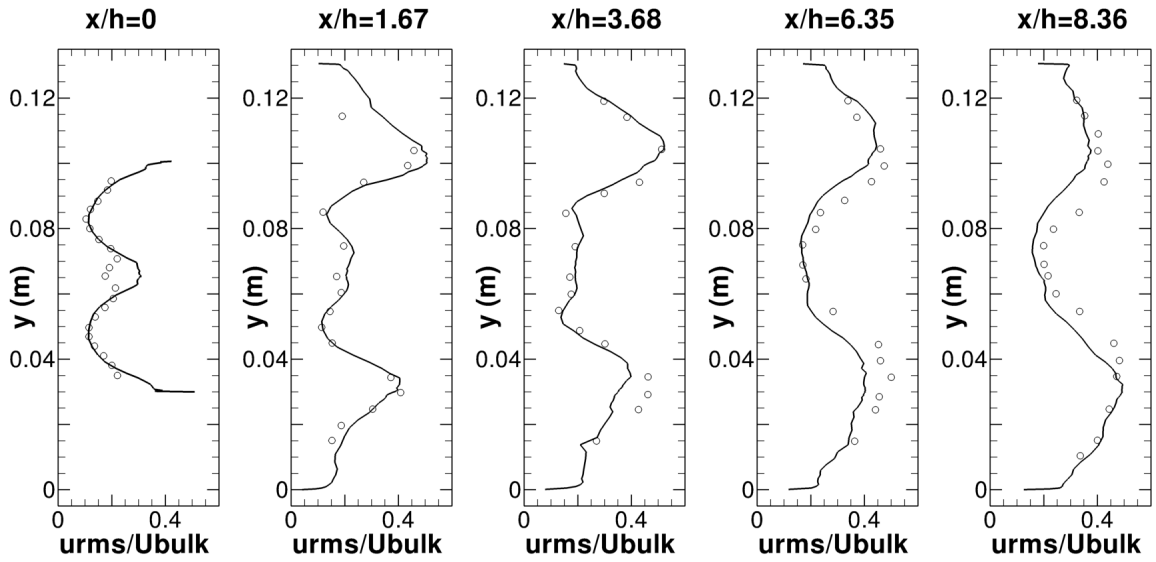

Figure 5.13: Normalised fluctuating streamwise velocity for case nc_1 at different axial positions. $U_{bulk} = 4.4m/s$. Experimental data (o) from Besson et al. [81]

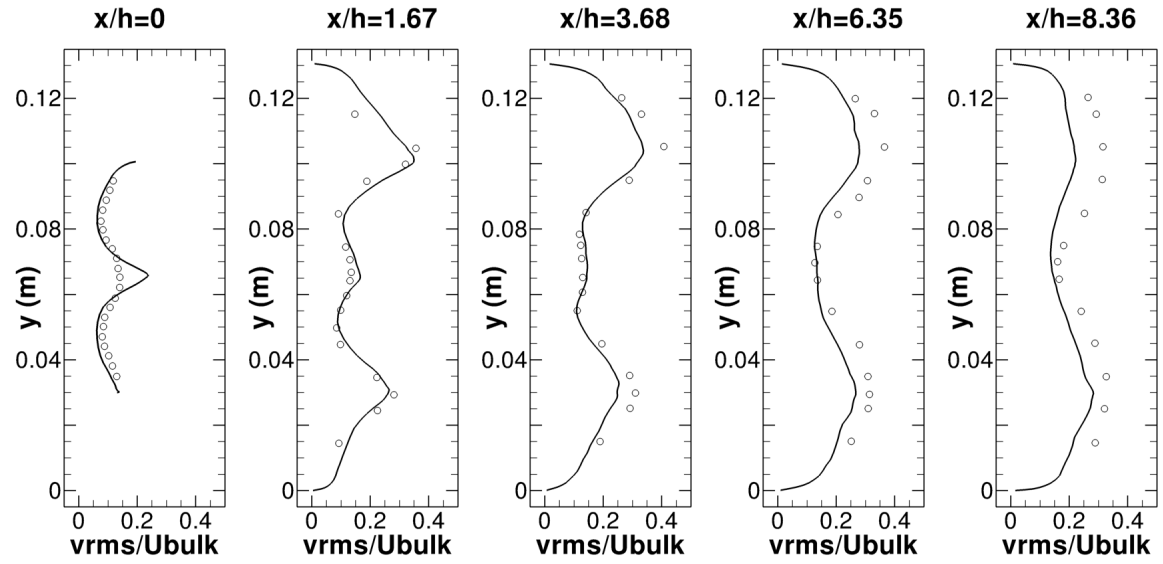

Figure 5.14: Normalised fluctuating transverse velocity for case nc_1 at different axial positions. $U_{bulk} = 4.4m/s$. Experimental data (o) from Besson et al. [81]

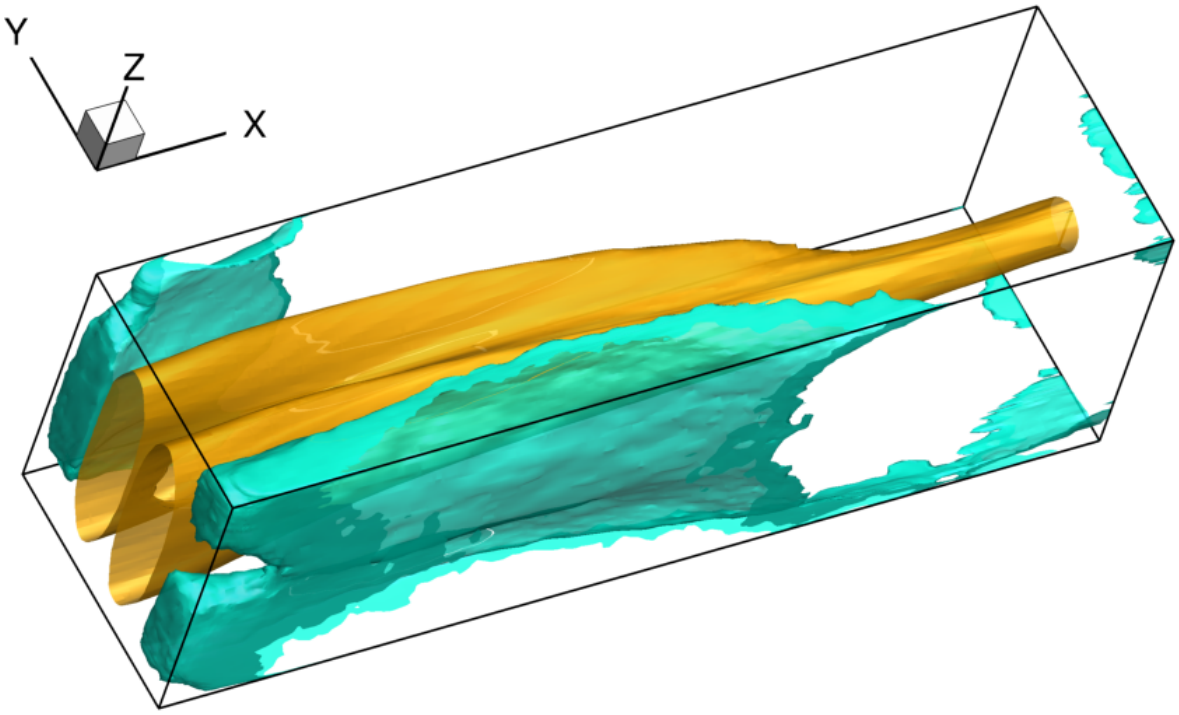

Figure 5.15: $\overline{u}$-isosurfaces $\overline{u} = 7.7m/s$ (orange) $\overline{u} = -0.1m/s$ (blue) in the combustion zone. Case $nc1$

Table 5.2 shows fuel chromatographic analyses (average composition by volume) and flamelet thermochemistry data required by the combustion model for cases c_1 and c_2. The flamelet data were extracted from a freely propagating laminar premixed flame calculation performed with the open-source code CANTERA [124], used together with the San Diego 05 chemical kinetic mechanism for propane/air combustion [145] which includes 46 species and 130 chemical reactions. Subscripts u and b refer to unburnt and burnt conditions, respectively. The differences in the flame parameters are due to the different equivalence ratio of the premixed mixture.

Case	ϕ	Crom. anal.	$\rho_u(kg/m^3)$	$\rho_b(kg/m^3)$	$T_b(K)$	$s_l(m/s)$
c_1	0.65	$C_{3.015}H_{7.818}$	1.306	0.194	1789.433	0.162
c_2	0.75	$C_{3.01}H_{7.85}$	1.294	0.177	1959.792	0.221

Table 5.2: Chromatographic analyses and flamelet thermochemistry data for cases c_1 and c_2

The mesh utilised for reacting simulations was the same as used for inert flow. For boundary conditions at the LES domain inlet plane, these were also identical to those used in the inert flow, as supported by experimental findings [82]. (However, the

presence of any acoustic/combustion interaction - neglected at present - will of course change the fluctuating velocity field and this is discussed further below).

5.4.4.1 Contour plots

One striking feature in the reacting flow, representing a qualitative change compared to its inert counterpart, is the recovery of symmetry of the mean flow in the transverse direction. This is due to the strong acceleration of the flow caused by the decrease in density and the gas expansion as a consequence of heat release. Note that the symmetry attained is restricted to the current case simulated of constant equivalence ratio, since a difference in equivalence ratio in the two supply ducts would produce a different situation. This main flow feature can be seen in Figure 5.16, where instantaneous and mean streamwise velocity contours are plotted in plane $z = 0$ for case c_1 (a closely similar velocity pattern is observed for case c_2). Two recirculation zones of the same size are found on upper and lower walls, consistent with experiments, with a time-mean length of $2.7h$ for c_1 and $2.39h$ for c_2. The value obtained for case c_2 is in very good agreement with experimental data [82], where a recirculation of length $2.3h$ was noted. This shortening of the recirculation zones compared to the inert case is again an indication of the strong acceleration provoked by heat release. The flame is stabilised in the two shear layers on the edges of the recirculation zones created behind the steps. Because of the much lower turbulence intensity in the central mixing layer compared to the shear layer, its influence on flame stabilisation can be expected to be low. For the axial distance covered by the computational domain, maximum values of $\overline{u}$ are increased by a factor of 2 relative to the corresponding inert case, showing consistency with experimental data [81] .

Close examination of Figure 5.16 shows that a very thin region of separation is found in the inlet ducts (also found in the inert case although not mentioned above), attached to the upper and lower walls $\approx 0.075m$ upstream of the expansion plane, beginning at the location of the wedge-shaped splitter plate end (indicated by the zero velocity $\overline{u}$-isosurface in Figure 5.16). This slight backflow is caused by the two incoming streams bending towards the symmetry plane, due to the expansion induced by the shape of the splitter plate tip. Such a region of reverse flow was also observed by Duchamp de Lageneste and Pitsch [175]. This phenomenon required some attention in the reacting simulation, since although this region is very thin, the unsteady nature of any reversed flow zone means that it can instantaneously stretch to the edge of the expansion plane. This can then cause reaction to occur upstream of the dump plane. A numerical strategy was therefore adopted to prevent any reaction taking place upstream of the dump plane (essentially no progress variable value greater than zero was allowed upstream of the dump plane).

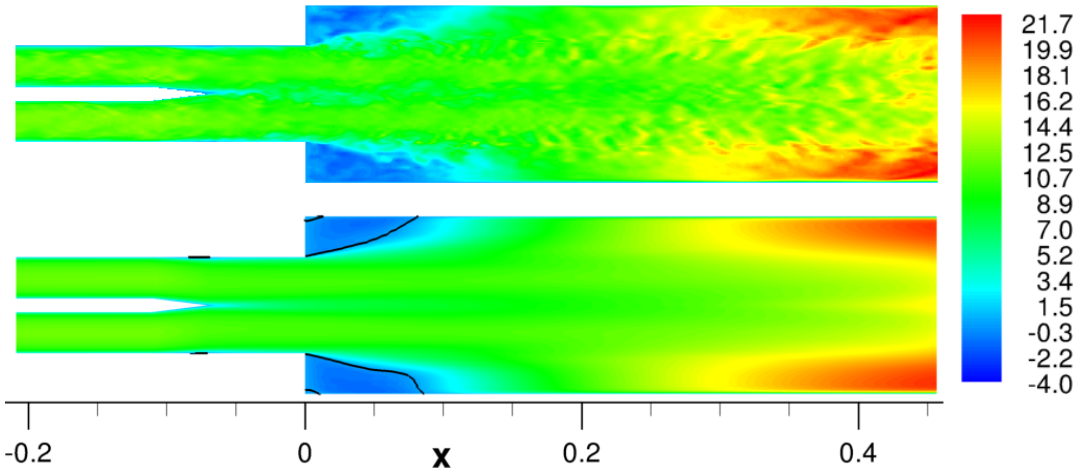

Figure 5.16: Instantaneous (top) and mean (bottom) streamwise velocity contours in plane $z = 0$ for case c_1. Black line indicates $\overline{u}$-isosurface ($\overline{u} = 0$)

Instantaneous and mean progress variable contours at plane $z = 0$ are displayed in Figure 5.17 for case c_1. The structure of the flame can be described as being composed of essentially three regions. A region attached to the upper and lower walls, where the temperature reaches its maximum value, indicating the presence of fully burnt gases in these areas. A second region of cold fresh reactants, located in the core of the duct. Finally, the region between these two zones that is best described as a reacting mixing layer, where large scale (i.e., macroscopic) mixing between cold fresh reactants and hot burnt gases takes place. This region extends from the step corners and grows in transverse width in the downstream direction. The two regions of combusting mixture merge where the core region ends. The instantaneous contours show the structure of the flame, which is wrinkled under the influence of the highly vortical turbulent flow, developed within the two shear layers. Note that some evidence of the turbulence generated by the splitter plate can be seen in these figures in the zone of reacting flow on the duct centreline in the region downstream of $x \approx 0.3m$. The flame brush also appears to flap symmetrically around the centreline. The solid black line represents the flame front, corresponding to a c-isosurface of $c = 0.5$. The equivalent plots corresponding to case c_2 are not presented, since the flame pattern remains essentially the same, with only small quantitative changes.

Contours of turbulent kinetic energy for case c_1 are displayed in Figure 5.18. Regions of high turbulent kinetic energy are found on the edge of the separation regions as mentioned above, confirming the mesh strategy adopted. In addition, Figure 5.18 now reveals how the wake originating from the tip of the splitter plate creates a region

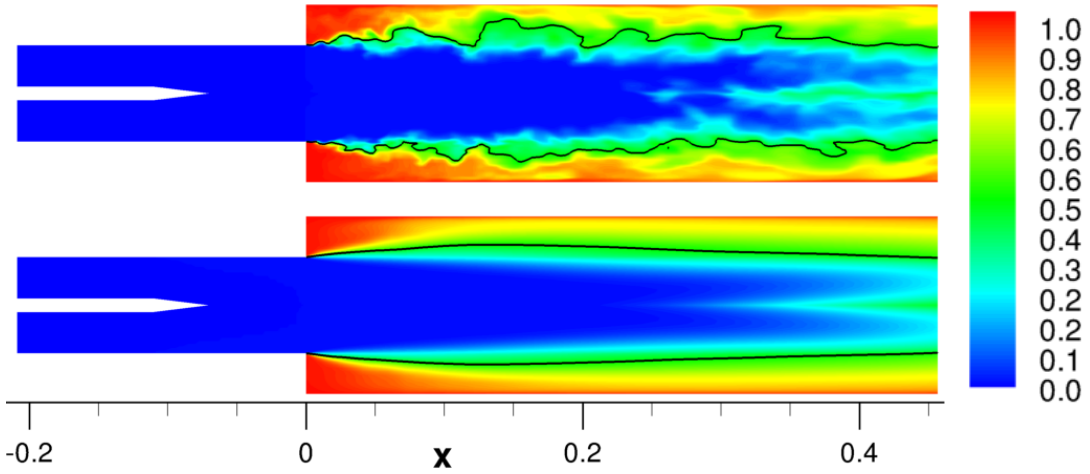

Figure 5.17: Instantaneous (top) and mean (bottom) progress variable contours in plane $z = 0$ for case c_1. Black line indicates c-isosurface ($c = 0.5$)

of considerable turbulence which enhances the reaction rate in the centreline vicinity. The highest levels are however definitely observed in the shear layers developing from the two step corners (recirculation zones are indicated by the $\overline{u}$-isosurface, $\overline{u} = 0$).

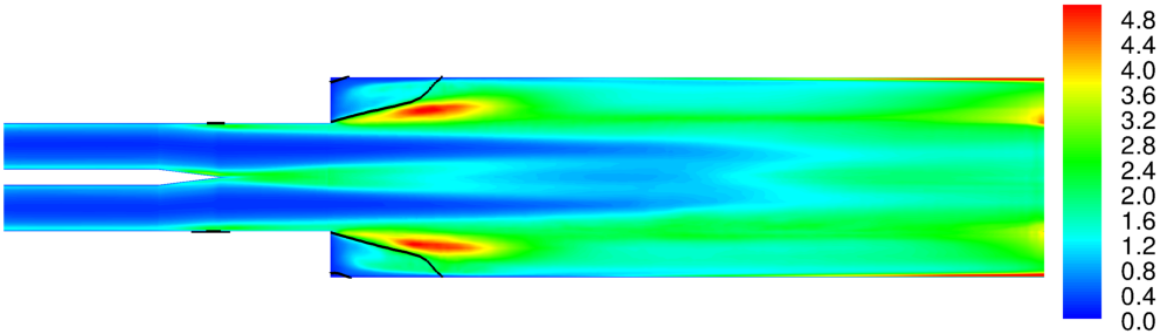

Figure 5.18: Turbulent kinetic energy (TKE) contours in plane $z = 0$. Black line indicates $\overline{u}$-isosurface ($\overline{u} = 0.0$)

As a qualitative illustration, a vortex-identification method, the so-called Q-criterion [191], was utilised to visualise predicted 3D vortex structures and evidence the high turbulence and strongly vortical nature characterising the flow. The variable Q is defined as:

$$Q = \frac{1}{2}\left(|\Omega_{ij}|^2 - |S_{ij}|^2\right) \tag{5.6}$$

where Ω_{ij} and S_{ij} are the vorticity and strain rate tensors, respectively:

$$\Omega_{ij} = \frac{1}{2}\left(\frac{\partial u_i}{\partial x_j} - \frac{\partial u_j}{\partial x_i}\right) \qquad \text{and} \qquad S_{ij} = \frac{1}{2}\left(\frac{\partial u_i}{\partial x_j} + \frac{\partial u_j}{\partial x_i}\right) \tag{5.7}$$

Thus, flow regions with $Q > 0$ will give the excess of rotation rate relative to the strain rate in those areas. To identify a vortex structure, the pressure in the eddy is required to be lower than the ambien pressure. The condition $Q > 0$ does not guarantee the existence of a pressure minimum inside the region identified by it however, the pressure condition is in most cases subsumed by $Q > 0$, therefore in this thesis the Q-critetion is used without the additional pressure condition.

Figure 5.19 shows computed isosurfaces of $Q = 5 \cdot 10^4\ s^{-2}$, coloured by mean axial velocity contours. Small scale vortices are detected, specially in the near-wall regions, and larger hairline vortices in the streamwise direction are also observed, mostly present in the shear layer region.

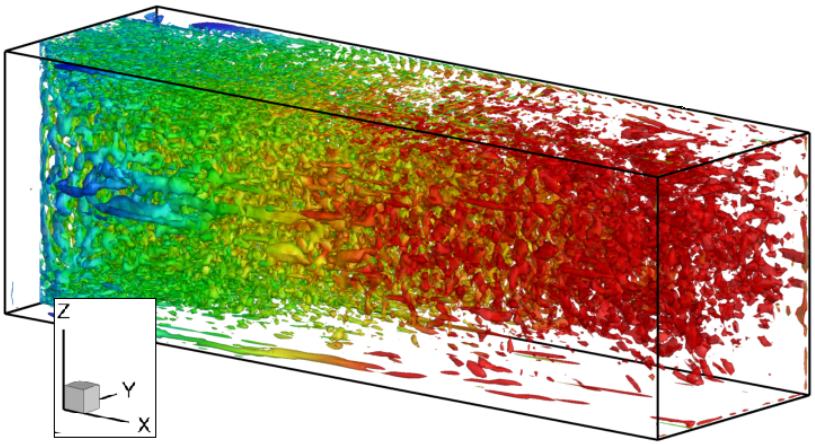

Figure 5.19: Isosurface of $Q = 5 \cdot 10^4\ s^{-2}$ in combustion zone. Case c_1

As previously mentioned, transverse symmetry was recovered for the reacting flow due to flow acceleration. Improved symmetry is also observed in the lateral direction. This is visible in the contour plots in a yz cross-section located $2H_{ch}$ downstream of the dump plane. Thus, Figures 5.20 (a) and (b) show instantaneous and mean streamwise velocity contours; again two central regions of higher velocity are observed, a consequence of the two incoming streams. Lower velocity regions near the walls are observed, particularly in the transverse direction. To further understand the flow structure, mean velocity vectors are displayed in Figure 5.20(c); low-speed fluid attached to the left and right walls moves from the four corners towards the central axis. At the centre of the left and right walls (Figure 5.20(d)) two pairs of vortices are observed. In each corner

(Figure 5.20(e)) fluid attached to the bottom (top) wall travels away from the corner and at some distance from the corner detaches to reverse and travel back to the corner, together with fluid attached to the lateral wall coming down (up) and fluid coming from the central region of the bottom (top) wall. In addition, at the centre of the top and bottom walls, a vortex is observed as fluid is convected into the centre of the combustion chamber along plane $y = 0$, bringing hot burnt products towards cold fresh reactants.

The flow structure in cross-sectional planes is further illustrated in Figure 5.21. Mean streamwise velocity contours are plotted at xy plane $z = -1h$ and yz planes $x = 2.3h$, $6h$, and $10h$. In the first two yz cross-sections, two elliptical high-speed areas are observed in the centre of the combustor. Further downstream an X-shape region of lower velocity is observed.

The aerodynamic structure of the flow plays a dominant role in shaping the flame structure, as seen in Figure 5.22, which provides instantaneous and mean progress variable contours in a yz plane downstream of the dump plane; these show great structural similarity with the velocity contours in Figure 5.20. A thick black line in Figure 5.22 indicates the flame front, represented by a c-isosurface=0.5. The instantaneous flame front is wrinkled by turbulence. The vortex-pair located near the left/right walls, at the centre of the lateral wall (Figure 5.20(d)), causes a stagnation region where hot burnt products accumulate, shrinking the area of non-fully burnt gases. In addition, in the corners, especially near the bottom wall, the effect of vortices (Figure 5.20(e)) on the flame dynamics is again observed. The vortices in the centre of the top/bottom walls create a deformation of the flame in this zone, stretching it and creating a strong impingement of reacting gases in the central core of unburnt reactants.

A comparison of numerical results and experimental visualisations regarding the mean flame shape is displayed in Figure 5.23 for case c_2. The mean flame shape was extracted from experiments using self-luminescence visualisations with a relatively long time exposure of $1/50s$, in the region behind the sudden expansion. In the numerical results, mean progress variable contours are plotted. The numerical data predict a cylindrical tube-like shape core region of unburnt gases, and a narrow flame brush, located between the core region and the upper and lower walls, that extends away from the step corners and gradually spreads in the downstream direction. The experimental visualisation shows a core region with a shorter length, a conical or triangular shape and also a wider flame brush, extending more quickly from the step corners towards the centreline. These discrepancies in the flame shape are believed to be due to the neglect in the current LES of any acoustic fluctuations that are certainly present in the experiments (see turbulence measurements for c_2 below). The inclusion of such a fluctuating velocity contribution would imply more vigorous motion of the instanta-

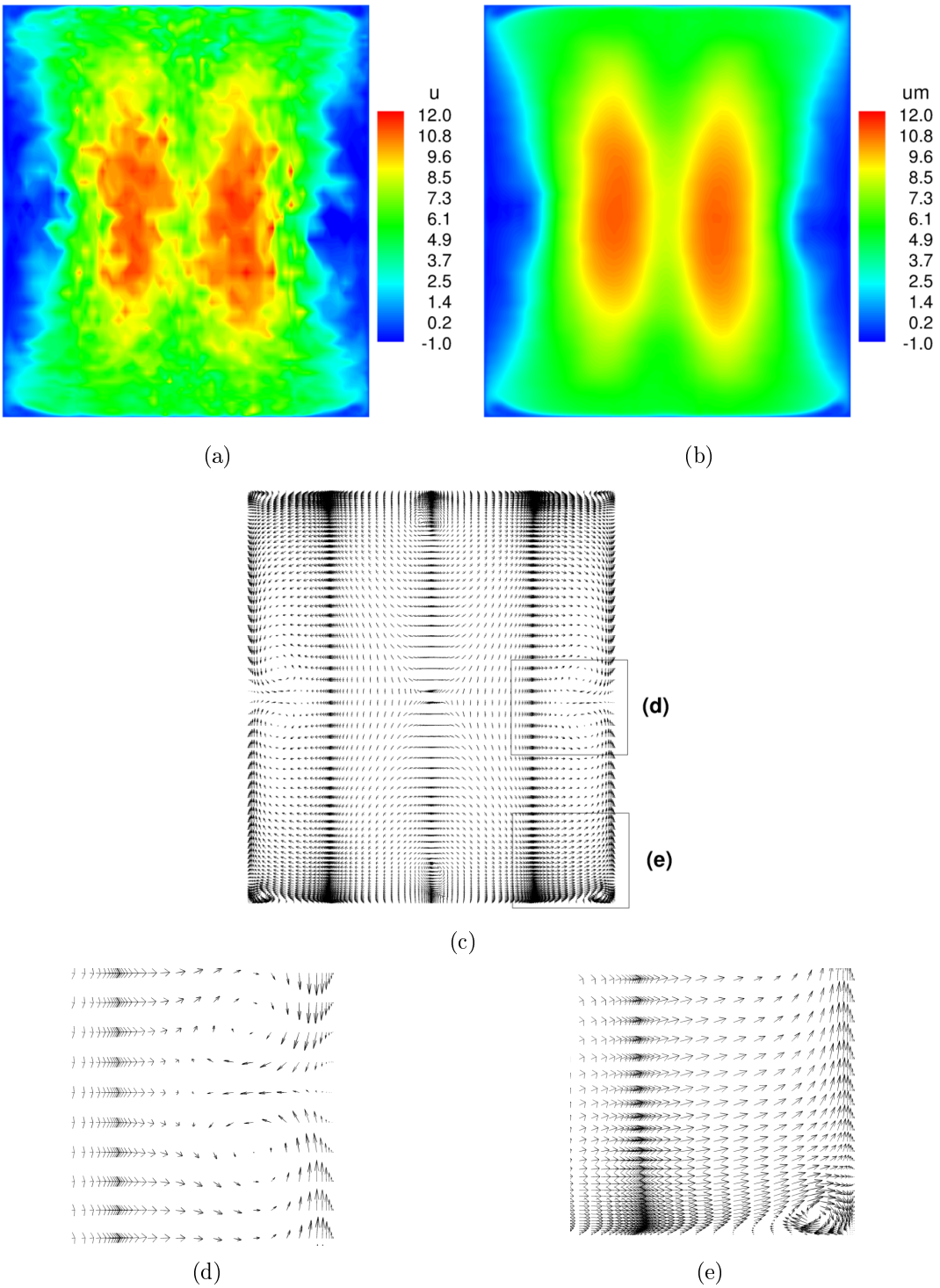

Figure 5.20: (a) Instantaneous and (b) mean streamwise velocity contours; (c), (d) and (e) mean velocity vectors. (d) and (e) show vortex details. yz-plane at $x = 2H_{ch}$ downstream of the expansion plane

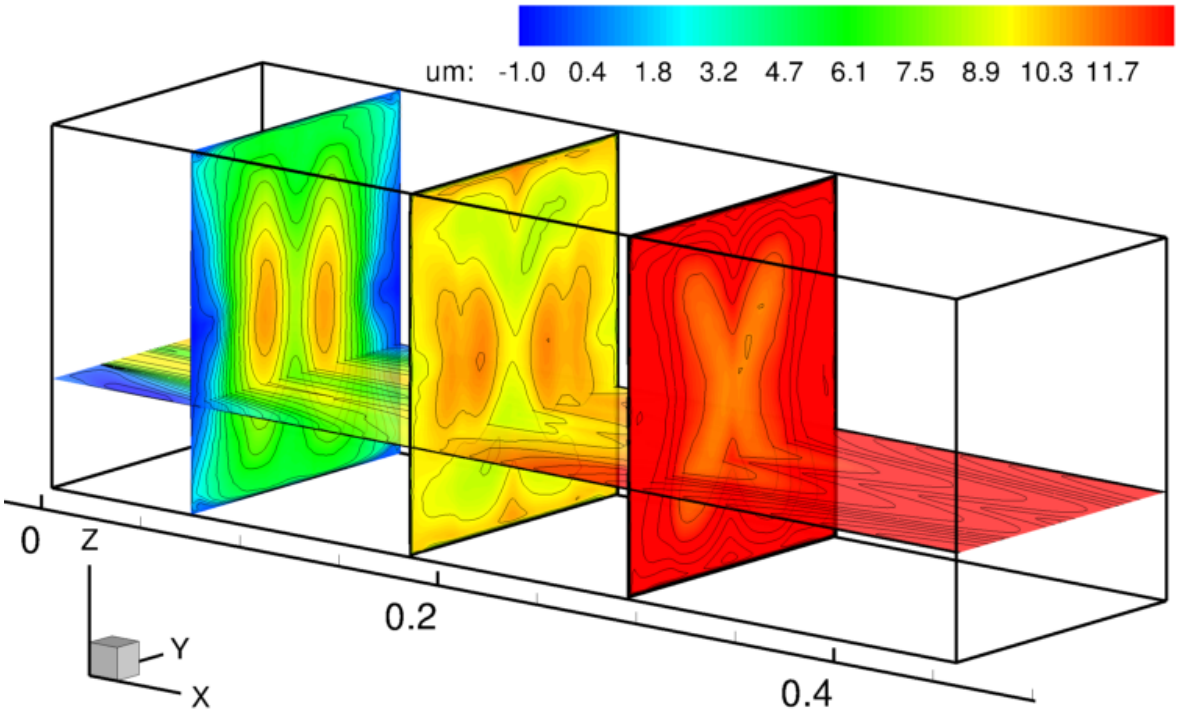

Figure 5.21: Mean streamwise velocity contours at an xy-plane and yz-planes at different axial location. Case c_1

neous flame brush as well as greater distortion by vortices shed from the dump corners, and these would cause a dramatic change in the mean flame shape and in particular its spread. The effects of including this acoustic velocity fluctuation are addressed in chapter 6.

5.4.4.2 Transverse profiles

In this section, transverse profiles of mean and fluctuating streamwise and transverse velocities are presented. Figure 5.24 again indicates the axial locations where experimental data are available. In general, for case c_1 (lower equivalence ratio) very good agreement is obtained for both mean and turbulence variables as shown in Figures 5.25-5.28. The mean flow profiles are characterised by symmetry of the streamwise velocity $\overline{u}$ and antisymmetry of the transverse velocity $\overline{v}$. The central part of the combustor duct does not exhibit the strong flow acceleration which is clearly observed in the near-wall region, indicating the regions where combustion has taken place and density has decreased. This is consistent with what was observed in the progress variable contours (Figures 5.17 and 5.22). A consequence of the strong and symmetric acceleration

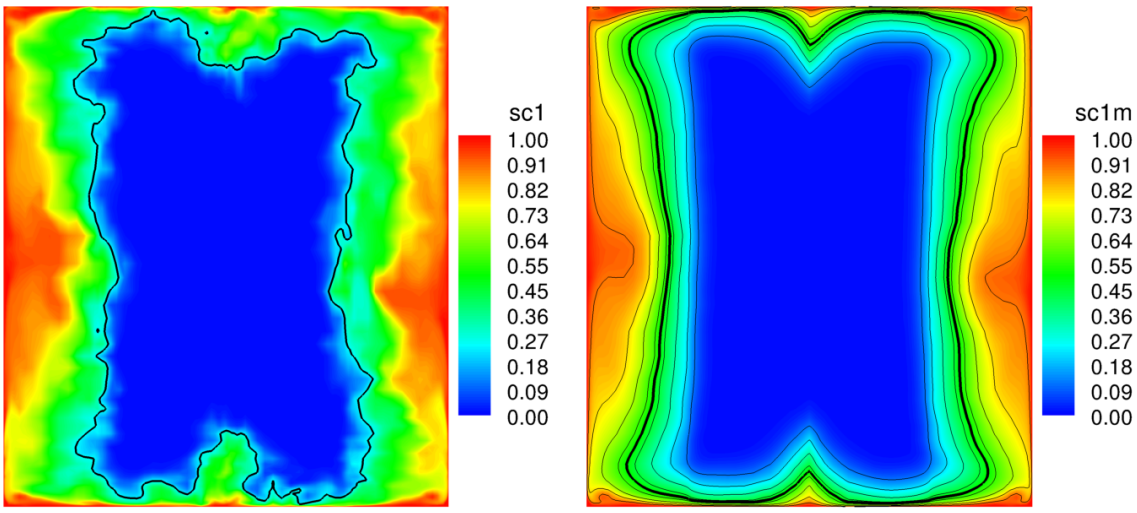

(a) (b)

Figure 5.22: (a) Instantaneous and (b) mean progress variable contours. Thick black line indicates c-isosurface ($c = 0.5$)

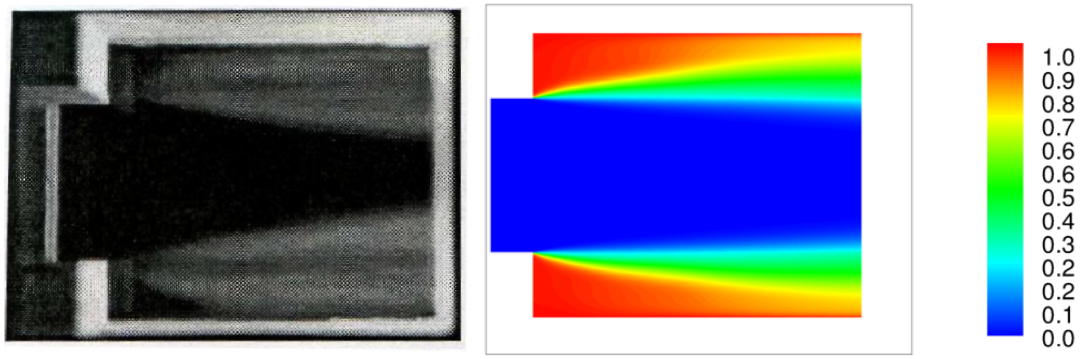

(a) (b)

Figure 5.23: Mean flame shape indicated by (a) visualisations with time exposure $1/50s$ [82] and (b) computed mean progress variable contours. Case c_2

is the shortening of the recirculation zones (with similar length on both upper/lower walls) compared to the inert case. As far as fluctuating velocities are concerned (Figures 5.27 and 5.28), these are not considerably modified in magnitude compared to cold flow, but the shape has changed considerably, with the location of the maximum values pushed towards the walls and the decrease in magnitude of these peaks in the downstream direction occurs more rapidly. In the far-field ($x/h \geq 7$), the reacting case c_1 exhibits much higher levels of u' and v', whilst the inert case presents higher fluctuating levels in the near-field ($x/h \leq 3$), in the development regions of the upper and lower shear layers. In addition, the double peak on the combustor centreline, associated with the wake developing from the splitter/trailing edge is still observed for c_1.

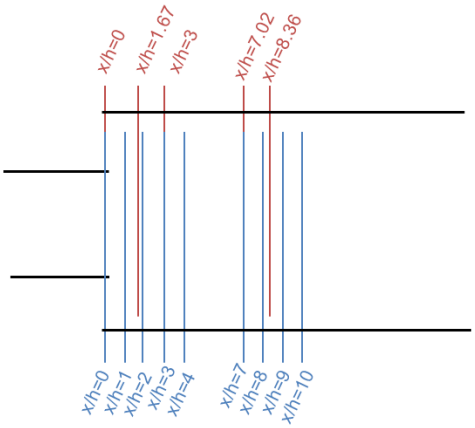

Figure 5.24: Axial positions where transverse profiles are extracted, for cases c_1 (red, top) and c_2 (blue,bottom)

Figure 5.25 shows excellent agreement with LDA measurements, at all axial positions for the mean streamwise velocity. LES results from Fureby [134] are also plotted, with similar results to those from the simulations presented in this work. Note that in Fureby [134], axial positions where transverse profiles were reported corresponded to axial positions where experimental data [81] for the inert case only were available. It is the author's belief that this was an error and thus LES results from Fureby [134] were extracted at the same axial positions as presented in this thesis, which correspond to available experimental data [81] for the reacting case only. The shape and magnitude of the mean transverse velocity (Figure 5.26) are very well predicted, especially in the central region of the combustor, although the magnitude of the upper and lower peak values is slightly overpredicted initially but slightly underpredicted further downstream. Note that the shape and magnitude of the transverse velocity is very similar to that obtained in the inert case.

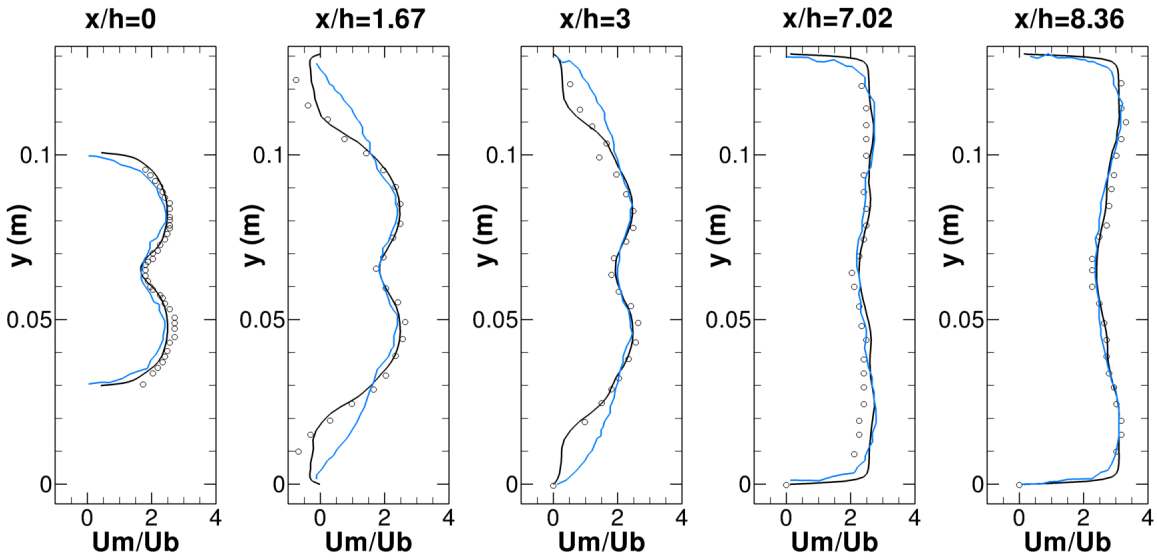

Figure 5.25: Normalised mean streamwise velocity for case c_1 at different axial positions. U_{bulk} = $4.4m/s$. Experimental data (o) from Besson et al. [81]. Blue line from Fureby [134]

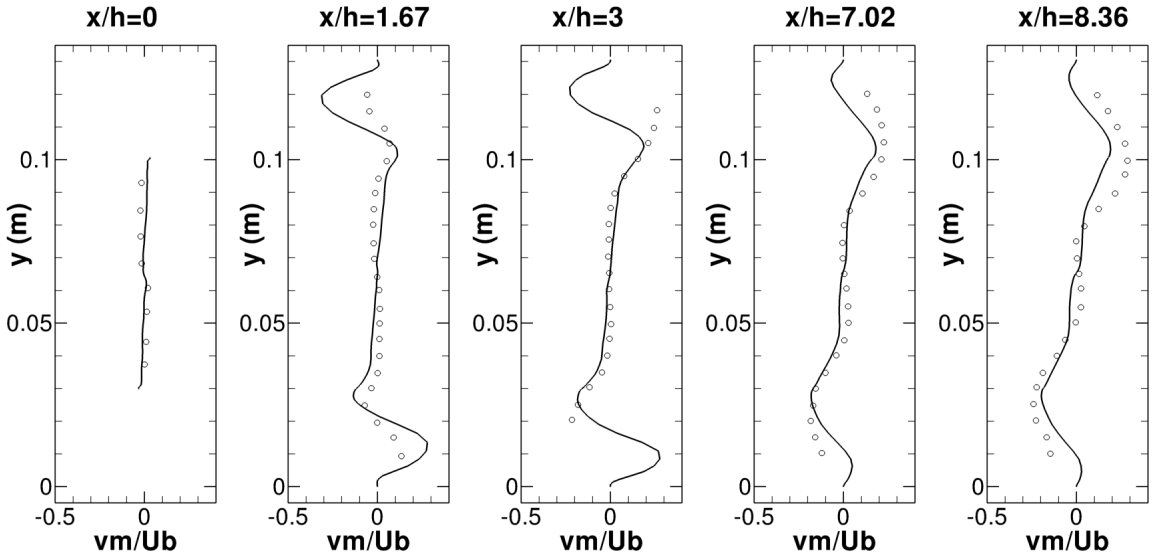

Figure 5.26: Normalised mean transverse velocity for case c_1 at different axial positions. U_{bulk} = $4.4m/s$. Experimental data (o) from Besson et al. [81]

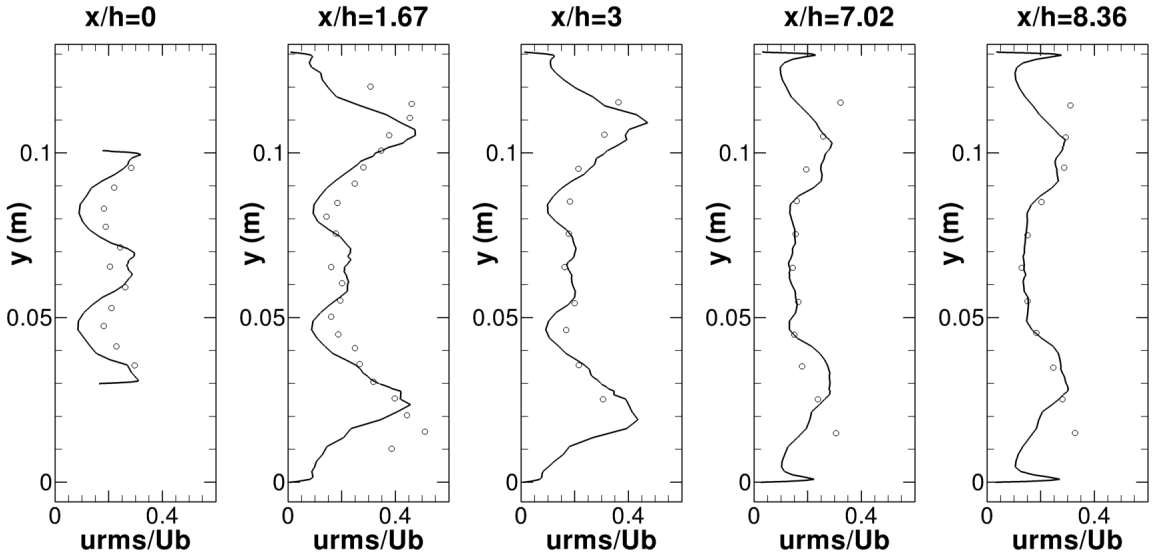

Figure 5.27: Normalised fluctuating streamwise velocity for case c_1 at different axial positions. $U_{bulk} = 4.4m/s$. Experimental data (o) from Besson et al. [81]

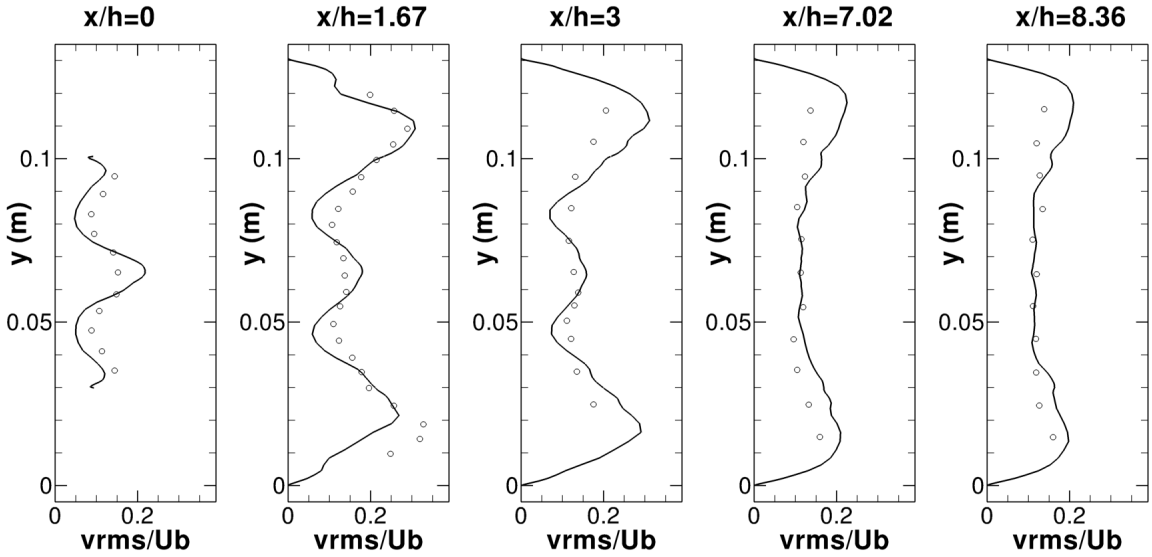

Figure 5.28: Normalised fluctuating transverse velocity for case c_1 at different axial positions. $U_{bulk} = 4.4m/s$. Experimental data (o) from Besson et al. [81]

Regarding reacting case c_2, it is interesting right away to note that very good agreement is again obtained for mean velocities, but not so for the turbulence quantities compared to the c_1 results. Streamwise velocity profiles, shown in Figure 5.29, especially for axial distance $x/h \leq 7$ show virtually the same behaviour as Figure 5.25 for case c_1. For positions $x/h \geq 8$ underprediction is obtained, and this is very likely due to a too slow reaction rate predicted by the current combustion model, at least with $\beta = 0.2$. The streamwise velocity underprediction was also reported in [117, 118, 134] for some of the combustion models tested. This discrepancy certainly cannot be explained by measurement uncertainties.

Similarly, Figure 5.30 shows mean transverse velocity profiles for case c_2, again with reasonable agreement with experimental data as observed for the c_1 simulation. Once more, the main feature is the antisymmetry of the profiles, showing similar results, in shape and magnitude, to the profiles obtained for the inert case. For positions $x/h < 2$ the agreement is excellent, accurately reproducing magnitude and shape of the measured data. For positions $x/h = 2$, 3 and 4, the magnitude of peaks located at positions $y^* = 0.3$ and $y^* = 4$ is overpredicted, although shape and magnitude in the centreline region is very well reproduced. For locations $x/h \geq 7$, the antisymmetry in the transverse direction is perfectly captured, although peaks at position $y^* \approx 0.9$ are found to be slightly shifted towards the lower wall.

The largest discrepancy between experimental data and LES results for case c_2 is found in the fluctuating streamwise velocity profile predictions (Figure 5.31). The magnitude is significantly underpredicted, both in the initial region near position $x/h = 0$ and in the far-field near position $x/h = 10$. This is now clear evidence of the effect of a thermo-acoustic oscillation, which was noted by the experimentalists to be absent at $\phi = 0.65$ (c_1) but present and strong at $\phi = 0.75$ (c_2). The presence of a plane wave fluctuation, which would be measured by the LDA as "turbulence", would have the effect of flattening the radial profile shapes seen in case c_1 and this is indeed so (compare Figure 5.27 (c_1) with Figure 5.31 (c_2)). Neglecting the acoustic motion observed in the experiments, would considerably decrease the fluctuating energy level. Experiments [82] in fact (see measured spectra presented below) revealed that the contribution of the periodic coherent motion to the total streamwise velocity fluctuation accounted for approximately 80% of the fluctuating energy. Note that no pulsating mode was observed in the experiments for case c_1, supporting the fact that different thermal and acoustic behaviour characterises the flames for the two reacting cases. As a result of the plane wave effect, the double peak behind the expansion plane is no longer observed in the measured data, but still remains in the numerical results.

Further support for this argument is provided on examination of the fluctuating transverse velocity profiles for case c_2 (Figure 5.32). The quantitative agreement between

LES and measurements for the transverse fluctuations is effectively the same for both flows c_1 and c_2 (compare Figure 5.28 (c_1) with Figure 5.32 (c_2)). This is again what would be expected if the unsteady acoustic wave is planar and axially propagating, since this would affect the axial LDA measurements but leave the transverse turbulence measurements almost unchanged.

5.4.4.3 Power Spectral Density of axial velocity fluctuations

As mentioned in the previous section, a distinctive peak of energy at a frequency of approximately 50Hz was exhibited in the measured axial spectra in the experimental data for case c_2, confirming the presence of a strong pulsating acoustic mode. This was totally absent in the spectra for inert flow and also absent or very weak in combusting case c_1. Such a thermo-acoustic instability is commonly found in dump combustors, as reported by Schadow and Gutmark [85] due to combustion developing in unstable shear layers from the step corners and if strong enough can lead to vortex shedding. In the numerical results presented in this chapter, no acoustic effects have been included and thus no peaks in the spectra can be predicted. Experimental and numerical spectra of fluctuating streamwise velocity at a point located in the approach ducts, on the centreline and $5h$ upstream of the expansion plane are plotted in Figure 5.33. A quasi-flat low-frequency region (up to 100Hz) is found in both simulations and experiment, followed by a $-5/3$ law decay, characteristic of an equilibrium turbulence energy cascade. After a decade or so of energy decrease, in the LES the $-5/3$ decay is replaced by a much faster decrease at higher frequency. In the measured data a very strong peak at 50Hz is observed (also perhaps the next harmonic) and of course the $-5/3$ decay continues to the highest frequency resolvable by the LDA.

In the same location where the spectra shown in Figure 5.33 were extracted, probability density functions (PDF) of the streamwise velocity component were computed, together with skewness and flatness factors, and are compared with experimental PDFs in Figure 5.34. The shape of the PDF for the reacting LES results is very similar to that obtained for the corresponding inert flow. However, a total departure of the Gaussian-like shape of the PDF in the experimental data is clearly exhibited in Figure 5.34(b), where the velocity range is much wider and displays a bimodal character, associated with the presence of a strong pulsating axial wave motion.

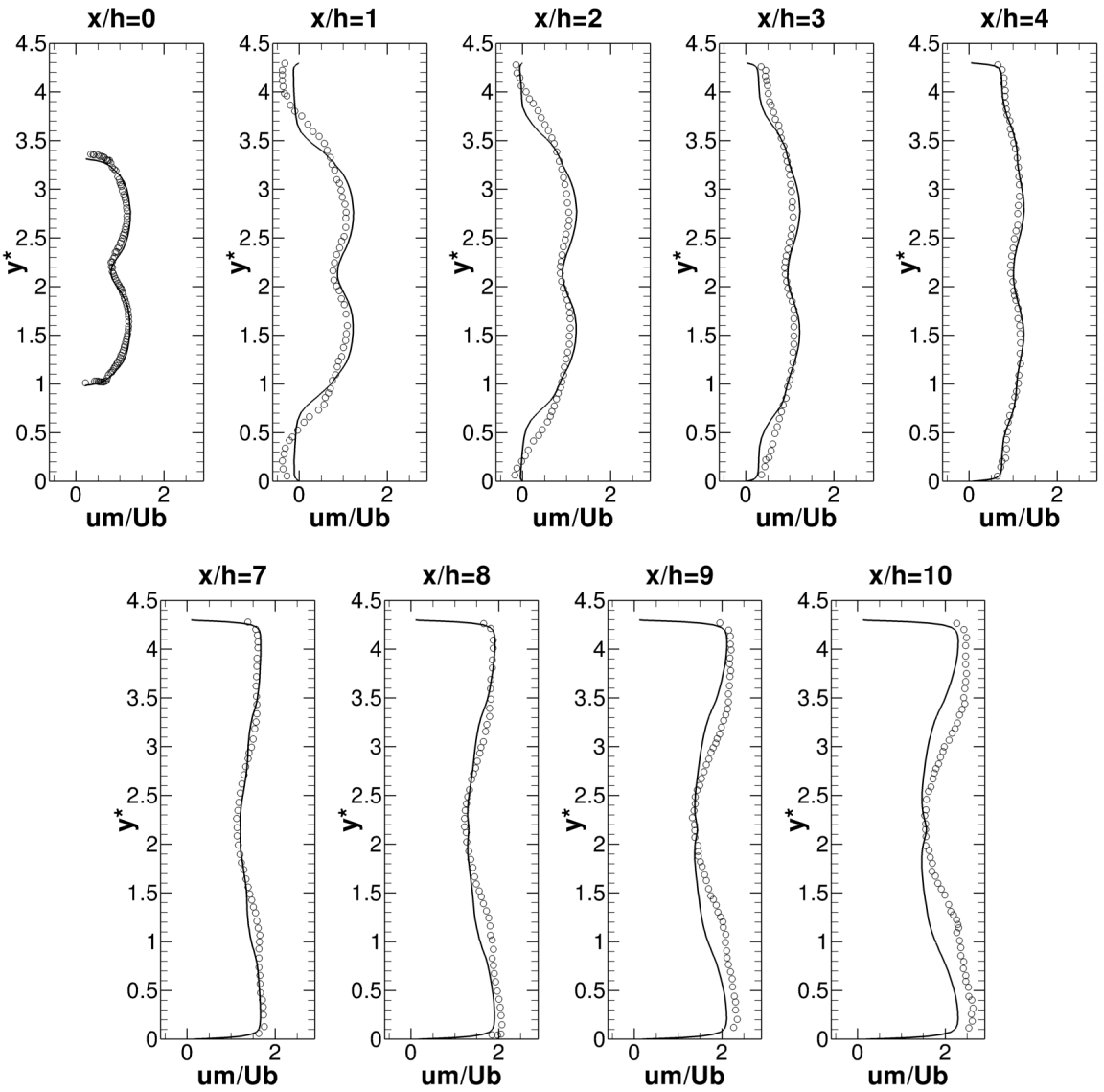

Figure 5.29: Normalised mean streamwise velocity for case c_2 at different axial positions. U_{bulk} = $11m/s$. Experimental data (o) from Nguyen et al. [82]

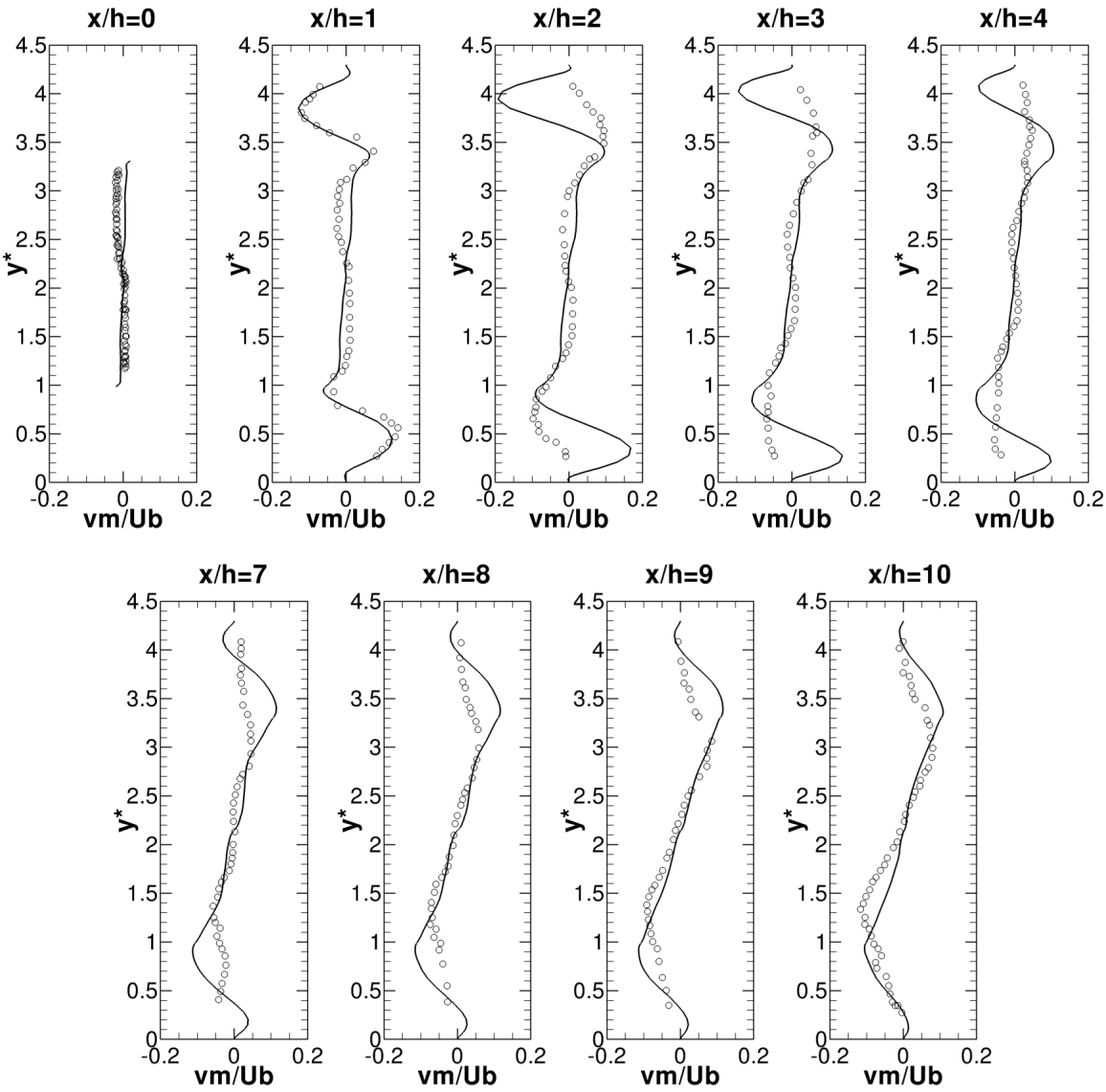

Figure 5.30: Normalised mean transverse velocity for case c_2 at different axial positions. U_{bulk} = $11m/s$. Experimental data (o) from Nguyen et al. [82]

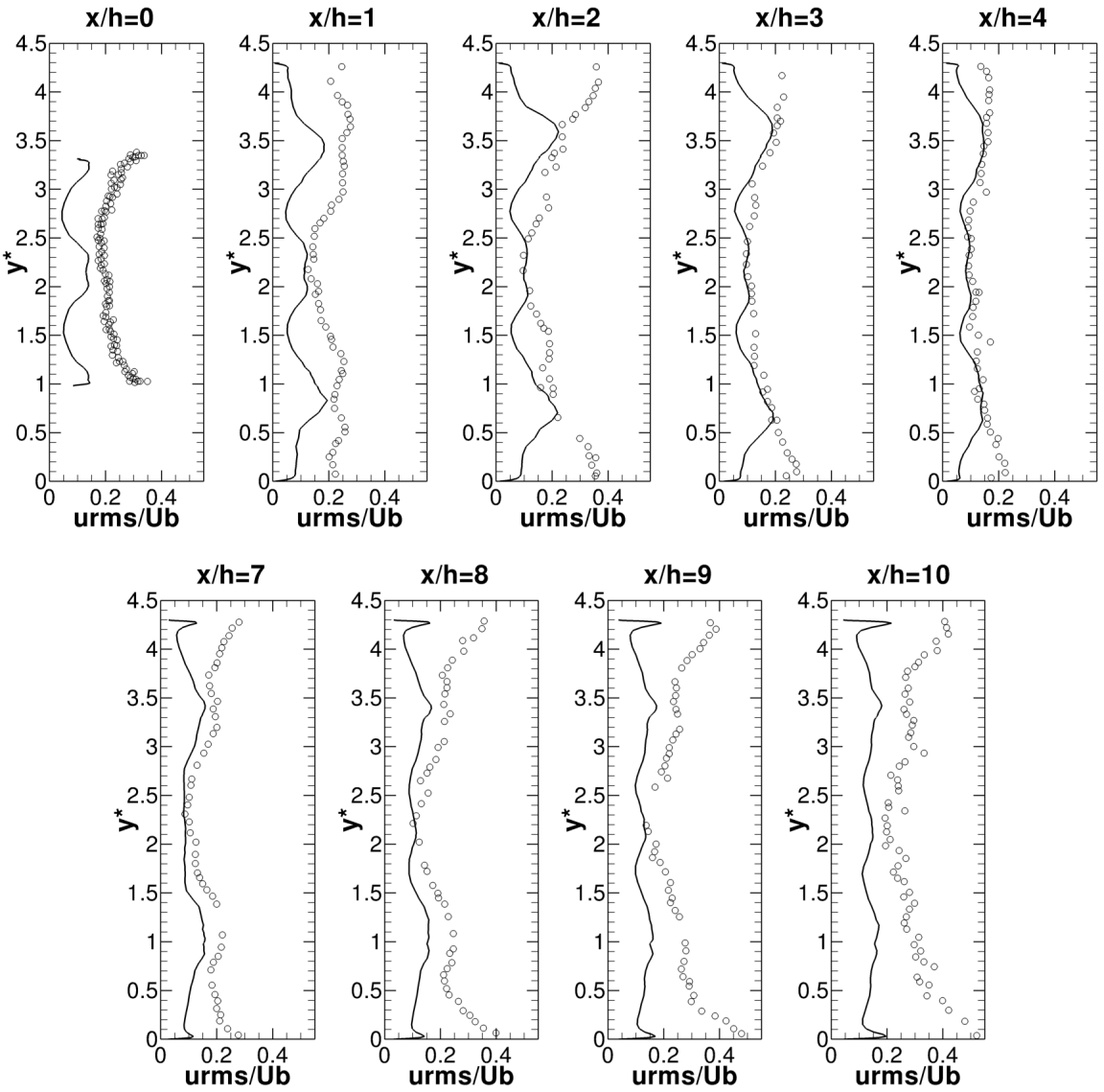

Figure 5.31: Normalised fluctuating streamwise velocity for case c_2 at different axial positions. $U_{bulk} = 11m/s$. Experimental data (o) from Nguyen et al. [82]

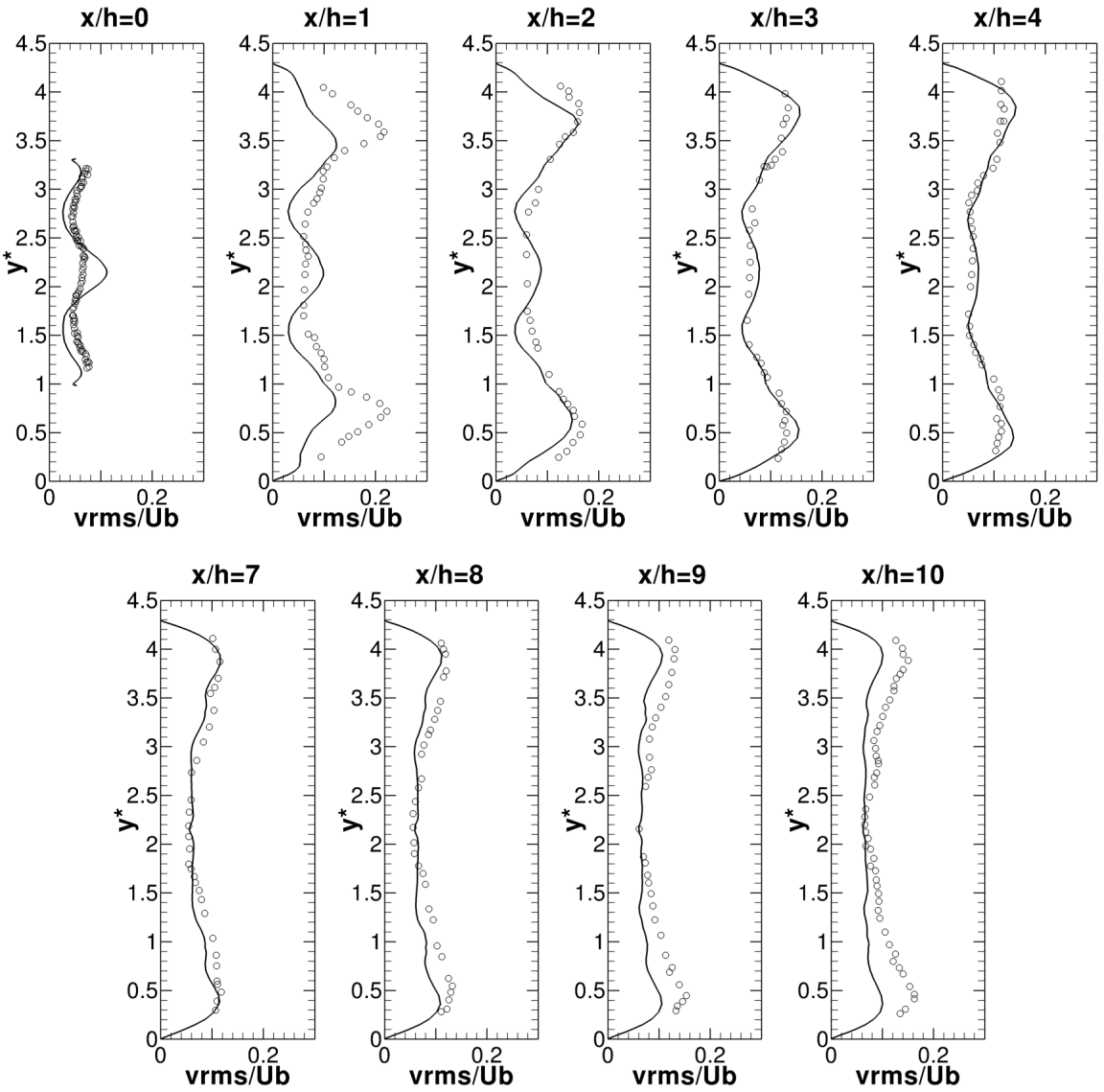

Figure 5.32: Normalised fluctuating transverse velocity for case c_2 at different axial positions. $U_{bulk} = 11m/s$. Experimental data (o) from Nguyen et al. [82]

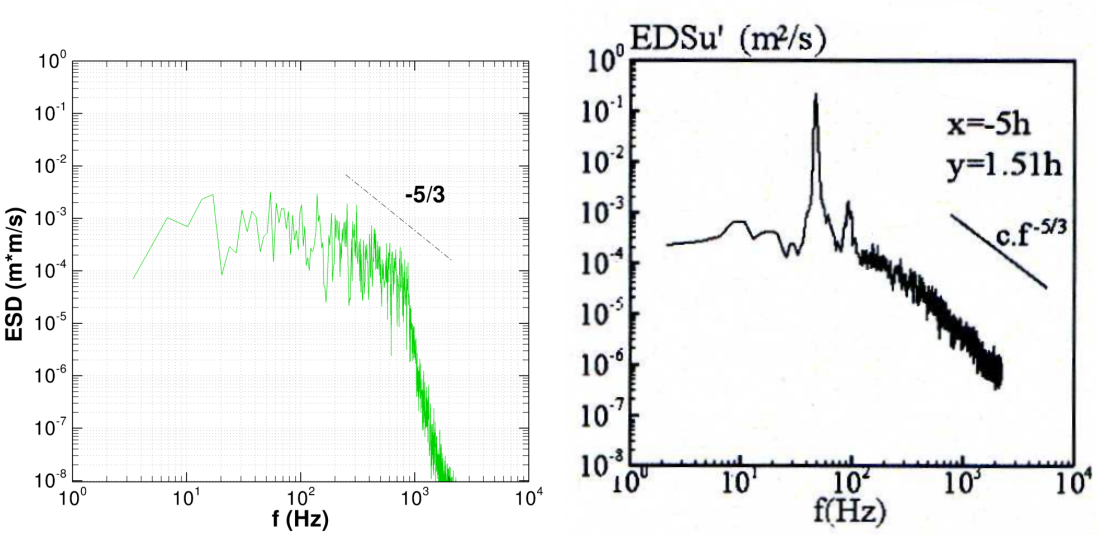

(a) (b)

Figure 5.33: Energy density spectra of streamwise velocity fluctuations at $x = -5h$ and centred in the transverse and spanwise directions from (a) LES simulations and (b) experimental data [82]. Case c_2

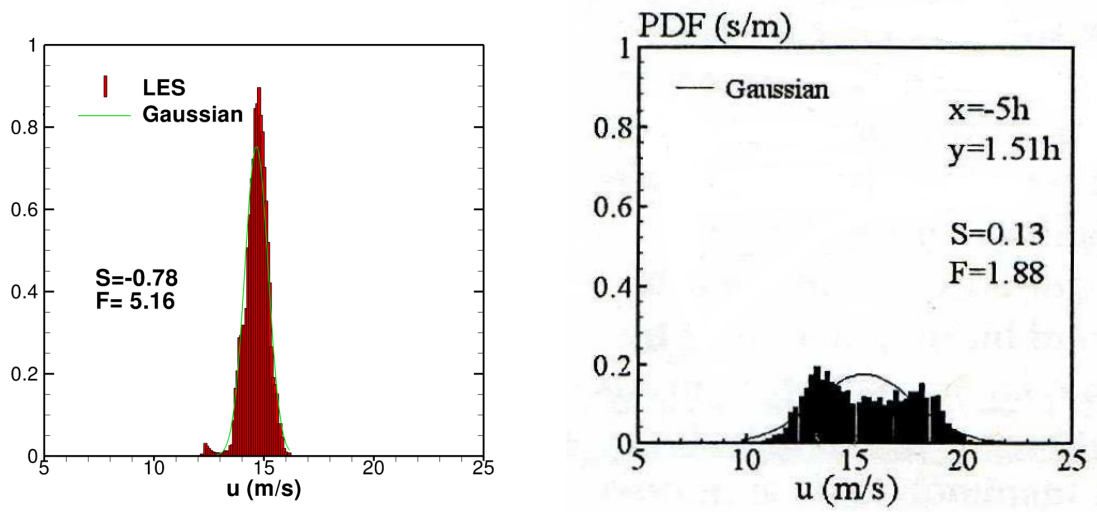

(a) (b)

Figure 5.34: Energy density spectra of streamwise velocity fluctuations at $x = -5h$ and centred in the transverse direction from (a) LES simulations and (b) experimental data [82]. Case c_2

5.4.4.4 Conclusions

The validation of the implementation of the premixed combustion model described in chapter 2 into the LULES code has been carried out by comparing the ORACLES measurements for two equivalence ratios $\phi = 0.65$ (c_1) and $\phi = 0.75$ (c_2) with LES results. In general very satisfactory results were achieved. The agreement between experimental data and LES results was in general good for both mean and fluctuating turbulent data. This was also mainly true for case c_2 although a significant discrepancy was found in the fluctuating velocity particularly for the axial component. However, this discrepancy was attributed to the neglect of a periodic coherent (acoustic) unsteady velocity contribution, caused by a strong pulsating plane acoustic wave observed in the experiments as indicated by a peak in the spectrum for u' which was totally absent in the current LES. The next chapter describes how the effects of acoustic waves can be included in an incompressible LES with inlet forcing, and reacting case c_2 is ideal to assess and validate this methodology. In addition to this, in both cases c_1 and c_2 the measured axial velocity further downstream was underpredicted by the LES. This was evidence of a too slow reaction rate provided by the FSD combustion model, at least for the parameter value $\beta = 0.2$ as used in this chapter. The next chapter also includes an assessment on the LES predictions of altering the value of β in the FSD model.

Chapter 6

Incompressible combusting LES and acoustic network model - two way coupling

6.1 Introduction

The main objective of this chapter is to outline the methodology for two-way coupling of acoustic wave analysis and incompressible LES simulations of reacting flows. The first coupling mode described is the extraction of information from an acoustic network analysis to derive an acoustically sensitised inlet boundary condition, aimed at mimicking the primary inlet flow unsteadiness caused by acoustic waves (which would be reproduced automatically with a compressible code) and are observed in the experiment. To determine the unsteady "acoustic forcing" that must be prescribed in an incompressible LES, a network model of the test rig geometry is established and the modeshape at the specified frequency observed in the experiment predicted.

The second coupling mode to be investigated describes how information can be extracted from an incompressible combusting LES which includes an inlet forced pulsation mode at a range of amplitudes to study the way in which this modulates and alters the flame dynamics and will be the major driving influence on flame response. In other words this second coupling mode explains how Flame Transfer Functions are deduced from the LES, and in particular perturbation amplitude dependent FTFs, sometimes also referred to as a Flame Describing Function (FDF). The identification of a burner response to acoustic or acoustically induced perturbations, can be seen as an essential ingredient of predictive methods for combustion thermo-acoustic instability [192–196].

In this chapter, results concerning the reacting flow c_2 (see Table 5.1 in chapter 5) including acoustic wave effects are presented. This case has been selected since the results presented earlier indicate clearly the strong presence of a self-sustained thermo-acoustic limit cycle at this equivalence ratio. Comparison is also made with results

for the same case when no acoustic effects were included, taken from chapter 5. A thorough analysis of the flame response to varying amplitudes of inflow perturbations is carried out next and predicted FTFs obtained. Finally, these LES-extracted FTFs are incorporated into an acoustic network model to examine the possibility of prediction of self-sustained limit cycle behaviour. As previously mentioned in chapter 5, to ensure convergence of the mean values presented in the next sections, all simulations have been run to a minimum of 15 flow through times.

6.2 Acoustically sensitised incompressible LES inlet boundary conditions

As already described in §5.3, a data-mined precursor method with time looped read-in has been successfully used to generate unsteady velocity LES inlet boundary conditions with realistic turbulent characteristics. Velocity profiles generated agreed very well with measured data for inert flow. Some reacting experiments however, particularly case c_2, exhibited evidence of a strong plane acoustic wave component (at 50Hz) that was neglected in the results presented in the previous chapter. This periodic component will now be included by means of adding an acoustically sensitised inlet boundary perturbation. In the experiments this coherent periodic motion was observed only in the streamwise direction, since a peak was present in the spectrum for the streamwise velocity component, whereas no peak was visible for the transverse velocity [197]; it has here therefore been added only to the axial velocity (u).

The nature of the incoming flow revealed in the ORACLES case c_2 experiments suggests a triple-decomposition of the instantaneous incoming streamwise velocity (only u needs to be considered as an acoustic plane wave is assumed), as proposed in [82] :

$$u(x_{in}, y, z, t) = \bar{u}_{x_{in}}(y, z) + u'_p(x_{in}, t) + u'_s(x_{in}, y, z, t) \tag{6.1}$$

where x_{in} indicates the location of the LES domain inlet plane, $\bar{u}$ stands for the long time-averaged contribution, u'_p is a periodic coherent (acoustic) contribution, and u'_s represents stochastic turbulent fluctuations. The periodic fluctuation at any location x in the whole geometry may be assumed to be of the form:

$$u'_p(x, t) = U_{bulk} A(x) sin(2\pi f t) \tag{6.2}$$

where U_{bulk} is the mean bulk velocity, A(x) determines the acoustic velocity perturbation amplitude, which will depend on axial location within the experimental geometry, since an acoustic mode shape will be present, and f is frequency.

As confirmed by experimental data [82] , the stochastic contribution upstream of the dump plane ($x = -0.1495m$) was not modified by the presence of combustion (even in case c_2), only by acoustics; the increase in the level of the fluctuating streamwise velocity observed was purely due to the appearance of a strongly energetic plane wave motion. Thus, the method adopted in section §5.3 to specify the mean and stochastic turbulent fluctuations, $\overline{u}$ and u'_s, at the LES domain inlet may be retained and only the periodic contribution u'_p at the LES domain inlet plane needs to be determined. For low acoustic frequencies (50Hz), whose wavelengths are long in comparison with the duct diameter, only plane acoustic waves carry energy [198] . The acoustic component u'_p in an incompressible simulation has to be input as a superimposed numerical forcing at the LES domain inlet. The experiments indicate that the acoustic frequency was f=50Hz, and the measured rms of the periodic fluctuation at an axial location in the inlet duct at $x_M = -0.1495m$ upstream of the dump plane (see [82]) was:

$$\sqrt{\overline{u'^2_{p,x_M}}}/U_{bulk} = 0.18 \tag{6.3}$$

In contrast to previous authors' attempts to include inlet forcing [117, 118], in the present work the resonant acoustic modes of the whole experimental geometry have been determined from the LOTAN code described in chapter 4. LOTAN was set up for the experimental geometry shown in Figure 5.1(a) (NB. There are some uncertainties, e.g. geometric and dimensional details not available in the published material on the experiments, particularly in connection with the correct description of inlet and exit acoustic impedances which will be further addressed below). Figure 6.1 presents a schematic corresponding to the simplest possible interpretation. Boundary conditions were set assuming an acoustically closed boundary ($u'_p = 0$) at the left hand end (the porous plate location) and an acoustically open end ($p'_p = 0$) at the right hand end where the combustor chamber terminates (before entering a water cooled diffuser) (probably) open to atmosphere. Finally a STEADY calculation was performed as defined in chapter 4. This predicted a resonant mode at a frequency 50.35Hz which is closely related to the half wave mode of the approach ducts (55.5Hz). Secondly, to estimate the modal characteristics of the 50Hz plane acoustic wave in the ORACLES geometry, a FORCED calculation at 50Hz was performed, locating the source of forcing at the dump plane. The predicted mode shape is displayed in Figure 6.2.

It is worth mentioning that a frequency of 50Hz gives a Strouhal number $S_t = fh/U_{dp} \approx 0.19$, based on the step height $h = 0.0299m$ and the mean streamwise velocity at the dump plane $U_{dp} \approx 8m/s$; this is close to the value of 0.2 typical of vortex shedding frequencies observed behind obstacles. It is therefore likely that the thermo-acoustic frequency is such that it locks onto at a natural frequency mode driven by a vortex shedding process [117].

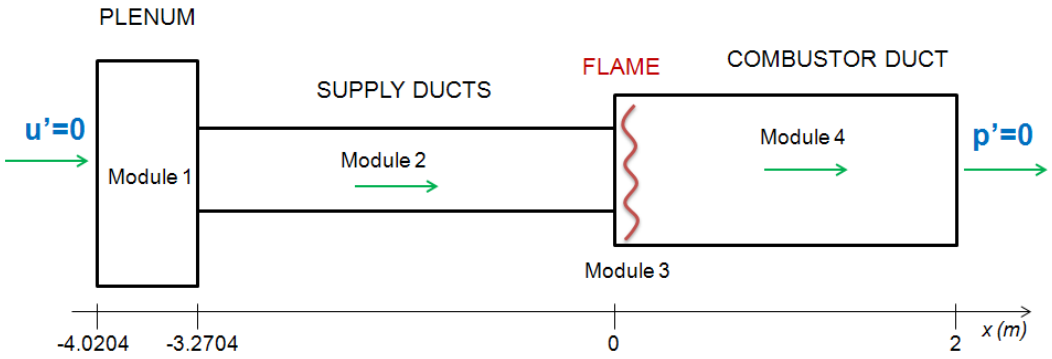

Figure 6.1: 2D sketch of the LOTAN configuration

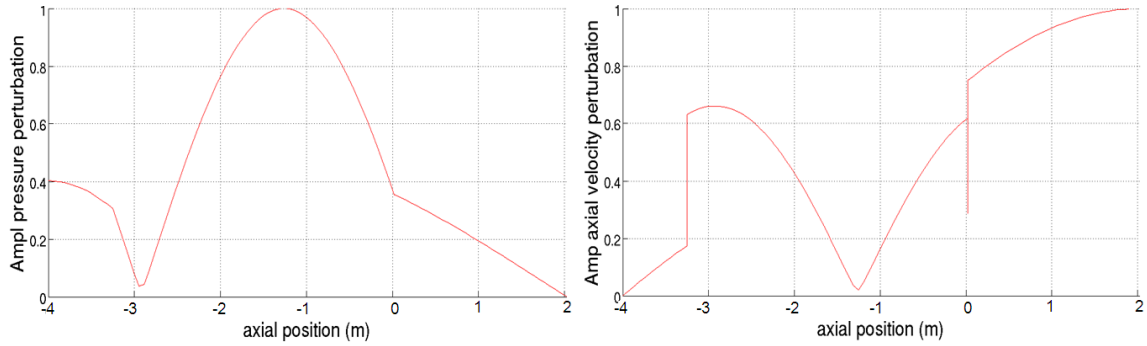

Figure 6.2: Non-dimensional pressure (left) and acoustic velocity (right) of 50Hz mode obtained from LOTAN

If linearity of the acoustic field is assumed, the dimensional amplitude of the acoustic velocity $U_{bulk} \cdot \mathrm{A}(x)$, at the self-sustained conditions determined by the flame response in the experiments, can be evaluated at any location x once the dimensional amplitude at one location is fixed for the dimensionless mode shape shown in Figure 6.2. Thus, at the measurement location x_M, $\mathrm{A}(x_M)$ is "calibrated" using equation (6.2) and the measured rms in equation (6.3) giving a value of $\mathrm{A}(x_M) = 0.26$. Then, values of acoustic velocities at other points in x can be scaled linearly according to the dimensional value $\mathrm{A}(x_M) = 0.26$ and the modeshape in Figure 6.2 (b). Note also that according to the modeshape (Figure 6.2 (b)), the amplitude at the dump plane $x_{dpl} = 0$ will be slightly higher ($\approx 5\%$) than at the measurement plane $x_M = -0.1495m$. In incompressible LES predictions, however, the periodic forcing component amplitude will stay sensibly constant between the LES domain inlet (at $x \approx -0.15m$) and the dump plane. It is arguable that the most important acoustic perturbation characteristic to be included is the fluctuating velocity at x_{dpl}, where vortex shedding is initiated. Therefore, the

dimensional amplitude of the forcing velocity at the LES inlet plane has been selected to create the perturbation amplitude evaluated from the modeshape at x_{dpl}. The value identified for A(x_{dpl}) following this argument is 0.29, and this is the value which has been used initially to dimensionalise the periodic forcing component u'_p at the LES domain inlet. Note also, however, that, as stated above, the acoustic network analysis has had to be set up making some assumptions about the experimental geometry and assuming idealised boundary conditions; therefore the above analysis cannot be taken as perfectly accurate.

The value of A=0.29 resulted in very good agreement with experimental rms data at x_M. Given the uncertainties and simplifications in the LOTAN calculation a small deviation from the value 0.29 was explored, and A=0.31 gave the best fit (Fig 6.3(b)). The mean streamwise velocity from forced LES predictions in the approach ducts is shown in Figure 6.3(a), and as expected did not differ from the unforced prediction (A=0), exhibiting very good agreement with experimental data. Figure 6.3(b) shows that in comparison with the A=0 unforced result, using A=0.31 gives excellent agreement with the measured fluctuating axial rms value. The approach followed in the present work offers an alternative route for determining acoustically sensitised incompressible LES inlet conditions compared to the trial and error approach of [116–118].

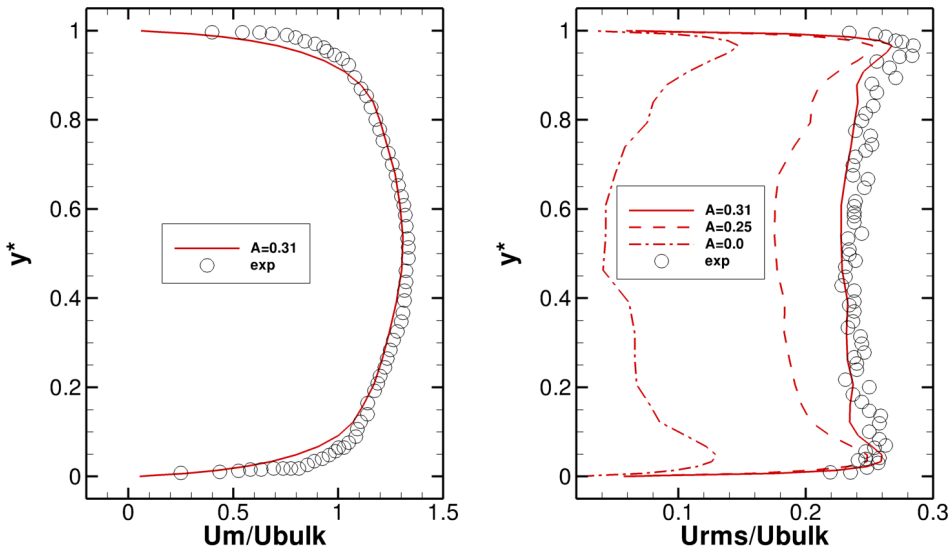

(a) (b)

Figure 6.3: (a) Mean and (b) fluctuating streamwise velocity in inlet duct ($x = -0.1495m$, $z = 0$) for reacting case c_2 and forcing amplitude A=0.31 with experimental data (symbols). (b) fluctuations for simulations with no periodic forcing and various forcing.

Further support for this approach comes from examination of LES predicted spectra for axial velocity from this forced simulation at two different points located on the centreline of the approach duct and in the flame front region. These show well-defined peaks at 50Hz, as displayed in Figure 6.4 (red line). Spectra for the axial velocity at the same points for the unforced calculation are also displayed (green line). It is apparent that even in the approach duct there is some interaction between the acoustic forcing and the turbulence since the level of fluctuating energy in the approach duct (Figure 6.4(a)) is higher when forcing is applied, consistent with Figure 6.3(b). Note also that in contrast to this the spectrum for the forced case at the point located in the flame (Figure 6.4(b), red line) reveals rather little increase in overall energy level, although harmonics of the 50Hz mode appear in spite of forcing being applied at a single frequency. These observations are typical of unsteady flow in dump combustors, as reported in [199], who attributed these changes to the mechanism of combustion developing in unstable shear layers, such as the ones created at the two step corners in the ORACLES experiment.

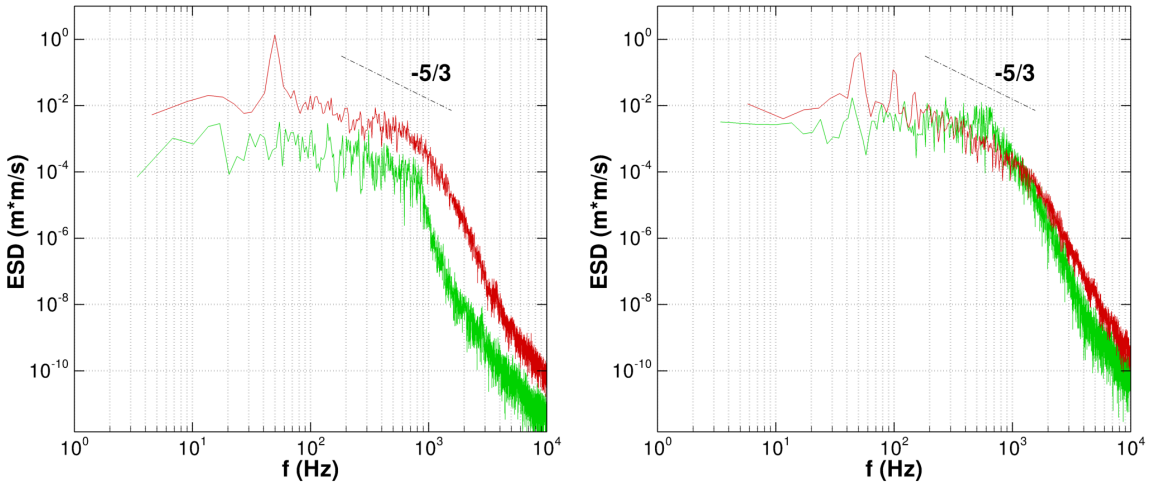

Figure 6.4: Spectra of fluctuating streamwise velocity at (a) point in inlet duct ($x = -0.1495m$, $y = 0.0202m$) and (b) point in flame front region for unforced (green line) and forced (red line) calculations. Both points located in plane $z = 0$.

The probability density functions (PDFs) of the streamwise velocity component have been computed at a point on the centreline of the upper approach duct, ($x = -0.1495m$ and $z = 0$). PDFs from unforced and forced calculations and also from measured data are plotted in Figure 6.5. The agreement with measured data (Figure 6.5(c)) is very good for the forced case (Figure 6.5(b)), and the skewness and flatness factors (see

equation 5.5 for definition) accurately fit the experimental values. Although the two spikes are shifted slightly to the left, peaking at values of 12 m/s and 18 m/s whereas the experimental values are 13 m/s and 19 m/s, the measured shape is well represented. Reference to the measured PDFs for reacting case c_1 in the previous chapter shows that any evidence of an acoustic mode was much weaker compared to case c_2, with no evidence of any bimodal PDF.

6.3 Results of forced reacting flow simulation

6.3.1 Contour plots

In this section, xy plots of different variables are shown. The symmetry of the mean flow, due to the strong acceleration caused by the flame still remains when the periodic coherent motion is included. In Figure 6.6, instantaneous and time-averaged streamwise velocity contours on plane $z = 0$ are displayed. Identical upper and lower recirculation zones of length $2.5h$ were obtained. This value compares well with the $2.3h$ experimental value reported in [82]. The value obtained is slightly higher than the value provided in the previous chapter for an unforced simulation of case c_2 ($2.4h$); the inclusion of the periodic coherent contribution does not influence any of the mean flow features to any great extent.

Instantaneous contours of progress variable in plane $z = 0$, showing the flame shape at different instants during a period of forced oscillation, are depicted in Figure 6.7. A dramatic change in flame shape is evidenced when forcing is applied, as the flame front transitions between a broadly cylindrical shape and a triangular shape at different parts of the cycle. A clear vortex roll-up process taking place in the vicinity of the step corners can be distinguished. The flapping of the instantaneous flame brush is intensified significantly under forcing conditions, following a cyclic process where the flame front continuously expands and shrinks, with a consequent considerable broadening of the mean flame brush. The flame shape and location are changed dramatically by the oscillation. This creates pockets of unburned gases at the dump plane that penetrate outwards towards the combustor wall as they travel downstream. The triangular flame front is wrinkled by turbulent large scale eddy distortion. Zero phase has been chosen to coincide with a zero and increasing acoustic perturbation velocity at the dump plane. Between phase angle $\psi = 0$ and $\psi = \pi/2$, when the incoming mass flow rate reaches its maximum value at the dump plane, there is a pulse of cold mixture injected into the combustor. A counterrotating vortex pair is created in the shear layers at the step corners, bringing fresh reactants into the step region that decrease the local temperature. As fresh reactant enters the combustor, the central core elongates downstream, transporting colder mixture and reducing the temperature further downstream. From

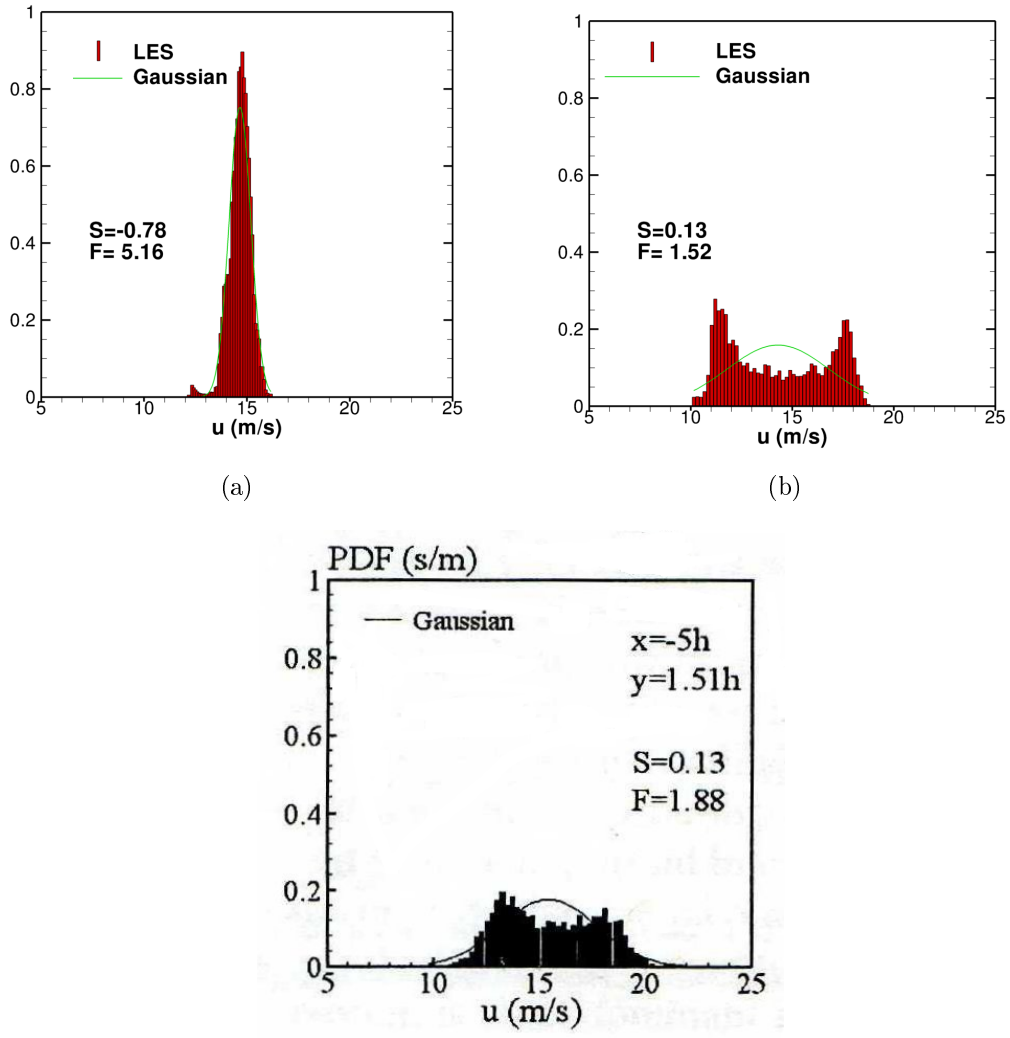

Figure 6.5: Probability density functions (PDFs) of streamwise velocity on the centreline of the upper inlet duct and $0.15m$ upstream of the dump plane for case c_2 from LES calculations (a) with no forcing and (b) under forced conditions with A=0.31, and (c) from experimental data [82]

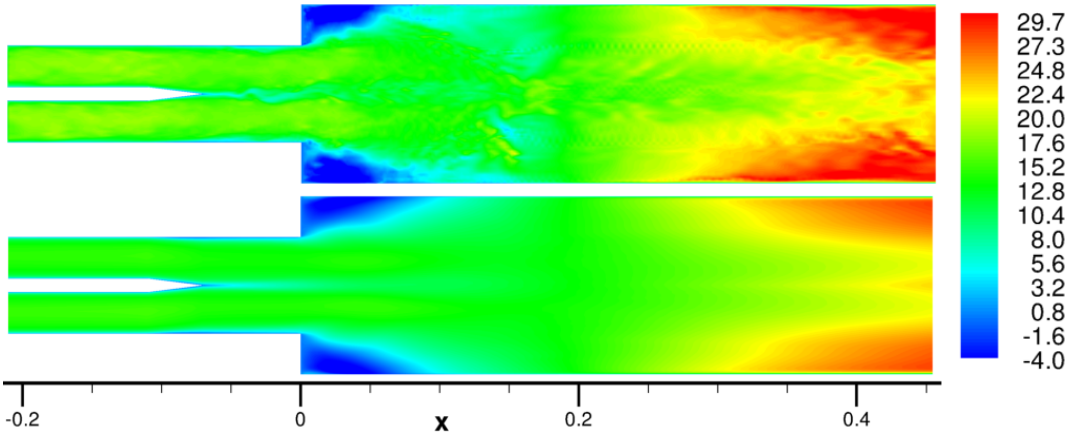

Figure 6.6: Instantaneous (top) and mean (bottom) streamwise velocity contours on plane $z = 0$ for case c_2 under forced conditions with A=0.31

phase angle $\psi = \pi$, the flame front broadens and impinges on upper and lower walls at a phase angle of around $\psi = 5\pi/4$; this is when the flame front has its shortest and most cylindrical shape. At this time, a pocket of cold reactants detaches from the central main core and moves towards the exit of the combustor. At phase angle $\psi = 3\pi/2$, the mass flow rate of cold reactants at the dump plane reaches its minimum and the flux of fresh mixture into the step corner regions is reduced, allowing the temperature to remain high due to stagnant hot burnt gases. The interaction of the flame with upper and lower walls is intensified compared to the unforced case, since the flame front moves backwards and forwards at the same time that it expands and shrinks cyclically under the influence of forcing. These cyclic unsteady processes will clearly be a major driving influence on the Flame Transfer Function.

To indicate the shape of the instantaneous forced flame in the experiments, self-luminescence visualisation pictures with a short time exposure of 1/500 were captured (Figure 6.8). This visualisation corresponds to a spanwise integration of the combustion zone but is still a good guide to the instantaneous shape and it allows to recognise the periodic sequence of flame morphology that is associated with the flapping of the two anchored flame brushes; at the instant captured in Figure 6.8 the flame front is close and moving towards the walls.

Figure 6.9 shows time-averaged numerical predictions for progress variable under both forced and unforced conditions together with a long time exposure self-luminescence visualisation taken from the experiments. A clear qualitative improvement in representing the flame pattern observed in the experiments is achieved when forcing is applied. For the unforced case, a cylindrical flame front between cold and reacting gases is

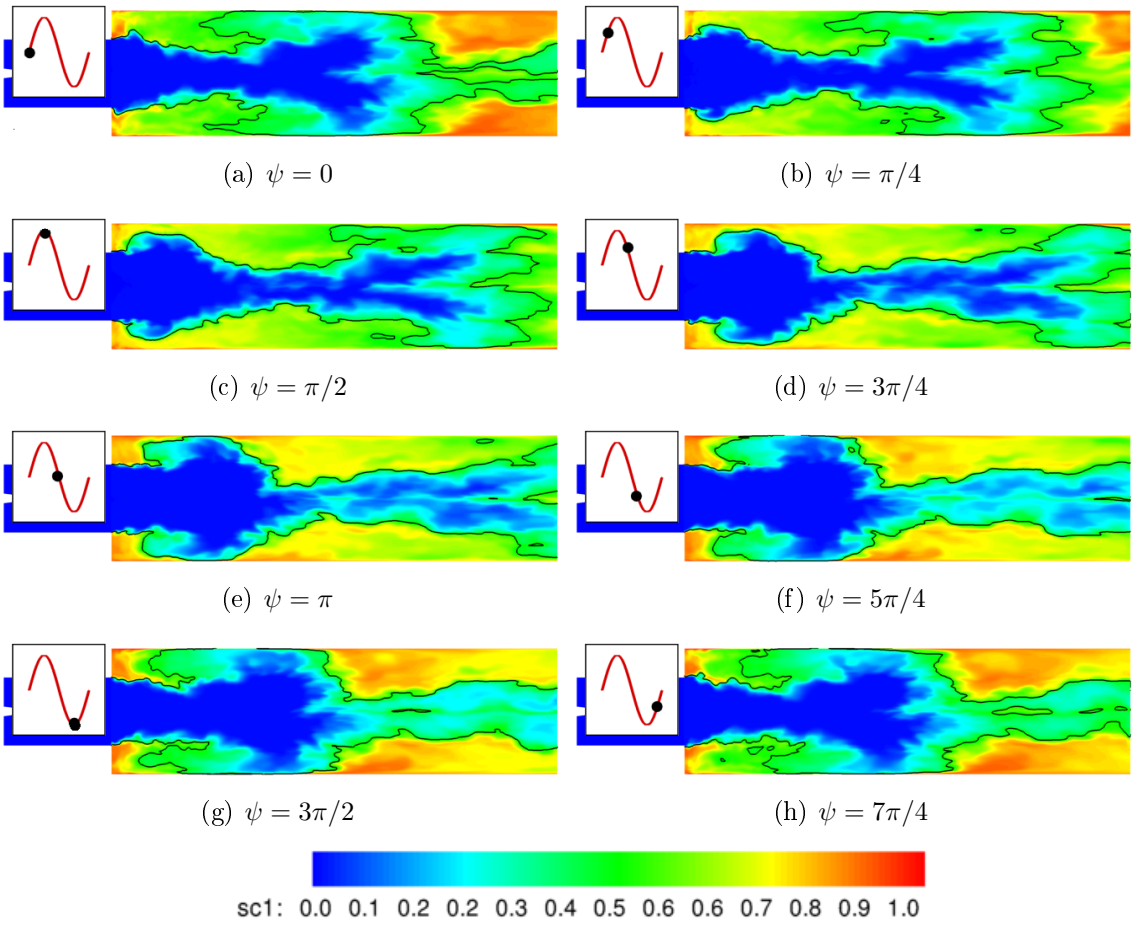

Figure 6.7: Instantaneous progress variable (plane $z = 0$) at different phase angles $\psi = 0$, $\pi/4$, $\pi/2$, $3\pi/4$, π, $5\pi/4$, $3\pi/2$ and $7\pi/4$ in an acoustic cycle (f=50Hz, A=0.31). Black line indicates c-isosurface ($c = 0.5$)

obtained, whereas an inwards oriented triangular shape is recovered when forcing is included, reproducing the measured data. The symmetric flapping of the instantaneous flame brushes in the forced case creates a wider (compared to the unforced case) mean flame brush, which is well predicted in size only when forcing is applied. A smaller region of almost stagnant hot burnt gases in the upper and lower corners is observed for the forced case, again consistent with experimental visualisation, and a consequence of the vortex roll-up process. It is worth noting that by comparing the experimental visualisations in Figures 6.8 and 6.9 it is apparent that the mean flow structure is far from being representative of any instantaneous state of the flame.

Contour plots of predicted mean turbulent kinetic energy (TKE) are presented in Fig-

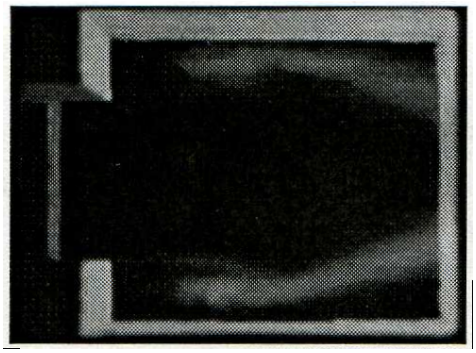

Figure 6.8: Experimental self-luminescence visualisation picture ((short) 1/500s time exposure) in combustion zone downstream of the dump plane

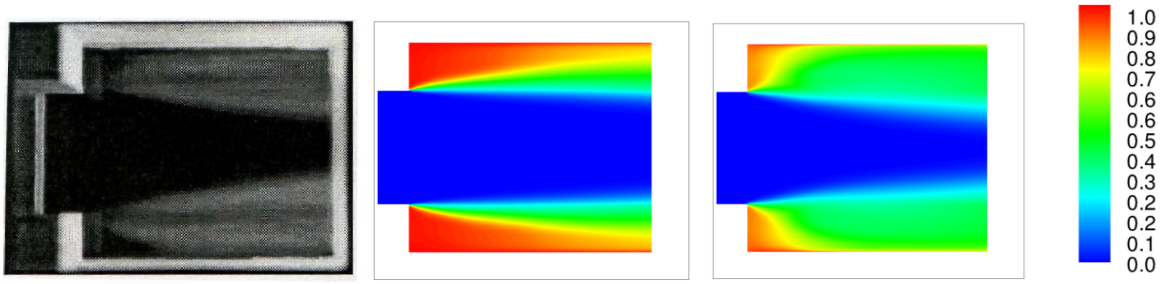

Figure 6.9: (Left) Experimental self-luminescence visualisation ((long) 1/50s time exposure) and numerical time-averaged progress variable contour in the combustion zone downstream of the dump plane for unforced (middle) and forced (right) cases. Plane $z = 0$

ure 6.10. The spatial distribution of the TKE contours is very similar to that obtained for the unforced case (see Figure 5.18), with peak values in the shear layers developing from the two step corners, a region of low TKE in the centre of the combustor and a region of moderately high TKE caused by the wake originating at the tip of the splitter plate. Despite this similarity, it is obvious that much higher levels of "apparent" TKE are obtained when forcing is applied, due to the increased streamwise velocity fluctuation level. This increased fluctuating energy includes the periodic contribution, which of course is not strictly "turbulence", but is picked up as such by the averaging process. This is most evident in the approach ducts, where a value of approximately $3.2m^2/s^2$ is obtained on the centreline, compared to the value of 0.22 m^2/s^2 obtained in the unforced case. Likewise, peak values reached in the shear layers regions are 6.6 m^2/s^2 and 13.2 m^2/s^2, and values in the dump plane and centreline of the combustor are 1.9 m^2/s^2 and 3.38 m^2/s^2, for unforced and forced calculations, respectively.

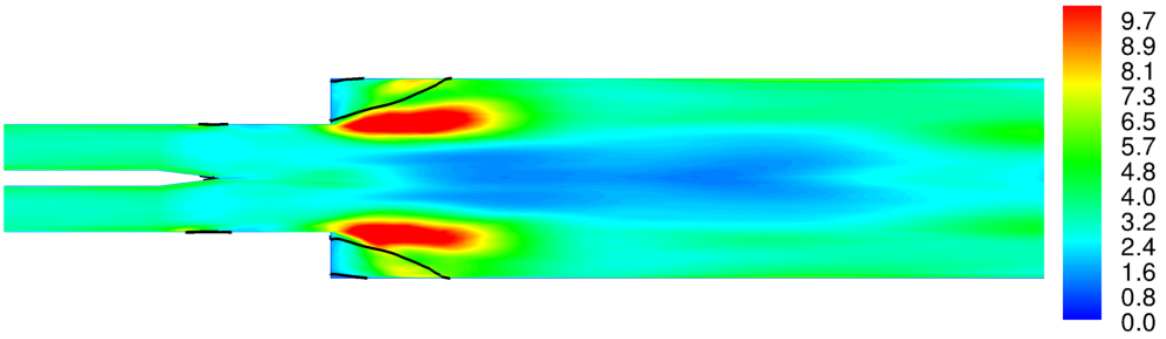

Figure 6.10: Turbulent kinetic energy (TKE) contours in plane $z = 0$ for case c_2 under forced conditions. Black line indicates $\overline{u}$-isosurface ($\overline{u} = 0.0$)

6.3.2 Transverse profiles

Transverse profiles of statistical moments of axial and transverse velocities are presented in this section (Figures 6.11-6.14); these plots include profiles from the unforced simulation for comparison purposes, corresponding to results already seen in chapter 5.

As mentioned earlier, mean streamwise velocity profiles are characterised by perfect symmetry, whereas antisymmetric behaviour is observed in the mean transverse velocity. These features are not modified by the periodic motion. Fluctuating velocities are also characterised by symmetry, with peaks located on both sides of the combustor centreline. Local maxima found on the combustor centreline (wake of the splitter plate), are scarcely observed in the measured data, although predicted results exhibit these maxima in regions near the dump plane. In general, a considerable increase in fluctuating velocity amplitudes is observed when forcing is applied.

The axial positions where comparison with measured data is made are the same as used earlier (see Figure 5.24).

Figure 6.11 shows transverse profiles of mean streamwise velocity. The agreement with the experimental data is very good when forcing is introduced with profiles not differing much from the unforced results, but where there are differences these are (by and large) marginal improvements. For $x/h \leq 4$, the agreement is excellent and predicted results show a clear improvement near both lower and upper walls with respect to the unforced case. At axial locations $x/h \geq 7$ CFD results underpredict experimental data. This tendency was already observed in the unforced calculation. As already pointed out, the combustion model employed is responsible for this, implying a lower heat release than measured, thus less reduced density. The same value of the FSD parameter β has been used so far and this will be explored further below.

Transverse profiles of mean transverse velocity are shown in Figure 6.12. The agreement with LDA measurements is good, reproducing perfectly the antisymmetric behaviour and also the magnitude of the profiles. At $x/h = 0$ the agreement is excellent. The largest discrepancy is observed at axial location $x/h = 1$, where a flat predicted profile underestimates the measured double peak observed in the experiments. The peaks in the predictions do appear but only further downstream. For axial positions $x/h \geq 2$ the shape of the predicted profiles where forcing is included accurately describes the measured data, with a clear improvement over the unforced case.

Fluctuating velocity profiles are plotted in Figures 6.13 and 6.14 and it is here where the largest change is brought about by forcing. At positions $x/h = 0$ to $x/h = 4$ the predicted streamwise profiles reproduce the measured data very well when forcing is introduced, although some overprediction occurs near the walls (where the LES mesh is not wall-resolving). The transverse fluctuations capture the shape but overpredict the magnitude. Between $x/h = 4$ to $x/h = 7$ the experimental data for axial fluctuations shows a noticeable increase; this is reproduced also by the forced calculation, although overpredicted in strength. This is the region of wall vortex interaction, which seems to be too intense in the current forced simulation. At positions $7 \leq x/h \leq 9$, the predicted results overestimate the measured data for both fluctuating components, although the shape is captured correctly.

LES predictions from Duwig [118] and Duwig and Fureby [117] for mean and fluctuating velocities at several axial positions have also been plotted in the figures above, represented by blue and green lines, respectively. In both cases the amplitude of forcing used was A=0.27. Duwig [118] used a progress variable approach and modelled both subgrid transport and subgrid reaction with a flamelet closure from [136]. Thus, a π function is introduced to model these two terms. $\pi = \pi(\tilde{c}, a)$ followed a Gaussian distribution (in physical space) of the heat release, where a was a nondimensional parameter relating the integral reaction rate across the front to diffusion. The π function forced the progress variable to range from 0 to 1 and also the π-diffusion balance led to correct filtered flame propagation speed. Duwig and Fureby [117] investigated two different flamelet modelling: first a filtered flamelet model based on a π function, $\pi(\tilde{c}, a)$, such as the one used by Duwig [118]; second a propagation flamelet model from [134], with a fractal flame wrinkling factor model used to close the filtered flame front displacement term. Results for the two flamelet modelling approaches showed small differences. The results from Duwig [118] and Duwig and Fureby [117] are very similar, in magnitude as well as in shape, to those obtained in the present project. For $x/h \geq 7$, especially at $x/h = 10$, a higher magnitude for mean and fluctuating velocities was obtained in [118] and [117], attributed to the combustion model inducing a higher flow acceleration. At these axial locations, measured data were overpredicted by results from

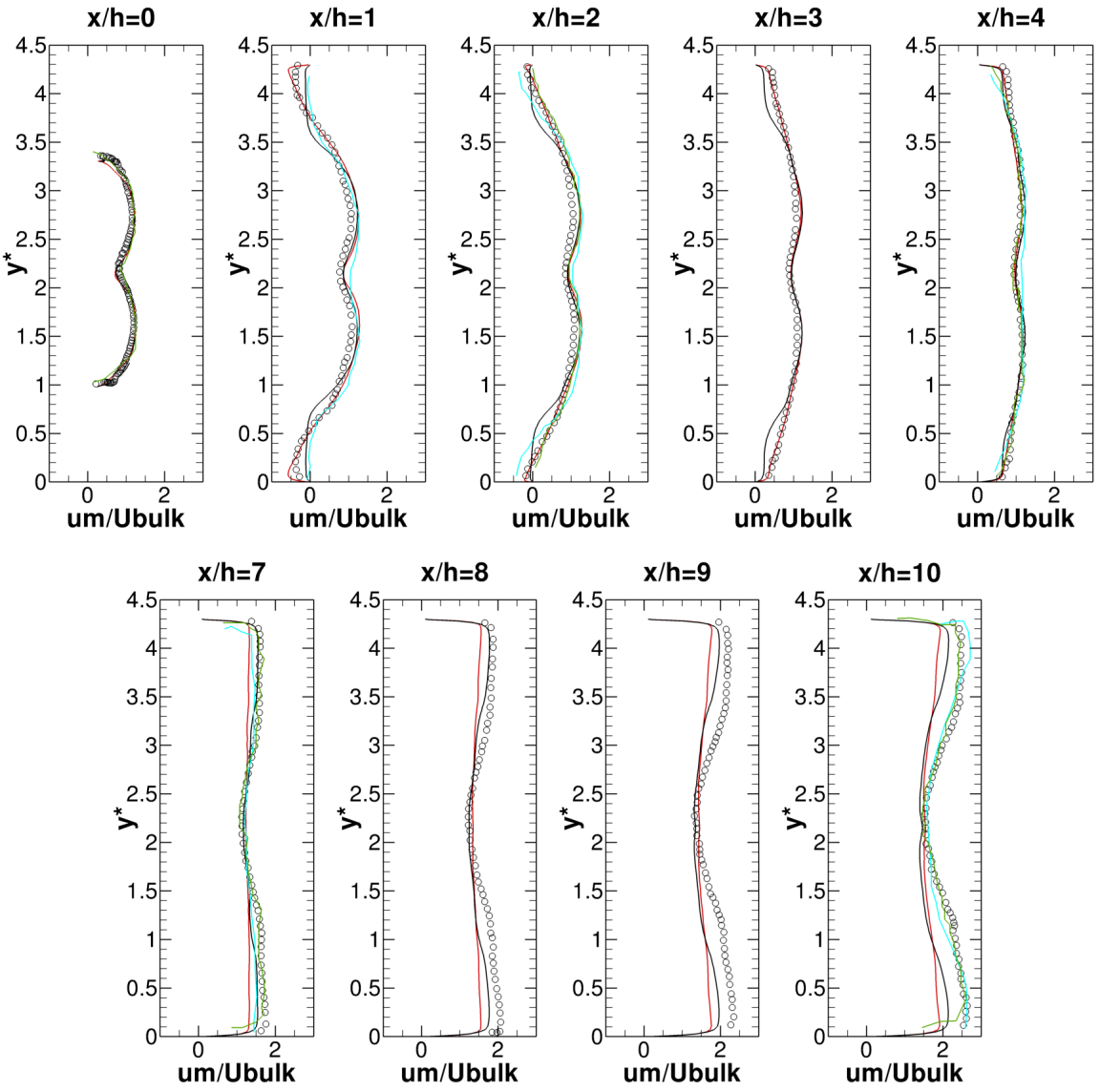

Figure 6.11: Normalised mean streamwise velocity for case c_2 at different axial positions for forced (red line) and unforced (black line) cases. $U_{bulk} = 11m/s$. Experimental data (o) from Nguyen et al. [82]. Blue line from Duwig [118]. Green line from Duwig and Fureby [117]

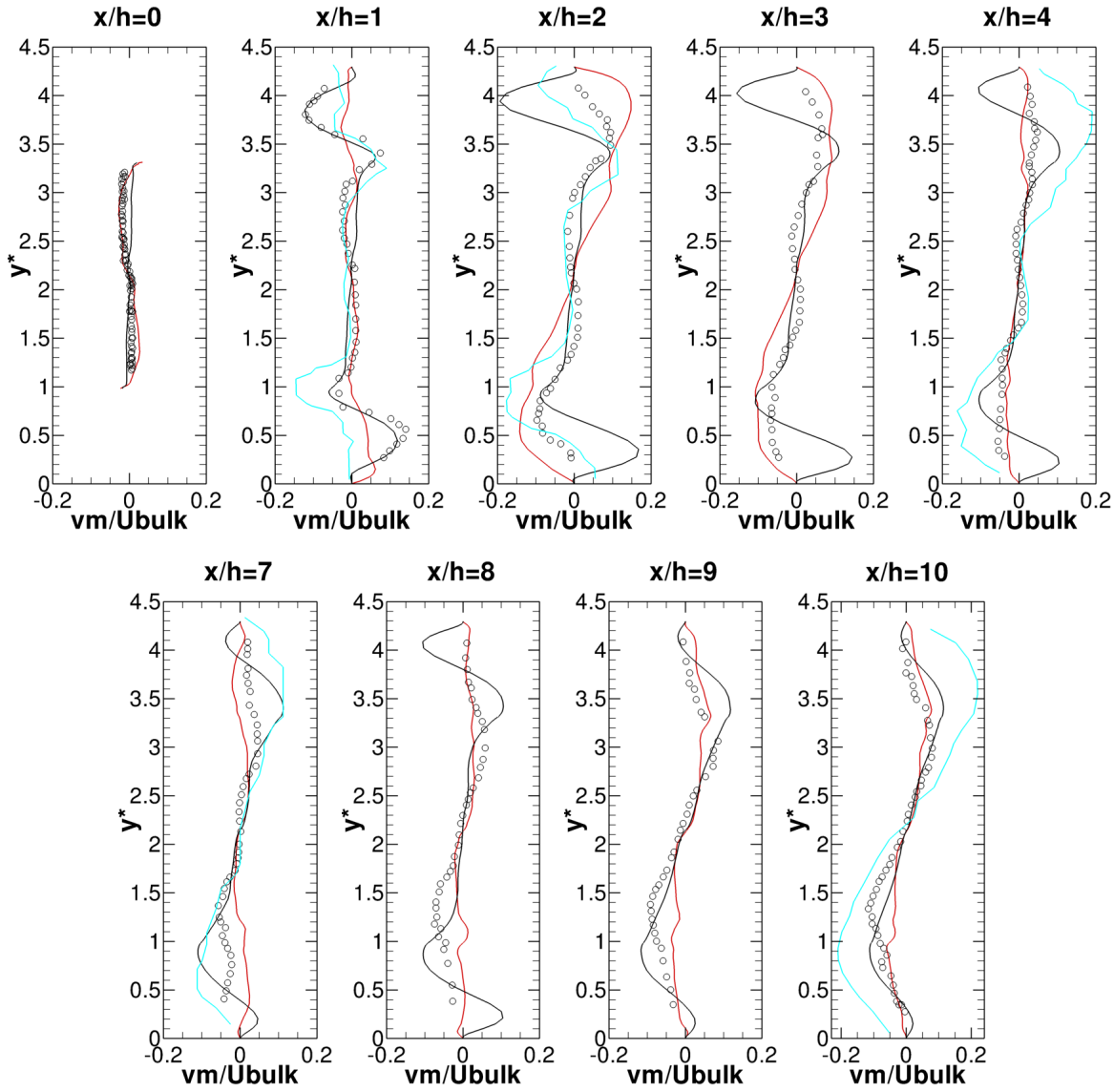

Figure 6.12: Normalised mean transverse velocity for case c_2 at different axial positions for forced (red line) and unforced (black line) cases. $U_{bulk} = 11m/s$. Experimental data (o) from Nguyen et al. [82]. Blue line from Duwig [118]

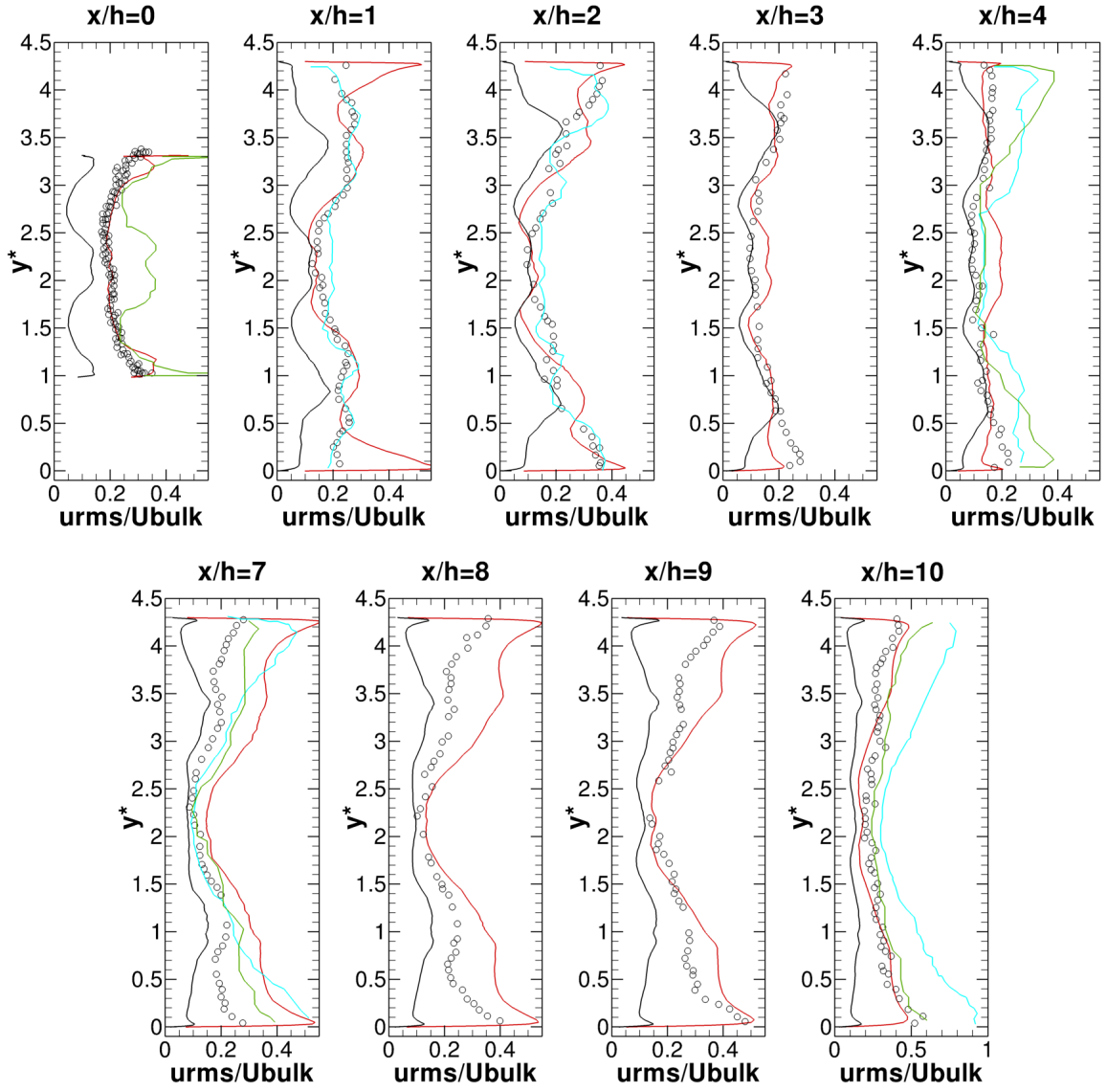

Figure 6.13: Normalised fluctuating streamwise velocity for case c_2 at different axial positions for forced (red line) and unforced (black line) cases. $U_{bulk} = 11m/s$. Experimental data (o) from Nguyen et al. [82]. Blue line from Duwig [118]. Green line from Duwig and Fureby [117]

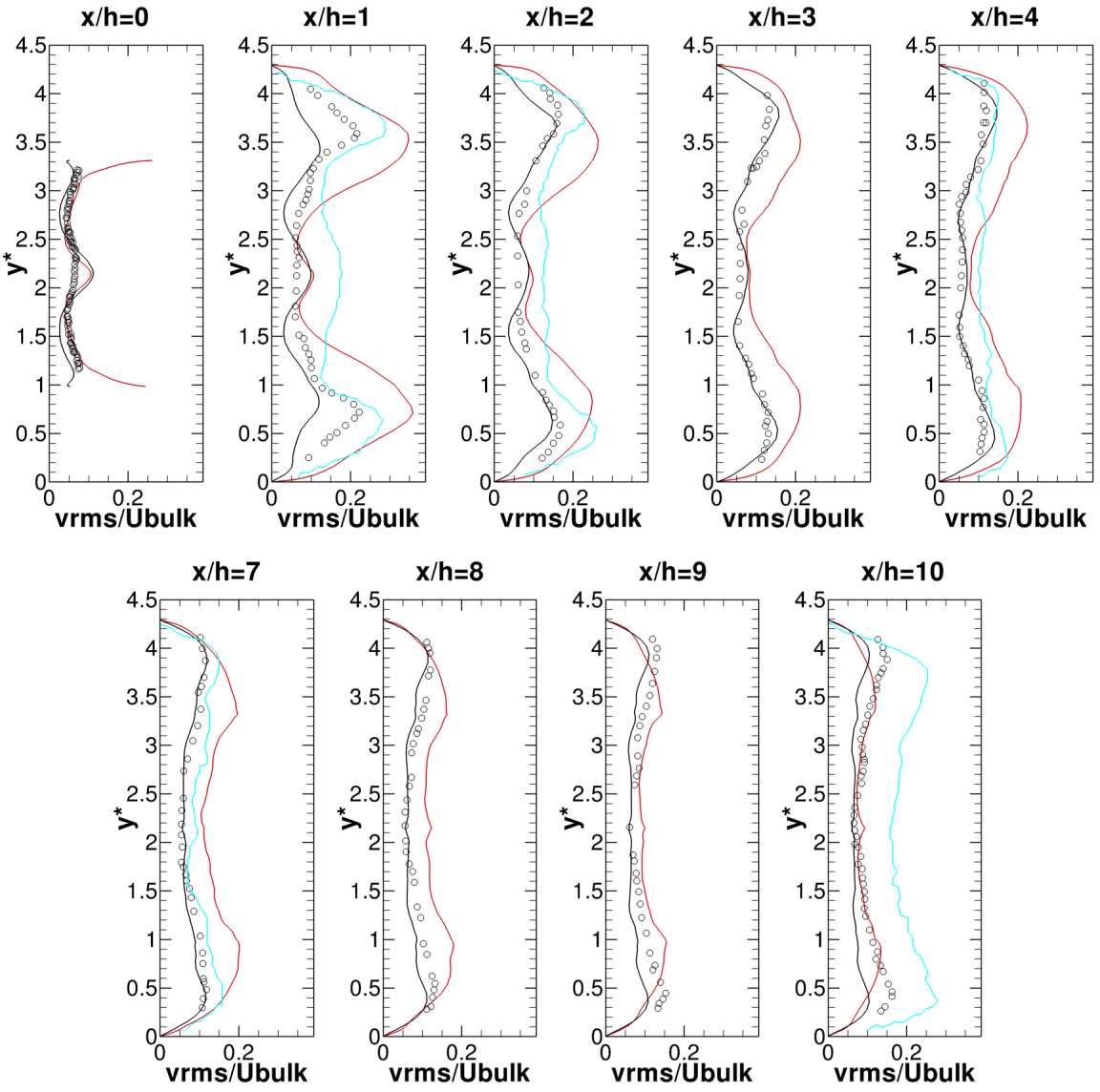

Figure 6.14: Normalised fluctuating transverse velocity for case c_2 at different axial positions for forced (red line) and unforced (black line) cases. $U_{bulk} = 11m/s$. Experimental data (o) from Nguyen et al. [82]. Blue line from Duwig [118]

Duwig and Duwig and Fureby compared to better agreement obtained in the present simulations. For $x/h \leq 4$ results presented in this work and those from Duwig and Duwig and Fureby are very similar, achieving comparable accuracy with measurements.

6.3.3 3D contour plots

Figure 6.15 displays c-isosurfaces of the progress variable ($c = 0.5$) to illustrate the flame morphology. Results for unforced and forced cases are shown to emphasise the dramatic change in flame dynamics when forcing is included. The roughly cylindrical flame front shape in Figure 6.15(a) contrasts with the triangular shape observed in Figure 6.15(b), after the vortex pair induced by inlet forcing, originated at the step corners. In addition, the modified interaction of the flame with upper and lower walls is clearly observed in Figure 6.15(b).

6.4 Flame response - extraction of amplitude dependent Flame Transfer Function (FTF) calculations and incorporation into thermo-acoustic network model

6.4.1 Introduction

To predict thermo-acoustic phenomena, it is necessary to estimate the flame response to flow field perturbations. This is described analytically via a Flame Transfer Function (FTF). In the context of the perfectly premixed ORACLES flame considered here (where the equivalence ratio is constant) the FTF may be expressed as the ratio of normalised heat release rate fluctuations to normalised inlet mass flow rate perturbations:

$$FTF(f, A) = \frac{\dot{Q}'(f, A)/\overline{\dot{Q}}}{\dot{m}'(f, A)/\overline{\dot{m}}} \tag{6.4}$$

where $\overline{\dot{Q}}$ and $\overline{\dot{m}}$ are long time-averaged heat release rate and mass flow rate respectively, $\dot{Q}'(f, A)$ and $\dot{m}'(f, A)$ are fluctuating heat release rate and fluctuating mass flow rate, f indicates frequency and A $=|\dot{m}'(f, A)|/\overline{\dot{m}}$ corresponds to the forcing amplitude. Once known, the FTF can be incorporated as a source term in a thermo-acoustic network model, as described by Dowling and Stow [6]. For the present flow conditions pressure, density and temperature fluctuations at the inlet are small compared to their mean

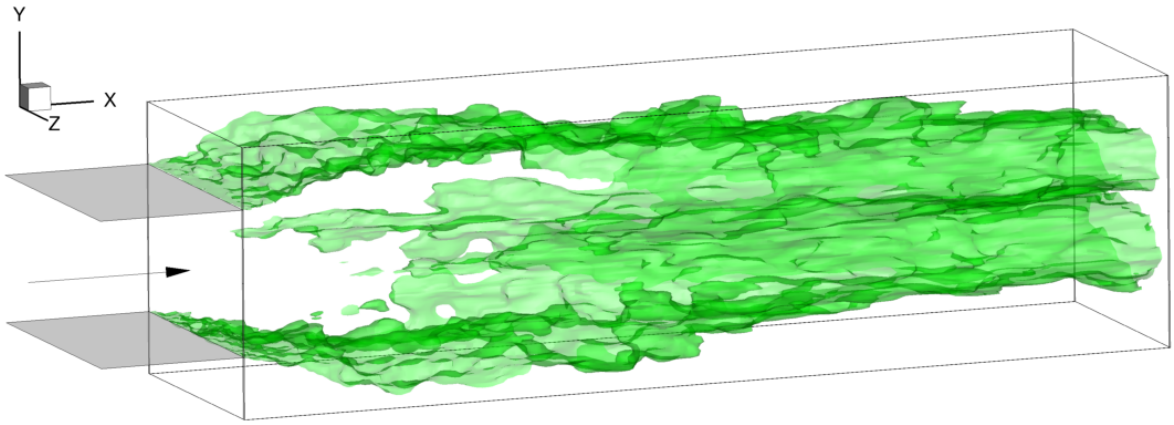

(a)

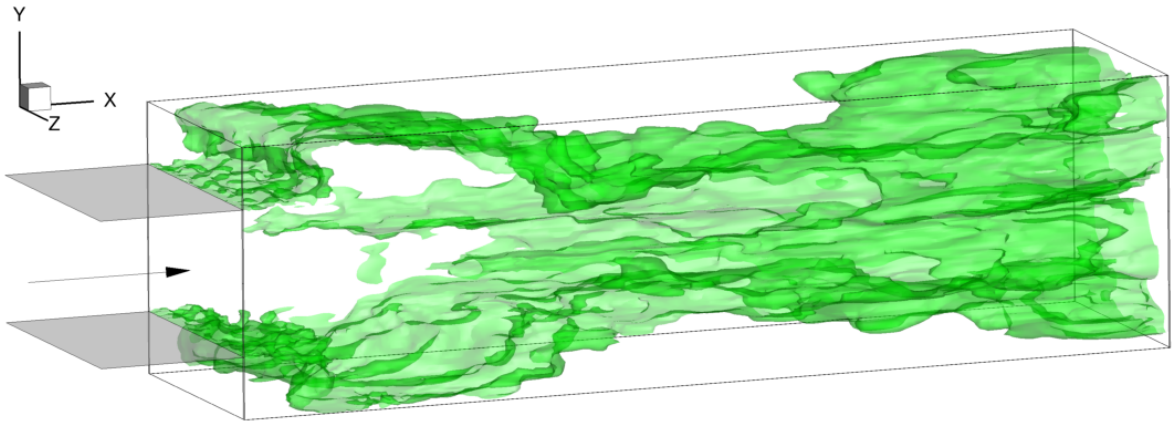

(b)

Figure 6.15: Flame shape visualised by instantaneous c-isosurfaces ($c = 0.5$) for (a) unforced case and (b) forced case c_2 at phase angle $\psi = \pi/4$

values. In addition, although velocity perturbations are small compared to the speed of sound, they are larger compared to the mean flow velocity, making it a reasonable assumption that inlet velocity fluctuations have the major influence on the unsteady combustion. Furthermore, at the dump plane:

$$\frac{u'}{\overline{u}} \approx \frac{\dot{m}'}{\overline{\dot{m}}} \tag{6.5}$$

Both analytical and experimental studies [91, 92, 105] show that both linear and nonlinear regimes can be identified in the flame response to perturbations for a given frequency. In the linear regime, the gain (amplitude of FTF in equation (6.4)) remains constant as forcing amplitude A is increased, up to the point where nonlinear effects become important and the gain then begins to decrease with increasing A. This is relevant in order to understand the mechanism of limit cycle combustion instability: the linear response determines the frequency and growth rate of the instability and the nonlinear response determines the final amplitude of the instability [200–202]. In general, the flame acts as a low pass filter, that is the gain decreases when frequency is increased, for a fixed forcing amplitude [95].

A numerical study of flame response based on a series of combusting LES simulations of the ORACLES test case c_2 at different forcing amplitudes and fixed frequency has been performed and is presented in the next sections. First, the procedure used to calculate the unsteady heat release rate is described, as well as two different approaches to extract the FTF from numerical simulation results. Secondly, results of extracted FTFs are shown, linear and nonlinear regimes are identified, and saturation mechanisms discussed. Finally, the LES predicted amplitude dependent FTFs are introduced as a source term into a thermo-acoustic network model, to examine stability predictions and explore the possibility of identifying an equilibrium, self-sustained limit cycle behaviour.

6.4.2 Instantaneous heat release rate calculation

For a given volume Ω of the combustor, the total heat release rate within this volume at any instant of time is given by :

$$\dot{Q}_\Omega = \int_\Omega \dot{\omega}_T d\Omega \tag{6.6}$$

where $\dot{\omega}_T$ is the heat release rate per unit volume due to combustion:

$$\dot{\omega}_T = -\sum_{k=1,N} \Delta h^0_{f,k} \dot{\omega}_k \tag{6.7}$$

$\Delta h^0_{f,k}$ and $\dot{\omega}_k$ are the enthalpy of formation and the reaction rate per unit volume, respectively, of species k.

Assuming a single-step irreversible chemical reaction, with fuel and oxidiser as reactants, the heat release rate, $\dot{\omega}_T$, the fuel reaction rate, $\dot{\omega}_F$, and the chemical reaction term in the progress variable transport equation, $\dot{\omega}_c$, are related via:

$$\left.\begin{aligned}\dot{\omega}_T &= -Q_{hr}\,\dot{\omega}_F \\ \dot{\omega}_c &= -\dot{\omega}_F / Y_F^1\end{aligned}\right\} \Longrightarrow \dot{\omega}_T = Q_{hr}\,Y_F^1\,\dot{\omega}_c \tag{6.8}$$

where Q_{hr} is the fuel heat capacity (for propane $\approx 46.600 kJ/kg$) and Y_F^1 is the fuel mass fraction in the unburnt mixture (≈ 0.046 for combustion of propane in air at $\phi = 0.75$).

When a CFD simulation is performed on a discretised computational domain, equation (6.6) can be recast as:

$$\dot{Q}_\Omega = \int_\Omega \dot{\omega}_T d\Omega \equiv \sum_i \dot{\omega}_{T,\Delta\Omega_i} \Delta\Omega_i \tag{6.9}$$

where $\Omega = \sum_i \Delta\Omega_i$, and $\Delta\Omega_i$ represents a discretisation control volume.

An algebraic Flame Surface Density approach has been employed to model the frame front displacement (equation (2.38)); thus, assuming that $\rho_u s_l \Sigma = \dot{\omega}_c$ the total heat release rate can be written

$$\dot{Q}_\Omega = \sum_i \dot{\omega}_{T,\Delta\Omega_i} d\Omega_i = \sum_i Q_{hr}\,Y_F^1\,\dot{\omega}_{c,\Delta\Omega_i} \Delta\Omega_i = \sum_i Q_{hr}\,Y_F^1\,\rho_u s_l \Sigma_{\Delta\Omega_i} \Delta\Omega_i \tag{6.10}$$

and this total instantaneous heat release rate within volume Ω ($\dot{Q}_\Omega$) may be calculated at the end of every LES time step. Once the time-series of heat release rate is obtained, time-averaging to obtain $\overline{Q}_\Omega$ and hence Q'_Ω may easily be performed.

6.4.3 FTF calculation

Two different methodologies to extract an FTF from LES numerical results have been used and compared, namely *cycle-averaging* and *Fourier series analysis*. In both cases time-series of the mass flow rate at the dump plane (the signal) and the time-series of the total instantaneous heat release rate within the combustor volume (equation (6.10), the response) were stored for every LES time step. Only an integer number of complete cycles from these time-series is then considered, again taking zero phase to coincide with the time of zero and increasing unsteady mass flow rate at the dump plane. The two methodologies for post-processing these data to deduce the FTF are briefly explained below:

(a) **Cycle-averaging.** A sample period, $(0, N_{cy}T)$, of signal and response is analysed, where N_{cy} is the total number of cycles saved from the simulation, $T = 1/f$ is the period and f is the forcing frequency. Every interval $(nT, (n+1)T)$, for any $0 \leq n < N_{cy}$, is divided into 1000 equispaced intervals, $I_{i,n} = (nT + i\Delta t, nT + (i+1)\Delta t)$, where $0 \leq i < 999$ and $\Delta t = T/1000$. For a fixed interval i, values of signal and response belonging to intervals $I_{i,n}$, for any $0 \leq n < N_{cy}$, are averaged (summed and divided by total number of instances). This is repeated for each interval i. At the end of the process 1000 averaged values (for both signal and response) are obtained, for 1000 time points in the interval (0,T). Then the resulting curves for signal and response are normalised by their respective time-averaged values ($\overline{\dot{m}}$ and $\overline{\dot{Q}}$). The magnitudes of normalised fluctuating mass flow rate, $|\dot{m}'|/\overline{\dot{m}}$, and normalised fluctuating heat release rate, $|\dot{Q}'|/\overline{\dot{Q}}$ (where $\dot{m}' = \dot{m} - \overline{\dot{m}}$ and $\dot{Q}' = \dot{Q} - \overline{\dot{Q}}$), are then evaluated, enabling the gain (K) of the FTF to be calculated ($K = (|\dot{Q}'|/\overline{\dot{Q}})/(|\dot{m}'|/\overline{\dot{m}})$). The phase of the FTF corresponds to the phase difference between the maximum amplitudes of the cycle-averaged normalised signal and response curves. Figure 6.16 plots a schematic of the variables used in the FTF parameter calculation.

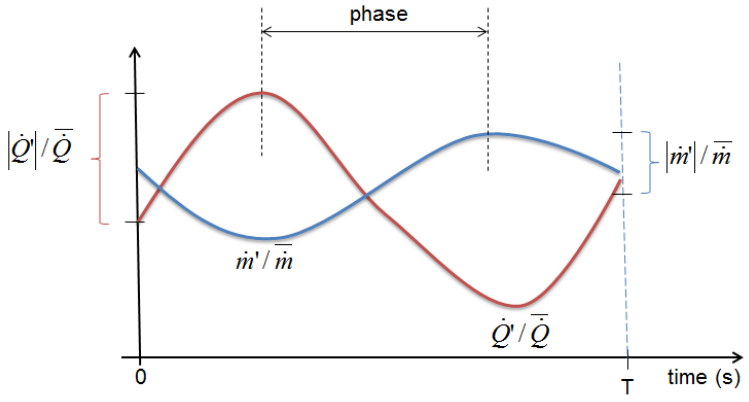

Figure 6.16: Sketch with variables used in the FTF parameters calculation

(b) **Fourier series analysis.** The main attraction of the Fourier series method is its ability to express any periodic function as a sum of simple waves mathematically represented by sines and cosines.

For a periodic function $g(x)$ integrable on $[-\pi, \pi]$, the numbers:

$$a_n = \frac{1}{\pi}\int_{-\pi}^{\pi} g(x)\cos(nx)dx, \quad n \geq 0 \tag{6.11}$$

and

$$b_n = \frac{1}{\pi}\int_{-\pi}^{\pi} g(x)\sin(nx)dx, \quad n \geq 1 \tag{6.12}$$

are referred to as *Fourier coefficients*. The *partial sums of the Fourier series* for g are:

$$(S_N g)(x) = \frac{a_0}{2} + \sum_{n=1}^{N} [a_n \cos(nx) + b_n \sin(nx)] \tag{6.13}$$

which approximates the value $g(x)$ and also satisfies:

$$\lim_{N\to+\infty} (S_N g)(x) = g(x) \tag{6.14}$$

The infinite sum:

$$\frac{a_0}{2} + \sum_{n=1}^{+\infty} [a_n \cos(nx) + b_n \sin(nx)] = g(x) \tag{6.15}$$

is called the *Fourier series* of g.

If Euler's formula is used:

$$e^{inx} = \cos(nx) + i\sin(nx) \tag{6.16}$$

then a compact formulation of equation (6.15) can be written:

$$g(x) = \sum_{n=-\infty}^{+\infty} c_n e^{inx} \tag{6.17}$$

where the Fourier coefficients c_n are then given by:

$$c_n = \frac{1}{2\pi}\int_{-\pi}^{\pi} g(x)e^{-inx}dx \tag{6.18}$$

Hence, Fourier coefficients a_n, b_n and c_n may be related via:

$$c_n = \begin{cases} \frac{1}{2}(a_n - ib_n) & n > 0 \\ \frac{1}{2}a_0 & n = 0 \\ \frac{1}{2}(a_{-n} + ib_{-n}) & n < 0 \end{cases} \tag{6.19}$$

This Fourier series analysis can easily be generalised to any function $f(t)$ which is periodic in all $\mathbb{R}$, with period T, and integrable in an interval $[a, a+T]$. It then follows that:

$$f(t) = \sum_{n=-\infty}^{+\infty} c'_n e^{i2\pi\frac{n}{T}t} \tag{6.20}$$

where the coefficients c'_n are defined by :

$$c'_n = \frac{1}{T}\int_a^{a+T} f(t)e^{-i2\pi\frac{n}{T}t}dt \tag{6.21}$$

a is an arbitrary choice, although the most popular choices are 0 and $-T/2$. Equations (6.20) and (6.21) are equivalent to equations (6.17) and (6.18) once a change of variable $x := \frac{2\pi t}{T}$ is imposed. Thus, if $f(t)$ is a periodic function in the interval $[-T/2, T/2]$ it follows that $f(t) = f(x\frac{T}{2\pi}) =: f(x')$ and $f(x')$ is a function with period 2π in the interval $[-\pi, \pi]$ to which the Fourier analysis described above can be applied.

Likewise, equation (6.19) still holds, with the corresponding a'_n, b'_n and c'_n defined as:

$$a'_n = \frac{1}{(T/2)}\int_{-T/2}^{T/2} f(t)\cos\left(2\pi\frac{n}{T}t\right)dt \tag{6.22}$$

$$b'_n = \frac{1}{(T/2)}\int_{-T/2}^{T/2} f(t)\sin\left(2\pi\frac{n}{T}t\right)dt \tag{6.23}$$

and

$$c'_n = \frac{1}{T}\int_{-T/2}^{T/2} f(t)e^{-i2\pi\frac{n}{T}t}dt \tag{6.24}$$

Note that due to the sine and cosine properties, it is possible to recover the contribution of each individual wave in the Fourier series by integration. In particular, when Euler's formula is used, the Fourier series can be written in terms of the basic waves $e^{2\pi i\xi}$, which allows the Fourier coefficients to be complex valued. The usual interpretation of these complex numbers is that they give both the amplitude (size) and phase (angle) of a specific wave.

There is also a close relation between Fourier series analysis and the Fourier transform of an integrable function $f : \mathbb{R} \longrightarrow \mathbb{C}$. The latter is defined by:

$$\hat{f}(\xi) = \int_{-\infty}^{+\infty} f(t)e^{-i2\pi\xi t}dt \tag{6.25}$$

If the variable t represents time (s), then ξ represents frequency (Hz).

If f is a function which is zero outside an interval, and T is large enough that the interval $[-T/2, T/2]$ contains all regions in which f is not identically zero, then the n^{th} series coefficient c'_n is given by equation (6.24). It directly follows that

$c'_n = \hat{f}(n/T)$, since the function f is zero outside the interval $[-T/2, T/2]$.

This analysis has been applied to the function $f(t)$ describing the time series of the unsteady instantaneous heat release rate (see Figure 6.17, where both unsteady instantaneous mass flow rate (signal) and heat release rate (response) are plotted). The function is assumed to be periodic, with period $T = 1/\xi$, where ξ represents frequency . Likewise, the function is considered over an interval long enough that it can be assumed to contain the complete time series. Thus, in order to calculate the amplitude and phase of a specific wave $e^{i2\pi\xi}$ (or frequency $\xi = n/T$) the complex valued coefficient $c'_n = \hat{f}(\xi) = \hat{f}(n/T)$ must be evaluated. If the wave to be quantified corresponds to the predominant frequency $1/T$, rather than its harmonics, then c'_1 is calculated, defined from (6.24). Numerical integration (using a Trapezoidal rule) of equations (6.22) and (6.23) is performed and equation (6.19) is utilised to calculate the value of c'_1. In the Fourier transform, negative frequencies ξ must be included. Waves $e^{i2\pi\xi}$ and $e^{-i2\pi\xi}$ both complete one cycle per second, although they represent different frequencies in the Fourier transform. However, in the Fourier series analysis, they represent the same wave, thus the total amount of a wave at frequency n/T corresponds to $c_n + c_{-n} = a_n + ib_n$, for $n > 0$.

A trapezoidal rule approximation is applied to the Fourier coefficients, e.g. for equation (6.22):

$$a'_n = \frac{1}{(t_N - t_0)/2} \sum_{i=1}^{N} \int_{t_{i-1}}^{t_i} f(t) \cos(2\pi \frac{n}{T} t) dt \tag{6.26}$$

and each integral in the summation is approximated using:

$$\int_{t_{i-1}}^{t_i} f(t) \cos(2\pi \frac{n}{T} t) dt \approx (t_i - t_{i-1}) \frac{f(t_{i-1}) \cos(2\pi \frac{n}{T} t_{i-1}) + f(t_i) \cos(2\pi \frac{n}{T} t_i)}{2} \tag{6.27}$$

6.4.4 FTF results

One characteristic feature of the ORACLES experiment is that a long flame zone downstream of the dump plane exists. The fully burnt state is attained approximately $1.2m$ downstream of the dump plane, which demands a longer computational domain than was needed for comparison with the region in which the velocity and turbulence measurements described above were made. In addition, flame acoustic compactness is no longer clearly valid as an approximation since the acoustic wavelength at frequency

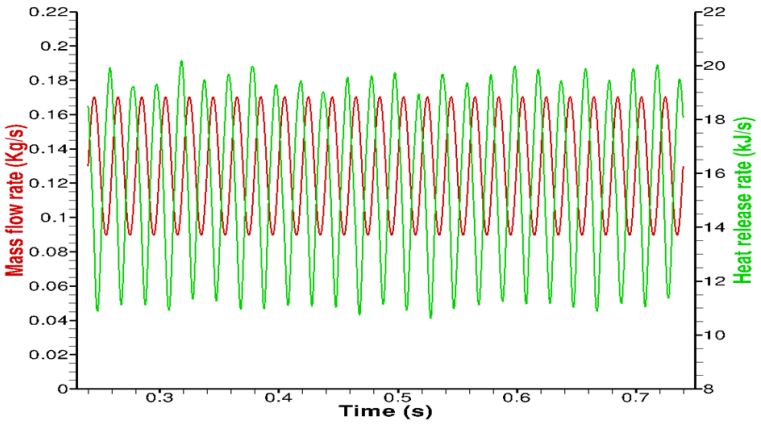

Figure 6.17: Unsteady instantaneous mass flow rate and heat release rate for case c_2

f=50Hz and an intermediate temperature of $1000K$ is around $12m$, only ten times the total flame length. Thus the burning process can no longer be assumed to take place in a thin flame front in comparison to the acoustic wavelength. The heat release is axially distributed over a considerable length and the local flame response to inlet perturbations, in amplitude and phase, will be highly dependent on axial position. Therefore, in order to ensure adequate capture of the physics of this distributed flame and to ensure this is properly represented in the extracted FTFs, the following approach was adopted: (1) for LES calculations to determine FTFs the computational domain was extended, in order to include a significant percentage ($\approx 90\%$) of the total heat release, (2) this extended computational domain was subdivided into axial slices and the volume-averaged unsteady heat release rate as defined above was evaluated separately for each slice, in order to ensure that the local flame response had been captured accurately, and (3) LES predictions for a range of forcing amplitudes at 50Hz frequency were carried out for the extended computational domain.

The computational domain was extended from $x = 0.45m$ to $x = 1.1m$ downstream of the dump plane. Thus, extra blocks were added in the axial direction and a similar cross-section and axial mesh resolution as used in previous simulations was maintained, leading to a mesh of $\approx 4.5 \cdot 10^6$ grid nodes. This domain contains $\approx 90\%$ of the total mean heat release. Figure 6.18 shows the predicted local time-averaged heat release versus axial distance observed for simulations at different forcing amplitudes. The local mean heat release is expressed in Figure 6.18 as a percentage of the maximum achievable mean heat release for this equivalence ratio ($\overline{\dot{Q}}_{total} = 280kW$, obtained from CANTERA[124] or from the formula $\overline{\dot{Q}}_{total} = \overline{\dot{m}} \cdot Y_F^1 \cdot Q_{hr}$). It is noticeable that for most of the combustor the distribution remains approximately the same for different

forcing amplitudes. However, in the first part of the combustor ($0 < x < 0.2m$), appreciable differences are visible. This is undoubtedly caused by the changing strength of mixing of hot and unburnt gases induced by the different strength of vortices shed from the dump plane and subsequently rolling up as the forcing amplitude increases. The different turbulence characteristics under increasing forcing conditions prompts a change in the flame dynamics which augments the heat release rate. In [117], flame response to inlet velocity perturbations at different forcing amplitudes was analysed for the same ORACLES test case. However, the computational domain used extended only $0.6m$ downstream of the dump plane, a length that probably does not contain a high enough percentage of the total mean heat release. However, no FTF analysis was performed in [117].

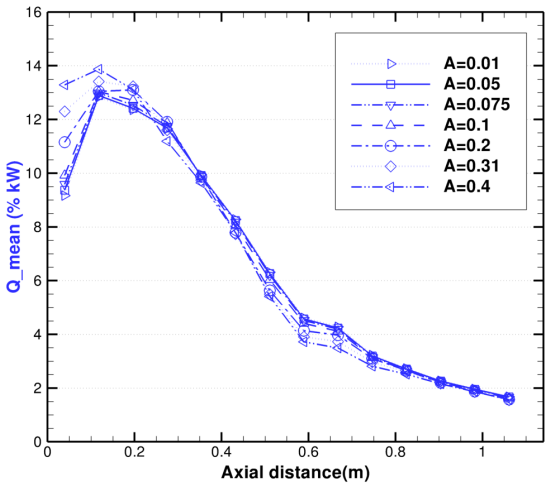

Figure 6.18: Percentage of time-averaged heat release versus axial distance for different forcing amplitudes

For the results presented in this section, the LES predicted flame was divided into 14 uniform axial slices of length $\approx 0.08m$. Coarser discretisations, between 2 and 10 slices were also considered, and an asymptotic behaviour in the FTF calculations was observed (to be described below). The consideration of an axially varying FTF for a single flame has been previously explored experimentally [94, 203], analytically [198] and numerically [94, 98].

The forcing amplitudes employed varied between A=0.01 and A=0.4. Figure 6.19 shows instantaneous progress variable contours on the combustor vertical symmetry plane for the unforced case and forced cases at different amplitudes at a phase angle of $\pi/2$ relative to the reference signal (the inflow mass flow rate). At this phase, the mass

flow rate at the dump plane reaches its maximum value. As A increases, the flame surface at this point in the cycle becomes progressively more distorted, and changes from a cylindrical to a triangular shape, together with consequent shortening of the central cold unburnt flow zone. In addition, a vortex roll-up starts to become visible beyond an amplitude of A=0.2, although some evidence is already noticeable for A=0.1. This roll-up process becomes more vigorous as A increases, and has the immediate consequence of transporting fresh cold mixture from the central core into the corner region, which notably decreases the temperature in that zone and in the vicinity of the upper and lower walls, as can be seen in Figure 6.19. No significant change in flame pattern is observed in the forced case at A=0.01 with respect to the unforced case, except for a slightly increased waviness of the flame front. Similarly, forced cases at amplitudes A=0.31 and A=0.4 exhibit virtually identical counter-rotating vortices and flame shape, except for the complete downstream detachment of a pocket of fresh gases which occurs at the highest amplitude. These pictures supply evidence which supports the idea that the vortex roll-up process is the main mechanism introducing nonlinear effects and hence saturation: (i) it causes a shortening of the flame, with an associated nonlinear reduction in flame area and thus in heat release rate; (ii) a thickening of the flame front is also observed and the increased macroscopic mixing provokes a decrease of temperature in the whole combustor with consequent decrease in maximum heat release achieved. Thus, nonlinear effects are expected to be noticeable beyond an amplitude of A=0.2. The mechanism of saturation taking place in the ORACLES combustor was as that explained in [117], thus due to the formation of large pockets of unburnt gases occupying the central part of the combustor, these slowing down the combustion rate and modifying the flame response to perturbation. This formation of large cold pockets of gas is obviously a direct consequence of the roll-up process, since the increased backflow near the step corners widens the flame front and also decreases the momentum in the streamwise direction, all with a resultant enlargement of the central region of unburnt gases.

Figures 6.20-6.27 show c-isosurfaces ($c = 0.5$) for the same range of forcing amplitudes at a phase angle of $\pi/2$ relative to the reference signal. The change in flame shape observed in the 2D images of Figure 6.19 is confirmed in these 3D visualisations, with a clear shortening and also progressive transition from a cylindrical to a triangular shape. The vortex roll-up process is clearly visible. In addition, increased interaction with the wall (not shown in Figure 6.19) is observed, starting at amplitude A=0.2 and becoming more noticeable for amplitudes A=0.31 and 0.4.

In terms of FTF calculations, LES results obtained with the smallest amplitude A=0.01 have not been considered in what follows, since the magnitude of the periodic heat release oscillations were only of the same order as the magnitude of the stochastic turbulent oscillations, so that perturbation at the specified frequency of 50Hz was not

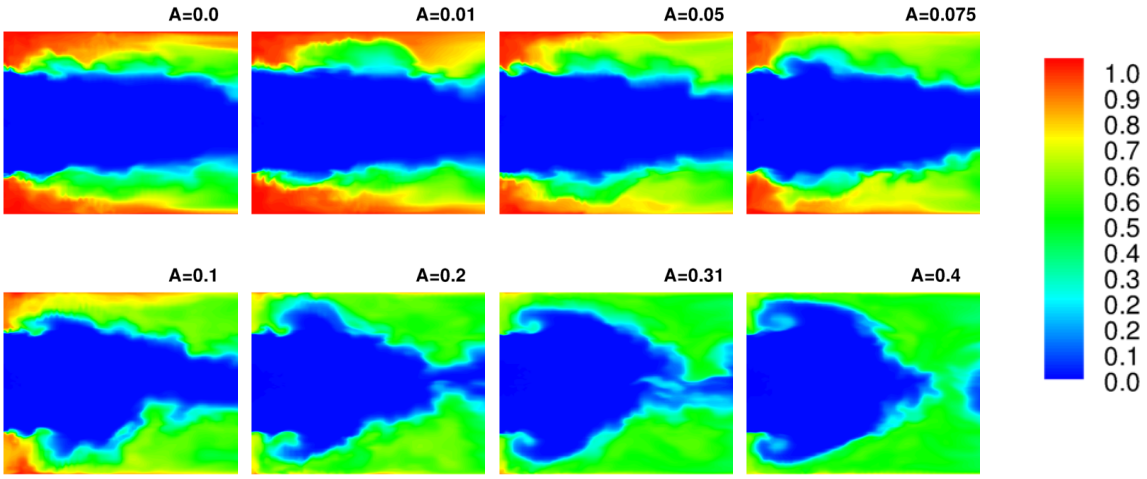

Figure 6.19: Instantaneous progress variable contours for unforced case and forced cases at a phase of $\pi/2$ relative to the reference signal for forcing amplitudes A=0.01, 0.05, 0.075, 0.1, 0.2, 0.31 and 0.4 ($z = 0$ plane, from dump plane to a distance $x = 0.17m$)

discernible above the level of background turbulent fluctuations. Spectra of the fluctuating local heat release (in an axial slice extending from $0.39m$ to $0.47m$ downstream of the dump plane) for all forcing amplitudes are shown in Figure 6.28(a). It can be clearly seen that the higher the amplitude, the more the energy content at 50Hz stands out. Harmonics are also visible, especially for amplitudes A=0.31 and 0.4. The increasing amplitude of harmonics at high forcing frequencies is considered to be further evidence of nonlinearity. Time-series of the fluctuating heat release rate for both the unforced and the forced case at A=0.01 are displayed in Figures 6.28(b) and 6.28(c), for the same axial slice as used in Figure 6.28(a). No coherent motion at 50Hz is apparent, therefore no valid information (i.e. no FTF) at that frequency could be extracted.

To further demonstrate that no valid coherent motion at 50Hz could be extracted for A=0.01, a coherence factor was used, defined as:

$$\gamma_{sr}(f) = \frac{|P_{sr}(f)|}{\sqrt{P_{ss}(f)P_{rr}(f)}} \tag{6.28}$$

where $P_{sr}(f)$, $P_{ss}(f)$ and $P_{rr}(f)$ denote the signal (mass flow rate)-response (heat release) cross-spectrum, the signal power spectrum and the response power spectrum, respectively. This factor may be used to identify the degree of coherence between signal and response oscillations at a specific frequency, and it ranges from 0 to 1, with 0 indicating no coherence and 1 complete coherence. Also, $\gamma_{sr}(f)$ indicates whether meaningful transfer function data can be obtained from signal and response oscilla-

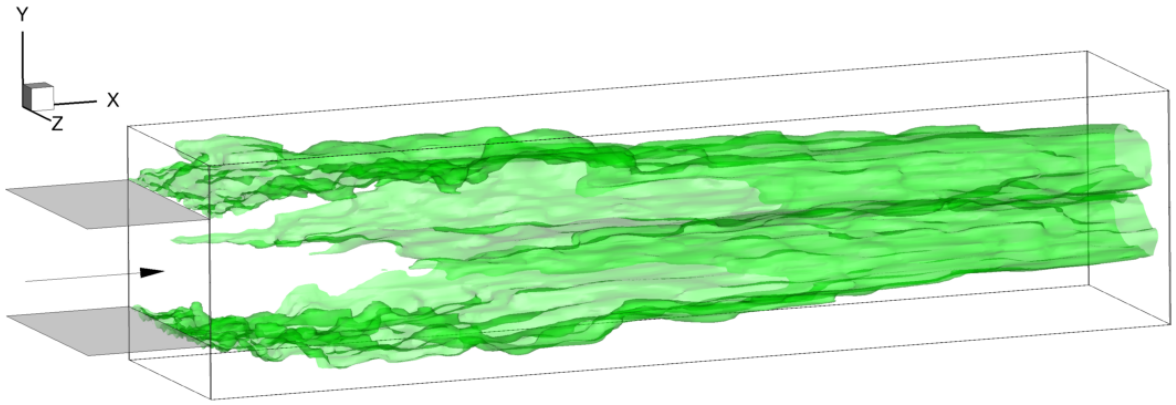

Figure 6.20: Flame shape visualised by instantaneous c-isosurfaces ($c = 0.5$) for unforced case c_2

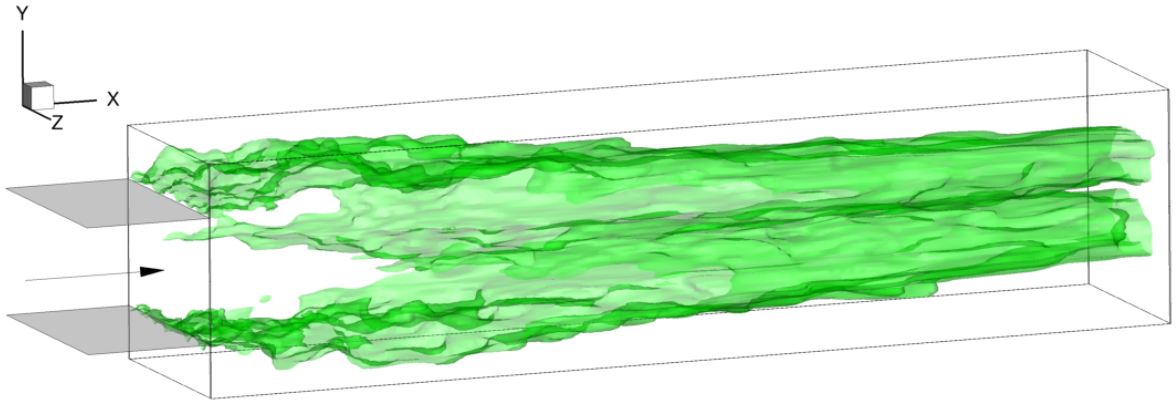

Figure 6.21: Flame shape visualised by instantaneous c-isosurfaces ($c = 0.5$) for forced case c_2 at phase $\psi = \pi/2$ and amplitude A=0.01

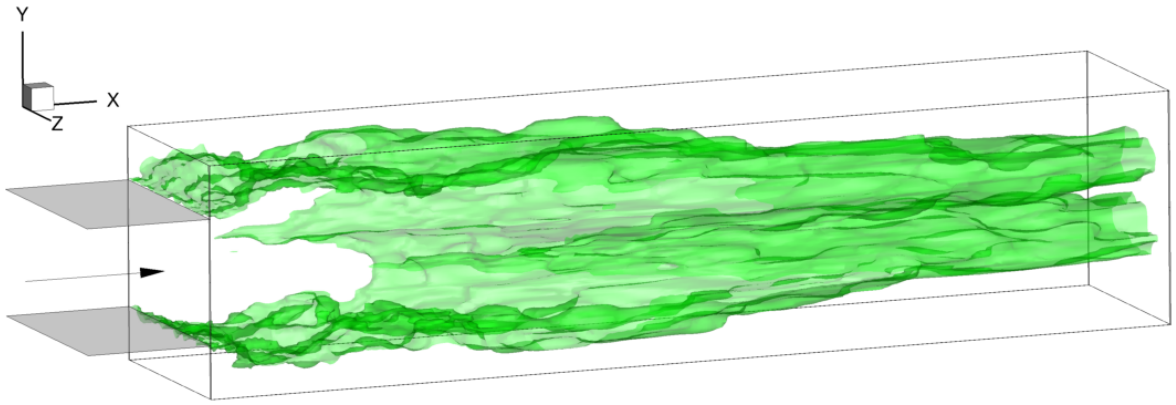

Figure 6.22: Flame shape visualised by instantaneous c-isosurfaces ($c = 0.5$) for forced case c_2 at phase $\psi = \pi/2$ and amplitude A=0.05

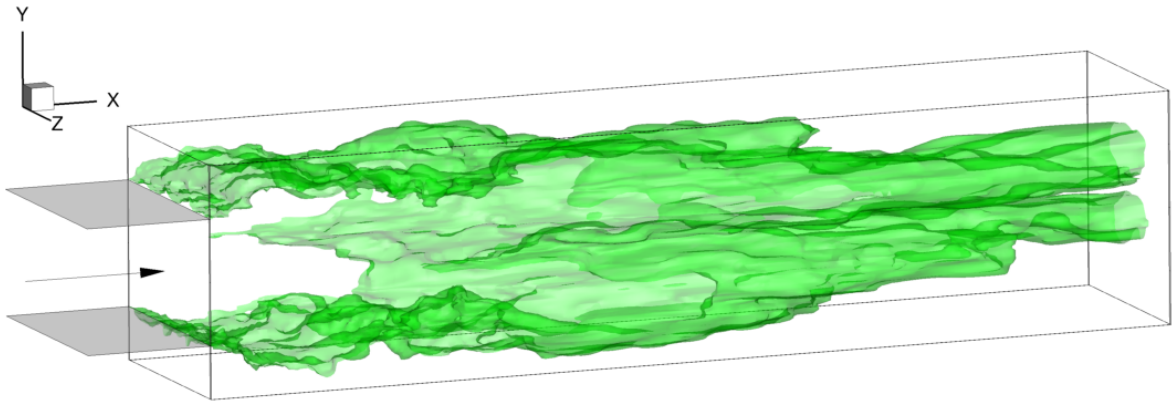

Figure 6.23: Flame shape visualised by instantaneous c-isosurfaces ($c = 0.5$) for forced case c_2 at phase $\psi = \pi/2$ and amplitude A=0.075

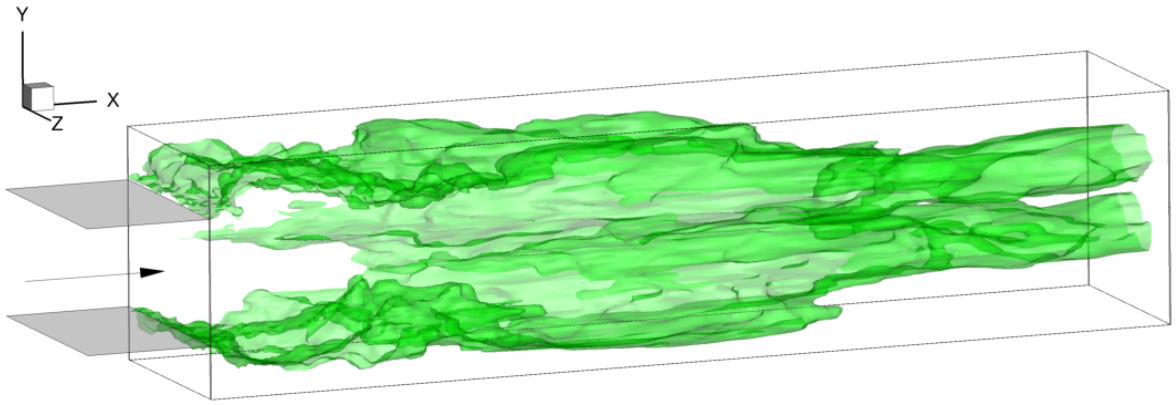

Figure 6.24: Flame shape visualised by instantaneous c-isosurfaces ($c = 0.5$) for forced case c_2 at phase $\psi = \pi/2$ and amplitude A=0.1

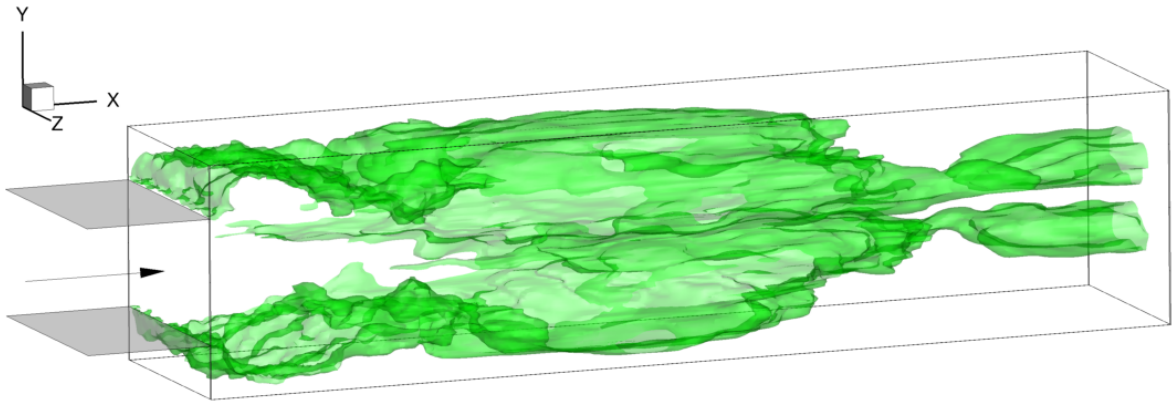

Figure 6.25: Flame shape visualised by instantaneous c-isosurfaces ($c = 0.5$) for forced case c_2 at phase $\psi = \pi/2$ and amplitude A=0.2

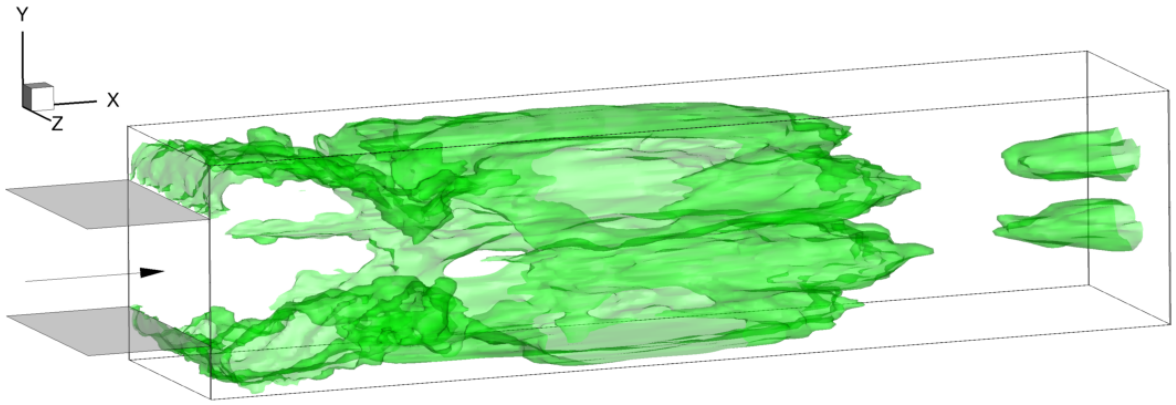

Figure 6.26: Flame shape visualised by instantaneous c-isosurfaces ($c = 0.5$) for forced case c_2 at phase $\psi = \pi/2$ and amplitude A=0.31

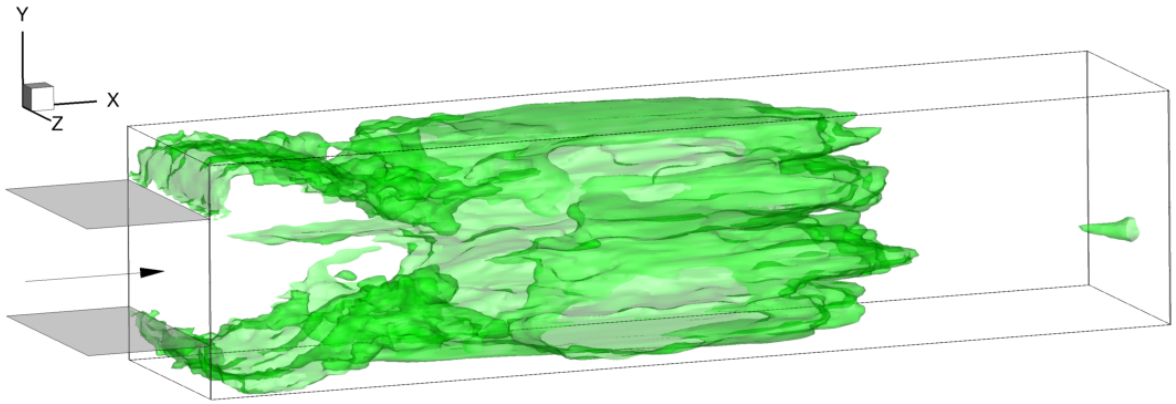

Figure 6.27: Flame shape visualised by instantaneous c-isosurfaces ($c = 0.5$) for forced case c_2 at phase $\psi = \pi/2$ and amplitude A=0.4

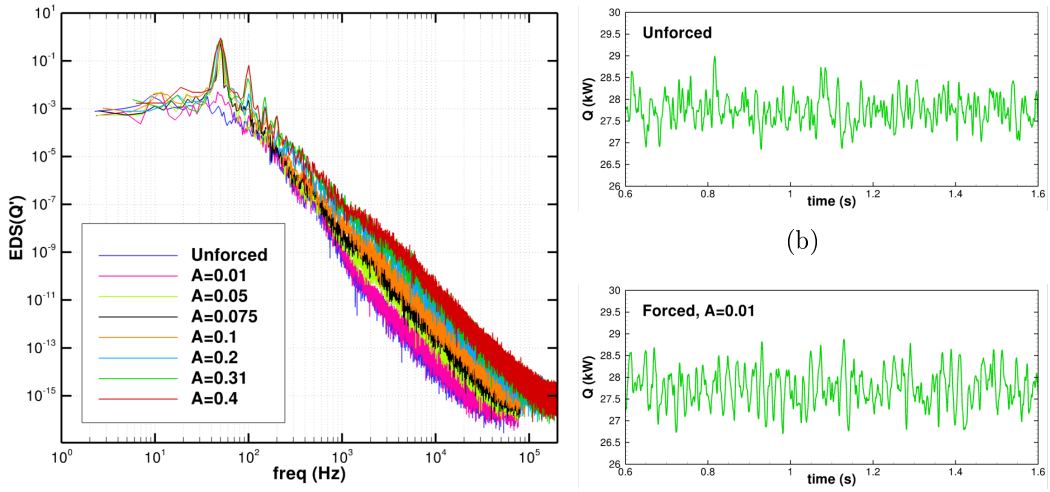

Figure 6.28: (a) Spectra of fluctuating heat release rate at point in flame front region for different forcing amplitudes; time-series of local heat release rate for slice centred at $0.42m$ downstream of the dump plane for (b) unforced case and (c) forced case with A=0.01

tions. Figure 6.29 shows coherence factors for amplitudes A=0.01, 0.05, 0.1 and 0.4. There is a significant increase in γ_{sr} from amplitude A=0.01 to 0.05, going from values around 0.4 to 0.97. As the amplitude is increased, the coherence factor remains at values larger than 0.97 for frequencies close to 50 Hz for all amplitudes. The use of the coherence factor to ensure validity of the FTF calculation has been previously used in [94, 102].

Using the two methodologies described above (§6.4.3), gains were evaluated. Figure 6.30 shows the axial distribution of the gain deduced from the local heat release FTFs. For these FTF calculations, between 25 and 65 complete acoustic cycles were included in the analysis, to ensure good resolution. For both methodologies, the expected non-linear effects are evident, with gains varying with A, and exhibiting decreasing levels of gain for increasing forcing amplitude. Local gains obtained with A=0.31 and A=0.4 were quite similar, indicating the saturation effect characteristic of a limit cycle. No linear regime, where the gain was independent of forcing amplitude, was seen clearly. Furthermore, for both methods the gain function showed a relatively similar axial dependence. Predicted gains were quite similar for both methods, but the Fourier method seemed to produce smoother distributions. Figures 6.30(c) and 6.30(d) display gain as a function of forcing amplitude for various individual axial slices showing clear decrease in gain with amplitude for all flame slices. In general, both methodologies consistently exhibited a very similar two-peak trend (Figures 6.30 (a) and (b)), with maximum and

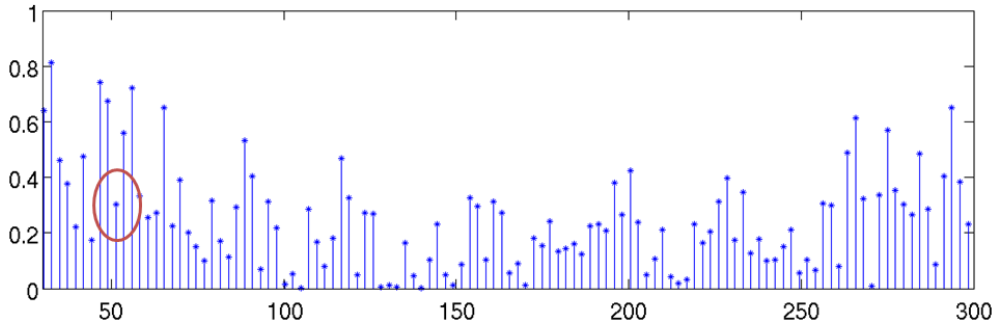

(a)

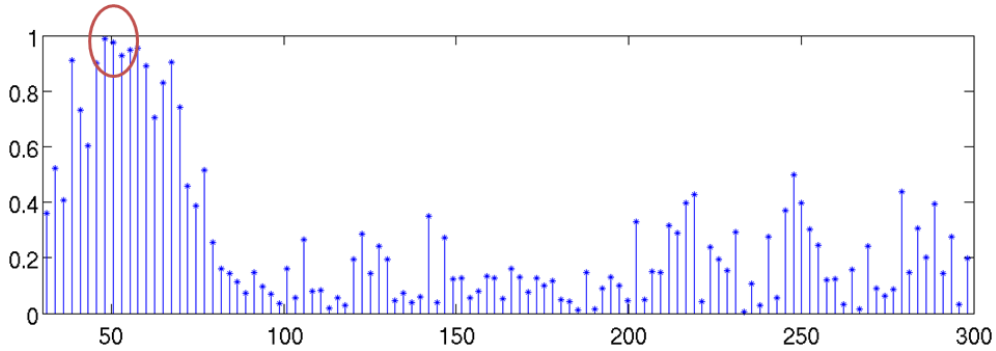

(b)

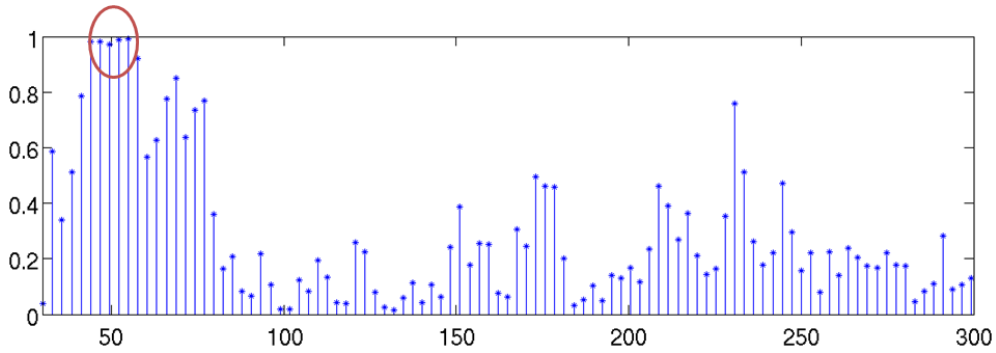

(c)

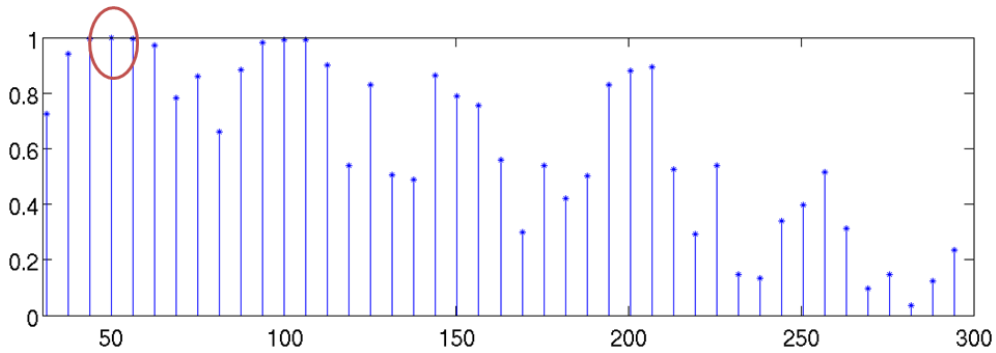

(d)

Figure 6.29: Coherence factor (equation (6.28)) for amplitudes A = 0.01(a), 0.05(b), 0.1(c) and 0.4(d)

minimum values located in roughly the same axial positions (physical interpretation of FTF magnitude and shape will be addressed later). In general, the Fourier analysis method was considered to provide smoother data and will be used from here on.

Local time-delay (or phase) as a function of axial location is plotted in Figure 6.31, for both cycle-averaged and Fourier series methods. A pure convective time-delay is also plotted, calculated from an area-averaged convective velocity $\hat{u}_{s_i}$, evaluated in the central axial position of every axial slice as:

$$\hat{u}_{s_i} = \frac{1}{A\hat{\rho_{s_i}}} \int_A \bar{\rho}\bar{u} dA, \qquad \text{where} \quad \hat{\rho_{s_i}} = \frac{1}{A} \int_A \bar{\rho} dA \tag{6.29}$$

where $\bar{}$ indicates a time-averaged value. It can be seen that for time-delay, the difference between the two methods of analysis is very small. The average slope of the curves is the same for both methods, with a small decrease in the slope in the region $0.25 - 0.55m$. The slope is in very good agreement with that identified from the convective time, with a maximum error of 10% at around $x = 0.4m$. The slope of the curves initially reflects a pure convective time, based on the inflow mean velocity, then the slope decreases and flattens out towards the end. This is because the convective time is reduced due to the increase in bulk velocity, as the flow is accelerated in the downstream region.

6.4.5 Incorporation of the extracted FTFs into LOTAN acoustic network code

In this section a description is presented of the methodology followed to incorporate FTF information extracted from the LES simulations into the thermo-acoustic network model LOTAN. A description is also given of different tests performed to examine accuracy, consistency and robustness of the LES results. First the parameters required from the LES in order to specify an unsteady flame in LOTAN are presented. A check has been carried out to determine the sensitivity to the number of slices chosen and this is also presented, along with an assessment of the consistency between the different flame configuration results. Finally, further interpretation of the axial dependence of the flame response to input velocity perturbations is provided.

As pointed out earlier, the axially extended nature of the ORACLES flame requires a spatially distributed local analysis. This is required to capture the possibility that at different axial positions the relationship of the local unsteady heat release to the inlet acoustic perturbation may be different implying that the response of the flame may change substantially depending on the particular part of the flame considered. According to the Rayleigh criterion [204], there will be some flame regions where heat

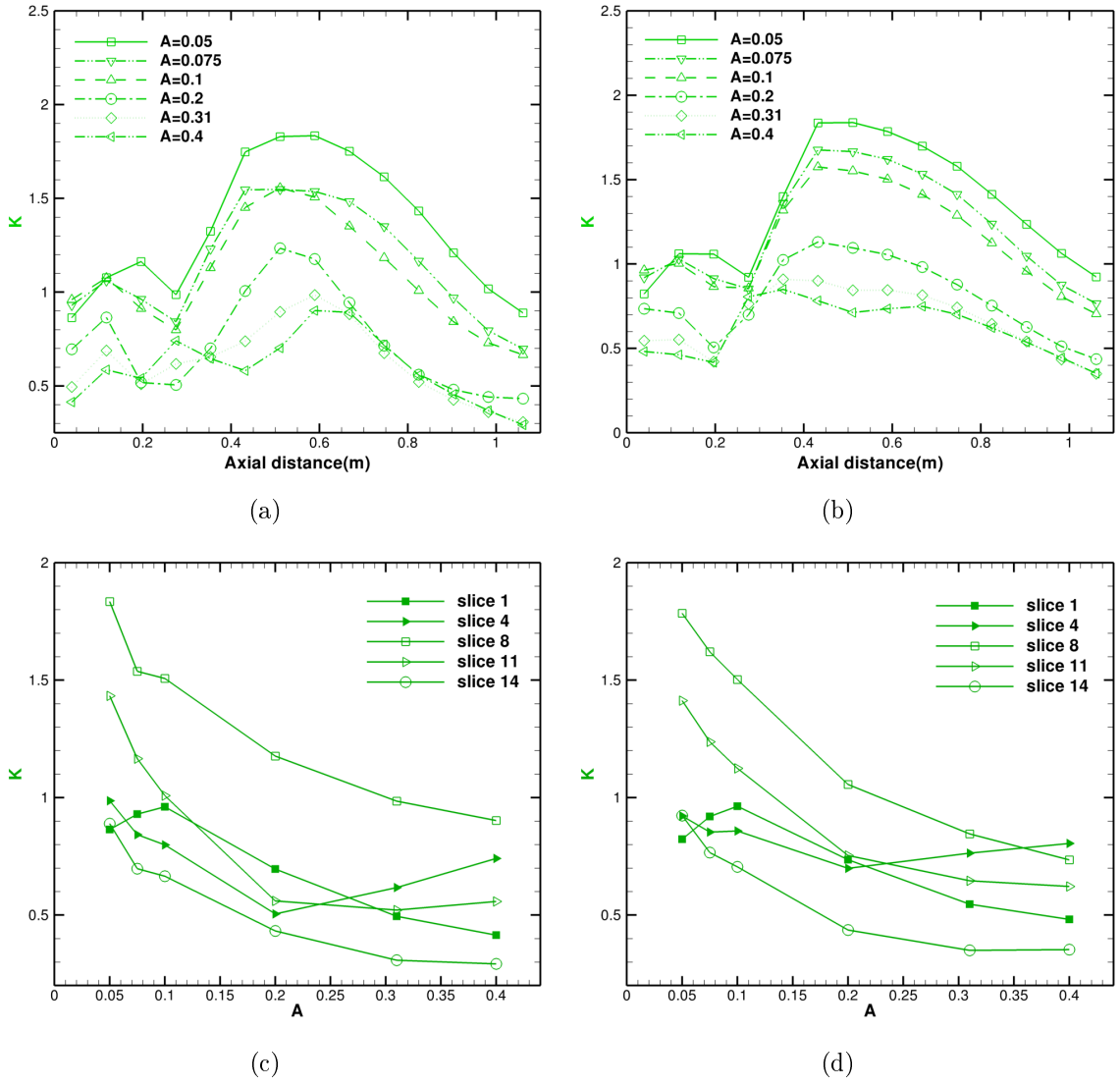

Figure 6.30: Local gain versus axial distance for different forcing amplitudes using (a) cycle-averaging and (b) Fourier analysis methods. Local gains versus forcing amplitude in specified axial slices using (c) cycle-averaging and (d) Fourier analysis methods.

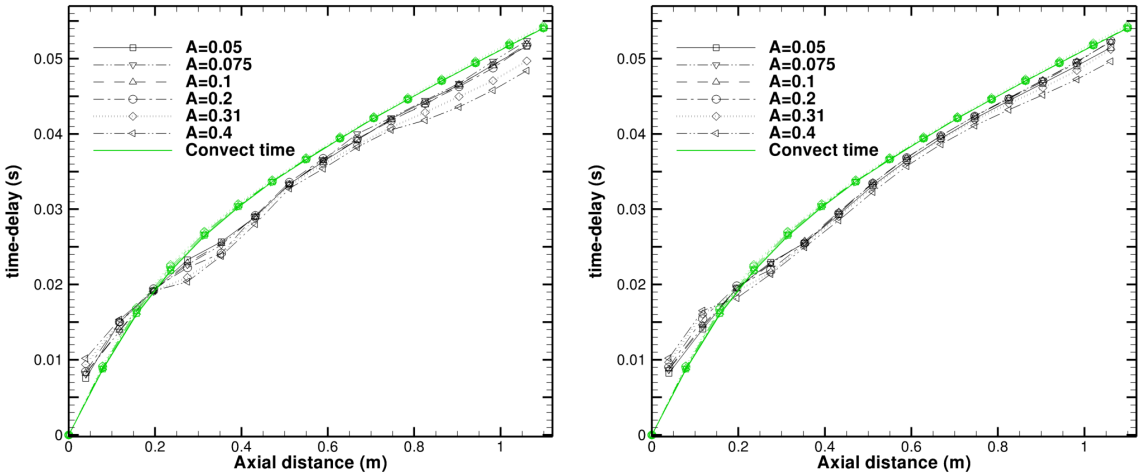

(a) (b)

Figure 6.31: Convective times and local time-delays versus axial distance for different forcing amplitudes using (a) cycle-averaging and (b) Fourier analysis methods

release and acoustic pressure are in phase producing instability amplification, whereas in other regions instability damping will occur. The overall net balance over the entire domain and over time will establish the global flame-acoustic coupling and the ultimate stability of the system.

An acoustic network model of the ORACLES geometry (Figure 5.4(a)) was set up using the LOTAN code [167], as schematically depicted in Figure 6.1. The so-called *time-delay* [205] flame model was utilised in order to model the flame-acoustic interaction. In this model, the local unsteady heat release is described via:

$$\dot{Q}' = |\dot{Q}'|e^{-i2\pi f\tau} = KA\overline{\dot{Q}}e^{-i2\pi f\tau} \tag{6.30}$$

Three parameters are therefore required to specify the unsteady flame model: a mean heat release rate $\overline{\dot{Q}}$, a gain K, and a time-delay τ all obtained from the FTFs described above, extracted from the LES simulations. Local values of the 3 parameters were extracted for each axial flame slice considered.

A study was first carried out to identify the minimum number of axial slices into which the flame had to be divided to capture the unsteady heat release distribution accurately. Different flame configurations were tested, consisting of 1 to 14 uniform length axial flame slices. Larger spatial gradients in the parameters to be captured were expected in the first quarter of the combustor, and hence some nonuniform flame slice

lengths were also investigated, with refinement into shorter slices in this region with flame slice numbers of 6, 8 and 10 flames. Figure 6.32 illustrates schematically the different flame configurations analysed. Local parameters for these flame slice distributions were calculated and input into LOTAN. Figure 6.33 shows LOTAN predictions for frequency and growth rate of the mode closest to 50Hz obtained for the different flame slice configurations. For frequency, as the spatial discretisation increased, the frequency of the mode increased slightly from $\approx 48\ Hz$ to $\approx 51\ Hz$, with slight decrease as forcing amplitude increased: for flame slice numbers greater than around 7 and up to 14 the results did not change. Regarding the growth rate (note: a negative growth rate indicates a stable situation), results for 1, 2, 3 and 4 flames indicated a gradual increment in growth rate towards a less stable situation, the last clustering with results for 6 and 7 flames. Results for 10 and 14 flames are almost coincident. In summary, it is clear that an asymptotic tendency of the predicted curves is observed, with evidence of some improvement with refinement in the first part of the combustor. The 10 and 14 flame slice configurations gave almost identical results suggesting that the 14 flame configuration certainly provided adequate spatial resolution.

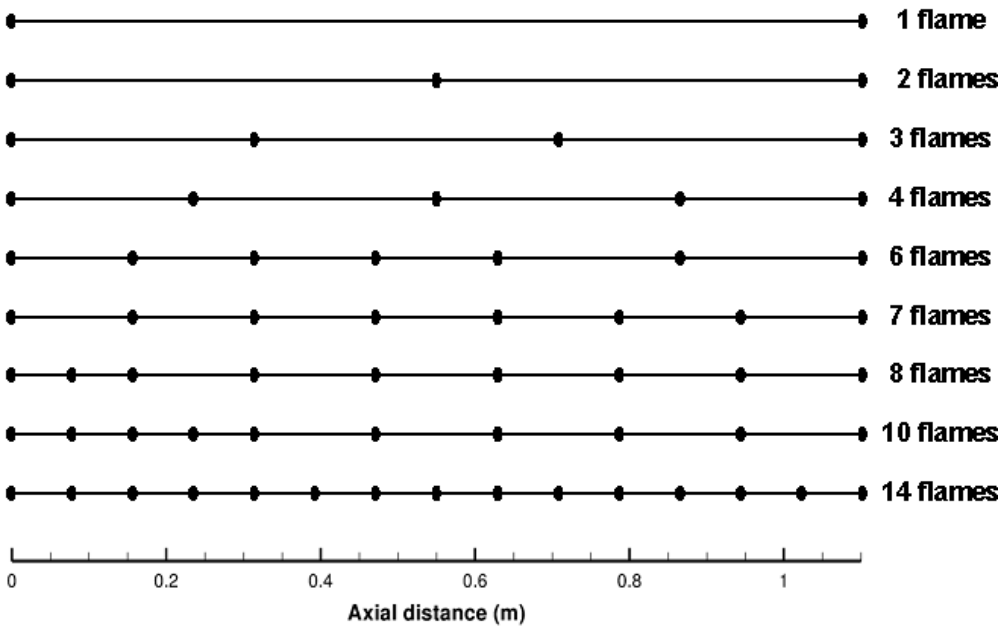

Figure 6.32: Axial slices distribution for different flame configurations

As noted above, for all configurations tested, the predicted growth rate shown in Figure 6.33(b) was negative, indicating the 50 Hz mode (with parameters extracted from the current LES) was predicted as being stable, although a tendency towards instability

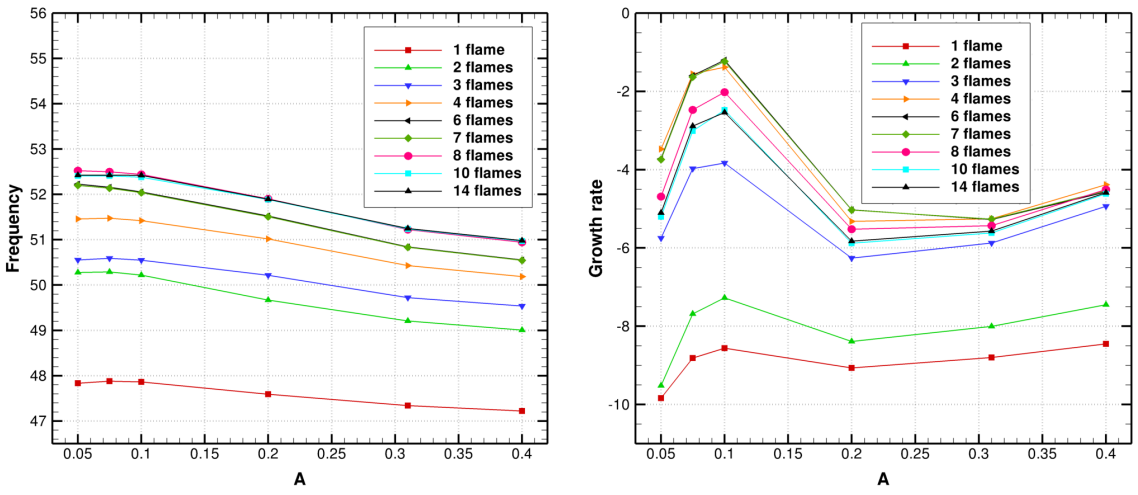

(a) (b)

Figure 6.33: (a) Frequency and (b) growth rate LOTAN predictions for different flame configurations

was observed at an amplitude of A=0.1 and a move towards an unstable state was also evident for higher amplitudes.

During the process of dividing the flame into slices, it was important to ensure that conservation of total heat release in the whole computational domain was maintained. Thus, the summation of mean and fluctuating heat release distributions over the flame slices covering the domain should remain constant:

$$\overline{\dot{Q}} = \sum_{i=1}^{N} \overline{\dot{Q}}_i \qquad \text{and} \tag{6.31}$$

$$\dot{Q}' = \sum_{i=1}^{N} \dot{Q}'_i = \sum_{i=1}^{N} A\overline{\dot{Q}}_i K_i e^{-i2\pi f \tau_i} \quad \forall N = 1, 2, 3, 4, 6, 7, 8, 10 \text{ or } 14 \tag{6.32}$$

where $\overline{\dot{Q}}$ and $\dot{Q}'$ are the mean and fluctuating heat release, respectively, for a 1 flame slice configuration (i.e. directly from the LES calculation) and the subscript i indicates a particular axial slice. This was another reason for choosing the Fourier analysis technique since discrepancies in these summations were obtained when using the cycle-averaging method, whereas the Fourier method errors were very small.

As a final check that the division into 14 flame slices was sufficient to capture all the physics, three finer discretisations were tested, using 17, 20 and 23 slices (see

Figure 6.34). The refinement was concentrated in the region between the dump plane and $x = 0.7m$, since this is where heat release was concentrated. Since the most refined description of the flame response extracted directly from LES corresponded to 14 slices, to avoid further expensive LES calculations it was necessary to devise a valid interpolation procedure to obtain the local parameters $\overline{\dot{Q}}_i$, K_i and τ_i for the 17, 20 and 23 flame configurations. First, local time delays (τ_i's) were computed directly by linear interpolation from the 14 flame configuration results. Secondly, the local mean heat release rates ($\overline{\dot{Q}}_i$'s) were calculated as described below, enforcing mean and fluctuating total heat release rate conservation:

1. $\overline{\dot{Q}}_{i,1}$ and $\overline{\dot{Q}}_{i,2}$ were linearly interpolated, where subscripts 1 and 2 indicate the 2 slices obtained by dividing into 2 any slice of the 14 flames configuration.
2. $\overline{\dot{Q}}_{i,1}/2$ and $\overline{\dot{Q}}_{i,2}/2$, as the heat is now released in half of the volume as it was for $\overline{\dot{Q}}_i$.
3. Finally, an adjustment was applied, in order to ensure that $\overline{\dot{Q}}_i = \overline{\dot{Q}}_{i,1} + \overline{\dot{Q}}_{i,2}$:

$$\overline{\dot{Q}}_{i,1} = \overline{\dot{Q}}_{i,1} \frac{\overline{\dot{Q}}_i}{\overline{\dot{Q}}_{i,1} + \overline{\dot{Q}}_{i,2}} \qquad \text{and} \qquad \overline{\dot{Q}}_{i,2} = \overline{\dot{Q}}_{i,2} \frac{\overline{\dot{Q}}_i}{\overline{\dot{Q}}_{i,1} + \overline{\dot{Q}}_{i,2}} \tag{6.33}$$

In addition, once mean heat releases and time-delay had been calculated, gains $K_{i,1}$ and $K_{i,2}$ in a specific slice i were determined in order to enforce fluctuating heat release conservation, thus

$$\dot{Q}'_i = \dot{Q}'_{i,1} + \dot{Q}'_{i,2} \tag{6.34}$$

This ensures that the fluctuating heat release in the whole domain will be also conserved. Fluctuating heat release is a complex valued quantity, therefore the following system of equations was solved to obtain $K_{i,1}$ and $K_{i,2}$:

$$\Re(\dot{Q}'_i) = \Re(\dot{Q}'_{i,1}) + \Re(\dot{Q}'_{i,2}) = A\overline{\dot{Q}}_{i,1} K_{i,1} \cos(2\pi f \tau_{i,1}) + A\overline{\dot{Q}}_{i,2} K_{i,2} \cos(2\pi f \tau_{i,2}) \tag{6.35}$$

$$\Im(\dot{Q}'_i) = \Im(\dot{Q}'_{i,1}) + \Im(\dot{Q}'_{i,2}) = A\overline{\dot{Q}}_{i,1} K_{i,1} \sin(2\pi f \tau_{i,1}) + A\overline{\dot{Q}}_{i,2} K_{i,2} \sin(2\pi f \tau_{i,2}) \tag{6.36}$$

Figure 6.35 shows the frequencies and growth rates predicted by LOTAN for these finer flame discretisations. This clearly demonstrated that further refinement had little effect and the 14 flame slice configuration could be used with confidence.

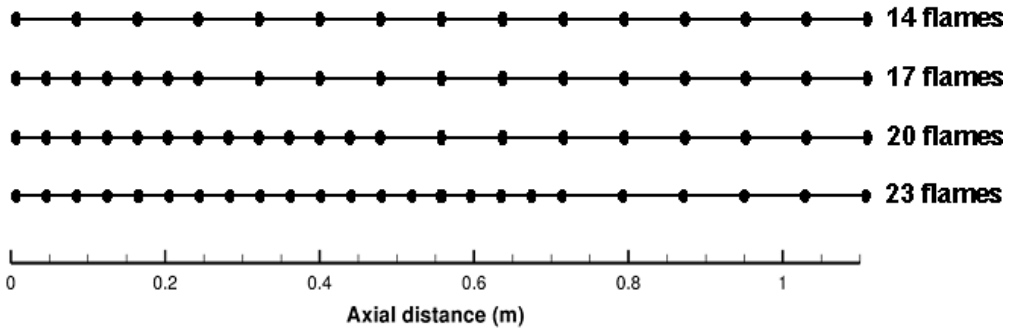

Figure 6.34: Axial slices distribution for different flame configurations

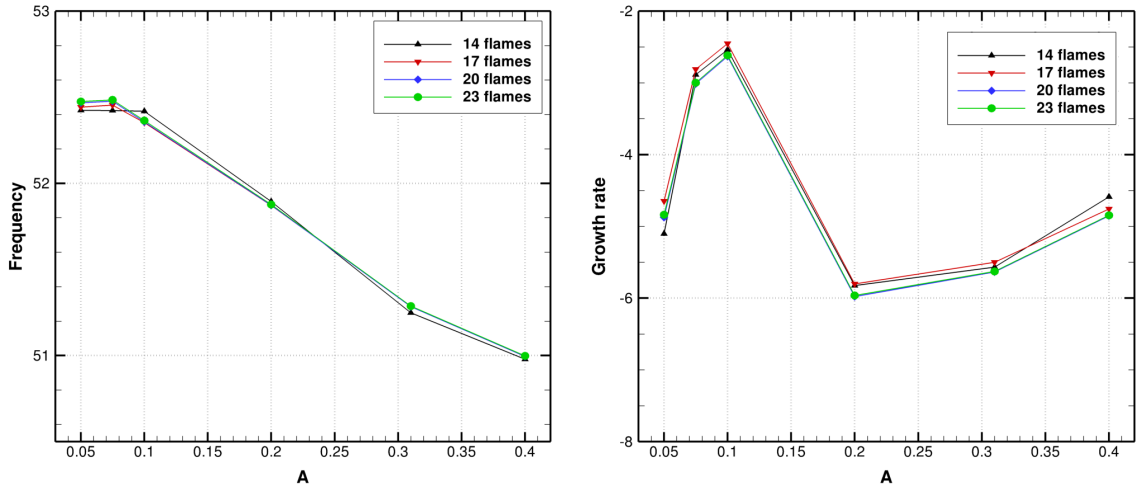

(a) (b)

Figure 6.35: (a) Frequency and (b) growth rate LOTAN predictions for different flame configurations

In the previous section, the axial dependence of the parameters $\overline{\dot{Q}}$, K, and τ was identified as characterising the flame response. An estimation of the contribution (damping or exciting) of each individual flame slice to the global acoustic energy balance was then carried out to understand better the detailed nature of this overall flame description. A LOTAN calculation was first carried out in which only the steady heat release in each of the flame slices in the network was considered (no fluctuating component). This LOTAN prediction identified a stable 50Hz mode, and the magnitude of the (negative) growth rate was noted (GR_{st}). Following this, the unsteady heat release in each flame slice was individually "switched on", using the time-delay model with parameters from

a forced LES with A=0.31. For every flame slice i that was activated in this way, a growth rate prediction, GR_i was identified from LOTAN. To obtain a relative growth rate representing the effect of each particular flame slice nature (increasing or decreasing the steady state stability) GR_i was subtracted from GR_{st}. Figure 6.36 shows the phase and relative growth rates versus axial distance which result from this analysis. Very similar patterns were observed for other forcing amplitudes. The blue dashed lines indicate axial locations where the phase is approximately 0.01s, or $\pi\ rad$. According to equation (6.30), this produces a negative minimum in the unsteady heat release and a potential region for acoustic damping (mass flow and heat release are out of phase). Likewise, the red dashed lines correspond to a phase of 0.02s or $2\pi\ rad$, which implies a positive and maximum value of the unsteady heat release and thus a potential for excitation (mass flow and heat release in phase). Figure 6.36 also shows the relative growth rates obtained; positive and negative values may be interpreted as contribution of the local unsteady heat release to the stability of the mode (more unstable or stable, respectively). Figure 6.36 therefore identifies the regions which either amplify or damp the acoustic feedback. These data indicate that it is the first $0.6m$ of flame length which has the largest effect; further downstream the contribution to changing stability is overall small and neutral. This is to be expected, since the magnitude of the unsteady heat release reaches a maximum at around $x = 0.1m$ and then decreases exponentially with axial distance, as shown in Figure 6.18. This supports the decision above to carry out extra refinement in the upstream region of the combustor duct.

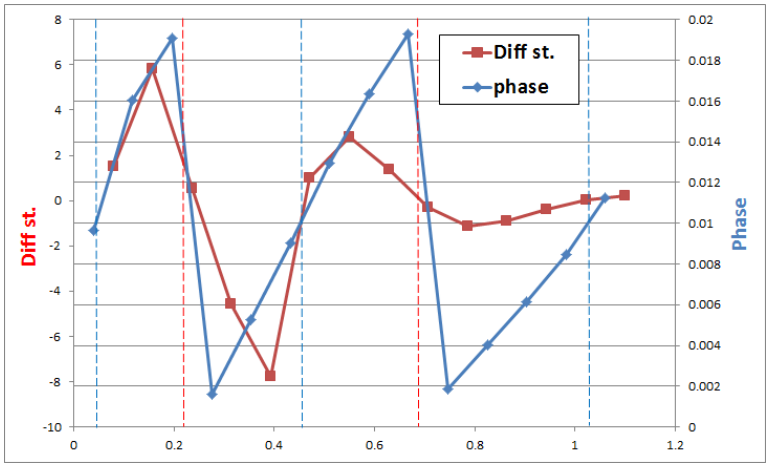

Figure 6.36: Phase and relative growth rate versus axial distance using the Fourier analysis method

Based on the above analysis, the flame zone up to $x \approx 0.2m$ seems to make the largest contribution to instability; a second destabilising zone occurs at $x \approx 0.5m$, correspond-

ing to the location where flame wall interaction takes place. In between these regions, a zone of strong damping is present. It is rather disappointing to see that this first attempt at LES-derived FTF/acoustic analysis does not display strong evidence of flame instability or limit cycle behaviour. Of course, only a chosen value of β has been explored and the sensitivity to varying this was examined next.

6.5 Sensitivity to variations in the FSD combustion model and parameter (β)

The current combustion model of Boger et al. [57] was modified by changing the model constant β. Also, an alternative FSD combustion model proposed by Chakraborty and Klein [73] was implemented and analysed. For the sake of simplicity, hereafter the results from the combustion model of Boger et al. are referred to as BOGER0-2, BOGER0-3 or BOGER0-4 (for values of β=0.2, 0.3 and 0.4) and results from the model of Chakraborty and Klein are designated as CHAKRABORTY.

6.5.1 BOGER0-2, BOGER0-3 and BOGER0-4 models

A detailed description of the Boger et al. model has been given in §2.3.5.3. In the present section, attention is focused only on the sensitivity of predictions to the value chosen for the model parameter β.

As pointed out earlier, for the ORACLES experiments, assessment of sensitivity to the β parameter can only be carried out using velocity and turbulence measurements, since no species or temperature data were provided. The axial velocity exhibits streamwise flow acceleration induced by the heat release, and the extent of acceleration predicted can be used as a measure of combustion model performance. $\beta = 0.2$ has been used for the LES results presented so far; however, the flow acceleration obtained with this value was observed to underpredict the measured data (see transverse profiles of $\overline{u}$ in Figure 6.11) and thus two larger values, β=0.3 and 0.4, were considered. Larger values will increase the flame front displacement term, with a consequent increase in heat release rate and hence induced axial flow acceleration.

6.5.2 CHAKRABORTY model

Chakraborty and Klein [73] have proposed an alternative power-law based algebraic FSD model in the context of combusting LES. It was based on two sets of DNS

databases of freely propagating statistically planar turbulent premixed flames, with similar turbulent Reynolds number Re_t and varying rms turbulent velocity fluctuation to unstrained laminar flame speed ratio, u'/s_l, integral length scale to laminar flame thickness ratio, l_t/δ_l^0, and heat release parameter, τ. One flame belongs to the corrugated flamelet (CF) regime and the other to the thin reaction zone (TRZ) regime. By explicitly LES filtering the DNS databases, expressions for fractal dimension D and inner cut-off η_i were proposed:

$$D = 2 + \frac{1}{3}\, erf(2Ka) \tag{6.37}$$

$$\eta_i = \left[0.345Ka^{-2}e^{-Ka} + 6.41Ka^{-1/2}\left(1 - e^{-Ka}\right)\right]\delta_l^0 \tag{6.38}$$

where Ka is the Karlovitz number and δ_l^0 stands for the Zel'dovich or diffusive flame thickness. According to the formulation of a generalised FSD, Σ_{gen}, first proposed by Boger et al. [57] , and the expression Σ_{gen} in terms of D proposed by Gouldin et al. [206], Chakraborty and Klein then proposed a new model:

$$\Sigma_{gen} = |\nabla \overline{c}| \left[e^{-\Theta\Delta/\eta_i} + (1 - fe^{-\Theta\Delta/\eta_i})(\Delta/\eta_i)^{D-2}\right] \tag{6.39}$$

where model constants $\Theta = 0.26$ and $f = 2.5$ were chosen.

The model represented in equations (6.37), (6.38) and (6.39) was designed to fulfil the following criteria:

(1) The volume averaged FSD $\langle \Sigma_{gen} \rangle$ should not change with any change in filter width because the total flame surface area remains unchanged irrespective of the value of Δ

(2) The model should be valid in both CF and TRZ regimes

(3) $\lim_{\Delta \to 0} \Sigma_{gen} = \lim_{\Delta \to 0} \overline{|\nabla c|} = |\nabla c|$ should hold

An extensive comparison of their proposed model with 13 other algebraic FSD models was carried out. The CHAKRABORTY model predicted the DNS deduced FSD with either greater or at least similar accuracy (based on the criteria described above) compared to the other 13 models for both test cases. Despite this good performance of the CHAKRABORTY model, it was noted that further experimental comparison was necessary in order to validate the constants used in the expressions of D and η_i proposed. The model as proposed has therefore been implemented in the present combustion LES code and applied to an ORACLES c_2 flame calculation.

6.5.3 Results

6.5.3.1 Progress variable and flow field results

Figure 6.37 plots contours of mean streamwise velocity in plane $z = 0$ for all combustion models analysed for a forced flame with $A = 0.31$. By comparing the first 3 rows the effect of increasing the β parameter may be assessed. BOGER0-3 shows an appreciable difference with respect to BOGER0-2, with increased flow acceleration. This is accompanied by a shortening of the two corner recirculation zones, with a length of $2.31h$ for both upper and lower zones, matching well with the $2.3h$ observed in experimental data [82] and improving on the value $2.5h$ obtained with $\beta = 0.2$. There is a clear increase in the local magnitude of $\overline{u}$, especially from $x \approx 0.3m$ downstream. On the third row, the calculation with $\beta = 0.4$ is presented. The same tendency of increased flow acceleration is again shown. However, recirculation zones are now shorter ($2.10h$) than the experimental value of $2.3h$. The general flow pattern remains otherwise the same as in the two previous cases. In the bottom row, contours from the model CHAKRABORTY are given. This shows a significant decrease in flow acceleration. Longer recirculation zones ($2.7h$) are obtained. The most dramatic feature is the change in flow structure: no multiple accelerated burnt gas features can be seen compared to all the BOGER model predictions.

Instantaneous contours of the progress variable, at a phase $\psi = \pi/2$ relative to the reference signal, are presented in Figure 6.38 for all models. Results using β=0.3 in Figure 6.38 show a clear increase in the rate that the progress variable moves towards 1 in the computational domain, relative to the β=0.2 results, consistent with the increased acceleration observed in the previous figure. This is especially visible in the step region, where a greater volume of fully burnt gases is now observed and also in the second half of the domain. Furthermore, the flame front (represented by the c-isosurface $c = 0.5$) is considerably reduced in extent in the region from $x = 0.1 - 0.4m$, with a consequent reduction of the interaction of the flame with upper and lower walls. In addition, no secondary or detached flame front is obtained in the second half of the combustor. On the third row, contours obtained from model BOGER0-4 are presented and the changes continue to follow the trend observed in the velocity field as β is increased. In the step region, an even larger region of fully burnt gases is observed, and increased c magnitude values are visible near $x \approx 0.15m$ compared to the BOGER0-3 combustion model. The c-isosurface ($c = 0.5$) is very similar to that obtained with $\beta = 0.3$, although the region within this isosurface is slightly reduced. Contours of instantaneous progress variable obtained with the model CHAKRABORTY are plotted in the bottom row. As might be expected the region of gases with $c < 0.5$ covers a much larger extent compared to all BOGER model results, with a long flame front which interacts strongly with upper and lower walls and extends up to the domain exit plane. There is a noticeably different spatial structure with pockets of unburnt gases being

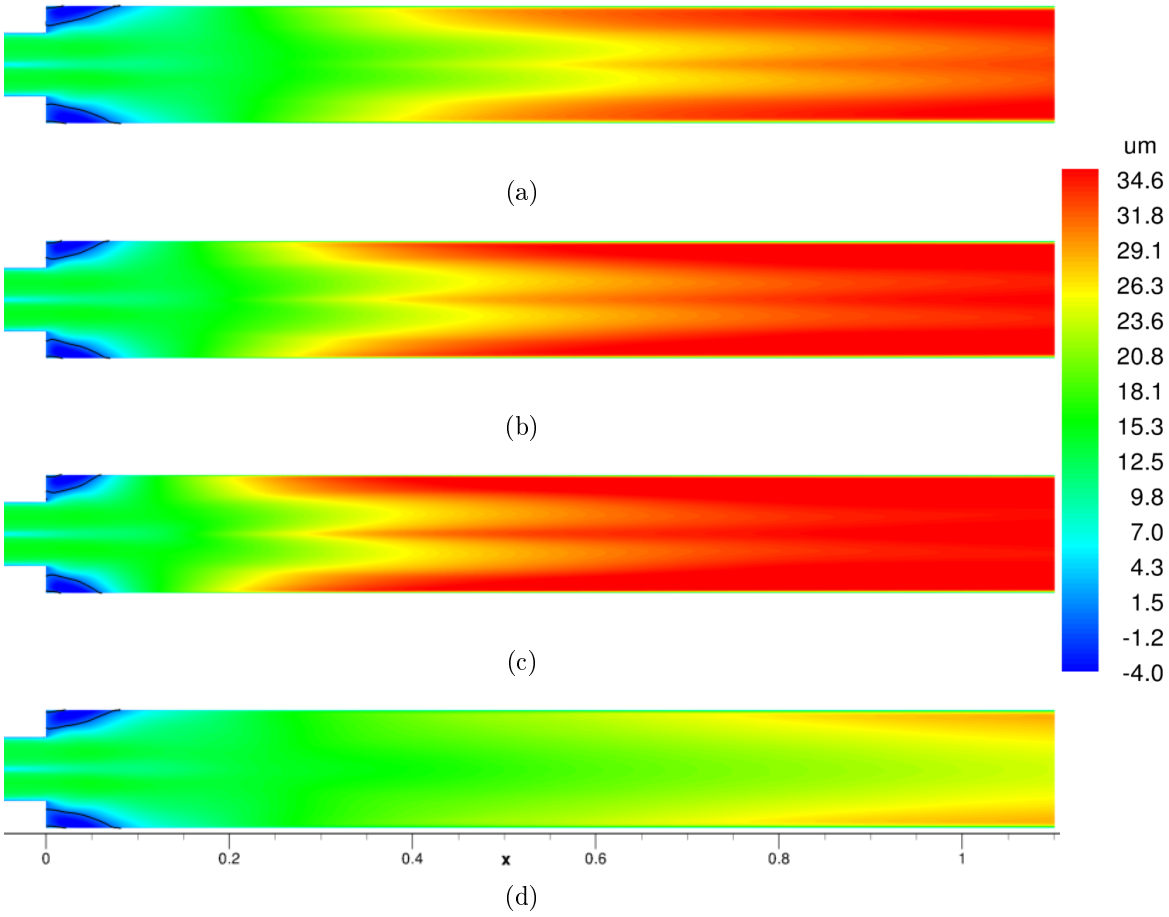

Figure 6.37: Mean streamwise velocity contours in plane $z = 0$ for forced case c_2 (A=0.31) using BOGER0-2 (a), BOGER0-3 (b) , BOGER0-4 (c) and CHAKRABORTY (d) models. Black line indicates $\overline{u}$-isosurface ($\overline{u} = 0$)

convected downstream, progressively being consumed as they approach the combustor exit. The region of fully burnt gases is located only in a thin layer parallel to upper and lower walls. Finally, the differences noted above are reflected in the values of global heat release rate achieved by the end of the domain. For BOGER0-2, the value computed was $257.5kW$, whereas BOGER0-3 displayed the larger value of $273.9kW$ and BOGER0-4 as large as $278.51kW$. Not surprisingly, the global heat release obtained for the CHAKRABORTY model was $194.3kW$, far below the value $280kW$ corresponding to complete consumption of the fuel entering the combustor at this flow rate and equivalence ratio. On the basis of these results the CHAKRABORTY model performs very poorly compared to experimental ORACLES data, whereas an increased β value in the BOGER model shows evidence that it might improve velocity predictions over the $\beta = 0.2$ results.

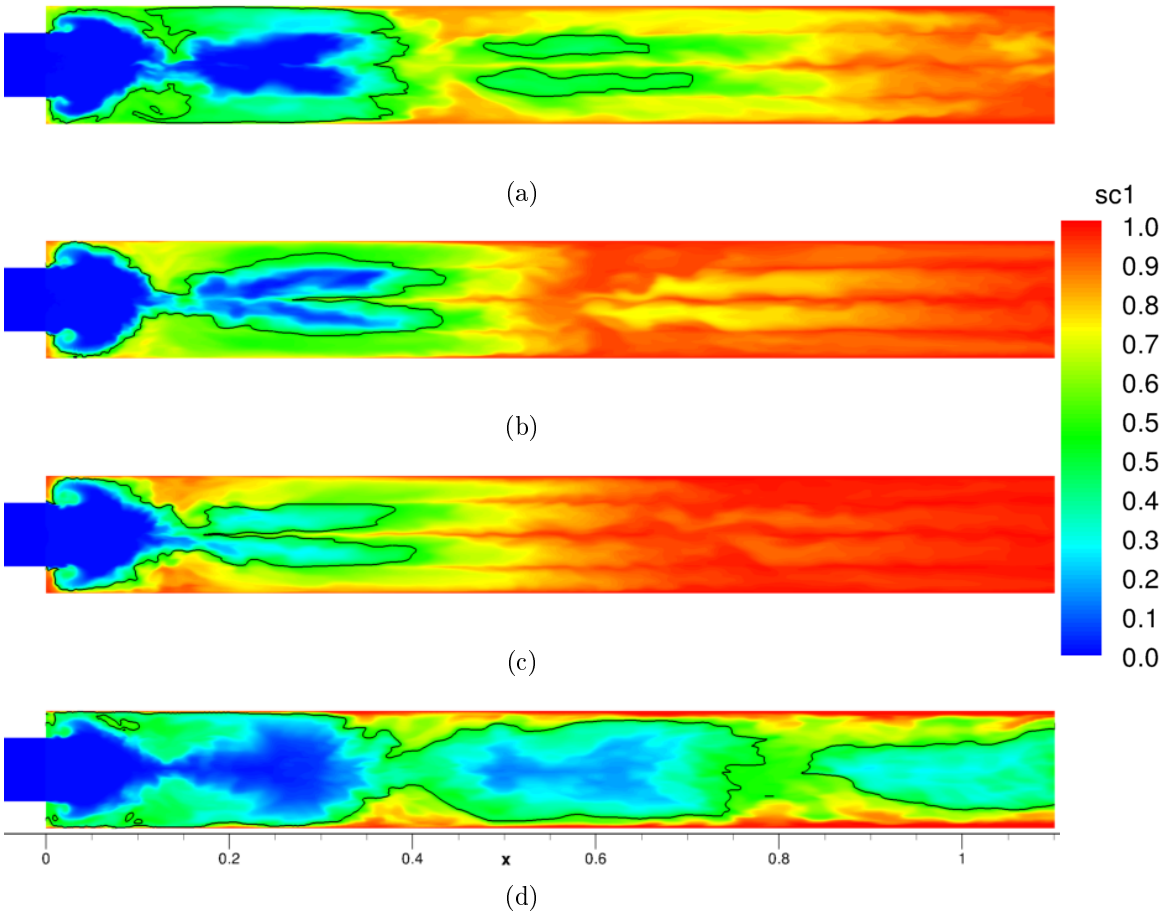

Figure 6.38: Instantaneous progress variable contours in plane $z = 0$ for forced case c_2 (A=0.31), at a phase $\psi = \pi/2$ relative to the reference signal, using BOGER0-2 (a), BOGER0-3 (b), BOGER0-4 (c) and CHAKRABORTY (d) models. Black line indicates c-isosurface (c=0.5)

As a final quantitative assessment of the four combustion models, transverse profiles of mean and fluctuating streamwise and transverse velocities from LES simulations and experimental measurements are compared in Figures 6.39-6.42.

The most noticeable difference between the four models is observed in the profiles of mean streamwise velocity in Figure 6.39. It is best identified in the profiles for $x/h \geq 7$. Thus, at positions $x/h = 7$ and downstream the magnitude of $\overline{u}$ is well predicted by results from BOGER0-3, whereas it is underpredicted by models CHAKRABORTY and BOGER0-2, and overpredicted by BOGER0-4. The CHAKRABORTY model clearly performs worst of all models explored.

The profiles of mean transverse velocity in Figure 6.40 shows profiles which differ less than for $\overline{u}$, but overall it is still BOGER0-3 that shows best performance.

Fluctuating rms velocity profiles are displayed in Figures 6.41 and 6.42. For u_{rms}, results for all four models are very similar in magnitude and in shape. Similarly, little difference is observed in the transverse rms as the combustion model is altered; the early ($x/h < 4$) profiles of the BOGER0-4 model show larger overprediction for u_{rms}. In general once again BOGER0-3 performs best when the whole combustor duct domain is considered.

Finally, Figure 6.43 shows the axial distribution of the LES predicted percentage of mean heat release corresponding to the four combustion models. For BOGER0-3 and BOGER0-4, the shape described by the corresponding curves is very similar to that obtained with BOGER0-2, with a local maximum located at axial distance $x = 0.12m$ and exponentially decreasing downstream. The main difference between these three results is the peak value and the heat release in the first $0.3m$ of combustor duct. The maximum value was $\approx 13\%$ of total mean heat release ($280kW$) for BOGER0-2, but increased to 18% for BOGER0-3 and rose again to 23.5% for BOGER0-4. Contrarily, for CHAKRABORTY, the curve shows a maximum value immediately after the expansion plane with a peak of just $\approx 12\%$. For all four models the percentage of mean heat release is almost coincident for all forcing amplitudes analysed for $x \geq 0.1$, whereas it varies considerably for $x < 0.1$, with a gradual increase of up to 4% as the forcing amplitude is raised. The reason for these amplitude differences is clearly the change in predicted strength of the counter-rotating vortices in the early part of the duct which enhance turbulence and increase the combustion rate. The strength of this roll-up process and the resulting compactness of the flame determines the axial distribution. In general, throughout the combustor length, results from the CHAKRABORTY model show a much lower level of local mean heat release, especially in the first half of the combustor up to $x = 0.5m$. Given the poor performance of the CHAKRABORTY model in the velocity/turbulence comparison discussed above, and the fact that the overall heat release is so slow in comparison with measurements, it was deemed not worthwhile to process this particular simulation to extract FTF information. Similarly, BOGER0-4 overpredicted the heat release rate and acceleration, so only the BOGER0-2 and BOGER0-3 models are compared.

6.5.3.2 FTF results

The main objective of this section is to assess how the observed variations in the LES solutions brought about by combustion model changes ($\beta = 0.3$ rather than 0.2) influence the extracted FTFs and LOTAN acoustic predictions. LES simulations at

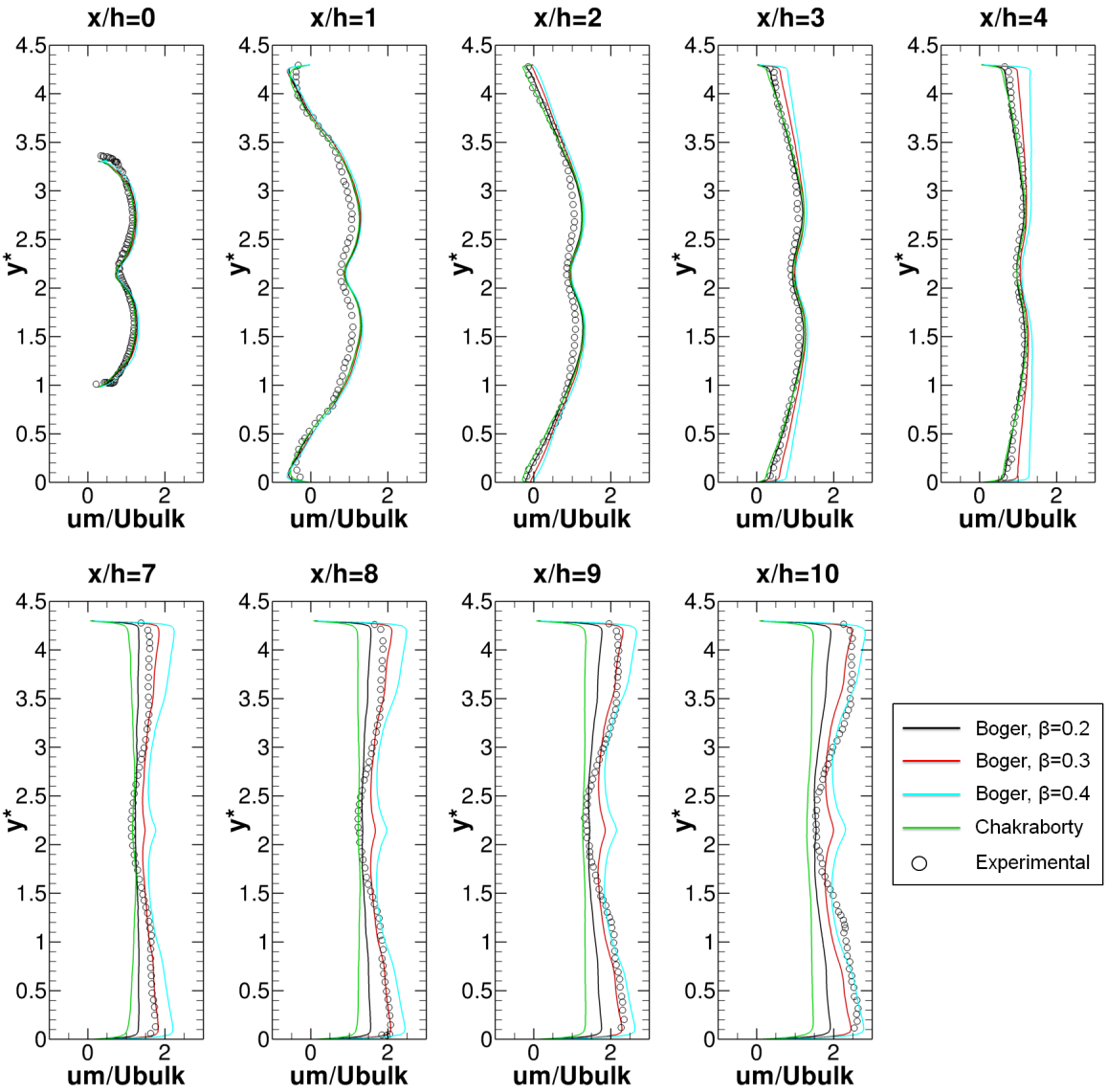

Figure 6.39: Normalised mean streamwise velocity for case c_2 at different axial positions for different combustion models. $U_{bulk} = 11m/s$. Experimental data (o) from Nguyen et al. [82]

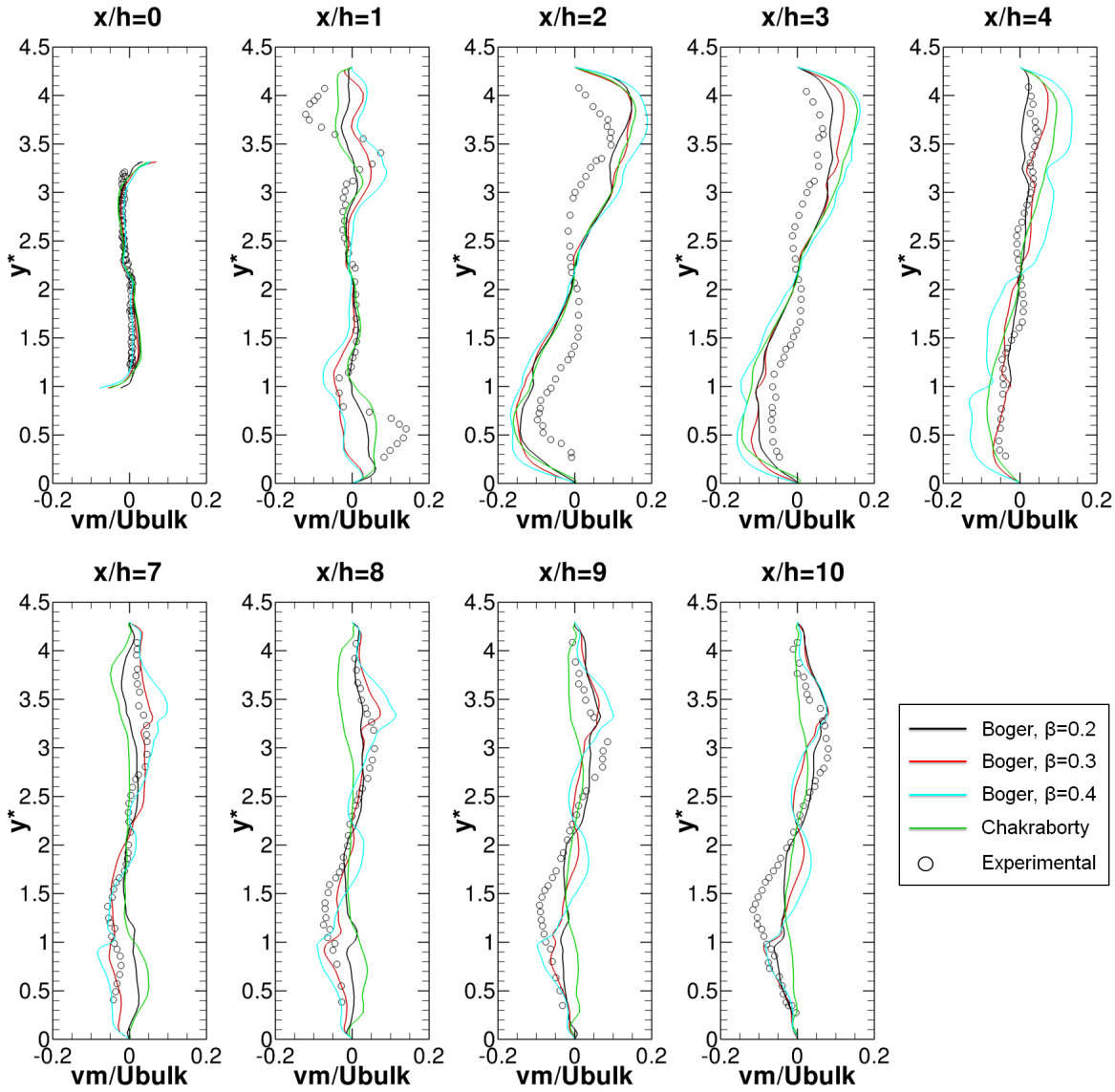

Figure 6.40: Normalised mean transverse velocity for case c_2 at different axial positions for different combustion models. $U_{bulk} = 11m/s$. Experimental data (o) from Nguyen et al. [82]

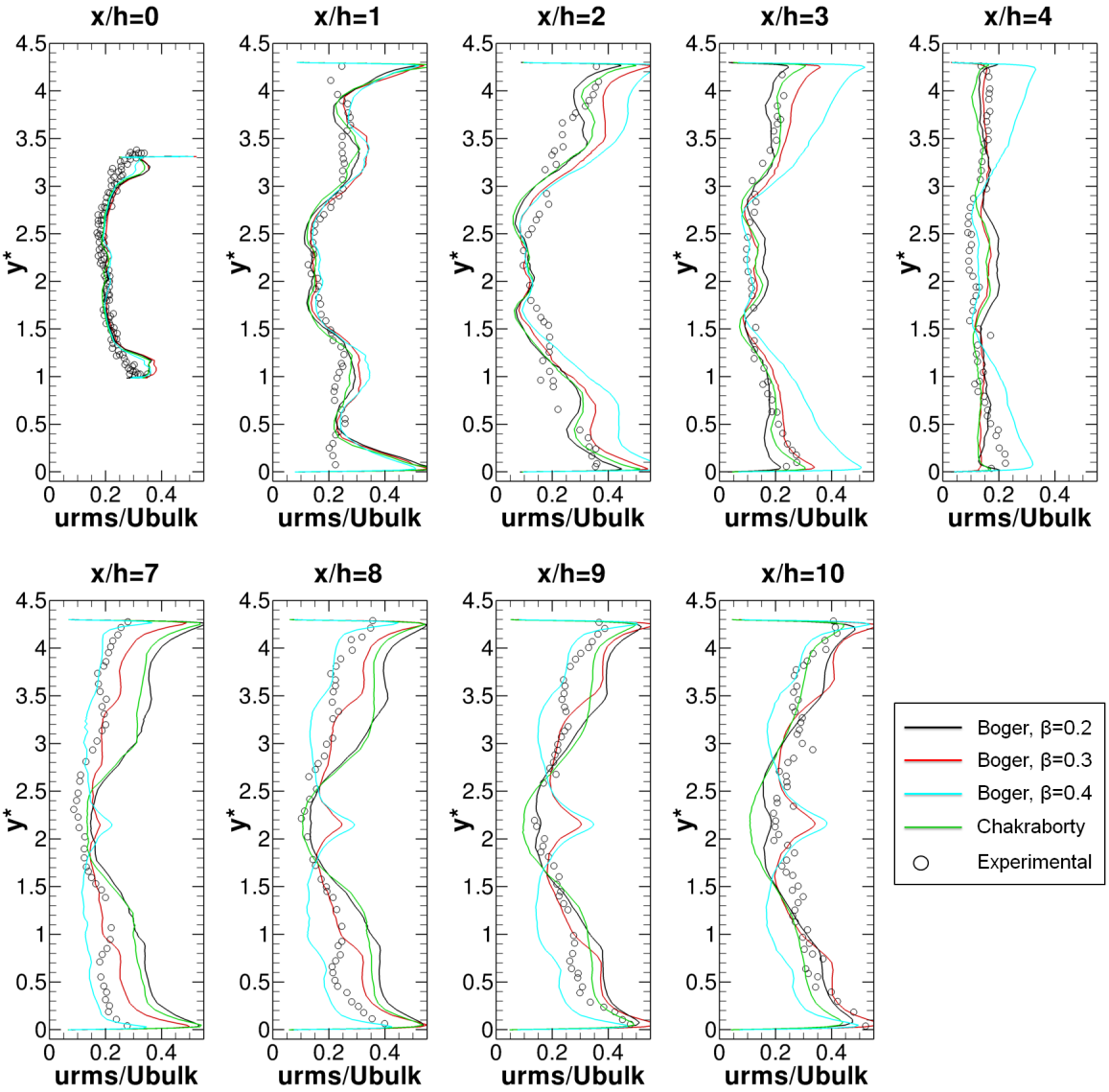

Figure 6.41: Normalised fluctuating streamwise velocity for case c_2 at different axial positions for different combustion models. $U_{bulk} = 11m/s$. Experimental data (o) from Nguyen et al. [82]

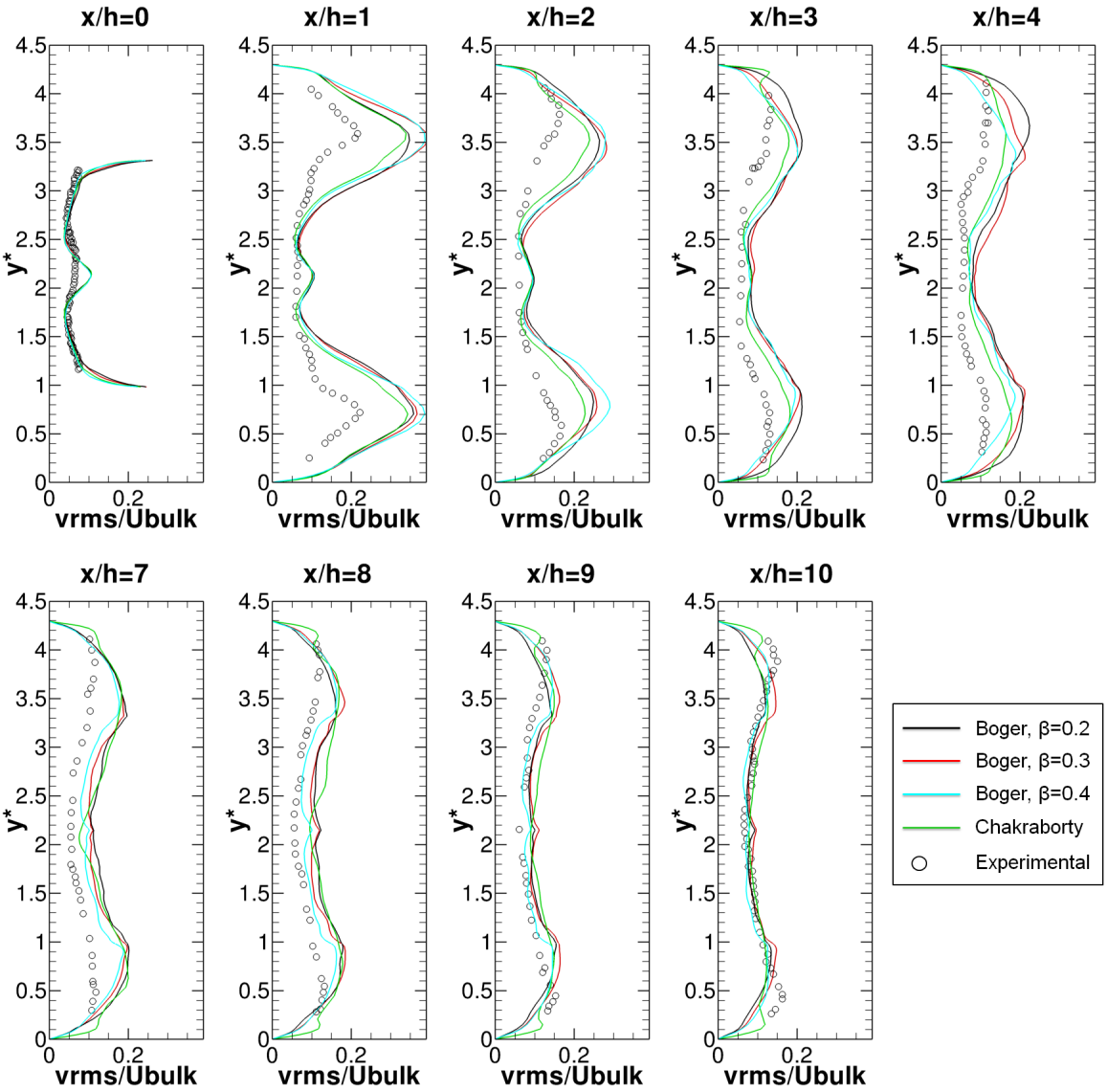

Figure 6.42: Normalised fluctuating transverse velocity for case c_2 at different axial positions for different combustion models. $U_{bulk} = 11m/s$. Experimental data (o) from Nguyen et al. [82]

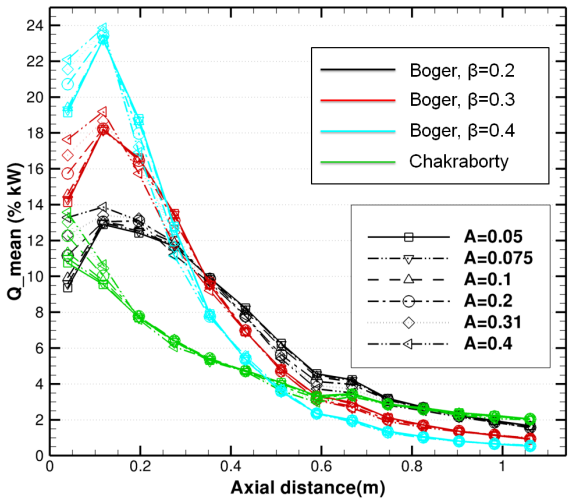

Figure 6.43: Percentage of time-averaged heat release versus axial distance for different forcing amplitudes and combustion models BOGER0-2, BOGER0-3, BOGER0-4 and CHAKRABORTY

different forcing amplitudes (A=0.05-0.4) for BOGER0-3 were used to compute axially distributed FTFs as before. The computed FTFs were then incorporated into LOTAN and the acoustic predictions are assessed and compared below.

Figure 6.44 shows predicted gain and time-delay parameters versus axial distance for BOGER0-3. In Figure 6.44(a), the curves depart in several significant ways from those obtained for BOGER0-2 (Figure 6.30(b)). There is still a local maximum at $x \approx 0.4m$ although this has decreased slightly in peak amplitude and is a sharper peak than before. In the region $x \leq 0.2m$ the curves are flatter and lower in magnitude compared to BOGER0-2. Downstream of $x \approx 0.6m$ the magnitude of the gains for BOGER0-3 has decreased with respect to BOGER0-2, although a second peak has now occurred in this region. A noticeable linear portion at low forcing amplitudes is observed in BOGER0-3, with gains for A=0.05,0.075 and 0.1 exhibiting almost coincident profiles; this linearity was not so clearly visible for BOGER0-2. The saturation effects at higher amplitudes are not as clear in BOGER0-3 compared to BOGER0-2 although an asymptotic behaviour is still visible. Regarding time-delay, comparison of Figures 6.44(b) and 6.30(d) shows these are very similar. Compared to the BOGER0-2 results the slope has decreased, reaching a maximum value of around 0.039s compared to the previous value of 0.053s. This is a consequence of the stronger flow acceleration induced by the higher β value.

The variation of predicted frequency and stability of the 50Hz mode were obtained by transferring the data in Figures 6.44 into the LOTAN acoustic network code and

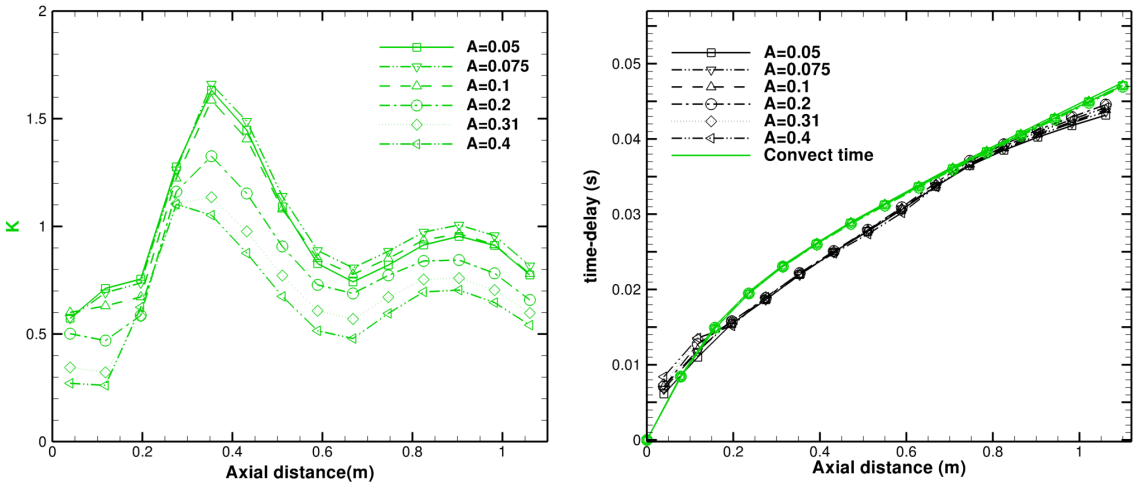

(a) (b)

Figure 6.44: (a) Gain and (b) time-delay versus axial distance for different forcing amplitudes using combustion model BOGER0-3 and Fourier series analysis method

are compared below with the $\beta = 0.2$ results. Regarding frequency BOGER0-2 and BOGER0-3 show different slopes but the frequency is close to 50Hz for all amplitudes. For both values of β the predicted growth rate remains negative, indicative of a stable mode. The tendency to move closer to the unstable region at higher frequencies is present in both results with the $\beta = 0.3$ showing a much stronger tendency. Given the improved comparison with the measured velocity field for $\beta = 0.3$, this has to be taken as the best result using the current coupled hybrid approach. These $\beta = 0.3$ predictions imply that unstable region would be reached just above $A = 0.4$. It is believed, given the evidence of saturation and gains decreasing with amplitude, that if the flame response has crossed into the unstable domain at A>0.4, it is likely that it would have returned into stable behaviour as amplitude increased further. A possible limit cycle behaviour would then have been predicted for an amplitude above 0.4 (note the experimentally observed self-sustained limit cycle amplitude was A=0.31). It would have been useful to confirm this with more LES solutions at higher amplitude but time did not allow for this.

A sensitivity analysis of the LOTAN stability prediction to the precise values of gain (K) and time-delay (τ) was explored by taking the distributions for K and τ for $\beta = 0.3$ from Figure 6.44 and perturbing these before transferring into LOTAN; K was changed by +/- 30% and τ by $0.1ms$, which corresponds to a variation of approximately 10% of the time-delay in the sensitive first part of the combustor ($x \leq 0.2m$). Figure 6.46(a) shows LOTAN growth rate predictions with varying time-delay and Figure 6.46(b)

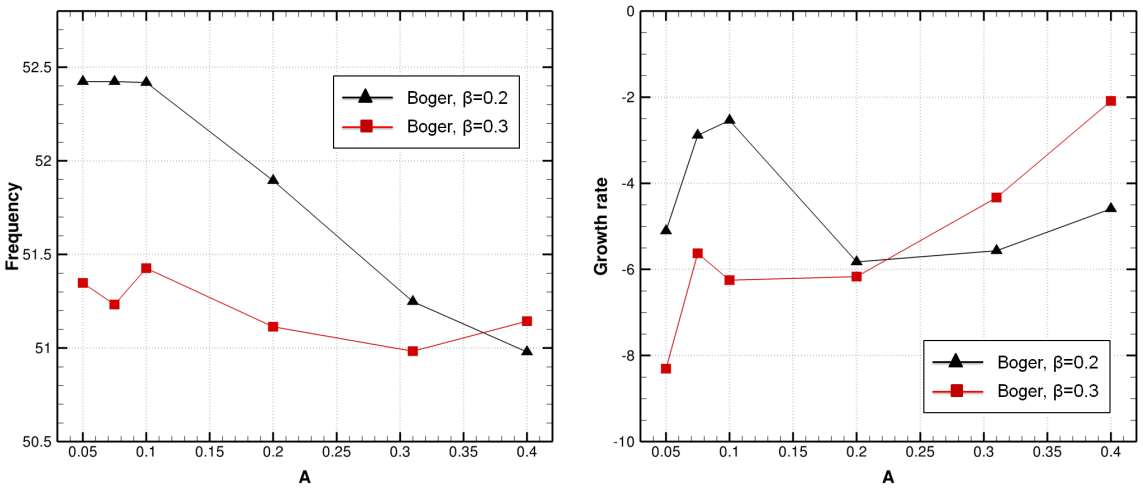

(a) (b)

Figure 6.45: (a) Frequency and (b) growth rate LOTAN predictions for combustion models BOGER0-2 and BOGER0-3

displays LOTAN growth rate predictions with varying gain magnitude. In both cases there is a relatively small sensitivity to these changes, although the +30% change in K does imply the shift into the unstable regime occurring at a lower value of A. Note that variations in the mean heat release ($\overline{\dot{Q}}$) would produce similar results as those obtained when varying gains, also indicating low sensitivity of LOTAN to $\overline{\dot{Q}}$.

6.6 Sensitivity to parameters in the acoustic model

In addition to the sensitivity of the hybrid LES/LOTAN predictions of flame response to variations in combustion model information explored in the previous section (§6.5) it was also necessary to examine the sensitivity to the uncertainties necessarily present in the set-up of the LOTAN acoustic model, since some of the geometry configuration and boundary conditions parameters had to be estimated. Hence, LOTAN calculations were carried out to vary acoustic model details such as boundary conditions and geometric dimensions (e.g., plenum and exhaust section dimensions) in the LOTAN set-up using FTFs from the best available LES simulation with $\beta = 0.3$. LOTAN predictions from these calculations are presented in this section. These are presented in the figures below, where red lines (with red square symbol) are LOTAN growth rate prediction corresponding to the $\beta = 0.3$ case shown in Figure 6.45; this curve is repeated in all figures below for comparison purposes.

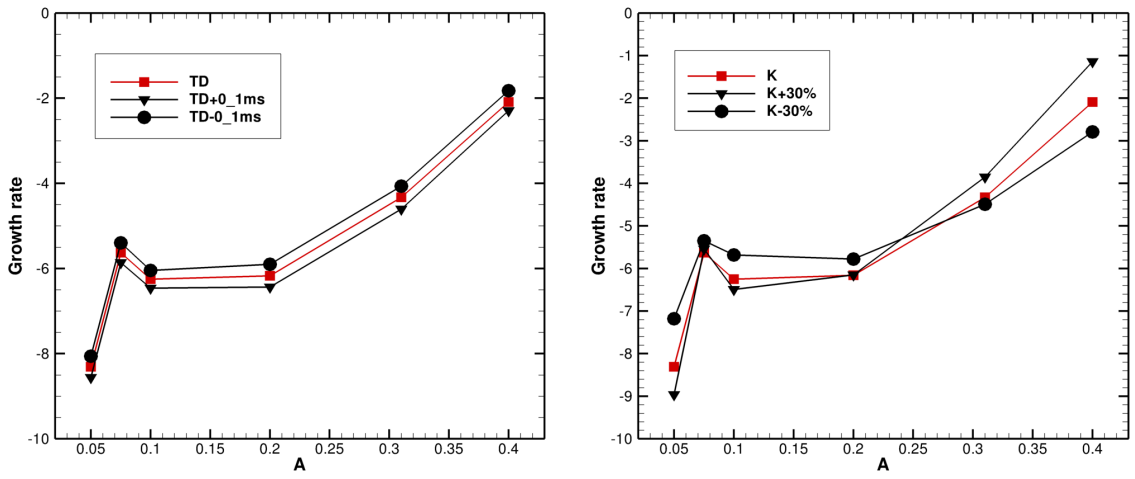

(a) (b)

Figure 6.46: Growth rate LOTAN predictions for different combustion model parameters: (a) time-delay and (b) gain.

Figure 6.47(a) shows LOTAN growth rate predictions for varying inlet reflection coefficient (referred to as IRC). Initially the coefficient was set to 1.0 (an acoustically closed inlet); it was increased and decreased by 0.1. Similarly, Figure 6.47(b) displays predictions for varying outlet reflection coefficient (referred to as ORC), set initially to -1.0 (an acoustically open end) and again increased and decreased by 0.1. The shape of the growth rate curve with varying A is not altered by these changes, instead the curve is shifted upwards and downwards, indicating that by changing the reflection coefficients, the amount of acoustic energy entering/leaving the system is altered, and this ultimately affects the level of stability of the response. Note that by increasing the IRC to 1.1 or decreasing the ORC to -1.1 the curve shifts towards unstable behaviour, showing a marginally unstable response for A=0.4 in both cases. Note also that changing these acoustic boundary conditions has a much larger effect than changing the combustion model or heat release data.

Initially, no exhaust diffuser section had been included in the LOTAN model although it was present in the sketches shown for the test rig (see Figure 5.1) in the experimental papers (e.g. [82]) but since no dimensions were given this was omitted in the acoustic network model. Also a gap between the combustor end and the exhaust section inlet was assumed (hence an acoustically open end outlet condition was used) since this was also shown in the test rig sketch. As part of this sensitivity study an exhaust diffuser section was therefore included in the LOTAN set-up and its length and area

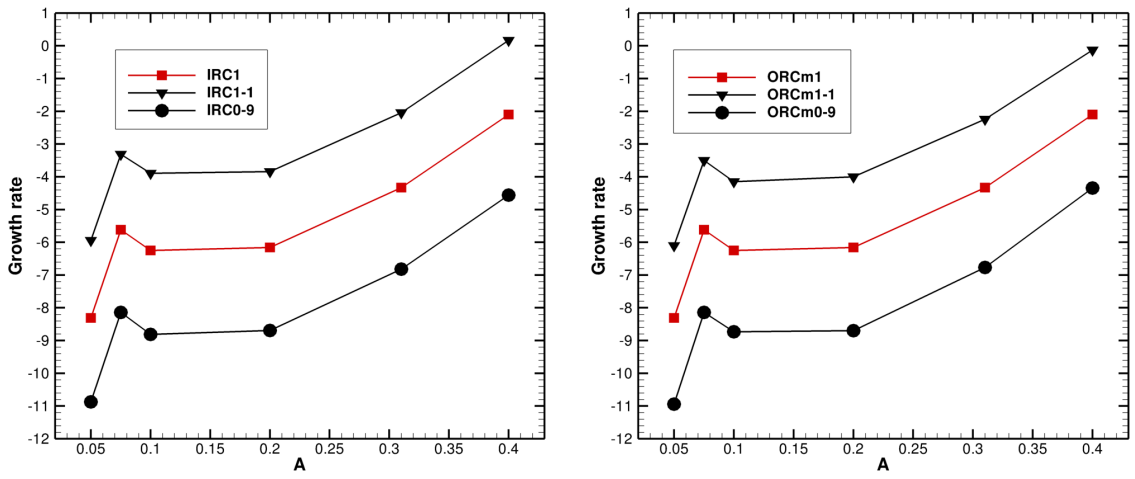

(a) (b)

Figure 6.47: Growth rate LOTAN predictions for different reflection coefficients at (a) inlet and (b) outlet.

ratio varied. Initially a length (L) and area ratio (AR) of $1m$ and $1.5m$ were assumed; these values were simply obtained by assuming the sketch provided in [82] was to scale. An acoustically open end condition was set at diffuser exit. L was varied between 0.5 and 1.5 m and AR between 1.25 and 1.75. Figure 6.48 presents the results obtained. The reference case (no exhaust diffuser) is the red line/red solid symbols, the case with baseline L/AR is the black line/black open symbols, and variation in diffuser geometry are shown in black line/black solid symbols. Once again it is striking how strong the response of the stability curve is to some of these acoustic network/boundary condition changes. The presence of the exhaust diffuser in terms of its baseline geometry has a dramatic effect (compare red line/red solid symbols with black line/black open symbols in Figure 6.48), shifting the growth rate curve upwards so that the stable region is entered at A≈0.3. Changing L at constant AR has a strong effect (Figure 6.48(a)), but changes of AR at constant L (Figure 6.48(b)) has little effect. The shape of the growth rate curve does not change for any of the acoustic geometry/parameter changes, but calculations of these variations has not been explored. The main message is that lack of precise knowledge of the correct acoustic representation of the ORACLES rig is the highest uncertainty in the present investigation, and has a large effect on the prediction of possible limit cycle prediction.

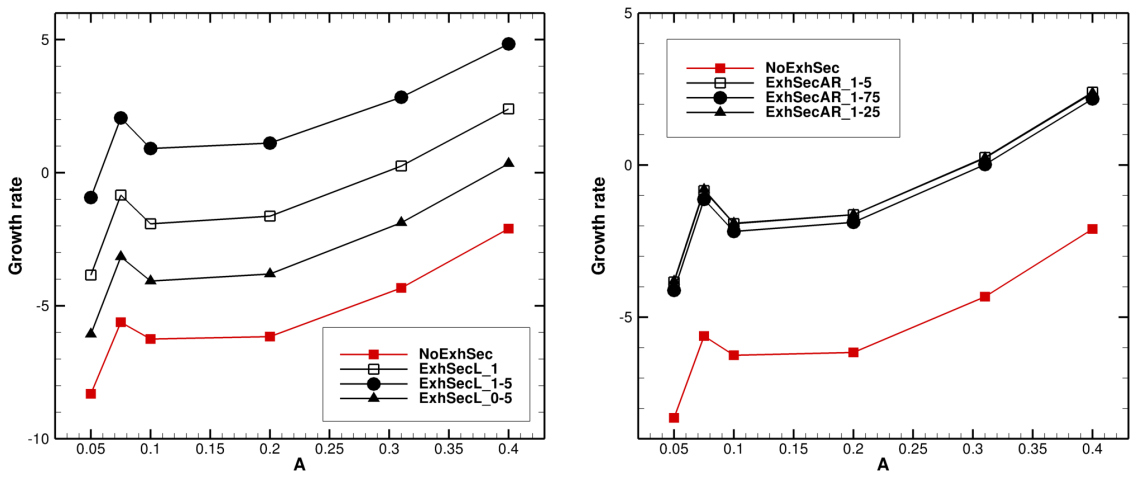

(a) (b)

Figure 6.48: Growth rate LOTAN predictions for (a) varying exhaust diffuser length with AR=1.5 and (b) varying AR with L=1m

6.7 Conclusions

A methodology to include acoustic wave effects in incompressible LES simulations has been developed and applied. This method consists of prescription of acoustically sensitised inlet boundary conditions that mimic the periodic velocity perturbation in frequency and magnitude associated with a plane acoustic wave. The resonant frequency and its amplitude may be calculated using a thermo-acoustic network model (LOTAN) provided that some experimental measurement is available at one point in the system to dimensionalise the linear acoustic prediction.

This procedure was applied to the reacting flow c_2 of the ORACLES test case. The results obtained were compared with those presented in the previous chapter with no acoustic forcing included. The improvement in fluctuating velocity profiles, as well as in flame shape and flame dynamics was clearly demonstrated, validating this methodology and confirming the necessity of including such dominant acoustic effects.

Periodic forcing was subsequently included at various amplitudes in LES calculations producing a dramatic change in the flame dynamics. This was analysed and quantified to extract amplitude dependent FTFs. These were converted into gain/time-delay and mean heat release data, were introduced into the acoustic network code LOTAN and resonant mode predictions were presented. For the baseline case of FSD SGS model represented by $\beta = 0.2$, too slow heat release and only stable response of the flame was

obtained. An alternative algebraic FSD model and variations in the parameter β were then explored. Increase of β to a value of 0.3 provided best agreement with measurements. Forcing amplitude dependent FTFs were again predicted and introduced into LOTAN, indicating a more unstable flame but still implying limit cycle behaviour (if any) at amplitudes greater than 0.4, the largest value studied in the present work.

Finally, a sensitivity study was carried out in LOTAN. First, gain and time-delay were varied. Predictions showed only small sensitivity to these changes. Second, acoustic boundary conditions and acoustic network model configuration were varied. These had been initially chosen to represent the experimental test case as far as could be judged, but some uncertainties were clearly present. Strong sensitivity of the growth rate predictions to the variation of some acoustic parameters was shown, especially by including an exhaust diffuser section after the combustor. Thus, any final conclusions on the ability of the hybrid approach to predict limit cycle behaviour was unfortunately hampered by the lack of certainty in the configuration of the acoustic network model.

Chapter 7

Conclusions and future work

7.1 Summary and conclusions

In this thesis an LES code, LULES, for low-Mach number (incompressible) turbulent premixed reacting flows has been used, further developed and applied to predict thermo-acoustic oscillations by combining it with an acoustic network model to form a hybrid, coupled prediction methodology.

The ORACLES test case was chosen for validation purposes, since this extensive experimental database is suitable for turbulence and combustion model assessment and specially designed for LES-based CFD. The ORACLES experiment exhibited (for some reacting cases) self-excited self-sustained thermo-acoustic instability (a strong plane wave at frequency 50Hz), which makes it an attractive option to explore flame dynamics and CFD-based Flame Transfer Function (FTF) evaluation.

A precursor calculation was initially set up, to generate LES inlet boundary conditions that matched experimental data. These data were stored and used in the main CFD calculation domain inlet plane.

Inert and reacting flow simulations for different flow and perfectly premixed (equivalence ratio) conditions have been conducted. The inert flow simulation results showed excellent agreement with measurements for both mean and second order statistics, in particular reproducing the experimentally observed asymmetry. For reacting flows, an algebraic Flame Surface Density (FSD) premixed combustion model was selected and applied to two reacting flow cases with equivalence ratios $\phi = 0.65$ (c_1) and $\phi = 0.75$ (c_2). Initially no account was taken of any acoustic effects and the agreement between experimental data for case c_1 and LES results was in general good for both mean and fluctuating turbulent data although some evidence of a too slow reaction rate was observed. For case c_2 the mean flow results were again good, displaying now more clearly the too slow reaction rate in the furthest downstream data comparison. However, a significant discrepancy was found in the prediction of the axial component fluctuating

velocity. This discrepancy was attributed to the neglect of a periodic coherent (acoustic) unsteady velocity contribution, caused by a strong pulsating plane acoustic wave that had been observed in the ORACLES experiments for the higher equivalence ratio (c_2) (indicated via a peak in the spectrum for measured u').

A methodology for including effects of acoustic waves in the incompressible LES simulation was therefore developed and implemented. Acoustically sensitised inlet boundary conditions were prescribed in the incompressible LES calculations. These were scaled to mimic the periodic motion found in the experiments. Thus, a periodic forcing (at the 50Hz frequency observed in the measurements) was added at the LES domain inlet, at a specific amplitude. This amplitude was calculated using the thermo-acoustic network code LOTAN. A single experimental measurement of the amplitude of the coherent plane wave was used to dimensionalise the mode shape predicted by LOTAN and hence quantify the magnitude of the perturbation added to the incompressible LES. This approach was an improvement on earlier "trial and error" attempts to achieve the same acoustic effect analogy. The results obtained were compared with measurements and indicated a noticeable improvement over the LES results with no acoustic forcing for the fluctuating velocity profiles, as well as the flame shape and flame dynamics, thus validating this methodology and confirming the necessity of including such dominant acoustic effects in the simulations.

The periodic forcing described above produced a dramatic response in the flame dynamics. This technique was therefore next used to derive forcing amplitude dependent FTFs (or a Flame Density Function, FDF) from a series of LES forced reacting simulations. These were analysed to produce gain and time-delay information as well as mean heat release, enabling to transfer a flame model into the acoustic network code LOTAN and resonant mode predictions to be carried out. Whilst the amplitude dependent gain data taken from the LES showed clear signs of non-linear effects at higher forcing amplitudes, gain decreasing with amplitude and saturation effects such as gain becoming independent of further amplitude increase, initial results predicted only stable behaviour with no indications of any limit cycle tendency.

Before undertaking a sensitivity analysis to examine how the LOTAN growth rate predictions would be affected by changes in modelling parameters, the question of the too slow heat release and hence underpredicted flow acceleration in the combustion chamber was addressed. Although an alternative FSD model was explored, this performed poorly, and a better option was to modify the value set for the single model constant in the algebraic FSD model used (β). This was increased to 0.3 and 0.4 and LES predictions analysed. $\beta = 0.3$ gave the best results in comparison with measurements and the FTFs deduced from these results, when transferred into LOTAN, shifted considerably towards the unstable regime at higher amplitudes. The indication was that

an unstable flame would be predicted at an amplitude just greater than 0.4. Given the evidence of decreasing gain with amplitude and signs of saturation in gain, it is believed that when the growth rate curve entered the unstable regime, return to stable behaviour would have occurred soon thereafter as forcing amplitude increased, which would have indicated a limit cycle behaviour, but unfortunately time was not available to carry out further LES solutions at higher amplitudes.

Both combustion model parameters (gain and time-delay) and geometric configuration and boundary conditions of the acoustic network were varied. By far the largest sensitivity was to the acoustic model variations. The network geometry and acoustic boundary conditions had been chosen initially to reflect the best representation of the experiment as rescaled in the published papers, but several uncertainties remained. Changing the network at the downstream end of the combustor by inclusion of an exhaust diffuser had a very strong effect such that the LOTAN predictions indicated an unstable regime at an amplitude of 0.3. Since this was close to the measured self-sustained limit cycle amplitude of 0.31, it was clear that these acoustic uncertainties were playing a large role in the hybrid coupled methodology predictions.

7.2 Future work

To enable the effectiveness of the hybrid coupled approach for predicting thermo-acoustics to be assessed in a final, controlled manner, the following pieces of work are recommended:

1. It would be worthwhile to carry out LES calculations ($\beta = 0.3$) at higher forcing amplitudes for the ORACLES geometry, deduce FTFs and transfer these into LOTAN (exhaust diffuser geometry included) to see if this would change the shape of the growth rate curve and provide evidence of a limit cycle predictive capability.

2. Although the algebraic FSD model chosen worked reasonably well after adjusting β, the importance of precise capture of the heat release in the region immediately after the dump step is such that it would be worthwhile exploring alternative combustion modelling approaches such as the G-equation [11]

3. The axially distributed nature of the ORACLES flame, and the lack of temperature and species information, means that an alternative test case would be preferable. To make this of greater relevance to aeroengine gas turbine applications a confined swirling flow would be a good choice. The present work has indicated, however, that any future test cases should provide not just as complete measurement data as possible, but also full details of the geometry and supply/exhaust conditions to allow an acoustic network model to be built.

4. If a suitable test case that had already been calculated with a fully compressible LES approach could be identified, it would be interesting to calculate this with the hybrid, coupled methodology to gather comparative studies on predictions and computational cost.

Bibliography

[1] How greenhouse gases emissions contribute to climate change. Accessed on July 2012. http://www.actionforourplanet.com/climate-change/4536958199, 2011.

[2] All about ACARE. Accessed on June 2012. http://www.acare4europe.org, 2012.

[3] Rolls-Royce progress on reducing environmental impact of the aviation industry. Accessed on July 2012. http://www.rolls-royce.com/reports/environment_report_07/reducing-en-impact/aviation.html, 2011.

[4] US Department of Energy Office of Fossil Energy National Energy Technology Laboratory. *The Gas Turbine Handbook, Lean Premixed Combustion Section, 3.2.1.2.* 2006.

[5] T. Lieuwen. Modeling premixed combustion-acoustic wave interactions: A review. *AIAA Journal of Propulsion and Power*, 19(5):765–781, 2003.

[6] A. P. Dowling and S. R. Stow. Acoustic analysis of gas turbine combustors. *AIAA Journal of Propulsion and Power*, 19(5):751–764, 2003.

[7] Overview of GEnx engine family. Accessed on July 2012. http://www.geaviation.com/engines/commercial/ genx, 2011.

[8] J.D. Anderson. *Computational Fluid Dynamics: The Basics with Applications.* Springer, 3rd edition, 1995.

[9] J.H. Ferziger and M. Perić. *Computational Methods for Fluid Dynamics.* Springer, 3rd edition, 2002.

[10] T. Poinsot and D. Veynante. *Theoretical and Numerical Combustion.* RT-Edwards, Flourtown, PA, USA, 2nd edition, 2005. ISBN 1-930217-10-2.

[11] F.A. Williams. *Combustion Theory.* Addison-Wesley, 2nd edition, 1965.

[12] K. K. Kuo. *Principles of Combustion.* John Wiley, New York, 1986.

[13] H. Tennekes and J.L. Lumley. *A First Course in Turbulence.* Cambridge, MA, MIT Press, 1974.

[14] S. B. Pope. *Turbulent Flows.* Cambridge University Press, 2000. ISBN 0 521 59886 9.

[15] N. Peters. *Turbulent Combustion.* Cambridge University Press, 2000.

[16] S.V. Patankar. *Numerical Heat Transfer and Fluid Flow.* McGraw-Hill, 1980.

[17] D.C. Wilcox. *Turbulence Modeling for CFD.* DCW Industries, Inc., La Canada, CA, 2004.

[18] Y. Mizobuchi, S. Tachibana, S. Ogawa, and T. Takeno. A numerical analysis on the structure of turbulent hydrogen jet lifted flame. In *Proceedings of the Combustion Institute*, volume 29, pages 2009–2015, 2002.

[19] L. Vervisch, P. Domingo, and R. Hauguel. Turbulent combustion in the light of direct and large-eddy simulation. In *Proceedings of the Third International Symposium on Turbulence and Shear Flow Phenomena, Sendai, Japan, 25-27 June*, pages 847–856, 2003.

[20] M. Germano. pages 321–346. in Direct and Large-Eddy simulation-III, edited by Kluwer Academic Publishers, Dordrecht, 1999.

[21] J.A. Langford and R.D. Moser. Optimal LES formulations for isotropic turbulence. *Journal of Fluid Mechanics*, 398:321–346, 1999.

[22] P. Sagaut. *Large Eddy Simulation for Incompressible Flows: An Introduction.* Springer, 2nd edition, 2001. ISBN 3 540 67890.

[23] F.K. Chow and P. Moin. A further study of numerical errors in large-eddy simulation. *Journal of Computational Physics*, 184:366–380, 2003.

[24] D. Veynante and L. Vervisch. Turbulent combustion modeling. *Progress in Energy and Combstion Sciences*, 28:193–266, 2002.

[25] P. Moin. Turbulent combustion modeling. In *Progress in Energy and Combustion Sciences*, volume 28, pages 193–266, 2002.

[26] U. Piomelli and J. R. Chasnov. *Large-eddy simulations: theory and applications*, pages 29–47. In Transition and turbulence modelling, edited by D. Henningson, M. Hallbäck, H. Alfreddson and A. Johansson, (Kluwer Academic Publishers, Dordrecht), 1996.

[27] M. Lesieur and O. Métais. New trends in Large-Eddy Simulations of turbulence. *Annual Review of Fluid Mechanics*, 28:45–82, 1996.

[28] J. Ferziger. *Large-Eddy Simulation: an introduction and perspective*, pages 29–47. in New tools in turbulence modelling, Les Editions de Physique, Springer Verlag, 1997.

[29] M. Lesieur. *Recent approaches in Large-Eddy Simulations of turbulence*, pages 1–28. in New tools in turbulence modelling, Les Editions de Physique, Springer Verlag, 1997.

[30] J.U. Schlüter, X. Wu, S. Kim, S. Shankaran, J.J. Alonso, and H. Pitsch. A framework for coupling Reynolds-Averaged and Large-Eddy simulations for gas turbine applications. *ASME Journal of Fluids Engineering*, 127:806–815, 2005.

[31] G. Medic, G. Kalitzin, D. You, E.V.D. Weide, J.J. Alonso, and H. Pitsch. Integrated RANS/LES computations of an entire gas turbine jet engine. *AIAA paper 2007-1117*, 2007.

[32] U. Piomelli, A. Scotti, and E. Balaras. Large eddy simulation of turbulent flows, from desktop to supercomputer. In *in Vector and Parallel Processing-VECPAR2000, edited by J.M.L.M. et al., Springer, Heidelberg*, pages 551–577, 2001.

[33] B. Wegner, C. Maltsev, C. Schneider, A. Sadiki, A. Dreizler, and J. Janicka. Assessment of unsteady rans in predicting swirl flow instability based on les and experiments. *International Journal of Heat and Fluid Flow*, 25:528–536, 2004.

[34] P.A. Durbin. pages 3–16. in Engineering Turbulence Modeling and Experiments 5, W. Rodi, N. Fueyo (Eds.), 2002.

[35] C.M. Coats. Coherent structures in combustion. *Progress in Energy and Combustion Science*, 22:427–509, 1996.

[36] A. Kerstein. Turbulence in combustion processes: modelling challenges. In *Proceedings of the Combustion Institute*, volume 29, pages 1763–1773, 2002.

[37] J. Janicka and A. Sadiki. Large Eddy Simulation of turbulent combustion systems. In *Proceedings of the Combustion Institute*, volume 30, pages 537–547, 2005.

[38] R.W. Bilger, S.B. Pope, K.N.C. Bray, and J.F. Driscoll. Paradigms in turbulent combustion resesarch. In *Proceedings of the Combustion Institute*, volume 30, pages 21–42, 2005.

[39] H. Pitsch. Large-eddy simulation of turbulent combustion. *Annual Review of Fluid Mechanics*, 38:453–482, 2006.

[40] D. Veynante. Large eddy simulations of turbulent combustion. Conference on Turbulence and Interactions TI2006, May29-June2, Porquerolles, France, 2006.

[41] F. Di Mare, W. Jones, and K. Menzies. Large-eddy simulation of a model gas turbine combustor. *Combustion and Flame*, 137(3):278–294, 2004.

[42] W. Kim, S. Menon, and H. Mongia. Large-eddy simulation of a model gas turbine combustor flow. *Combustion Sciencie and Technology*, 143(1):25–62, 2004.

[43] P. Moin. Advances in large eddy simulation methodology for complex flows. *International Journal of Heat and Fluid Flow*, 23:710–720, 2002.

[44] G. Eggenspieler and S. Menon. Large-Eddy simulation of pollutant emission in a DOE-HAT combustor. *AIAA Journal of Propulsion and Power*, 20(6):1076–1085, 2004.

[45] D. Haworth and K. Jansen. Large-eddy simulation on unstructured deforming meshes: towards reciprocating IC engines. *Computers and Fluids*, 29(5):493–524, 2000.

[46] C. Stone and S. Menon. Open-loop control of combustion instabilities in a model gas turbine combustor. *Journal of Turbulence*, 4:20, 2004.

[47] L. Selle, G. Lartigue, T. Poinsot, R. Koch, K.-U. Schildmacher, W. Krebs, B. Prade, P. Kaufmann, and D. Veynante. Compressible Large-Eddy Simulation of turbulent combustion in complex geometry on unstructured meshes. *Combustion and Flame*, 137(4):489–505, 2004.

[48] Y. Sommerer, D. Galley, T. Poinsot, S. Ducruix, F. Lacas, and D. Veynante. Large eddy simulation and experimental study of flashback and blow-off in a lean partially premixed swirler burner. *Journal of Turbulence*, 5:37, 2004.

[49] C. Angelberger, D. Veynante, and F. Egolfopoulos. LES of chemical and acoustic forcing of a premixed dump combustor. *Flow, Turbulence and Combustion*, 65 (2):205–222, 2000.

[50] J. Shinjo, Y. Mizobuchi, and S. Ogawa. LES of unstable combustion in a gas turbine combustor. *High Performance Computing*, 2858/2003:234–244, 2003.

[51] C.T. Wall and P. Moin. Numerical methods for large eddy simulation of acoustic combustion instabilities. Technical report, Tech. Rep. TF-91, Stanford, CA, Stanford University, 2005.

[52] L. Cheng, M. Dianat, A. Spencer, and J.J. McGuirk. Validation of LES predictions of scalar mixing in high-swirl fuel injector flows. *Flow, Turbulence and Combustion*, 88:143–168, 2011.

[53] J. Smagorinsky. General circulation experiments with the primitive equations: I. the basic experiment. *Monthly Weather Review*, 91:99–164, 1963.

[54] D. B. Spalding. Mixing and chemical reaction in steady confined turbulent flames. In *Proceedings of 13th International Symposium on Combustion, The Combustion Institute, Pittsburg*, pages 649–657, 1971.

[55] D. B. Spalding. Development of the Eddy-Break-Up model of turbulent combustion. In *Proceedings of 16th International Symposium on Combustion, The Combustion Institute, Pittsburg*, pages 1657–1663, 1976.

[56] Y. Huang, H. Sung, S. Hsieh, and V. Yang. Large-eddy simulation of combustion dynamics of lean-premixed swirl-stabilized combustor. *AIAA Journal of Propulsion and Power*, 19(5):782–794, 2003.

[57] M. Boger, D. Veynante, H. Boughanem, and A. Trouvé. Direct Numerical Simulation analysis of flame surface density concept for Large Eddy Simulation of turbulent premixed combustion. pages 917–927. 27th International Symposium on Combustion, The Combustion Institute, Pittsburg, 1998.

[58] E.R. Hawkes and S.R. Cant. A flame surface density approach to large eddy simulation of premixed turbulent combustion. In *28th International Symposium on Combustion, The Combustion Institute, Pittsburg*, pages 51–58, 2000.

[59] H.G. Weller, G. Tabor, A.D. Gosman, and C. Fureby. Application of a flame-wrinkling LES combustion model to a turbulent mixing layer. In *27th International Symposium on Combustion, The Combustion Institute, Pittsburg*, pages 899–907, 1998.

[60] W. Kim and S. Menon. Numerical modeling of turbulent premixed flames in the thin-reaction-zones regime. *Combustion Science and Technology*, 160:119–50, 2000.

[61] P. Flohr and H. Pitsch. A turbulent flame speed closure modelf for LES of industrial burner flows. In *Proceedings of the Summer Program, Center for Turbulence Research*, volume 65, pages 163–175, 2000.

[62] V.K. Chakravarthy and S. Menon. Large-eddy simulation of turbulent premixed flames in the flamelet regime. *Combustion Science and Technology*, 162:175–222, 2001.

[63] O. Colin, F. Ducros, D. Veynante, and T. Poinsot. A thickened flame model for large eddy simulations of turbulent premixed combustion. *Physics of Fluids*, 12 (7):1843–1863, 2000.

[64] C. Fureby and C. Löfström. Large eddy simulation of bluff body stabilized flames. *Proceedings of the Combustion Institute*, 25:1257–1264, 1994.

[65] T.D. Butler and P.J. O'Rourke. A numerical method for two dimensional unsteady reacting flows. In *16th International Symposium on Combustion, The Combustion Institute, Pittsburg*, pages 1503–1515, 1977.

[66] J.P. Légier, T. Poinsot, and D. Veynante. Dynamically thickened flame LES model for premixed and non-premixed turbulent combustion. In *Proceedings of the Summer Program 2000, Center for Turbulence Research, CA*, pages 157–168, 2000.

[67] C. Angelberger, D. Veynante, F. Egolfopoulos, and T. Poinsot. Large eddy simulations of combustion instabilities in premixed flames. In *Proceedings of the Summer Program, Center for Turbulence Research, NASA Ames/Standford University*, pages 61–82, 1998.

[68] H. Pitsch and L. Duchamp de Lageneste. Large-eddy simulation of premixed turbulent combustion using a level-set approach. In *Proceedings of the Combustion Institute*, volume 29, pages 2001–2008, 2002.

[69] M. Oberlack, H. Wenzel, and N. Peters. On symmetries and averaging of the g-equation for premixed combustion. *Combustion Theory and Modelling*, 5(4): 1–20, 2001.

[70] H. Pitsch. A consistent level set formulation for large-eddy simulation of premixed turbulent combustion. *Combustion and Flame*, 143:587–598, 2005.

[71] J. Piana, D. Veynante, S. Candel, and T. Poinsot. Direct numerical simulation analysis of the g-equation in premixed combustion. Technical report, Second ER-COFTAC Workshop on Direct and Large Eddy simulation, September 16-19 Grenoble, France, 1996.

[72] M. Boger and D. Veynante. Large eddy simulation of a turbulent premixed V-shaped flame. In *Advances in turbulence VIII, Proceedings of the Eighth European Turbulence Conference, CIMNE, Barcelona, Spain*, pages 449–452, 2000.

[73] N. Chakraborty and M. Klein. A priori direct numerical simulation assessment of algebraic flame surface density models for turbulent premixed flames in the context of large eddy simulation. *Physics of Fluids*, 20(8):085108, 2008.

[74] R. Knikker, D. Veynante, and C. Meneveau. A priori testing of a similarity model for large eddy simulations of turbulent premixed combustion. *Proceedings of the Combustion Institute*, 29:2105–2111, 2002.

[75] R. Knikker, D. Veynante, and C. Meneveau. A dynamic flame surface density model for large eddy simulation of turbulent premixed combustion. *Physics of Fluids*, 16(11):91–94, 2004.

[76] F. Halter, C. Chauveau, I. Gökalp, and D. Veynante. Analysis of flame surface density measurements in turbulent premixed combustion. *Combustion and Flame*, 156:657–664, 2009.

[77] M. Kirkpatrick, S.M. Armfield, A.R. Masri, and S.S. Ibrahim. Large eddy simulation of a propagating turbulent premixed flame. *Flow, Turbulence and Combustion*, 70:1–19, 2003.

[78] A.R. Masri, S.S. Ibrahim, and B.J. Cadwallader. Measurements and large eddy simulation of propagating premixed flames. *Experimental Thermal and Fluid Science*, 30:687–702, 2006.

[79] O. Stein, M. Freitag, F. Flemming, and A.M. Kempf. Lean premixed combustion in turbulent opposed nozzle flows: Algebraic modelling of the flame surface density for large eddy simulation. 3rd European Combustion Meeting, 11-13 April 2007, Chania, Crete, Greece, 2007.

[80] K. Wang. *Large-eddy simulation of turbulent variable density and reacting flows.* PhD thesis, Department of Aeronautical and Automotive Engineering, Loughborough University, 2007.

[81] M. Besson, P. Bruel, J.L. Champion, and B. Deshaies. Experimental analysis of combusting flows developing over a plane-symmetric expansion. *Journal of Thermophysics and Heat Transfer*, 14(1):59–67, 2000.

[82] P.D. Nguyen, P. Bruel, Pascal, and S. Reichstadt. An experimental database for benchmarking simulations of turbulent premixed reacting flows: lean extinction limits and velocity field measurements in a dump combustor. *Flow, Turbulence and Combustion*, 82(2):155–183, 2008.

[83] S. Candel. Combustion instabilities coupled by pressure waves and their active control. pages 1277–1296. 24th International Symposium on Combustion, The Combustion Institute, Pittsburg, 1992.

[84] T. Poinsot, A. Trouvé, D. Veynante, S. Candel, and Esposito E. Vortex-driven acoustically coupled combustion instabilities. *Journal of Fluid Mechanics*, 177: 265–292, 1987.

[85] K. C. Schadow, E. Gutmark, T. P. Parr, D. M. Parr, K. J. Wilson, and J.E. Crump. Large-scale coherent structures as drivers of combustion instability. *Combustion Science and Technology*, 64:167–186, 1989.

[86] T. Lieuwen, H. Torres, C. Johnson, and B. T. Zinn. A mechanism of combustion instability in lean premixed gas turbine combustors. *ASME Transactions*, 123: 182–189, 2001.

[87] J. G. Lee, K. Kim, and D. A. Santavicca. Measurement of equivalence ratio fluctuation and its effect in heat release during unstable combustion. *Proceedings of the Combustion Institute*, 28:415–421, 2000.

[88] T. Lieuwen and B. T. Zinn. The role of equivalence ratio oscillations in driving combustion instabilities in low nox gas turbines. *Proceedings of the Combustion Institute*, 27:1809–1816, 1998.

[89] G. A. Richards and M. C. Janus. Characterization of oscillation during premixed gas trubine combustion. *ASME Journal of Engineering for Gas Turbines and Power*, 120:294–302, 1998.

[90] D. Straub, G. Richards, M. J. Yip, W. A. Rogers, and E. H. Robey. Importance of axial wsirl vane location on combustion dynamics for lean premix fuel injectors. *AIAA paper 98-3909*, 1998.

[91] A. P. Dowling. A kinematic model of a ducted flame. *Journal of Fluid Mechanics*, 394:51–72, 1999.

[92] M. Fleifil, A. M. Annaswamy, Z. A. Ghoneim, and A. F. Ghoniem. Response of a laminar premixed flame to flow oscillations: A kinematic model and thermoacoustic instability results. *Combustion and Flame*, 106:487–510, 1996.

[93] T. Schuller, S. Ducruix, D. Durox, and S. Candel. Modeling tools for the prediction of premixed flame transfer functions. *Procedings of the Combustion Institute*, 29:107–113, 2002.

[94] B. Varoquié, J.P. Légier, F. Lacas, D. Veynante, and T. Poinsot. Experimental analysis and large eddy simulation to determine the response of non-premixed flames submitted to acoustic forcing. *Proceedings of the Combustion Institute*, 29:1965–1970, 2002.

[95] T. Schuller, D. Durox, and S. Candel. A unified model for the prediction of laminar flame transfer functions: Comparison berween conical and v-flame dynamics. *Combustion and Flame*, 134:21–34, 2003.

[96] A. X. Sengissen, J. F. Van Kampen, R. A. Huls, G. G. M. Stoffels, J. B. W. Kok, and T. H. Poinsot. LES and experimental studies of cold and reacting flow in a swirled partially premixed burner with and without fuel modulation. *Combustion and Flame*, 150:40–53, 2007.

[97] C. A. Armitage, R. Balachandran, E. Mastorakos, and R. S. Cant. Investigation of the nonlinear response of turbulent premixed flames to imposed inlet velocity oscillations. *Combustion and Flame*, 146:419–436, 2006.

[98] C. A. Armitage, R. S. Cant, A. P. Dowling, and T. P. Hynes. Linearised theory for LPP combustors dynamics. *ASME paper 2003-GT-38670, ASME IGTI Conference, Atlanta, Georgia, USA*, 2003.

[99] C. A. Armitage, A. J. Riley, R. S. Cant, A. P. Dowling, and S. R. Stow. Flame transfer function for swirled LPP combustion from experiments and CFD. In *ASME paper 2004-GT-53820, ASME IGTI Conference, Vienna, Austria*, 2004.

[100] A. Gentemann, C. Hirsch, K. Kunze, F. Kiesewetter, T. Sattelmayer, and W. Polifke. Validation of flame transfer function reconstruction for perfectly premixed swirl flames. *ASME paper GT-2004-53776, ASME IGTI Conference, Vienna, Austria*, 2004.

[101] A. Giauque, L. Selle, T. Poinsot, H. Buechner, P. Kaufmann, and W. Krebs. System identification of a large-scale swirled partially premixed combustor using LES and measurements. *Journal of Turbulence*, 6(21):21–31, 2005.

[102] T. Lieuwen and Y. Neumeier. Nonlinear pressure-heat release transfer function measurements in a premixed combustor. In *Proceedings of the Combustion Institute*, volume 29, pages 99–105, 2002.

[103] C. Külsheimer and H. Büchner. Combustion dynamics of turbulent swirling flames. *Combustion and Flame*, 131:70–84, 2002.

[104] D. Durox, T. Schuller, and S. Candel. Combustion dynamics of inverted conical flames. *Proceeding of the Combustion Institute*, 30:1717–1724, 2005.

[105] R. Balachandran, B. O. Ayoola, C. F. Kaminski, A. P. Dowling, and E. Mastorakos. Experimental investigation of the nonlinear response of turbulent premixed flames to imposed velocity oscillations. *Combustion and Flame*, 143:37–55, 2005.

[106] B. D. Bellows, Y. Neumeier, and T. Lieuwen. Forced response of a swirling, premixed flame to flow disturbances. *AIAA Journal of Propulsion and Power*, 22(5):1075–1084, 2006.

[107] A. L. Birbaud, D. Durox, S. Ducruix, and S. Candel. Dynamics of confined premixed flames submitted to upstream acoustic modulations. *Proceedings of the Combustion Institute*, 31:1257–1265, 2007.

[108] W. Polifke and Lawn C. On the low-frequency limit of flame transfer functions. *Combustion and Flame*, 151:437–451, 2007.

[109] S. H. Preetham and T. Lieuwen. Dynamics of laminar premixed flames forced by harmonic velocity disturbances. *AIAA Journal of Propulsion and Power*, 24(6): 1390–1402, 2008.

[110] S. Chaudhuri and B. M. Cetegen. Response dynamics of bluff-body stabilized conical premixed turbulent flames with spatial mixture gradients. *Combustion and Flame*, 156:706–720, 2009.

[111] D. Kim, J. G. Lee, B. D. Quay, and D. A. Santavicca. Effect of flame structure on the flame transfer function in a premixed gas turbine combustor. *ASME Journal of Engineering Gas Turbines Power*, 132:021502, 2010.

[112] K. T. Kim, J. G. Lee, H. J. Lee, B. D. Quay, and D. A. Santavicca. Characterization of forced flame response of swirl-stabilized turbulent lean-premixed flames in a gas turbine combustion. *ASME Journal of Engineering Gas Turbines Power*, 132:041502, 2010.

[113] C. Stone and S. Menon. Swirl control of combustion instabilities in a gas turbine combustor. In *Proceedings of the Combustion Institute*, volume 29, pages 155–160, 2002.

[114] R.E. Malecki, C.M. Rhie, R.G. McKinney, H. Ouyang, and S.A. Syed. Application of an advanced CFD-based analysis system to PW6000 combustor to optimise exit temperature distribution -Part I: Description and validation of the analysis tool. *ASME paper 2001-GT-62*, 2001.

[115] S. James, M.S. Anand, and B. Sekar. Towards improved prediction of aero-engine combustor performance using Large Eddy Simulations. *ASME paper GT2008-50199*, 2008.

[116] P. Domingo, L. Vervisch, S. Payet, and R. Hauguel. DNS of a premixed turbulent V flame and LES of a ducted flame using a FSD-PDF subgrid scale closure with FPI-tabulated chemistry. *Combustion and Flame*, 143(4):566–586, 2005. ISSN 0010-2180.

[117] C. Duwig and C. Fureby. Large eddy simulation of unsteady lean stratified premixed combustion. *Combustion and Flame*, 151:85–103, 2007. ISSN 0010-2180.

[118] C. Duwig. Study of a filtered flamelet formulation for large eddy simulation of premixed turbulent flames. *Flow, Turbulence and Combustion*, 79:433–454, 2007.

[119] S. M. R. Hosseini and C. J. Lawn. Non-linearities in the thermo-acoustic response of a premixed swirl burner. page Paper 590. Twelfth Internation Congress on Sound and Vibration, Lisbon, Portugal, 2005.

[120] A. P. Dowling. Nonlinear self-excited oscillations of a ducted flame. *Journal of Fluid Mechanics*, 346:271–290, 1997.

[121] R. B. Bird, E.E. Stewart, and E.N. Lightfoot. *Transport phenomena.* John Wiley and Sons Inc., 1960.

[122] J. Hirschfelder, C.F. Curtiss, and R.B. Bird. *Molecular Theory of Gases and Liquids.* New York: Wiley, 1954.

[123] E.R. Van Driest. On turbulent flow near a wall. *Journal of Aerospace Sciences*, 23(11):1007–1011, 1956.

[124] CANTERA, Object-oriented software for reacting flows. http://www.cantera.org, 2006.

[125] M. Barrere. Modeles de combustion. *Revue Générale de Thermique*, 148:295–308, 1974.

[126] K.N.C. Bray. Turbulent flows with premixed reactants in turbulent reacting flows. *Topics in Applied Physics*, page 115, 1980.

[127] N. Peters. Laminar flamelet concepts in turbulent combustion. volume 19, pages 1231–1250. 21st International Symposium on Combustion, The Combustion Institute, Pittsburg, 1986.

[128] R. Borghi. Mise au point sur la structure des flammes turbulentes. *Journal de chimie phisique*, 81:245, 1988.

[129] R.G. Abdel-Gayed and D. Bradley. Combustion regimes and the straining of turbulent premixed flames. *Combustion and Flame*, 76:213–218, 1989.

[130] R. Borghi and M. Destriau. *Combustion and flames, chemical and physical principles.* Editions TECHNIP, 1998.

[131] N. Peters. The turbulent burning velocity for large-scale and small-scale turbulence. *Journal of Fluid Mechanics*, 384:107–132, 1999.

[132] C. Duwig. A flamelet formulation for large eddy simulation. In *: I.P. Castro and P.E. Hancock (eds.) Advances in Turbulence IX*, pages 801–804. Proc. of 9th European Turbulence Conference, Southampton, UK, July, 2002.

[133] L. Vervisch, R. Hauguel, P. Domingo, and M. Rullaud. Three facets of turbulent combustion modelling: Dns of premixed v-flame, LES of lifted nonpremixed flame and rans of jet-flame. *Journal of Turbulence*, 5:1–36, 2004.

[134] C. Fureby. A fractal flame-wrinkling large eddy simulation model for premixed turbulent combustion. *Proceedings of the Combustion Institute*, 30(1):593–601, 2005. ISSN 1540-7489.

[135] F.F. Grinstein and C. Fureby. LES studies of the flow in a swirl gas combustor. *Proceedings of the Combustion Institute*, 30:1791–1798, 2005.

[136] C. Duwig and L. Fuchs. Study of flame stabilization in a swirling combustor using a new flamelet formulation. *Combustion Science and Technology*, 177:1485–1510, 2005.

[137] C. Duwig, L. Fuchs, P. Griebel, P. Siewert, and E. Boschek. Study of a confined turbulent jet: influence of combustion and pressure on the flow. *AIAA Journal*, 45(3):624–639, 2007.

[138] P.A. Libby and K.N.C. Bray. Countergradient diffusion in premixed turbulent flames. *AIAA Journal*, 19:205–213, 1981.

[139] I.G. Shepherd, J.. Moss, and K.N.C. Bray. Turbulent transport in a confined premixed flame. pages 423–431. 19th International Symposium on Combustion, The Combustion Institute, Pittsburg, 1982.

[140] D. Veynante, A. Trouvé, K.N.C. Bray, and T. Mantel. Gradient and countergradient scalar transport in turbulent premixed flames. *Journal of Fluid Mechanics*, 332:263–293, 1997.

[141] J. Piana, F. Ducros, and D. Veynante. Large eddy simulations of turbulent premixed flames based on the G-equation and a flame front wrinkling descriptions. 11th Symposium on Turbulence Shear Flows, Grenoble, France, 1997.

[142] J.A. Van Oijen, R.J.M. Bastiaans, G.R.A. Groot, and L.P.H. Goey. Direct numerical simulations of premixed turbulent flames with reduced chemistry: Validation and flamelet analysis. *Flow, Turbulence and Combustion*, 75(1-4):67–85, 2005.

[143] C. Fureby. A comparison of flamelet LES models for premixed turbulent combustion. *AIAA paper 2006-0155*, 2006.

[144] K.N.C. Bray and J.B. Moss. A unified statistical model of the premixed turbulent flame. *Acta Astronautica*, 4:291–319, 1977.

[145] San Diego mechanism 2005/12/01. Available online at http://maeweb.ucsd.edu/ combustion/cermech/index.html.

[146] G. Tang, Z.Y. Yang, and J.J. McGuirk. Numerical methods for large-eddy simulation in general co-ordinates. *International Journal for Numerical Methods in Fluids*, 46:1–18, 2004.

[147] Y. Morinishi, T.S. Lund, O.V. Vasilyev, and P. Moin. Fully conservative higher order finite difference schemes for incompressible flow. *Journal of Computational Physics*, 143:90–124, 1998.

[148] P. Beaudan and P. Moin. Numerical experiments on the flow past a circular cylinder at sub-critical reynolds number. Technical report, Report No. TF-62, Thermal Scienced Division, Department of Mechanical Engineering, Standford University, CA, 1994.

[149] G.F. Tang, Z.Y. Yang, G.J. Page, and J.J. McGuirk. Simulation of an impinging jet in crossflow using an LES method. *AIAA paper 2002-5959, Biennal International Powered Lift Conference, Virginia, USA*, 2002.

[150] G.F. Tang, Z.Y. Yang, and J.J. McGuirk. LES predictions of aerodynamic phenomena in LPP combustors. *ASME paper 2001-GT-465, ASME International Gas Turbine & Aeroengine Congress, New Orleans, USA*, 2001.

[151] M. Dianat, D. Jiang, Z.Y. Yang, and J.J. McGuirk. Simulation of scalar mixing in a co-axial jet flow. *Flow, Turbulence and Combustion*, 77:205–227, 2006.

[152] P.K. Sweby. High resolution schemes using flux limiters for hyperbolic conservation laws. *Journal on Numerical Analysis*, 21(5):995–1011, 1984.

[153] N. Branley and W.P. Jones. Large-eddy simulation of a turbulent non-premixed flame. In *Proceedings on the 11th Symposium on Turbulent Shear Flows, Grenoble, France, 8-10 Septembre*, 1997.

[154] L. Shunn and F. Ham. Consistent and accurate state evaluations in variable-density flow simulations. *Annual Research Briefs 2006. Center for Turbulence Research. Stanford University*, 2006.

[155] H. Forkel and J. Janicka. Large-eddy simulation of a turbulent hydrogen diffusion flame. *Flow, Turbulence and Combustion*, 65:163–175, 2000.

[156] C. D. Pierce. *Progress-variable approach for large-eddy simulation of turbulent combustion*. PhD thesis, Stanford University, Stanford, CA, 2001.

[157] A.W. Vreman, B.A. Albrecht, J.A. van Oijen, L.P.H. de Goey, and R.J.M. Bastiaans. Premixed and nonpremixed generated manifolds in large-eddy simulation of sandia flame d and f. *Combustion and Flame*, 153(3):394–416, 2008. ISSN 0010-2180.

[158] T. S. Lund. The use of explicit filters in large eddy simulation. *Computers and Mathematics with Applications*, 46(4):603 – 616, 2003. ISSN 0898-1221. Turbulence Modelling and Simulation.

[159] T. Brandt. Comparison between approaches to explicit filtering in large eddy simulation. *Journal of Structural Mechanics, Special issue for 18th Nordic Seminar on Computational Mechanics*, 38:59–62, 2005.

[160] T. Brandt. Study of large eddy simulation and smagorinsky model using explicit filtering. 36th AIAA Fluid Dynamics Conference and Exhibit,San Francisco, California, 2006.

[161] W. Deconinck. *Design and application of discrete explicit filters for large eddy simulation of compressible turbulent flows*. PhD thesis, Department of Aerospace Engineering, University of Toronto, 2008.

[162] T.F. Bogart. *Laplace Transforms and control systems theory for technology: including micro-processor based control systems*. John Wiley & Sons, 1982.

[163] S. Zeng and A. Manners. A multigrid solver for the solution of the pressure equation in Large-Eddy Simulations. Technical report, Dept. of Aero and Auto Eng., UTC Internal Report, Loughborough University, 1996.

[164] S. Hubbard and A.P. Dowling. Acoustic instabilities in premixed burners. *AIAA paper 95-2272*, 1998.

[165] B. Schuermans, V. Belluci, F. Guethe, F. Meili, P. Flohr, and C.O. Paschereit. A detailed analysis of thermoacoustic interaction mechanisms in a turbulent premixed flame. *ASME paper GT2004-53831*, 2004.

[166] C.C. Jahnke and F.E.C. Culick. Application of dynamical systems theory to nonlinear combustion instabilities. *AIAA Journal of Propulsion and Power*, 10 (4):508–517, 1994.

[167] S. R. Stow and A. P. Dowling. Thermoacoustic oscillations in an annular combustor. In *ASME paper 2001-GT-0037, ASME IGIT Conference, New Orleans, Louisiana, USA*, 2001.

[168] L. Crocco. Aspects of combustion instability in liquid propellant rocket motors. *Part I. Journal of the American Rocket Society*, 21:163–178, 1951.

[169] L. Crocco. Aspects of combustion instability in liquid propellant rocket motors. *Part II. Journal of the American Rocket Society*, 21,22, 1952.

[170] B.T. Chu and L.S.G. Kovasznay. Nonlinear interactions in a viscous heat-conducting compressible gas. *Journal of Fluid Mechanics*, 3:494–514, 1958.

[171] Simon R. Stow. LOTAN (Low Order Thermo-Acoustic Network model) version 2.4.6 user manual. Department of Engineering , University of Cambridge, 2005.

[172] S.R. Stow, A.P. Dowling, and T.P. Hynes. Reflection of circumferential modes in a choked nozzle. *Journal of Fluid Mechanics*, 467:215–239, 2002.

[173] A. Kurenov and M. Oberlack. Modelling turbulent premixed combustion using the level set approach for Reynolds Averaged models. *Flow, Turbulence and Combustion*, 74:387–407, 2005.

[174] P.D. Nguyen and P. Bruel. Deliverable D3.12-1, Project MOLECULES, No G4RD-CT-2000-0402. Available upon request: Pascal.Bruel@univ-pau.fr. 2003.

[175] L. Duchamp de Lageneste and H. Pitsch. Progress in large-eddy simulation of premixed and partially-premixed turbulent combustion. *Annual Research Briefs 2006. Center for Turbulence Research. Stanford University*, 2005.

[176] C. Safta, F. Ladeinde, X. Cai, and K. Alabi. A high-fidelity level-set flamelet approach for predicting turbulent reacting flows. Paper no. AIAA 2006-5090, 42nd AIAA/ASME/SAE/ASEE Joint Propulsion Conference, Sacramento, California, USA, 2006.

[177] M. Klein, A. Sadiki, and J. Janicka. A digital filter based generation of inflow data for spatially developing direct numerical or large eddy simulations. *Journal of Computational Physics*, 186(2):652–665, 2003.

[178] I. Veloudis, Z. Yang, J.J. McGuirk, and G.J. Page. Assessment of digital filter approach for generating large eddy simulation inlet conditions. In *Rodi, W., Mulas, M. (eds.), Proceedings of ETMM 6, Sardinia, Italy*, pages 307–316. Elsevier, Amsterdam, The Netherlands, 2005.

[179] L. Biferale, G. Boffetta, A. Celani, A. Crisanti, and A. Vulpiani. Mimicking a turbulent signal: sequential multiaffine processes. *Phisical Review*, 57(6):6261–6264, 1999.

[180] A. Huser and S. Biringen. Direct numerical simulation of turbulent flow in a square duct. *Journal of Fluid Mechanics*, 257:65–95, 1993.

[181] M. Rokni, C. O. Olsson, and B. Sundén. Numerical and experimental investigation of turbulent flow in a rectangular duct. *International Journal for Numerical Methods in Fluids*, 28(2):225–242, 1998.

[182] B. Rembold and L. Kleiser. Large-eddy simulation of compressible rectangular duct flow. *Proceeding in Applied Mathematics and Mechanics*, 2(1):352–353, 2003.

[183] U. Piomelli and E. Balaras. Wall-layer Models for Large-Eddy Simulations. *Annual Review of Fluid Mechanics*, 34:349–374, 2002.

[184] F. E. Ham, F. S. Lien, and A. B. Strong. Large-Eddy simulation of the square duct flow using a parallel PC cluster. *Journal of Fluid Mechanics*, 244:101–129, 2000.

[185] R. B. Dean. Reynolds number dependence of skin friction and other bulk flow variables in two-dimensional rectangular duct flow. *ASME Journal of Fluids Engineering*, 100(2):215–224, 1978.

[186] D.E. Abbott and S.J. Kline. Experimental investigations of subsonic turbulent flow over single and double backward-facing steps. *Trans. of ASME, Series D, Journal of Basic Engineering*, 84:317–325, 1962.

[187] D.J. Tritton. *Physical Fluid Dynamics*. Oxford Science Publications, Oxford, 1988.

[188] C. Duwig, M. Salewski, and L. Fuchs. Simulations of a turbulent flow past a sudden expansion: a sensitivity analysis. *AIAA Journal*, 46(2):408–419, 2008.

[189] R.W. Pitz and J.W. Daily. Combustion in a turbulent mixing layer formed at a rearward-facing step. *AIAA Journal*, 21(11):1565–1570, 1983.

[190] M.P. Escudier, P.J. Oliveira, and R.J. Poole. Turbulent flow through a plane sudden expansion of modest aspect ratio. *Physics of Fluids*, 14(10):3641–3654, 2002.

[191] J.C.R. Hunt, A. Wray, and P. Moin. Eddies, streams and convergence zones in turbulent flows. Technical report, Center for Turbulence Research Report, CTR-S88, 1988.

[192] L. Crocco. Research on combustion instability in liquid propellant rockets. In *Proceedings of the 12th International Symposium on Combustion, The Combustion Institute, Pittsburg*, pages 85–99, 1969.

[193] G. Hsiao, R. Pandalai, H. Hura, and H. Mongia. Combustion dynamic modelling for gas turbine engines. AIAA paper 98-3381, 34th AIAA/ASME/SAE/ASEE Joint Propulsion Conference, Cleveland, USA, 1998.

[194] U. Krüeger, H. Hüeren, S. Hoffmann, W. Krebs, P. Flohr, and D. Bohn. Prediction and measurements of thermoacoustic improvements in gas turbines with annular combustion systems. *Journal of Engineering Gas Turbine and Power*, 123(3):557–567, 2001.

[195] C.O. Paschereit, P. Flohr, and B. Schuermans. Prediction of combustion oscillations in gas turbine combustors. AIAA paper 2001-0484, 39th AIAA Aerospace Sciences Meeting and Exhibit, Reno, USA, 2001.

[196] W. Polifke, A. Poncet, C.O. Paschereit, and K. Doebbeling. Reconstruction of acoustic transfer matriced by instationary computational fluid dynamics. *Journal of Sound and Vibration*, 245:483–510, 2001.

[197] P.D. Nguyen. *Contribution expérimentale á l'étude des caractéristiques instationnaires des écoulements turbulents réactifs prémélangés stabilisés en aval d'un élargissement brusque symétrique.* PhD thesis, University of Poitiers, France, 2003.

[198] G. J. Bloxsidge, A. P. Dowling, and P. J. Langhorne. Reheat buzz: an acoustically coupled combustion instability. part2. theory. *Journal of Fluid Mechanics*, 193: 445–473, 1988.

[199] K.C. Schadow and E. Gutmark. Combustion instability related to vortex shedding in dump combustors and their passive control. *Progress in Energy and Combustion Science*, 18:117–132, 1999.

[200] T. Lieuwen. Nonlinear kinematic response of premixed flames to harmonic velocity disturbances. *Proceedings of the Combustion Institute*, 30:1725–1732, 2005.

[201] N. Noiray, D. Durox, T. Schuller, and S. Candel. A unified framework for nonlinear combustion instability analysis based on the flame describing function. *Journal of Fluid Mechanics*, 615:139–167, 2008.

[202] S. R. Stow and A. P. Dowling. Low-order modeling of thermoacoustic limit cycles. ASME paper 2004-GT-54245, ASME IGTI Conference, Vienna, Austria, 2004.

[203] P. J. Langhorne. Reheat buzz: an acoustically coupled combustion instability. part1. experiment. *Journal of Fluid Mechanics*, 193:417–443, 1988.

[204] L. Rayleigh. *The Theory of Sound.* Macmillan, London, 2nd edition, 1896.

[205] L. Crocco and S. Cheng. *Theory of combustion instability in liquid propellant rocket motors.* AGARDO-GRAPH number 8, Butterworths Science Publication, 2nd edition, 1956.

[206] F.C. Gouldin, K.N.C. Bray, and J.Y. Chen. Chemical closure for fractal flamelets. *Combustion and Flame*, 77:241–259, 1989.

Nomenclature

Roman Symbols

$\dot{m}$	Mass flow rate
$\mathcal{D}$	Mass diffusion coefficient
ρ	Density
A^+/A^-	Right/left travelling wave amplitudes
a_n,b_n,c_n,a'_n,b'_n,c'_n	Fourier coefficients
A_r	Expansion ratio
c	Progress variable
C_p	Specific heat capacity at constant pressure
C_s	Smagorinsky coefficient
D	Molecular diffusivity
d	Van Driest damping function
Da	Damköhler number
F	Flatness factor
h	Specific enthalpy
h	Step height
H_{ch}	Inlet channel height
$j_{k,i}$	i^{th} component of mass diffusion flux of species k into the mixture
K	Gain
k	Turbulent kinetic energy
Ka	Karlovitz number
l_t	Integral length scale
Le	Lewis number

M_k Molecular mass of species k

P Static pressure

Q Volume averaged heat release

q Conductive heat flux

Q_{hr} Fuel heat of reaction

R Reflection coefficient

R_u Universal gas constant

S Skewness factor

S Surface surrounding a volume V

s_d Displacement speed

S_{ij} Strain rate tensor

s_l Unstrained laminar flame speed

s_t Turbulent flame speed

Sc_t Turbulent Schmidt number

T Temperature

t Time

T_{relax} Relaxation time

u, v, w Velocities in x, y and z direction

u'_p Periodic coherent fluctuation

u'_s Stochastic turbulent fluctuation

u_τ Friction velocity

U_{bulk} Bulk velocity

u_i i^{th} component of mixture averaged velocity

V Volume

x, y, z Cartesian coordinates

x_i	Cartesian coordinate in i direction
Y	Reduced fuel mass fraction
y^+	Wall unit
Y_k	Mass fraction of species k
A	Forcing amplitude
c	Speed of sound
E	Total internal energy
f	Frequency
L	Turbulence macroscale
p(.)	Probability Density Function
Re	Reynolds number
s	Entropy
SLFM	Stationary Laminar Flamelet

Greek Symbols

Δt	Time step
δ_0^l	Diffusive/Zeldovich flame thickness
δ_{ij}	Delta dirac function
$\dot{\omega}_c$	Source term in progress variable equation
$\dot{\omega}_k$	Net rate of mass production of species k
$\dot{\omega}_T$	Heat release rate
ϵ	Dissipation rate of turbulent kinetic energy
η	Kolmogorov length scale
γ	Ratio of specific heats
κ	Von Kármán constant
κ	Wave number

λ	Thermal conductivity
$\mathcal{L}$	Laplace transform
μ	Dynamic viscosity
μ'	Bulk viscosity
μ_{SGS}	SGS viscosity
ν	Kinematic viscosity
ω	Frequency
Ω_{ij}	Vorticity tensor
ϕ	Equivalence ratio
ϕ	Reduced temperature
ψ	Phase
ψ_{ij}	Residual or SGS momentum flux
Σ	Subgrid scale flame surface density
τ	Time-delay
τ_{ij}	Viscous stress tensor
υ	Stoichiometric coefficient
Ξ	Subgrid scale flame wrinkling factor
ξ	Vorticity
G	Convolution kernel

Superscripts

$'$	Fluctuation above time or spatially averaged mean
$\hat{}$	Fourier transform/Filtering with test filter
-	LES filtering
$\tilde{}$	Density-weighted filtering
$\vec{}$	Vector

b Burnt stream

n Time step n

u Unburnt stream

$^+$ Wall units

Subscripts

b Burnt mixture

est Estimated value

F Fuel stream

in Inlet plane value

O Oxidiser stream

out Outlet plane value

u Fresh mixture

Z Impedance

Other Symbols

$*$ Convolution product

$\Delta h^0_{f,k}$ Standard heat of formation of species k at reference temperature T_0

Δ LES filter width

Δ_x Mesh spacing in direction x

Δ_y Mesh spacing in direction y

Δ_z Mesh spacing in direction y

$\langle\,\rangle$ Time average

$\langle\,\rangle_s$ Surface average

Symbols/Acronyms

CO Carbon monoxide

CO_2 Carbon dioxide

NO_x Nitrogen oxides

UHC Unburnt hydrocarbons

BML Bray-Moss-Libby model

CDS Central Difference Scheme

CF Corrugated Flamelet

CFD Computational Fluid Dynamics

CFL Courant-Friederichs-Lewy number

CLES Combusting Large Eddy Simulation

CV Control Volume

DFS Diffusive stability number

DNS Direct Numerical Simulation

EOS Equation Of State

ESD Energy Spectral Density

FSD Flame Surface Density

FTF Flame Transfer Function

LDA Laser Doppler Anemometry

LDV Laser Doppler Velocimetry

LES Large Eddy Simulation

LOTAN Low-Order Thermo-Acoustic Network

LPM Lean Premixed

LPP Lean-Premixed-Prevaporised

MG Multigrid

N-S Navier-Stokes

PDE Partial Differential Equation

PDF Probability Density Function

POD Proper Orthogonal Decomposition

RANS Reynolds-Averaged Navier-Stokes

RQL Rich-quench-lean

SGS Subgrid Scale

TFM Thickened-Flame Model

TKE Turbulent Kinetic Energy

TRZ Thin Reaction Zone

TVD Total Variation Diminishing

U-RANS Unsteady Reynolds-Averaged Navier-Stokes

List of Figures

List of Tables